Université de Liège – Faculté des Sciences Appliquées

Département d'Architecture, Géologie, Environnement et Constructions

Secteur *Structural Engineering*

A multiaxial constitutive model for concrete in the fire situation including transient creep and cooling down phases

Thomas Gernay

Ingénieur Civil des Constructions – Aspirant du F.R.S.-FNRS

Thèse présentée en vue de l'obtention

du grade de Docteur en Sciences de l'Ingénieur

Année académique 2011-2012

Université de Liège – Faculté des Sciences Appliquées

Département d'Architecture, Géologie, Environnement et Constructions

Secteur *Structural Engineering*

A multiaxial constitutive model for concrete in the fire situation including transient creep and cooling down phases

Thomas Gernay

Ingénieur Civil des Constructions – Aspirant du F.R.S.-FNRS

Thèse présentée en vue de l'obtention

du grade de Docteur en Sciences de l'Ingénieur

Année académique 2011-2012

Advisor

Prof. Dr. Ir. Jean-Marc Franssen

Research institute

Structural Engineering unit
Department ArGEnCo
Faculty of Applied Sciences
University of Liege, Belgium

Examination committee

Prof. Dr. Ir. Robert Charlier (chairman)	University of Liege Faculty of Applied Sciences	Department ArGEnCo Geomechanics and Geo- Engineering
Prof. Dr. Ir. Jean-Marc Franssen (advisor)	University of Liege Faculty of Applied Sciences	Department ArGEnCo Structural Engineering
Ass. Prof. Dr. Ir. Frederic Collin	University of Liege Faculty of Applied Sciences	Department ArGEnCo Geomechanics and Geo- Engineering
Emeritus Prof. Dr. Ir. Jean-Claude Dotreppe	University of Liege Faculty of Applied Sciences	Department ArGEnCo Structural Engineering
Prof. Dr. Ir. Luc Taerwe	Ghent University Faculty of Engineering	Department of Civil Engineering
Dr. Ir. Alain Millard	CEA - Atomic Energy and Alternative Energies Commission, France	Laboratoire de Mécanique Systèmes et Simulation
Prof. Dr. Ir. Ignacio Carol	Technical University of Catalonia, Spain	ETSECCPB–UPC School of Civil Engineering

Research funding

REMERCIEMENTS

Une thèse est un travail personnel, qui se nourrit néanmoins de la collaboration et de l'aide de nombreuses personnes. Au terme de ce travail, je souhaite exprimer ma gratitude à tous les collègues, membres de ma famille et amis qui m'ont soutenu et m'ont permis de le mener à bien.

Je souhaite avant tout remercier mon promoteur, le Prof. Jean-Marc Franssen, pour m'avoir suggéré ce sujet intéressant et pour m'avoir guidé durant mes recherches. Son expertise dans le domaine de l'ingénierie structurale au feu et la modélisation numérique a été une précieuse source d'inspiration, et sa rigueur m'a aidé à progresser en tant que chercheur. En outre, j'ai pris plaisir à intégrer sa dynamique équipe de recherches durant ces dernières années.

Toute ma gratitude va également au Dr. Alain Millard pour m'avoir accueilli durant six mois au centre C.E.A. de Saclay. L'expertise d'Alain a apporté beaucoup à ce travail et j'étais très heureux de travailler à ses côtés. Mon séjour à Paris a été pour moi une grande réussite tant sur le plan de la recherche que sur le plan humain et je l'en remercie. Par ailleurs, je le remercie d'avoir accepté de faire partie de mon jury de thèse.

Je remercie le Prof. Robert Charlier pour avoir accepté de faire partie de mon comité de thèse et en tant que tel pour m'avoir suivi et conseillé durant mes recherches. Je lui sais gré de ses conseils et des éclaircissements qu'il m'a apportés à plusieurs occasions. Je le remercie également d'avoir accepté la présidence de mon jury de thèse.

Je sais gré au Prof. émérite Jean-Claude Dotreppe de m'avoir incité à me lancer dans la recherche, ainsi que de m'avoir suivi durant ces années de thèse également en tant que membre de mon comité de thèse. Je le remercie en outre d'avoir accepté de faire partie du jury.

Je remercie le Prof. Ignacio Carol de l'UPC, le Prof. Luc Taerwe de Gent University ainsi que le Prof. Frédéric Collin pour avoir accepté de faire partie du jury de ma thèse.

Je remercie chaleureusement mes collègues de l'équipe feu de l'ULg : François Hanus, Christophe Peigneux, Thibaut Fohn, Baptiste Cowez, Nicola Tondini, Eric Wellens, Fabien Dumont et Adil Ouardani. Outre leur grande disponibilité, ils ont chacun participé à créer un environnement de travail très convivial et agréable. Je tiens à remercier tout particulièrement Christophe pour son amitié et pour son aide précieuse. Je remercie également Nicolas Blaise, Thomas Canor et Nicolas Lebrun pour l'assistance qu'ils m'ont chacun apportée en diverses occasions, ainsi que tous les autres collègues du service pour leur bonne humeur et le plaisir de partager un diner ou un café (et un croissant) avec eux. Je remercie aussi Chantal Marquet

et Sabine Houten pour leur contribution importante à la bonne vie du service, et leur réponse toujours souriante à mes nombreuses requêtes.

J'ai pris grand plaisir à côtoyer l'équipe du C.E.A. durant mon séjour chez eux et je tiens donc à remercier tous les membres du laboratoire LM2S pour leur accueil. Je remercie tout particulièrement Jean-Luc Fayard pour m'avoir intégré dans son équipe, pour m'avoir fait découvrir la vie du service et fait visiter diverses installations du centre ainsi que pour sa sollicitude durant tout mon séjour.

Je remercie Thomas Hansoulle du bureau Greisch pour nos discussions constructives, pour ses conseils et pour m'avoir apporté des éléments intéressants concernant les problèmes d'implémentation numérique. Je suis sûr que nous aurons encore l'occasion de collaborer à l'avenir et je m'en réjouis.

Je suis reconnaissant au Dr. Vassilis K. Papanikolaou ainsi qu'au Dr. Mihail Petkovski pour leur aimable autorisation d'utilisation de certaines de leurs illustrations dans ce travail. Je remercie également le Dr. Yihai Li pour son assistance dans la collecte des données de son essai au feu, simulé dans ce travail.

Enfin, j'exprime ma gratitude au FNRS pour m'avoir financé durant ma thèse ainsi qu'à l'Université de Liège.

Mes remerciements ne seraient évidemment pas complets sans souligner le soutien moral de ma famille et de mes amis. Je tiens à exprimer toute ma gratitude à ma maman, à Caroline et à Elodie pour leur soutien continu ainsi que pour le bonheur que j'ai d'être en leur compagnie. Merci de savoir écouter comme personne et conseiller judicieusement quand il le faut. J'ai une pensée pour mon papa, notamment parce qu'il m'a donné une curiosité précieuse pour mener à bien un tel travail. Je remercie également Véronique, Marc, Marie, Anthony, Perrine et Fanny, ainsi que Thibaut et Julien, pour leur précieuse amitié et leur présence quotidienne durant au moins une partie de ces années ; c'était une grande chance de pouvoir compter sur eux et de partager de nombreux moments au cours desquels nous avons parlé de bien d'autres choses que du comportement du béton. Je pense aussi à Sébastien, Justin, Olivier, Florent et Sam que je remercie de leurs visites occasionnelles à mon bureau qui agrémentaient mon quotidien de chercheur. Merci aussi à Benjamin, Julien R. et Marylène pour les bons moments partagés et les échanges de mails souvent absurdes, parfois abscons, mais toujours prompts à donner le moral. Enfin, avant tout, je remercie de tout mon cœur ma future épouse Julie, pour sa présence, son attention, son intelligence et son humour. Sa présence à mes côtés m'incite à entreprendre les projets les plus ambitieux, et chaque réalisation est aussi la sienne.

ABSTRACT

Purpose - The present thesis aims to develop an efficient and reliable multiaxial concrete model for implementation in finite elements softwares dedicated to the analysis of structures in fire. The need for proper concrete model remains a very challenging task in structural (fire) engineering because of the complexity of the concrete mechanical behavior characterization and the severe requirements for the material models raised by the development of performance-based design.

Methodology - The thesis opted for a phenomenological approach for modeling the thermo-mechanical behavior of concrete. The specifications of the model are based on the study of published experimental data of concrete samples tests and on the specific needs related to the applications in structural fire engineering. With these specifications in mind, a state of the art review of concrete models is conducted in order to choose the general theoretical framework that best fits the criteria for the development of the new model. The thesis presents the theoretical development of the model and its numerical implementation in a finite elements software. Numerical simulations of experimental tests are then performed to verify that the model satisfy the specifications.

Findings - The combination of elastoplasticity theory and damage theory allows to develop a phenomenological model suitable for concrete behavior modeling within the pragmatic and robust theoretical framework of continuum constitutive models based on smeared crack approach. The state of damage in concrete, assumed isotropic, is modeled by means of a fourth order damage tensor to capture the unilateral effect. When complex performance-based situations are considered, the effect of transient creep strain at high temperature must be taken into account by an explicit term in the strain decomposition. A generic transient creep model is therefore developed based on experimental data and the model is calibrated to yield the same results as the Eurocode implicit model in simple prescriptive situations. The concrete model comprises a limited number of parameters that can be identified by three simple tests; besides, a standard set of values to be used in predictive calculations is clearly defined for these parameters. Numerical simulations can deal with all stress states as the model is developed as fully three-dimensional. A large number of examples highlight the capabilities of the model that range from the modeling of sample tests to the modeling of large scale composite structures developing membrane action.

Limitations – Due to the assumption that damage and plasticity are driven by the same internal variables in the model, a limitation appears for capturing the concrete post-peak behavior in highly confined stress states. This assumption allows

for reducing the number of parameter but it restrains the domain of applicability of the model; it is suggested to adopt a different approach if the behavior in multiaxial compression at high confinement level has to be accurately captured. Another limitation of the model is related to the localization issue, which is only partly addressed in this work by means of the regularization of the crack energy. Further works should bring a more elaborated response while considering the case of reinforced concrete structures, in which numerous cracks develop. Finally, several simplifying assumptions have been adopted to restrain the scope of the research; for instance, the phenomenon of spalling has not been considered.

Practical implications - The thesis includes implications for the development of advanced numerical tools for the simulation of concrete structures at ambient temperature and at high temperature. The use of such advanced tools in the design may lead to significant reduction in the building costs and to improved robustness of the structures.

Value – The thesis contributes to fulfil an identified need to make available proper constitutive concrete model for implementation in finite elements softwares dedicated to the analysis of structures in fire. Special care is given to the numerical robustness of the model and to the clear definition of the material parameters as the model is intended to be used by structural (fire) engineers in real applications.

TABLE OF CONTENTS

TABLES AND FIGURES

Tables and figures

Tables and figures

Tables and figures

NOMENCLATURE

x	Scalar	$\underline{x}$	Vector (1st order tensor)
x_{20}	Scalar at ambient temperature	$\underline{\underline{x}}$	Matrix (2nd order tensor)
x_T	Scalar at temperature T	$\underline{\underline{\underline{x}}}$	4th order tensor
$\dot{x}$	Time derivative of x	δ_{ij}	Kronecker symbol
$x^{(s)}$	Value at time step (s)	T	Temperature
$x^{(i)}$	Value at iteration (i)	$x^{(n)}$	Value at internal iteration (n)
Δx	Increment of x between two steps or iterations	τ	Time
$\partial x/\partial y \, ; \partial_y x$	Partial derivative of function x with respect to variable y	$\varepsilon, \varepsilon_{tot}$	Total strain
$Dx/Dy \, ; D_y x$	Total derivative of function x with respect to variable y	ε_p	Plastic strain
dx	Total differential of x	ε_{el}	Elastic strain
ε_{tr}	Transient creep strain	ε_{th}	Free thermal strain
ε_σ	Instantaneous stress-related strain	ε_m	Mechanical strain
$LITS$	Load Induced Thermal Strain	ε_{cr}	Basic creep strain
ε_{c1}	Peak stress strain in uniaxial compression	ε_{vol}	Volumetric strain
ε_{t1}	Peak stress strain in uniaxial tension	υ	Poisson's ratio h
ε_{c0}	Ultimate strain in uniaxial compression	G_f	Fracture energy
ε_{t0}	Ultimate strain in uniaxial tension	E	Young modulus
f_c	Uniaxial compressive strengt	E_t	Tangent modulus
f_b	Equibiaxial compressive strength	σ	Stress
f_t	Uniaxial tensile strength	s	Deviatoric stress
f_{c0}	Limit of elasticity in uniaxial compression	p	Hydrostatic stress
α	Coefficient of internal friction	α_g	Dilatancy parameter
κ_{c1}	Accumulated plastic strain at peak stress in compression	l_c	Characteristic length
g_t , g_c	Crack energy density per unit volume	$\overline{G}_t$	Crack energy in tension
x_c	Adimensional compressive dissipated energy parameter	$\overline{G}_c$	Crack energy in compression

---

$\tilde{d}_c$ Compressive damage at peak stress

$\overline{\sigma}_i$ i[th] eigenvalue of the effective stress tensor

$\underline{n}_i$ i[th] normalized eigenvector corresponding to $\overline{\sigma}_i$

ψ Helmoltz free energy per unit mass

$\overline{\underline{\sigma}}^+ ; \overline{\underline{\sigma}}^-$ Positive and negative components of the effective stress tensor

$\overline{I}_1$ First invariant of the effective stress tensor

$\overline{J}_2$ Second deviator invariant of the effective stress tensor

$\underline{\underline{C}}_0$ 4th order isotropic linear-elastic stiffness

$F_t ; F_c$ Tensile and compressive yield functions

c_j Constraints for the status of yield function

$\overline{\underline{D}}_a$ Effective algorithmic modulus

$\overline{\underline{\sigma}}$ Effective stress tensor

$H(\bullet)$ Heaviside function

W Stored-energy function

$\mathcal{D}$ Dissipation per unit volume

$\overline{\sigma}^{tr}$ Trial (predictor) effective stress

$\underline{\underline{D}}$ 4th order damage tensor

d_t Tensile damage scalar

d_c Compressive damage scalar

$\underline{\underline{I}}$ 4th order identity tensor

$\underline{q}$ Set of plastic internal variables

ρ Specific mass

G_j Plastic potential associated to the yield function F_j

$\underline{\underline{D}}_t$ Tangent modulus (nominal algorithmic consistent)

$\underline{\underline{P}}^+ ; \underline{\underline{P}}^-$ 4th order projection tensors of the effective stress tensor

$\underline{\underline{Q}}^+ ; \underline{\underline{Q}}^-$ 4th order projection tensors of the rate of the effective stress tensor $\dot{\overline{\underline{\sigma}}}$

$\dot{\lambda}_j$ Plastic multiplier associated to the plastic potential G_j

κ_j Plastic internal variable associated to the yield function F_j

$\overline{\tau}_j(\kappa_j)$ Hardening function in the effective stress space associated to the yield function F_j

$\underline{\underline{H}}$ 4th order tensor for generalization of transient creep strain to multiaxial stress state

$\phi(T)$ Function considered for the calculation of the transient creep

$\underline{x} \cdot \underline{y} = z \quad \rightarrow \quad z = x_i y_i$ Tensor product contracted once (scalar product)

$\underline{\underline{x}} \cdot \underline{y} = \underline{z} \quad \rightarrow \quad z_i = x_{ij} y_j$ Tensor product contracted once

$\underline{\underline{x}} \cdot \underline{\underline{y}} = \underline{\underline{z}} \quad \rightarrow \quad z_{ij} = x_{ik} y_{kj}$ Tensor product contracted once (matrix mult.)

$\underline{\underline{x}} : \underline{\underline{y}} = \underline{\underline{z}} \quad \rightarrow \quad z_{ij} = x_{ijkl} y_{kl}$ Tensor product contracted twice

$\underline{x} \otimes \underline{y} = \underline{\underline{z}} \quad \rightarrow \quad z_{ij} = x_i y_j$ Tensor product

$\underline{\underline{x}} \otimes \underline{\underline{y}} = \underline{\underline{Z}} \quad \rightarrow \quad Z_{ijkl} = x_{ij} y_{kl}$ Tensor product

$\underline{\nabla} = \dfrac{\partial}{\partial x_i} \underline{e}_i$ Nabla (vector differential operator)

GENERAL INTRODUCTION

Problem

Elevated temperatures in buildings or other structures are the result of accidental situations such as fire or accident in nuclear vessel. Fire caused by the terrorist attacks on 9/11 was the cause of collapse of the twin towers of the World Trade Center. This same day, fire also developed in the 7-World Trade Center tower and resulted in the collapse of the structure, although the structure had not been directly damaged by the attack. Another example of fire in a skyscraper occurred in the Windsor Tower in Madrid, on 12 February 2005. The fire lasted for almost 24 hours but the main structure of the Windsor Tower, in reinforced concrete, resisted the high temperatures without collapsing. Elevated temperatures may also arise in nuclear vessel due to accidental situation in nuclear power plant. Such a disaster occurred at the Fukushima Daiichi Nuclear Power Plant, following the earthquake and tsunami on 11 March 2011.

It is the responsibility for the designer of a structure to take into account the effects of accidental situations. Elevated temperatures in the range between 100°C and 1000°C affect a structure because they lead to thermal elongations and because they affect the materials that make up the structure. Thermal elongations induce restraint loads in statically indeterminate structures. Materials subjected to elevated temperatures experience a decrease in their strength and stiffness properties; in addition, many other phenomena may appear and affect fire-exposed materials, depending on the considered material and other conditions. For instance fire-exposed concrete may experience explosive spalling. Wood is a thermally degradable and combustible material and therefore the behavior of fire-exposed wood is totally distinct from the behavior of non-combustible materials. Elevated temperatures in a structure thus result in a decrease in the load bearing capacity of the structure and possibly in the development of restraint forces in the structure. As a consequence, a structure subjected to elevated temperatures will collapse under gravity loads that are lower than the ultimate loads at ambient temperature. Combinations of loads that include elevated temperatures have to be verified by the designer of a structure. The discipline that aims at assessing the performance of building structures in accidental fire situations is referred to as structural fire engineering.

Structural concrete is widely used in civil engineering due to its many advantages. The advantages of structural concrete include the high durability in severe environmental conditions, the workability and formability into various structural components, the possible short duration of works on site due to the development of precast concrete, the high stiffness of structural concrete elements compared to steel structural elements. Another important advantage of structural concrete is its fire resistance. The high fire resistance of concrete structures is due to the high massivity of the concrete sections that limits the elevation of

---

temperature in the core of the section and in the steel rebars. As a result, fire resistance can be achieved in building structures made of concrete at economic costs. The use of structural concrete is thus common in applications where the fire resistance is an issue or in other applications where elevated temperature can arise such as in nuclear vessels.

The analysis of the nonlinear behavior of structures in fire can be performed by the numerical finite elements method. The numerical analysis of a structure subjected to fire may be divided into three parts: first, the evolution of the gas temperature in the compartment is established; secondly, the thermal analysis is conducted to determine the temperature distribution in the structural members; thirdly, the mechanical analysis is conducted to assess the behavior of the structure subjected to elevated temperatures. For these numerical simulations, temperature dependent constitutive relationships are required for the materials used in the structure such as, for instance, steel and concrete. The thermal analysis requires proper modeling of the thermal behavior of the different materials, whereas the mechanical analysis requires proper modeling of their mechanical behavior at elevated temperatures. The constitutive relationships that are used in the numerical analyses of structures in fire have important implications on the global behavior of the structure. Characterization of the properties at elevated temperatures of the different materials used in civil engineering has been the subject of many research efforts in the last decades. However, the development of reliable and accurate constitutive models remains an up-to-date, very challenging issue for several load bearing materials.

Constitutive relationships for modeling the mechanical behavior of concrete are highly needed due to the numerous applications of structural concrete. The main criteria that a constitutive model should fulfill are the reliability, the accuracy and the numerical robustness. It is also important that the parameters of the model can be identified by elementary tests. However, concrete is a complex composite material composed by aggregates and hydrated cement paste. The mechanical behavior of concrete is highly nonlinear and influenced by microcracking. In tension, concrete has a very low strength and brittle behavior, and it experiences softening. In compression, concrete exhibits inelastic volumetric expansion. At elevated temperatures, characteristic phenomena may develop such as explosive spalling or transient creep strain. For all these reasons, proper constitutive modeling of concrete, especially at elevated temperatures, is a difficult and still unaccomplished task.

Aim

The objective of the present thesis is to develop multiaxial constitutive relationships for concrete at elevated temperatures, for applications in structural fire engineering. The relationships have to capture accurately the behavior of structural concrete under complex multiaxial stress states, at ambient and elevated temperatures. The stress-temperature history has an influence on the material response and it has to be taken into account. Numerical robustness of the model is required as the model is intended to be implemented in numerical software to be used for the calculation of structures in fire. Finally, the developed model is intended to be used by structural fire engineers in real projects; for this reason, it should be a

generic model with reasonable amount of parameters that can be identified by elementary tests.

Presentation of the work

Chapter I aims to define the requirements of a multiaxial constitutive model for concrete at high temperature. Therefore, the thermo-mechanical behavior of concrete material is first discussed based on experimental tests given in the literature. As this thesis is oriented towards structural applications, special emphasis is given to the different phenomena that have implications at the structural level. Practical examples of structural applications are then considered to highlight particular requirements of models dedicated to structural fire engineering.

Chapter II presents a state-of-the-art review of the existing models for concrete. Intensive research has been done in the last decades on constitutive modeling of concrete at ambient temperature. Special care is given to the models based on the elastoplasticity theory and on the damage theory. For concrete at elevated temperatures, important research efforts have been done to develop uniaxial models but the multiaxial modeling is still suffering from a lack of experimental data. Therefore, only few multiaxial models have been reported in the literature. The phenomenon of transient creep strain is investigated in details in this study as it develops in fire-exposed concrete and has implications on the structural behavior; the existing models for transient creep strain are thus discussed. Beyond the review of the concrete theories, this chapter compares the different approaches with the aim to draw a general theoretical framework and to adopt the main assumptions for the new model developed in the next chapters.

Chapter III presents an original uniaxial constitutive model for concrete that includes an explicit term for transient creep strain. The theory of the model is presented and the implementation process in the software SAFIR for nonlinear calculation of building structures in fire is described. Then, the validation of the model is performed against experimental data given in the literature. Namely, several tests on concrete columns in fire are simulated using the uniaxial concrete model and the results are discussed.

In Chapter IV, an original multiaxial constitutive model for concrete at elevated temperatures is developed. The model is based on the coupling of plasticity and damage theories. The model contains an explicit term for computation of transient creep strain; this term is derived by generalization to multiaxial stress states of the uniaxial transient creep strain model developed in Chapter III. The theoretical aspects and implementation process of the model in the software SAFIR are given. The multiaxial constitutive model for concrete has been implemented for solid finite elements (fully multiaxial model) and for shell finite elements (plane-stress model).

Chapter V presents the validation of the developed multiaxial concrete model. Experimental tests performed in the literature on concrete samples are simulated with SAFIR to validate the ability of the model to capture the behavior of concrete subjected to different

stress and temperature paths. These tests also allow for calibrating the parameters of the model. Then, a series of experimental tests performed on structural elements are simulated with SAFIR. In order to demonstrate the predictive capability of the model, the values of the parameters used for the structural applications are the values fixed by calibration on the sample tests. Finally, numerical simulations of structures are conducted to validate the ability of the concrete model to be used for real applications. For instance, a full scale fire test performed on 27 February 2010 in Ireland on a steel-concrete composite floor is simulated with SAFIR using the new concrete model and the numerical and experimental results are compared.

CHAPTER I – REQUIREMENTS OF CONCRETE MODELS FOR STRUCTURAL FIRE ENGINEERING

The objective of this chapter is to examine the requirements of concrete constitutive models dedicated to applications in the field of structural fire engineering. These requirements are based, on the one hand, on the experimentally observed concrete behavior that models should be able to reproduce and, on the other hand, on the specific applications for which models are developed. Proper definition of these requirements is the preliminary step for the development of a new material model.

In the first part of the chapter, the phenomenological behavior of concrete material is described based on experimental tests published in the literature. The behavior is described at ambient temperature and then at elevated temperature. Obviously, an important requirement for concrete constitutive models is the ability to capture the phenomenological behavior of the material with sufficient accuracy.

In the last part of the chapter, specific applications of structural fire engineering are presented. These applications highlight the fact that severe requirements should apply to constitutive models intended to be used for the simulation of structures in fire. The numerical analysis by the finite element method of a structure comprises an important number of finite elements and integration points; therefore constitutive models should be robust. For structures subjected to natural fire, the analysis is conducted during the heating phase but also during the cooling phase of the fire, when the gas temperatures and, thus, the temperatures in concrete are cooling down from maximum to ambient temperature. As a consequence, the concrete model should also capture the behavior during cooling. Finally, the analysis on concrete samples may not reproduce the complexity and variety of situations in the stress-temperature domain that arise in a structure. In a heated structure, thermal gradients induce thermal stresses which create varying stresses in the cross section even if the load on the structure is constant during the fire. As a result, the consideration of the practical applications for which the model is developed leads to specific requirements for this model.

I.1. Mechanical behavior of concrete at ambient temperature

In this section, the mechanical behavior of concrete at ambient temperature is discussed based on experimental observations. Different types of loading are explored and the corresponding stress-strain curves are given. A phenomenological approach is adopted to describe the different aspects of the material behavior.

I.1.1. Uniaxial compression

Concrete exhibits a highly nonlinear behavior in uniaxial compression. Results of an experimental test in uniaxial compression on a cubical specimen (van Mier, 1984) are plotted in Fig. I.1-1. The left part of the figure shows the relationships between the axial and lateral strains ε_1 and ε_2 and the stress. The right part of the figure depicts the relationships between the volumetric strain ε_{vol} and the stress. The concrete response is approximately linearly elastic up to 30% of the maximum compressive strength. During this elastic phase, the material exhibits volumetric contraction. Above 30% of the maximum compressive strength, the concrete response becomes more and more nonlinear up to about 70-90% of the maximum compressive strength. The rate of volumetric strain changes sign and the volume of the sample comes back to its initial value. Eventually the material reaches the peak stress value which is the maximum compressive strength f_c. The maximum compressive strength measured on concrete cylinders typically ranges from about 12 MPa to 90 MPa; by definition it is referred to normal strength concrete (NSC) when the compressive strength is lower than 55 MPa and to high strength concrete (HSC) when it is higher than 55 MPa (European Committee for Standardization, 2004b). The axial strain corresponding to this maximum compressive strength is called strain at peak stress ε_{c1} and ranges between 1.8 ‰ and 2.8 ‰. Typically when concrete reaches the peak stress value, the volumetric strain ε_{vol} has become positive which means that the material exhibits volumetric expansion. This volumetric expansion under compressive loading is called dilatancy. Immediately after the peak stress value, the axial strain-stress curve descends. Concrete behavior has changed from nonlinear hardening to nonlinear softening. The axial and lateral strains continue increasing (in absolute value) whereas the stress decreases. This softening is associated with strong dilatancy. Finally, crushing failure occurs at an ultimate axial strain ε_{c0}.
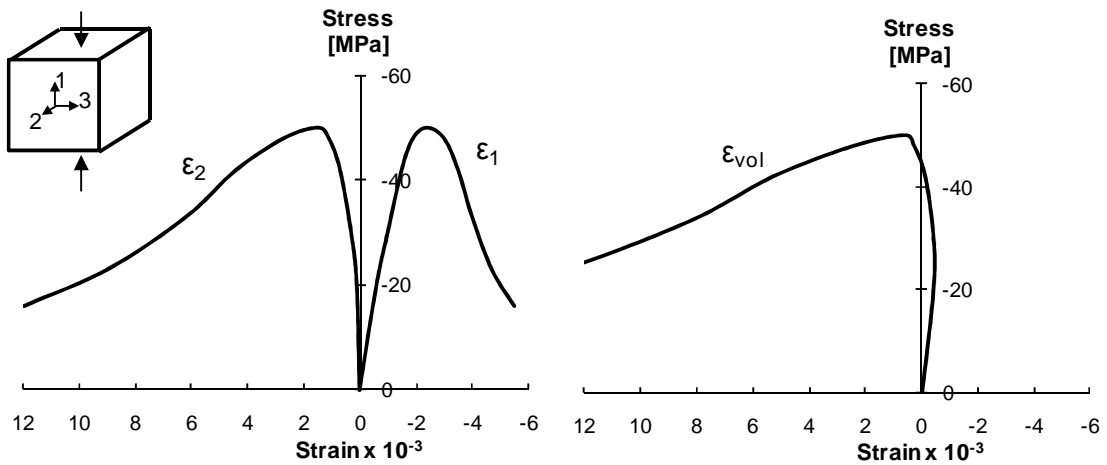
Fig. I.1-1: Concrete behavior in uniaxial compression (van Mier, 1984)
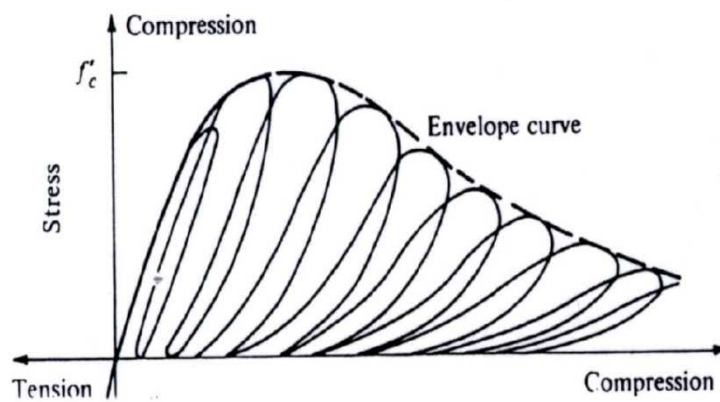
Fig. I.1-2: Cyclic behavior of concrete in uniaxial compression (from Karsan and Jirsa, 1969)

The main phenomena observed in Fig. I.1-1 are: nonlinear hardening, nonlinear softening and dilatancy. The nonlinear behavior of concrete that consists in hardening followed by softening is the result of the initiation and growth of microcracks in the cementitious matrix. Under uniaxial compression these microcracks propagate mainly in planes parallel to the direction of loading; these microcracks are called splitting cracks (Jirasek and Bazant, 2002). Concrete is a frictional material in which aggregates, as a granular material, are capable of undergoing extensive plastic flow (Ortiz, 1985). Dilatancy is the result of the inelastic split strains that develop in concrete.

Experimental data for concrete subjected to compressive cyclic loading has been given in the literature, see Fig. I.1-2 (Karsan and Jirsa, 1969). These experimental results show the degradation of the elastic properties and the development of inelastic strains in the material. The former phenomenon is the direct result of the microcracks. The latter phenomenon is due to the fact that, to some extent, the opening of microcracks is irreversible. Hysteretic unloading loops are also observed. This energy dissipation is probably the result of the friction between microcrack surfaces and of the water movement in loaded concrete.

I.1.2.   Multiaxial compression

Concrete is a pressure-sensitive material. Under multiaxial compression, the axial splitting phenomenon is inhibited or slowed down by lateral compressive stresses; the concrete is confined. This phenomenon increases the strength and ductility of concrete as compared to the uniaxial compression case. Experimental results of an equibiaxial compression test, i.e. with applied stress ratio $\sigma_1 : \sigma_2 = 1$ and $\sigma_3 = 0$, are given in Fig. I.1-3 (Kupfer, et al., 1969). The maximum compressive stress observed on the graph, called equibiaxial compressive concrete strength f_b, is higher than the uniaxial compressive strength f_c. As shown by various experimental studies (Papanikolaou and Kappos, 2007), the ratio between equibiaxial and uniaxial concrete strength f_b / f_c decreases with increasing concrete strength f_c; this ratio ranges from approximately $f_b / f_c = 1.20$ for $f_c = 20\,\mathrm{MPa}$ to approximately 1.08 for $f_c = 90\,\mathrm{MPa}$.
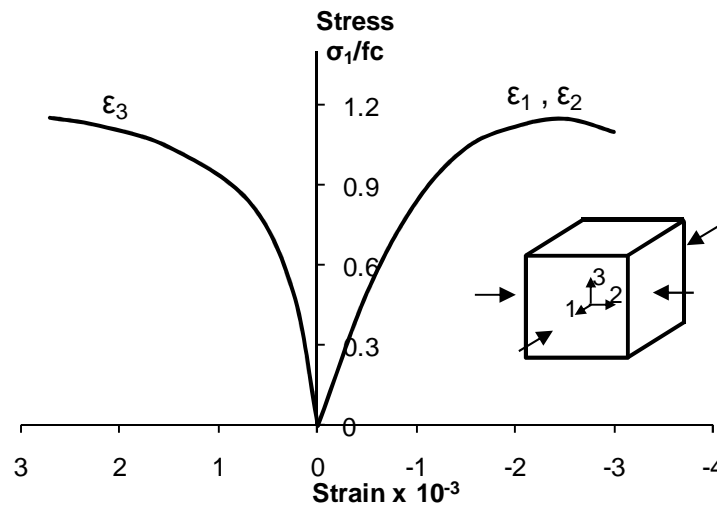
Fig. I.1-3: Concrete behavior in equibiaxial compressive loading (Kupfer, et al., 1969)

Under triaxial compression the confinement effect is more pronounced compared to biaxial compression. Fig. I.1-4 shows experimental results on the concrete response to triaxial compression (Imran, 1994). The concrete samples have been subjected to hydrostatic loading up to certain stress level; then the stress in direction 3 has been increased until failure of the specimen whereas the stresses in directions 1 and 2 were kept constant. The concrete strength and ductility increase with the confinement level. Highly confined concrete exhibits remarkable ductility. This may be explained by the closing of the pores which results from the hydrostatic pressure.

Recent experimentations on concrete cylinders have investigated the behavior of concrete in a very highly confined stress state (Poinard, et al., 2010). Fig. I.1-5 shows the evolution of the deviatoric stress s, defined as the difference between the axial stress σ_x and the confinement (hydrostatic) stress p, versus the axial strain ε_x and the circumferential strain ε_θ for a concrete sample confined with 200 MPa confinement stress p. The increase in

strength due to high confinement is dramatic as the maximum deviatoric stress increases from 40 MPa for the simple compression test to approximately 420 MPa for the test with 200 MPa confinement. The very brittle behavior observed in the uniaxial compression test is not reproduced in high confinement tests; concrete under high confinement exhibits a plateau after the peak stress. During the experiment, the concrete specimen has been subjected to various unloading-reloading sequences to examine the influence of confinement on the degradation of the elastic properties. Compared to the response in uniaxial compression plotted in Fig. I.1-2, the stiffness degradation is much less pronounced in case of high confining pressures as can be seen by observing the slope of the unloading branches in Fig. I.1-5.
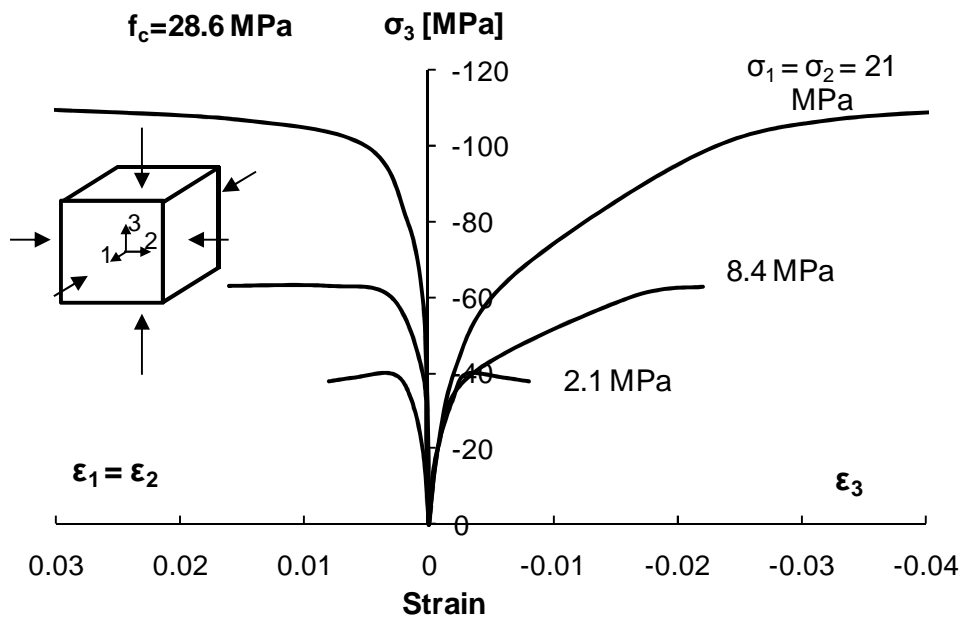
Fig. I.1-4: Concrete behavior in triaxial compression at various confinement levels (Imran, 1994)
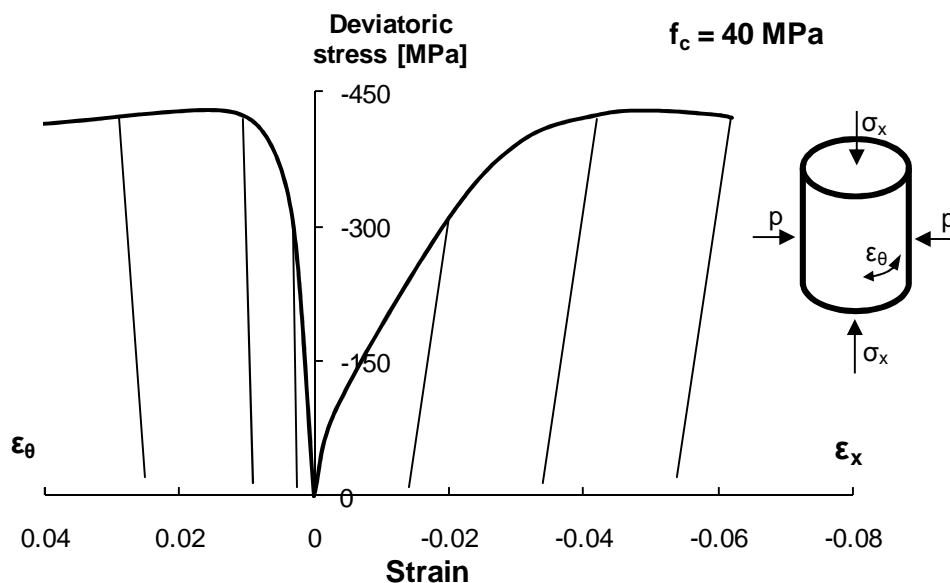
Fig. I.1-5: Triaxial test at 200 MPa confinement (Poinard, et al., 2010)

The authors have observed that at low confinement (less than 60 MPa for a concrete with a compressive strength of 40 MPa), the concrete behavior is cohesive-brittle and governed by damage phenomena, in the sense of stiffness loss, whereas under high confinement (higher than 150 MPa), the concrete behavior tends toward that of a granular material governed by plasticity, and the damage phenomenon is inhibited. That can be explained by the fact that at low confining pressure, behavior is governed by the porous and cohesive cement matrix and the failure is caused by a mechanism of considerable localized damage; this failure is characterized by a peak stress that reveals the brittle behavior of concrete. However under high confinement, the cement matrix is compacted and loses its cohesion during the hydrostatic phase; the concrete behaves like a granular stacking arrangement and failure is caused by diffuse damage without any loss of strain homogeneity (Poinard, et al., 2010).

I.1.3.   Uniaxial tension

Concrete is characterized by a dramatically lower strength in tension than in compression; the ratio between uniaxial tensile strength and compressive strength ranges from 0.05 to 0.10 (Hugues and Chapman, 1966). The low tensile strength of concrete results in tensile cracking at a very low stress compared with compressive stresses. The direction of the tensile cracks is normal to the axis of maximum principal stress. This tensile cracking leads to a degradation of the elastic properties of the material. The concrete response under uniaxial tension is illustrated in Fig. I.1-6 (Gopalaratnam and Shah, 1985). The response is almost elastic linear up to the maximum tensile strength. Beyond this point, the behavior is very brittle and concrete experiences softening. Finally, failure under uniaxial tension occurs at a very limited ultimate strain ε_{t0} compared to compressive loading.
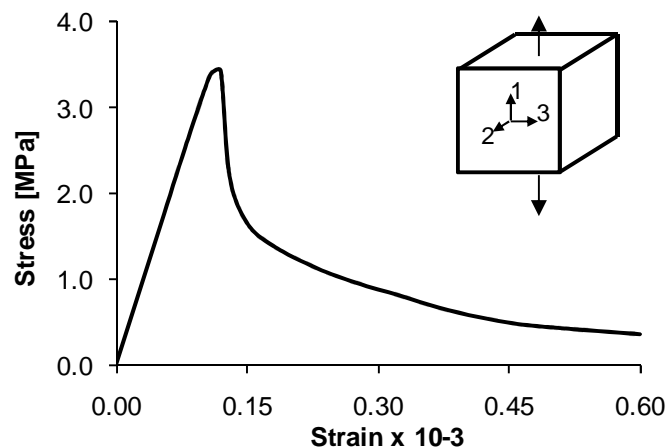
Fig. I.1-6: Concrete behavior in uniaxial tension (Gopalaratnam and Shah, 1985)

The cyclic behavior of concrete in uniaxial tension has been experimentally investigated, e.g. by Gopalaratnam and Shah (1985), and it is illustrated in Fig. I.1-7. Analysis of the concrete response during the unloading-reloading cycles confirms the degradation of the elastic properties that result from tensile cracking; the slope of the unloading branches decreases when the maximum strain applied in tension increases. The hysteretic phenomenon is less pronounced in uniaxial tension compared with uniaxial compression. This may be due

to the fact that the friction between microcrack surfaces, which is an important cause of the energy dissipation in concrete, is much likely to arise during compressive loading compared with tensile loading.
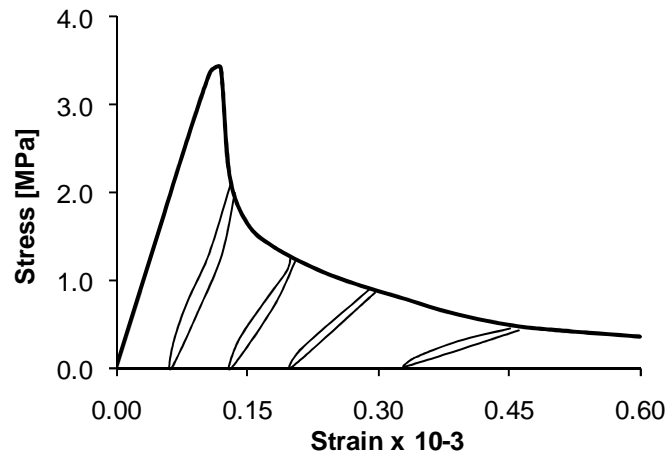
Fig. I.1-7: Cyclic behavior of concrete in uniaxial tension (Gopalaratnam and Shah, 1985)

I.1.4.   Failure criterion

Different authors have worked to establish the failure surface, or strength envelope, of concrete; this failure surface bounds the domain of maximum admissible stresses in the material, thus defining the largest possible resistance of the material. Concrete is a composite material composed by aggregates and a cementitious matrix and failure in concrete is driven by the cohesive strength of the cement paste and the frictional adhesion of aggregate interaction. Therefore, failure surface for concrete must reproduce pressure sensitivity on the one hand, and tensile strength limiters on the other (Menetrey and Willam, 1995).
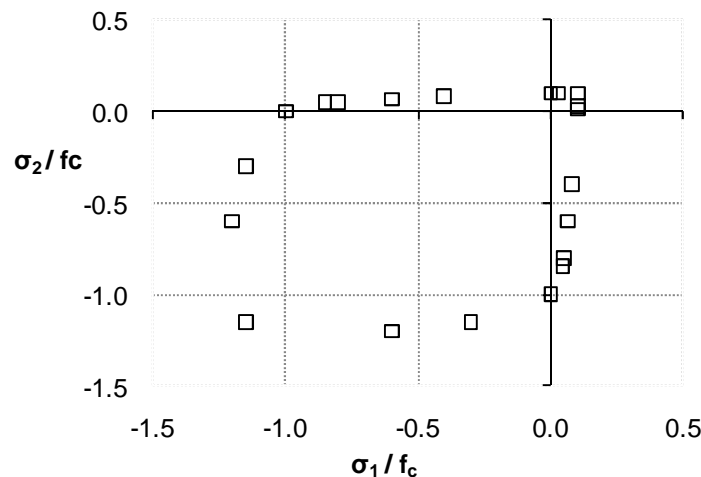
Fig. I.1-8: Test data of the biaxial strength envelope of concrete (Kupfer and Gerstle, 1973)

Experimental results of the biaxial strength envelope of concrete are plotted in Fig. I.1-8. Despite the almost four decades since they were obtained, these famous experimental results by Kupfer and Gerstle (1973) are still valid and used in the literature; see for instance

Jirasek and Bazant (2002). These results indicate that compressive loading in one direction increases the compressive strength in the perpendicular direction, compared to the uniaxial compressive strength. However, compressive loading in one direction decreases the maximum tensile stress that can be transmitted by the material in the perpendicular direction, because it promotes the development of cracks. This latter combination of principal stress corresponds, for instance, to pure shear.

Under multiaxial loading, the strength envelope in the principal stress space is a deformed cone, with three planes of symmetry that all intersect at the hydrostatic axis (Jirasek and Bazant, 2002), see Fig. I.1-9. By definition, the multiaxial stress can be decomposed into a hydrostatic component, which tends to change the volume of the stressed body, and a deviatoric component, which tends to distort the body. The hydrostatic part of the stress is measured on the hydrostatic axis, which is defined in the stress space by the relation $\sigma_x = \sigma_y = \sigma_z$. The deviatoric planes are perpendicular to the hydrostatic axis; they are defined by the relation $\sigma_x + \sigma_y + \sigma_z = \text{constant}$. The deviatoric part of the stress is measured on a deviatoric plane as the distance between the point that represents the stress and the hydrostatic axis. The deviatoric sections (octahedral plane projections) have the form of a rounded triangle whose shape changes from almost triangular for tensile and low compressive hydrostatic pressures to almost circular for high compressive hydrostatic pressures (Launay and Gachon, 1971). This variable shape of the deviatoric sections traduces the change from quasi-brittle to ductile behavior with increasing hydrostatic pressure (Grassl, et al., 2002).

The intersections of the strength envelope with halfplanes that start from the hydrostatic axis are called meridians, see Fig. I.1-9; these meridians are curved for concrete. They can be used for describing the change of shape of the deviatoric sections. These meridians are different for different values of the deviatoric polar angle θ, since the deviatoric section of the strength envelope is not circular.
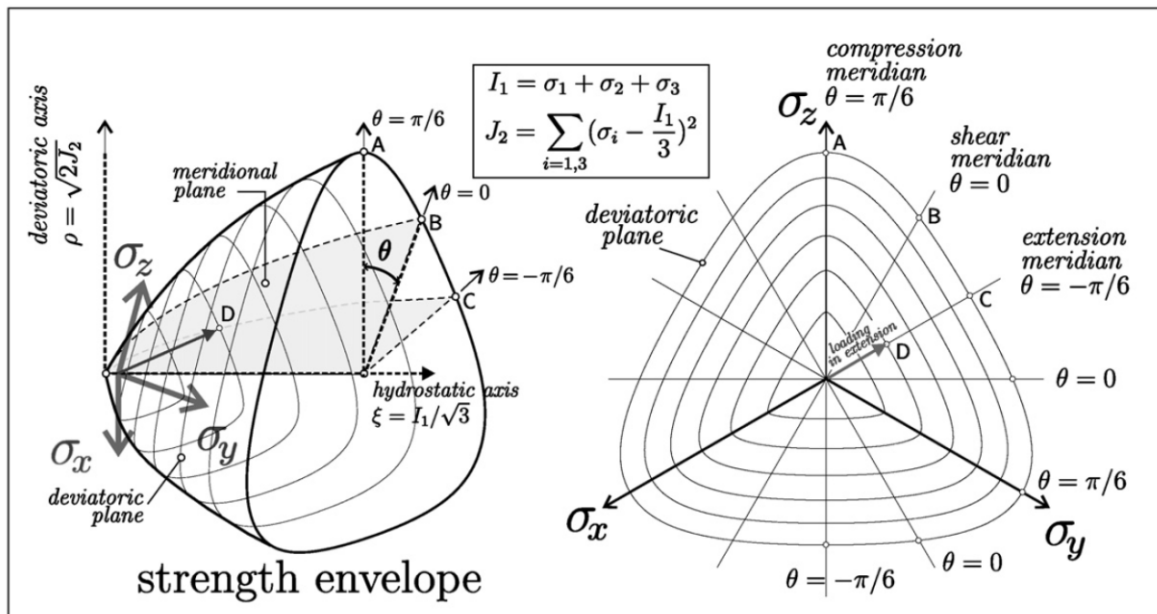
Fig. I.1-9: Multiaxial behavior of concrete: strength envelope, deviatoric sections and meridional planes (from Petkovski, 2010)

I.1.5.   Cyclic behavior in tension-compression

When subjected to uniaxial cyclic tensile-compressive loading, concrete exhibits a sudden recovery of stiffness during unloading from the tensile region to the compressive region. This phenomenon, called unilateral effect, is a consequence of closing the tensile cracks. The response in compression is not affected by the previous tensile loading because the previously opened tensile cracks are perpendicular to the cracks that develop in compression. Experimental results of the unilateral effect in concrete (Reinhardt, 1984) are plotted on Fig. I.1-10; these results have been obtained on concrete specimens with a rectangular cross-section subjected to cyclic tests up to the envelope curve in uniaxial tension and with large compressive lower stress. The softening behavior in tension and the degradation of the elastic properties due to tensile cracking is clearly visible in the tensile stress zone (positive values of the stress). The stiffness changes when the stress state switches from tension to compression; the material exhibits a virgin compressive stiffness due to closing of the tensile cracks under compressive stresses.
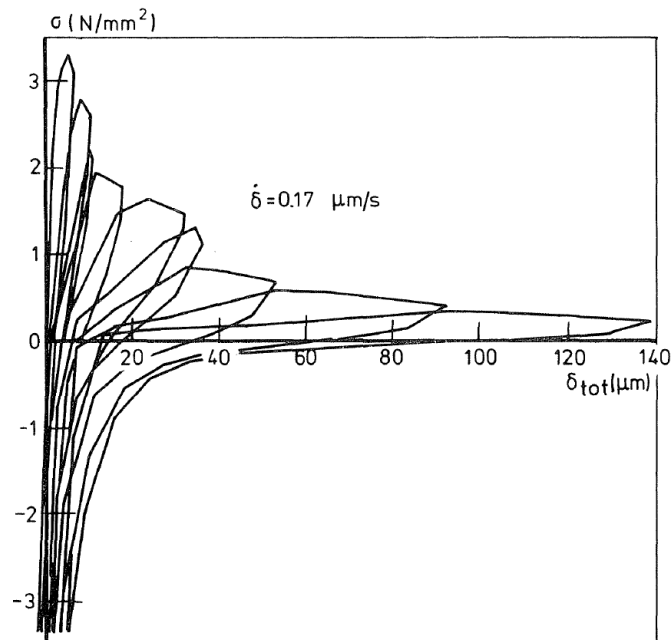
Fig. I.1-10: Cyclic tensile-compressive loading (from Reinhardt, 1984)

I.2. Mechanical behavior of concrete at high temperature

This section deals with the mechanical behavior of concrete at elevated temperature. At the micro-level, elevated temperatures cause the dehydration of concrete (Lin, et al., 1996). Microcracks may also develop in heated concrete due to the difference in thermal dilatation coefficient between the aggregates and the cement paste. These degradations affect the mechanical behavior of the material. As was the case in the previous section for ambient temperature, the concrete behavior at elevated temperature is discussed based on experimental observations. Analysis of the test data at elevated temperature leads to the definition of the evolution laws of the mechanical properties with temperature. Next, specific phenomena of heated concrete are presented: the free thermal strain, the transient creep strain and the spalling phenomenon.

I.2.1. Uniaxial compression

The concrete response in uniaxial compression depends on the temperature. Experimental stress-strain curves for concrete in uniaxial compression at different temperatures (Schneider, 1988) are plotted in Fig. I.2-1. The curves plotted on the graph are called instantaneous stress-strain curves because they result from a steady state test; loading of the concrete sample is performed at constant temperature. It can be seen that an increase in temperature results in a degradation of the stiffness and compressive strength of concrete. The decrease in stiffness and compressive strength of concrete due to temperature effects is irreversible. An increase in temperature also results in an increase in the material ductility.
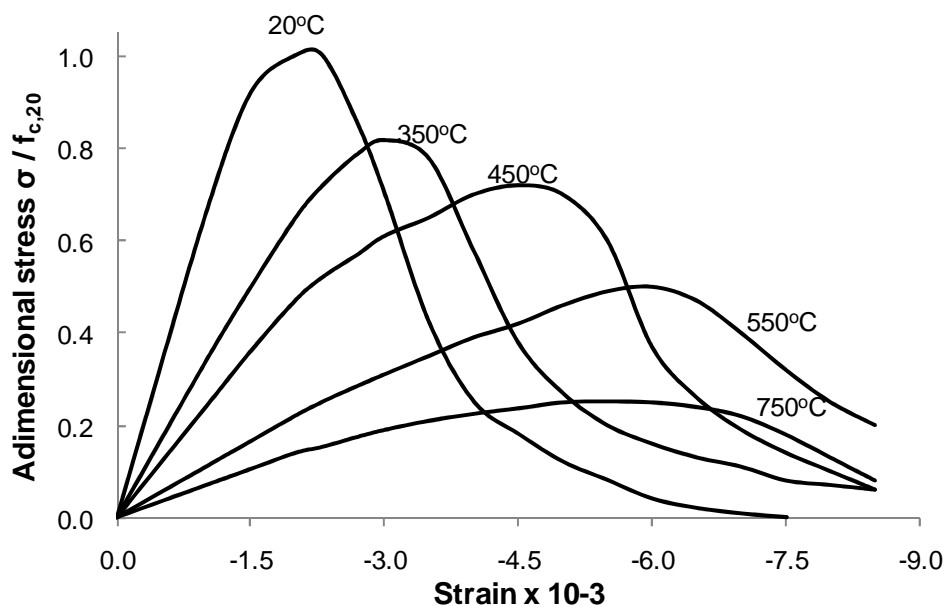
Fig. I.2-1: Instantaneous uniaxial compression response at high temperature (Schneider, 1988)

The concrete response in uniaxial compression at elevated temperature is influenced by many factors such as the type of aggregate or the water content. More information about the influence of these factors on the mechanical properties of concrete is given in Section I.2.4. In addition, the concrete response in uniaxial compression largely depends on the applied compressive stress during heating (Schneider, 1985). For this reason, an additional strain component is defined in heated concrete to make a distinction between concrete that is loaded at elevated temperature and concrete that is heated under load; this strain component is called transient creep strain. More information about transient creep strain is given in Section I.2.6.

I.2.2.   Biaxial compression

Experimental tests on the concrete behavior under equibiaxial compressive loading at elevated temperature have been published in the literature (Ehm and Schneider, 1985). The obtained stress-strain relationships are presented in Fig. I.2-2; during the tests simultaneous stress increase of the same order was applied in directions 1 and 2 whereas direction 3 was free. It can be seen that the stiffness and the equibiaxial compressive strength decrease with temperature increase.

The strength envelopes in biaxial compression at elevated temperatures have been experimentally established by Ehm and Schneider (1985), see Fig. I.2-3. The equibiaxial compressive strength f_b decreases with temperature but, at a given temperature, the decrease in equibiaxial compressive strength is smaller than the decrease in uniaxial compressive strength f_c. The confinement effect is more pronounced in heated concrete because elevated temperatures cause the degradation of the micro-structure and an increase in porosity. As a result, the strength envelope shape changes towards a more elongated shape at elevated temperatures.
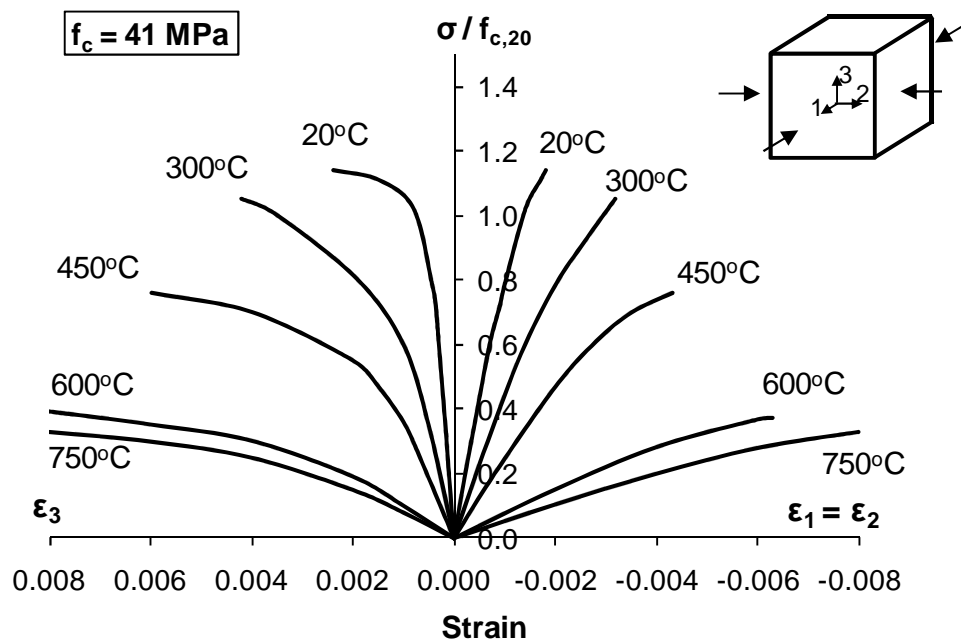
Fig. I.2-2: Equibiaxial compressive loading at high temperatures (Ehm and Schneider, 1985)

$$\sigma_1 (T) / f_{c,20}$$
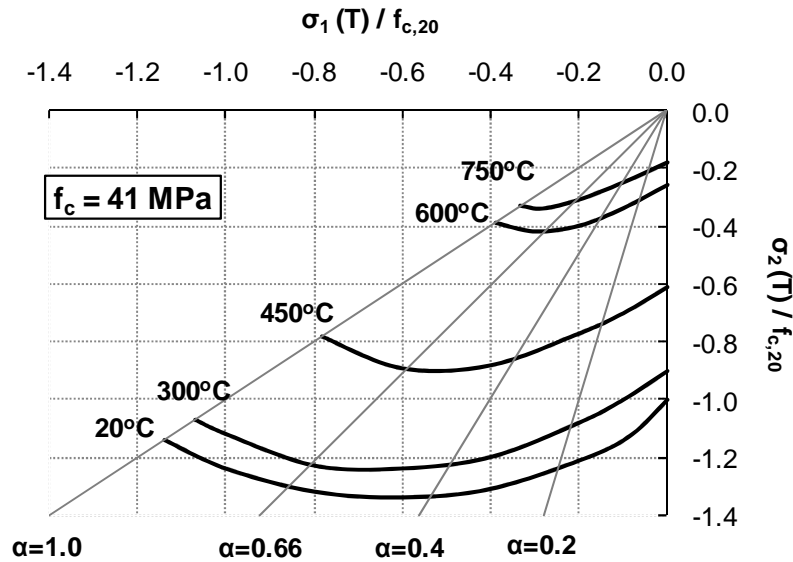
Fig. I.2-3: Bicompressive strength envelope at high temperatures (Ehm and Schneider, 1985)

I.2.3.   Uniaxial tension

The concrete stress-strain response in uniaxial tension is affected by temperature. The response to uniaxial tensile tests at high temperatures has been investigated on high strength concrete by Felicetti and Gambarova (1999), see Fig. I.2-4. It can be seen that the uniaxial tensile strength and the stiffness decrease with an increase in temperature. At a given temperature, the reduction in tensile strength is greater than in compressive strength. For instance at 250°C, the tensile strength obtained by Felicetti and Gambarova has already been reduced by 45% compared with its value at ambient temperature, whereas the diminution in compressive strength is about 10% at 250°C. Experimental results of the uniaxial tension test also show that the strain at peak stress remains approximately constant when temperature increases; however, the ductility after peak stress increases with temperature.
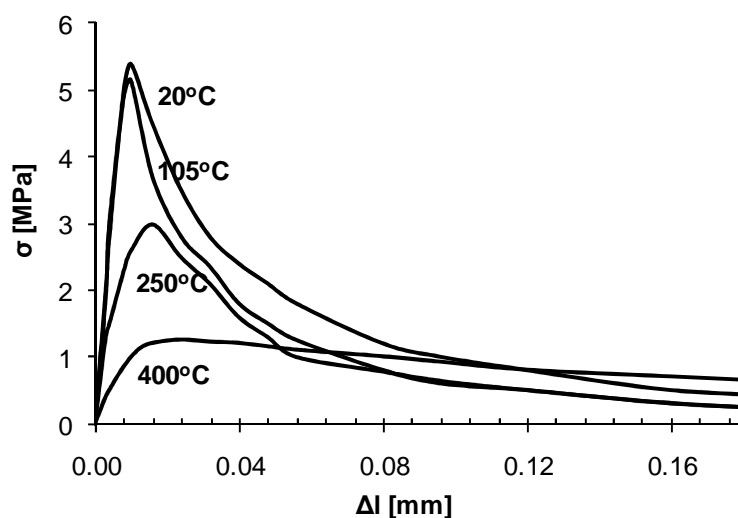
Fig. I.2-4: Uniaxial tension at high temperatures (Felicetti and Gambarova, 1999)

I.2.4.   Evolution of the mechanical properties with temperature

The analysis of the concrete response in uniaxial compression, biaxial compression and uniaxial tension has shown that the mechanical behavior of concrete depends on temperature. This section explores the temperature dependency of the characteristic parameters used to describe the concrete response illustrated in the previous sections. Although many experimental tests have been conducted to establish the temperature-dependency of some of the concrete material properties, e.g. the uniaxial compressive strength and elastic modulus, the effect of temperature is still poorly established for other concrete properties such as Poisson's ratio or fracture energy, due to a lack of experimental data. In addition, intensive research efforts are still needed in the field of concrete modelling at elevated temperatures as very few models are available for practical applications.

I.2.4.1.   *Uniaxial compressive strength*

The concrete compressive strength is affected by temperature. Many authors have performed experimental tests to characterize the variation of concrete compressive strength with temperature. These tests can be divided in different categories depending on the employed method. A first category of tests is interested in the steady-state compressive strength of concrete at elevated temperature; the concrete specimens are first heated to the pre-specified temperature and then they are loaded at a certain load rate (or strain rate) while the temperature is kept constant. A second category of tests is interested in the transient-state compressive strength of concrete at elevated temperature; the concrete specimens are first loaded and then they are heated at a certain heat rate while the applied load is kept constant. Indeed the compressive strength-temperature relationship is influenced by the compressive stress applied on the concrete specimen during heating (Schneider, 1985). A third category of tests is interested in the residual compressive strength of concrete after heating to given temperature and cooling down to room temperature. An additional loss of compressive strength is observed in concrete during cooling compared to the strength loss at maximum temperature (Li and Franssen, 2011).

In addition with the dependency on the test method, the compressive strength-temperature relationship is affected by many factors among which the aggregate/cement ratio and the type of aggregates are the most significant (Schneider, 1985). The decrease in strength of siliceous concrete occurs at lower temperatures compared to calcareous and lightweight concrete. By contrast, the original strength of concrete does not appear to have significant effect on the decreasing rate of the compressive strength with temperature. When the residual strength is assessed, the results also depend on the cooling regime adopted during the test.

Experimental results on the evolution of the concrete compressive strength with temperature are plotted in Fig. I.2-5. These experimental results have been obtained from steady-state tests performed on concrete with siliceous and carbonate aggregates (Abrams, 1971; Schneider, 1985). Typically, concrete experiences a slight increase in compressive strength approximately between 90°C and 200°C due to the drying that occurs during this period. Beyond this point, the compressive strength decreases slightly until approximately

400°C and then it decreases dramatically between 400°C and 800°C. At 800°C, the compressive strength of siliceous concrete has dropped to less than 20% of its value at room temperature, whereas for calcareous concrete it has dropped to around 30%.
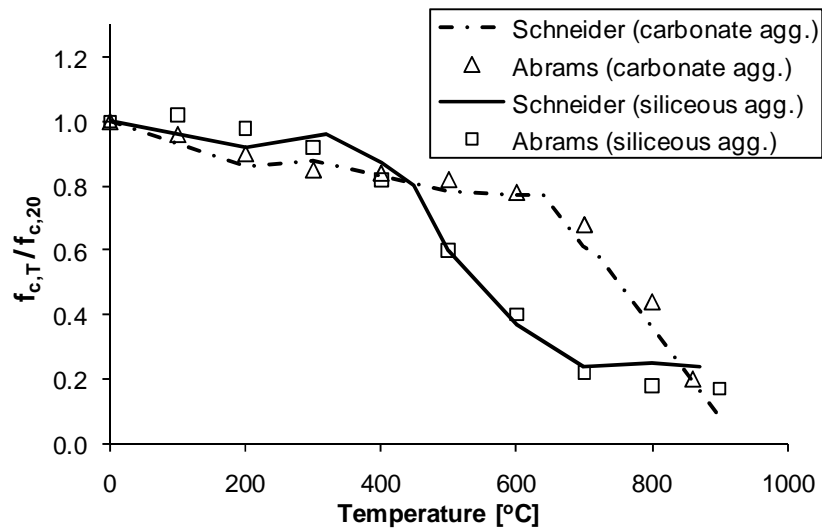
Fig. I.2-5: Evolution of the concrete compressive strength with temperature

I.2.4.2. *Elastic modulus*

The response in uniaxial compression at different temperatures shows that the elastic modulus of concrete decreases with increasing temperature (Fig. I.2-1). The elastic modulus-temperature relationship is affected primarily by the same factors influencing the compressive strength-temperature relationship. The type of aggregate has a strong influence; lightweight aggregate concretes indicate the lowest decrease in the modulus of elasticity and siliceous aggregate concretes the highest one (Schneider, 1985). The elastic modulus decreases monotonically as the temperature increases, unlike the behavior of the compressive strength. Experimental results on the variation of the elastic modulus with temperature (Anderberg, 1976; Felicetti and Gambarova, 1999; Schneider, 1988; Li, 1993 cited in Xiaoa and König, 2004) are plotted in Fig. I.2-6. A significant scatter in the experimental results is observed.
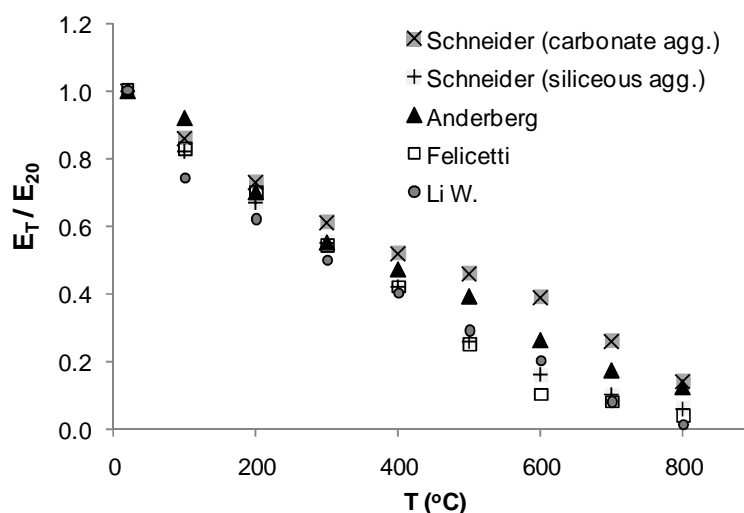
Fig. I.2-6: Evolution of the concrete elastic modulus with temperature

I.2.4.3. _Poisson's ratio_

There are few experimental data on the variation in Poisson's ratio with temperature. Experimental results are given by Maréchal (1970 cited in Schneider, 1985) and more recently by Luccioni, et al. (2003). These results are presented in Fig. I.2-7. In the tests by Luccioni, et al., the Poisson's ratio was evaluated after cooling down to ambient temperature using two different cooling regimes: a slow cooling regime (the specimen was left in the furnace) and a fast cooling regime (the specimen was rapidly cooled with spurts of cold water during half an hour). Results show that the Poison's ratio decrease with temperature increase. The decrease is greater when the specimen is cooled rapidly than when it is cooled slowly; the thermal shock produced by the rapid cooling probably leads to additional cracking induced by internal stresses.
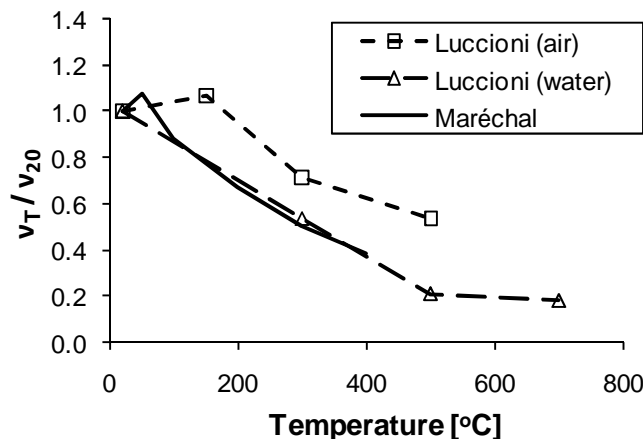
Fig. I.2-7: Evolution of Poisson's ratio with temperature

I.2.4.4. _Uniaxial tensile strength_

Research on the evolution of concrete tensile strength with temperature is limited. These tests are usually carried out using the cylinder splitting test method. It should be distinguished between the tests performed at high temperatures and the tests performed in the cold state after exposure to high temperatures and cooling back to ambient temperatures (tests on the residual properties). Test data indicate that the residual tensile strength is somewhat lower than the tensile strength at elevated temperatures (Schneider, 1985). The main factor that affects the tensile strength at high temperatures is the type of aggregate. Experimental results of the tensile strength at high temperatures can be found in the works by Anderberg and Thelandersson (1976), Schneider (1985) and Lie (1992); these results are presented in Fig. I.2-8. Tests results on the residual tensile strength after exposure to high temperatures obtained by Xu, et al. (2003) are also presented in Fig. I.2-8. Results show that the tensile strength is even more affected by high temperatures than the compressive strength.
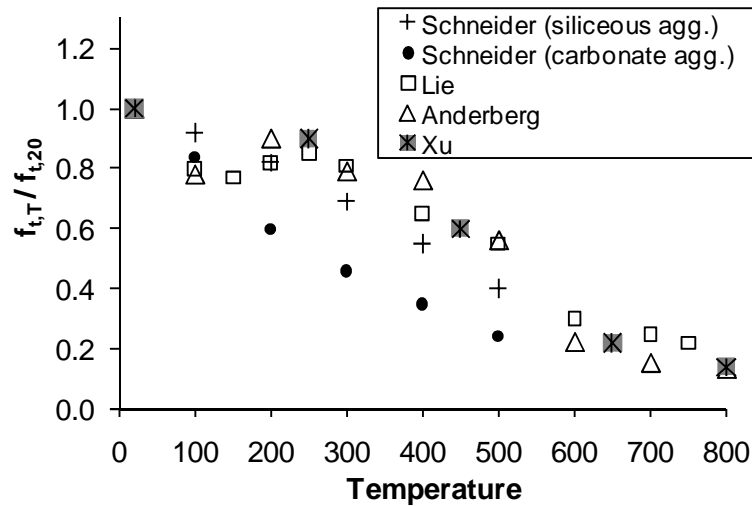
Fig. I.2-8: Evolution of the concrete tensile strength with temperature

I.2.4.5. *Fracture energy*

The fracture energy G_f is an important material property for concrete modelling; it can be defined as the energy absorbed to create a unit area of fracture surface (Menou, et al., 2006). Experimental results of temperature dependency of the fracture energy are reported in the literature (Baker, 1996; Nielsen and Bicanic, 2003; Menou, et al., 2006) but these results are difficult to compare due to difference in test specimens and test methods.

Experimental results from the literature are presented in Fig. I.2-9. All the presented tests are performed after cooling down to ambient temperature; the presented values are residual values. The tests performed by Menou, et al. (2006) are presented for ordinary (OC) and high-strength (M75C) concrete with calcareous aggregate and for high-strength concrete with silica-calcareous aggregate (M75SC). The tests performed by Nielsen and Bicanic (2003) are presented for basalt concrete (BC) and gravel concrete (GC). Baker (1996) has investigated the influence on the cooling regime; his results are presented for fast-cooled specimens and slow-cooled specimens.
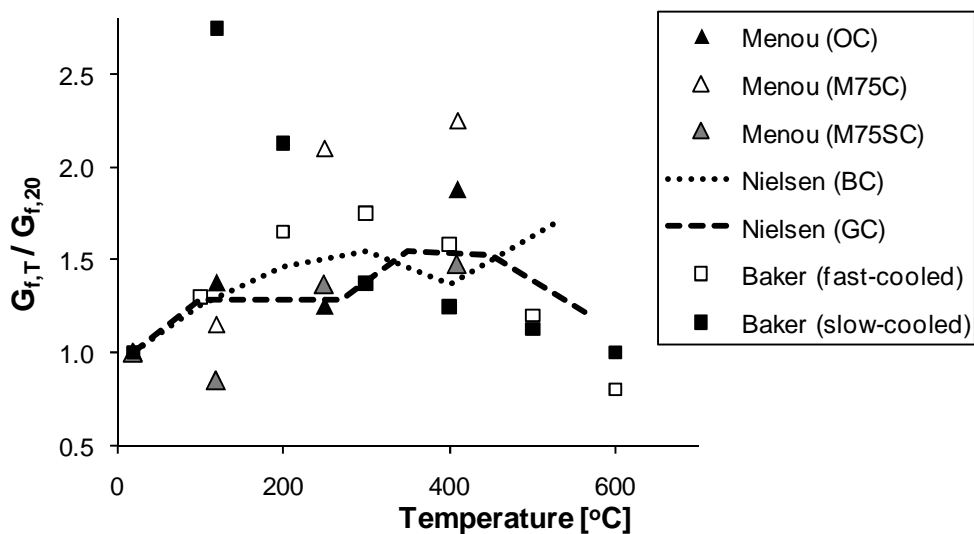
Fig. I.2-9: Evolution of the concrete fracture energy with temperature

A significant scatter in the experimental results is observed in Fig. I.2-9. The fracture energy seems to increase with increasing temperatures until it reaches a maximum at temperatures near 300°C-400°C; beyond this temperature the fracture energy has a tendency to decrease. Experiments by Baker show that the cooling regime has little influence on the fracture energy for temperatures beyond 300°C; yet for lower temperatures, the slow-cooled specimen exhibits much larger increase of the fracture energy compared to other results.

I.2.5.   Free thermal strain

The free thermal strain ε_{th} (FTS) is the strain that develops in concrete during heating an unstressed specimen. The free thermal strain measurements include the drying shrinkage component in addition with the thermal expansion, because the tests are performed with unsealed specimen. FTS of concrete is dominated by that of the aggregate; therefore the main factors affecting the free thermal strain of concrete are the aggregate type and content (Terro, 1998). Incompatibilities between the thermal strains of the aggregate and the cementitious matrix result in microcracking of concrete. Experimental data on the FTS (Schneider, 1988) are plotted in Fig. I.2-10. It can be seen that FTS is a non-linear function of temperature. Beyond 600°C, the FTS rate in most concrete decreases; in some cases the concrete shrinks due to chemical or physical reactions in the aggregates.
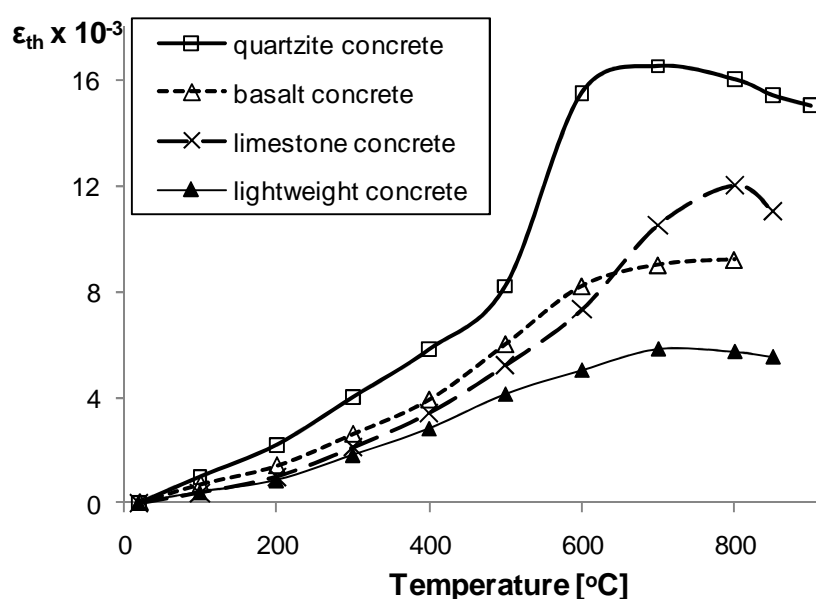
Fig. I.2-10: Free thermal strain (Schneider, 1988)

The FTS of concrete is partly irreversible (Schneider, 1988; Franssen, 1993). Experimental data on the residual free thermal strain of quartz and limestone concrete (Schneider, 1988) are given in Table I.2-1; these are the residual strains measured after heating to a defined maximum temperature and cooling down to ambient temperatures. Positive values indicate residual dilatation whereas negative values indicate residual shrinkage. The residual strains after cooling down to ambient temperature are positive (residual dilatation) for concrete heated up to less than 400°C and negative (residual contraction) for concrete heated above 400°C.

Type of concrete	T_{max} [°C]						
	200	300	400	500	600	700	800
Quartz	-0.3	-0.5	-0.2	+1.0	+2.0	+6.0	+4.0
Limestone	-0.6	0.0	+0.5	+1.6	+3.0	+5.5	+6.0

Table I.2-1: Residual thermal strains in ‰ of quartz and limestone concrete after cooling

I.2.6.   Transient creep strain

The total strain ε_{tot} that develops in heated concrete strongly depends on the applied stress during heating. Therefore transient tests aim to measure the total strain-temperature relationship for different load levels. In a transient test, the concrete specimen is first loaded up to a given load; it is then subjected to a constant heating rate while the applied load is kept constant. It is recommended that the heating rate be in the range of 0.1 °C/min to 10 °C/min (Schneider, 1985). Heating is continued until failure occurs. The total strain is measured during all the process. Results of transient tests (Anderberg and Thelandersson, 1976; Schneider, 1988) are plotted in Fig. I.2-11 for different applied stress levels α, with the applied stress level defined as the ratio between the applied stress and the compressive strength at ambient temperature. These transient tests have been performed by Schneider (α = 0.0; α = 0.10) and by Anderberg and Thelandersson (α = 0.225; α = 0.45; α = 0.675). It can be seen that the total strain decreases with an increase of the applied stress level during heating. Beyond certain level of applied stress during heating, concrete can be observed to shrink rather than expand due to thermal expansion. This considerable contraction of concrete heated under stress compared with the free thermal strains cannot be explained only by the development of "instantaneous stress-related strains" in the sense of Fig. I.2-1.
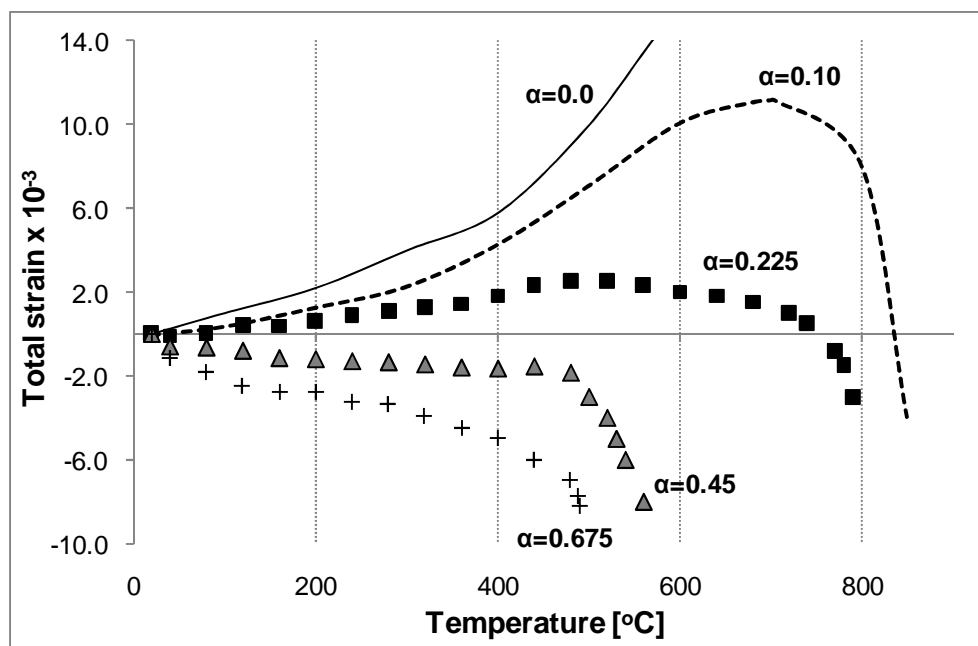
Fig. I.2-11: Total strain response versus temperature in transient tests performed at different applied stress levels (Anderberg and Thelandersson, 1976; Schneider, 1988)

The total strain ε_{tot} measured in transient tests is composed of free thermal strain ε_{th} and mechanical strain ε_m. The mechanical strain-stress relationship at a given temperature can be derived from transient tests data. For the considered temperature, the total strains corresponding to the different applied stress levels are read on Fig. I.2-11. Then, by subtracting the free thermal strain from the total strains, the mechanical strains ε_m corresponding to the different applied stress levels at the considered temperature are found and the mechanical strain-stress curve can be plotted for this temperature. The process can be repeated for the different temperatures. The mechanical strain-stress curves are different from the instantaneous strain-stress curves of Fig. I.2-1 obtained from steady-state tests; this results from the fact that the applied stress during heating affects the total strain in concrete or, in other terms, that the test procedure in terms of loading-heating history has an influence on the stress-strain relationship. Therefore the concept of transient creep strain has been introduced to account for the additional strain that develops in concrete heated under load, compared to concrete loaded at elevated temperature.

The concept of transient creep strain is explained in Fig. I.2-12. The variables temperature, stress and strain are plotted for concrete specimens subjected to steady-state test and transient test. The specimen subjected to steady-state test is first heated uniformly to a pre-defined temperature and then loaded while the temperature is kept constant. The strain that appears at the end of the heating process is only composed of free thermal strain, whereas the strain at the end of the experiment is the sum of FTS and instantaneous stress-related strain. In the transient test, the specimen is first loaded up to a given load and then heated while the load is kept constant. The strains at the end of the latter and the former experiment are different even though the final stress and temperature are the same. The difference in final strain is denoted as the transient creep strain. Note that for more readability in Fig. I.2-12, the strain components have been added in absolute values even though FTS is opposed to the other strains in compression.
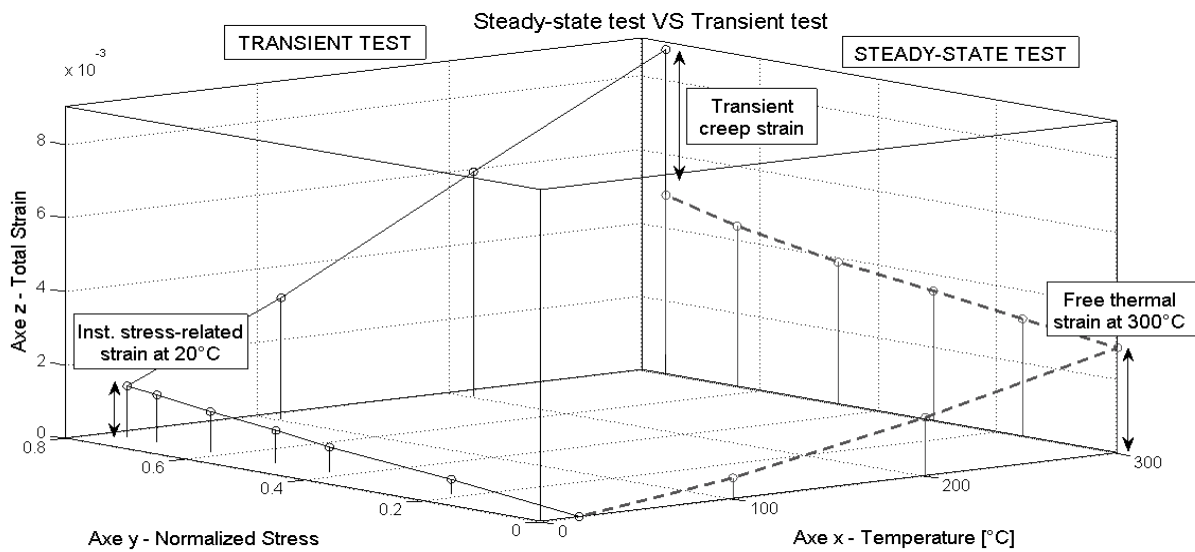
Fig. I.2-12: Concept of transient creep strain

By definition, the transient creep strain ε_{tr} can be indirectly determined by comparing the total strains obtained by transient tests and steady-state tests; results derived from experimental tests on concrete with siliceous aggregates (Schneider, 1988) are plotted in Fig. I.2-13. The results show a nonlinear relationship between transient creep strain and temperature; the nonlinearity becomes significant beyond 500°C. On the other hand, experimental results show that transient creep strain can be linearly related to applied stress level for levels up to nearly 0.6-0.7 (Terro, 1998). Transient creep strain is irrecoverable and occurs only on first heating. Based on experimental observations by Khoury, et al. (1985a-b) and by Schneider (1988), transient creep seems to be nearly independent of time, type of concrete, moisture and thermal expansion of concrete. However, it is affected by the aggregate-cement ratio; it is generally thought that the origins of transient creep are in the cement paste and that the addition of aggregate restrains it (Law and Gillie, 2008). According to different authors, transient creep strain is due to transformations in the chemical composition of the concrete (probably, in the C-S-H of the cementitious matrix) during first heating under applied stress (Schrefler, et al., 2002; Li and Purkiss, 2005). It should be noted that the fact that it does not depend on time makes the term "transient creep" quite improper, but this term has imposed itself in the literature.
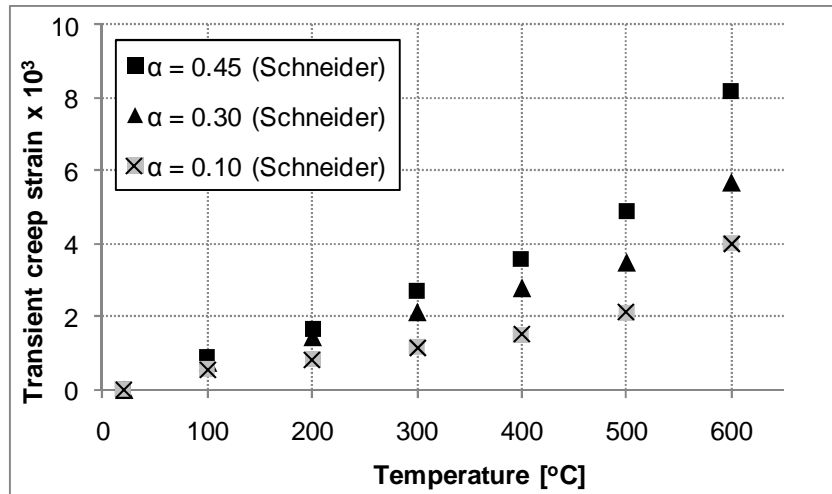
Fig. I.2-13: Relationship between transient creep strain and temperature for different pre-applied stress levels (derived from transient tests by Schneider, 1988)

According to the previous discussion, the macroscopically measurable strains in heated concrete (i.e. the total strains ε_{tot}) can be subdivided into individual strain components according to Eq. I.2-1:

$$\varepsilon_{tot} = \varepsilon_{th} + \varepsilon_{\sigma} + \varepsilon_{tr} + \varepsilon_{cr} \qquad \text{Eq. I.2-1}$$

where ε_{th} is the free thermal strain, ε_{σ} is the instantaneous stress-related strain, ε_{tr} is the transient creep strain and ε_{cr} is the basic creep strain.

Other authors have adopted another approach to account for the effect of stress during heating. They define the Load Induced Thermal Strain (LITS) as the difference between the free thermal expansion of concrete when it is heated without load, and the net thermal

expansion when it is heated under load (Khoury, et al., 1985b). The net thermal expansion excludes the initial elasto-plastic strain at ambient temperature. Experimental data of LITS, derived from transient tests by Schneider (1988) and Persson (2003) with different levels of applied stress α during heating, are plotted in Fig. I.2-14. Therefore, the LITS is a general term that comprises different strain components in heated concrete, including transient creep strain. According to this approach, the macroscopically measurable strains in heated concrete (i.e. the total strains) can be subdivided into individual strain components according to Eq. I.2-2:

$$\varepsilon_{tot} = \varepsilon_{th} + \varepsilon_{\sigma}^{20°C} + LITS \qquad\qquad \text{Eq. I.2-2}$$

where $\varepsilon_{\sigma}^{20°C}$ is the strain due to the applied stress at ambient temperature (this is an instantaneous stress-related strain).

The LITS comprises the following strain components: transitional thermal creep (ttc), drying creep, basic creep and changes in elastic strain (Khoury, et al., 1985b). Transitional thermal creep, by far the largest component of LITS, develops during, and for a few days following, heating of sealed concrete under load. It is irrecoverable, occurs only on first heating and probably has its origins in the cement paste (Law and Gillie, 2008). Drying creep is the shrinkage that results from the evaporation of water in unsealed concrete that is heated. In fact, transient creep strain refers to the sum of transitional thermal creep and drying creep. Basic creep is defined as the strain that develops when only time is changing with all other conditions such as stress and temperature being constant. In fire situation, this basic creep strain is often very small compared to the other strains in concrete due to the short period of the fire (Li and Purkiss, 2005); it can thus be omitted for structural fire engineering applications. Changes in elastic strains account for the elastic components of LITS which result from the temperature dependency of the elastic modulus.
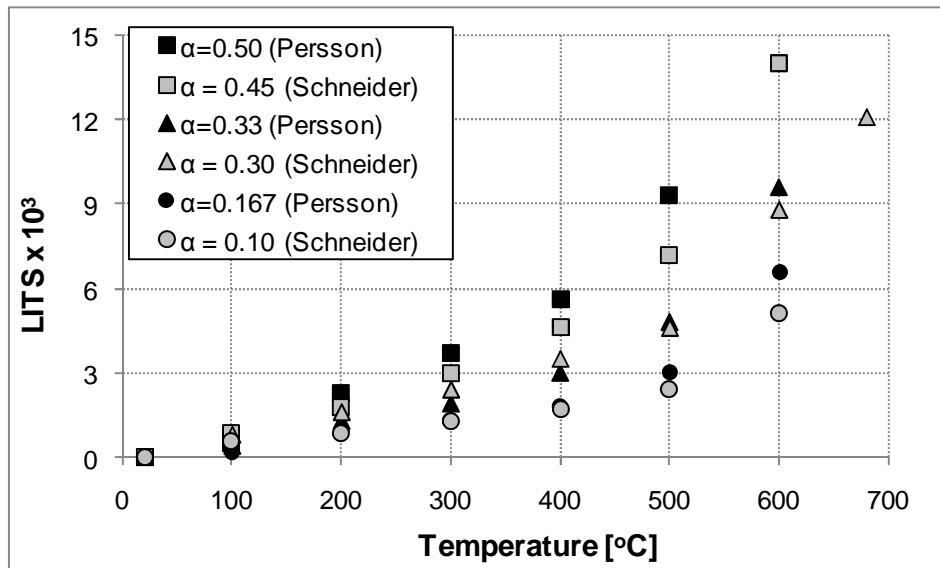
Fig. I.2-14: Relationship between LITS and temperature for different pre-applied stress levels (experimental data from Schneider (1988) and Persson (2003))

It was noted by Terro (1998) and more recently by Pearce, et al. (2004) that no data exist on transient creep strain or LITS under tensile state of stress and, to the author's knowledge, such information is still missing. The main reason is probably the fact that concrete is usually designed to be used in compression. Moreover, the tensile properties of concrete are difficult to measure.

I.2.7.   Spalling

Spalling may be observed in fire-exposed concrete as a result of the combined effect of stresses (mechanical and thermal) and pore pressure (Tenchev and Purnell, 2005). It is often explosive, occurring as a single explosion or a series of explosions and characterized by typically loud explosive noises. Concrete layers of 100-300 mm in length and 15-20 mm in depth may be removed by each explosion, which is dangerous for the integrity of the structure and may cause physical damage on impact (Majorana, et al., 2010).

High strength concrete is more prone to spalling than normal strength concrete. This can be explained by the fact that higher strength is achieved by reducing the water/cement ratio, which induces lower permeability and therefore enhances pore pressure spalling. High heating rates increase the probability of explosive spalling because they generate excessive temperature gradients in the concrete, thus inducing significant compressive stresses close to the heated surface and tensile stresses in the interior regions. Combination of external applied loads resulting in compressive stresses with thermal stresses due to the temperature gradients increase the susceptibility of concrete members to spalling. Other factors influence the occurrence of spalling such as the section shape (acute-angled corners are critical), moisture content and permeability (through their effects on pore pressure) or the type of aggregate (probability of thermal stress spalling is less for concrete with a low thermal expansion aggregate), see (Majorana, et al., 2010). Recent research has proved that explosive spalling could be eliminated by adding polypropylene fibers (0.05-0.1% by weight) in a concrete mix; the result was very effective even in high strength concrete (60-110 MPa).

I.3. Performance-based approach in structural fire engineering

This section reviews a few recent applications of structural fire engineering. Recent developments in computational analysis tools such as finite element analysis have allowed engineers to simulate the behavior of complex structures. Therefore up-to-date research in structural fire engineering includes a number of applications that are of prime practical importance in the field but bring complex structural behaviors into play. For instance, modelling the behavior of a structure during and after the cooling phase of a fire is an essential yet challenging task for engineers (Fletcher, et al., 2007); this calculation may be particularly important regarding the safety of the fire fighters. Modelling the membrane action in a fire-exposed composite structure has significant outcome as it allows for a dramatic reduction of the costs in insulation material. However, the complexity and variability of these applications lead to the need for constitutive models with specific requirements. Hence the objective of this section is to investigate the specific requirements for concrete models intended to be used in finite elements software for the simulation of structures in fire.

I.3.1. Natural fire and cooling down phase

I.3.1.1. *Description of the problem*

The analysis of the behavior of a structure in fire requires that the evolution of the gas temperature in the compartment be established first. Based on the definition of this temperature evolution, the thermal analysis may be performed to determine the temperature distribution in the structural elements; then the mechanical analysis is conducted to assess the behavior of the structure in fire. In the prescriptive approach, the time-temperature curves that are used are taken from international standards such as the ISO fire defined by the International Standards Office (1975) or the ASTME fire designed by the American Society for Testing and Materials (2007). As the temperature of these standard fires is continuously increasing, the temperatures in the element are also continuously increasing and the load bearing capacity of the structure is continuously decreasing. As a consequence, verification of the structure at the required fire resistance time guarantees stability at any previous instant in the fire.

The search for achieving fire safety through alternative, cost effective solutions has lead to an increased use of performance-based approach for fire safety design (Meacham and Custer, 1992; Kodur, 1999). If the behavior of a structure or structural element is assessed in a performance based environment, a more realistic representation of the fire will be used that comprises not only a heating phase but also a cooling phase during which the temperature of the fire is decreasing back to ambient temperature. When a realistic fire scenario is considered, the required duration of stability may be longer than the duration of the heating phase; it may even be required that the structure survives the total duration of the fire until complete burnout. In this situation, verification of the structure in the load domain at the time

of maximum gas temperature does not guarantee against collapse at a later stage. The load bearing capacity of the structure continues decreasing after the moment of maximum gas temperature, will reach a minimum value and eventually may recover partially or completely when the temperatures in the structure are back to ambient. For the designer, this implies that verification must be performed in the time domain by a step-by-step iterative method (Dimia, et al., 2011).

The continuation of degradation of the load bearing capacity after the moment of maximum gas temperature is due to two main reasons.

Firstly, the temperatures in the structure may continue increasing while the gas temperature is decreasing. For an unprotected steel structure, this will be the case until the gas temperature has become lower than the steel temperature. For a thermally protected steel structure, the increase of steel temperature will continue for a longer time due to the inertia of the insulation. For a concrete structure, the zones of the members that are near the surface will exhibit a decrease soon after the gas temperature has become lower than the surface temperature but the central zones may have their temperature still increasing for a significant duration, all the more if the section is massive.

The second reason is to be found in the material behavior. Steel recovers strength and stiffness as soon as its temperature decreases, completely or partially depending on the type of steel and the maximum reached temperature (Kirby, et al., 1986), but concrete remains severely damaged after cooling. Not only doesn't concrete recover its strength, but there is an additional loss of strength during cooling from maximum temperature to ambient (Li and Franssen, 2011). A comprehensive study on the residual compressive strength of concrete after exposure to fire has been conducted by Annerel (2010). This study showed that different parameters influence the residual compressive strength, e.g. the cooling method and the storage conditions after heating. It was notably found that a higher cooling rate leads to a higher strength loss; the additional strength loss can reach 33% in case of thermal shock caused by immersion in water compared with the residual strength in case of natural cooling in the oven. These results have practical significance as the intervention of the fire fighters usually leads to quenching of the structure in water and the possible effects of such intervention on the material mechanical behavior should be taken into account in the analysis of the structural behavior during the cooling phase.

Due to the delayed increase of temperature in the structure, the irrecoverable damage of heated concrete and the additional loss of concrete strength during cooling, there may be a risk of delayed collapse for concrete structures subjected to natural fire. For the fire fighters, the possibility of collapse occurring after the time of maximum gas temperature, if confirmed, might be a real threat. The intervention of fire fighting forces will usually lead to a decrease of the fire temperatures and, if collapse occurs during this phase, it may be at a time when fire brigades are in or at near vicinity of the fire compartment and they may be endangered by the collapse. Collapse during the beginning of the cooling phase of a fire occurred, for example, in a full scale fire test conducted in 2008 by Wald and Kallerova (2009) in the Czech Republic. The composite steel concrete floor working in tensile membrane action collapsed briefly after the wood based natural fire entered in the cooling phase and one of the possible

failure modes that are suspected is by failure of the concrete compression ring that was established in the slab.

A structural failure that would occur at a later stage, when the temperatures in the compartment are back to ambient, may be an even higher threat because it would occur at the time of first inspection, not only by the fire brigades but also possibly by other people. Such a tragic incident occurred in Switzerland in 2004 when seven members of a fire brigade were killed by the sudden collapse of the concrete structure in an underground car park in which they were present after having successfully fought the fire (Hody, 2004).

These events show that considering the response of structures during and after the cooling phase of a natural fire is a necessary task in structural fire engineering. The two reasons that explain why the load bearing capacity of a structural element may continue decreasing after peak gas temperature indicate that concrete structures are more prone to this phenomenon than steel structures. Hence proper modelling of concrete structures subjected to natural fire is an important, up-to-date issue. Therefore the concrete constitutive model must capture the material behaviour in situations of increasing and decreasing temperatures. The material properties must be defined not only at ambient and elevated temperatures but also after heating and cooling back to ambient temperatures (i.e., the residual properties).

I.3.1.2. *Implications for concrete constitutive models*

Concrete constitutive models developed for structural fire engineering applications may be employed for assessing the response of concrete structures during and after the cooling phase of a fire; for this reason concrete models must capture properly the mechanical behavior of concrete in these situations. The evolution of the material properties during and after the cooling phase must be specified in the model and these evolution laws should properly reflect experimental data. This requirement was not considered in prescriptive design because only the heating phase of the fire was considered; for this reason simplified models have sometimes been used for concrete at high temperatures, but these simplified models are not adapted to performance-based design.

Special attention is required for the phenomena in heated concrete that are irreversible, e.g. the free thermal strain or the transient creep strain. The transient creep strain is irrecoverable and occurs only under the first heating (Anderberg and Thelandersson, 1976); test data indicate that no transient creep occurs during the cooling of concrete after temperature exposure (Schneider, 1988). In terms of requirements for the concrete model, it is very important that the transient creep strain be properly calculated during the heating of the material and then that this strain component be treated as irreversible during cooling. The effect of treating transient creep strain as a recoverable strain would lead to an erroneous estimation of the unloading stiffness of the material during cooling. The consequence on the structural analysis would be, for instance, an erroneous estimation of the load distribution in a statically indeterminate structure (Gernay, 2012). The free thermal strain has also been discussed in the previous section; it has been shown that a residual free thermal strain is experimentally observed in concrete after exposure to high temperatures. The residual values of the free thermal strain must be properly calculated as a function of the maximum temperature reached in the material.

In conclusion, concrete models used for the simulation of structures subjected to natural fire must properly capture the evolution of the mechanical properties during and after the cooling phase of the fire.

I.3.2.   Stress-temperature paths in a structural element

I.3.2.1.   *Description of the problem*

The kind of demand that is being imposed on a material model may be quite different when it comes to modeling a structural element than when it is used to model experimental tests made on cylinder with a quite simple stress-strain-temperature history. Because of transient thermal gradients inherent to concrete sections, different points in the structure are expected to experience different and complex stress-strain-temperature histories. The following simple example illustrates this aspect and therefore can help to establish specific demands imposed on constitutive models that are developed for modeling structural elements. The example has been numerically analyzed to derive the stress-temperature paths in a structural element during a natural fire. All simulations have been performed with the software SAFIR (Franssen, 2005) and with the current thermal and mechanical models of Eurocode 2 (European Committee for Standardization, 2004b). The results would of course be quantitatively different with another model but the exercise has been performed to show the trends, not to obtain precise values.

The model is a concentrically loaded circular siliceous concrete column of 4 m height, with a section of 300 mm diameter reinforced with four 16 mm diameter rebars covered by 40 mm of concrete. The concrete has a compressive strength of 30 MPa and a tensile strength of 3 MPa whereas the steel of the bars has a yield strength of 500 MPa. The ultimate load bearing capacity of this column at room temperature is 2309 kN.
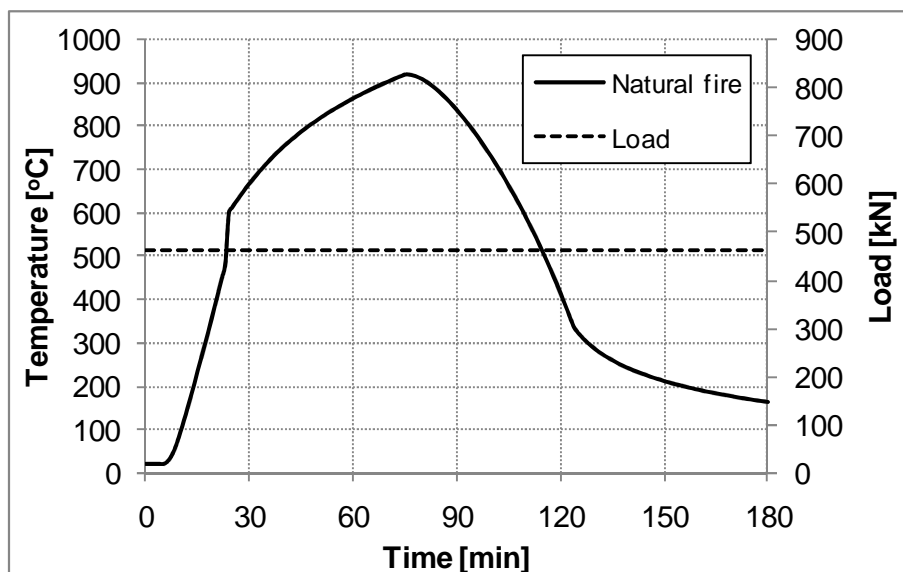
Fig. I.3-1: Evolution of the load and temperature applied to the column

The column is first axially loaded with a load of 462 kN and then subjected to the natural fire curve shown in Fig. I.3-1. The temperature distribution in the sections was determined by a 2D non linear transient analysis, see Fig. I.3-2. No collapse occurs during the numerical simulation and no buckling of the column is observed.
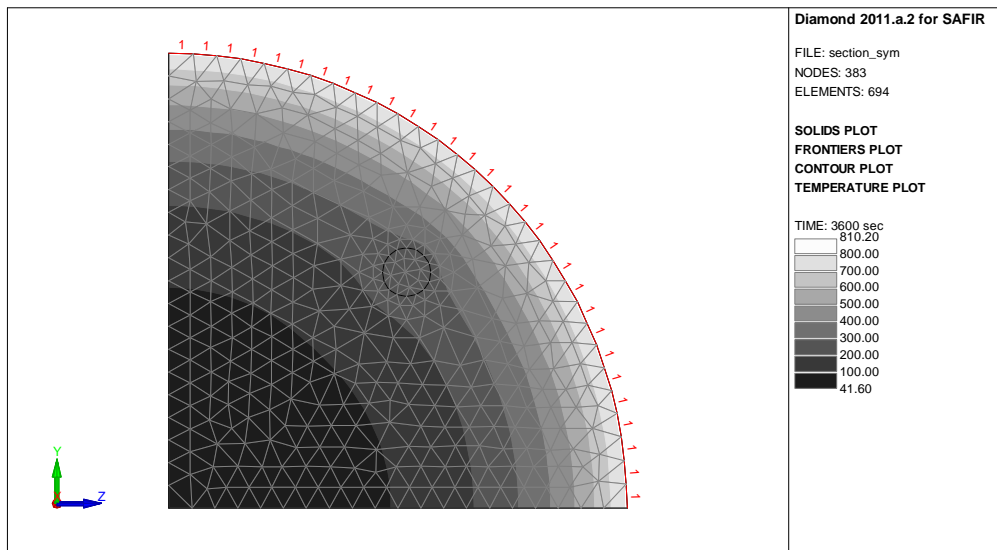
Fig. I.3-2: Temperature distribution in the column after 1 hour exposure to natural fire

The stress-temperature paths observed at different points across the section at mid level of the column are plotted in Fig. I.3-3 (compression is positive). Points A to F are distributed on a radius in the section, with point A at the center and point F at the surface.
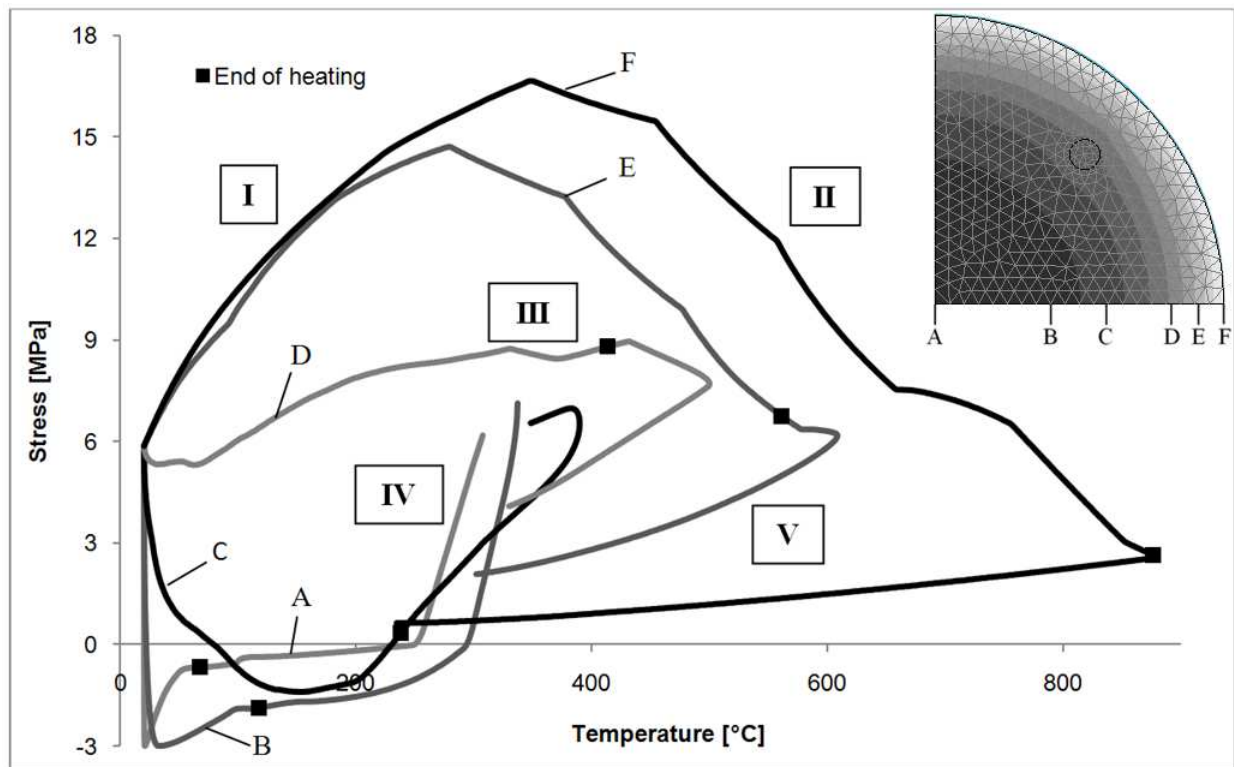
Fig. I.3-3: Evolution of the stress and temperature in different parts of the column section

The stress and temperature evolutions across the section during the fire are complex and significantly different depending on the position in the section. Before the fire starts, the entire section is submitted to a compressive stress of about 6 MPa; this stress is the same in the whole section because the column is axially loaded and the temperature is constant across the section, equal to 20°C. At the beginning of the fire, the temperature starts to increase in the compartment and at the surface of the section but the core of the section still remains at ambient temperature during a certain period of time, due to the thermal insulation given by the surrounding concrete material. The resulting temperature gradients that develop across the concrete section cause thermal stresses that result in an increase in compressive stresses in points E and F, which are located near the surface; indeed, thermal extension of this peripheral part of the section is restrained by the central part of the section, which remains colder. By equilibrium the central part of the section is unloaded and develops tensile stresses, see points A and B. During the first minutes of the fire, the entire compressive load is thus transferred to the peripheral part of the section whereas the central part is totally unloaded.

As the fire develops, the high temperatures in the peripheral part of the section lead to a significant decrease in strength and stiffness of the material in this area; the compressive stresses thus start to decrease in the peripheral part (points F and E) and these stresses are progressively redistributed to the core of the section (first point D, then C, B and A). This progressive redistribution of compressive stresses from the peripheral part to the central part of the section under increasing temperatures is observed until the end of the heating phase, which is noted by a black square on the curves. The end of the heating phase then leads to temperature decrease in the section; this decrease arises immediately at the surface of the section (point F), but the effect is delayed for the core of the section, as was the case for temperature increase. During the cooling phase, the observed redistribution of compressive stresses from the peripheral part to the central part of the section continues as the thermal extension of the peripheral part is partly recovered. In the core of the section (points A and B), the effect of thermal inertia of the section is so significant that the temperature continues to increase until the end of the simulation, i.e. 180 minutes, whereas the maximum gas temperature is reached after 75 minutes. At the end of the natural fire, this central part of the section sustains the most part of the load, although the temperature has become almost constant in the section; the reason is the fact that mechanical properties (stiffness and strength) of this central part have not been damaged as significantly as the properties of the peripheral part, as the maximum temperature reached in the core has been limited compared with the maximum temperature at the surface.

From the analysis of the stress-temperature paths plotted in Fig. I.3-3, it is possible to extract five different situations:

    I.   increasing stress and increasing temperature;
    II.   decreasing stress and increasing temperature;
    III.   approximately constant stress and increasing temperature;
    IV.   increasing stress and approximately constant temperature;
    V.   decreasing stress and decreasing temperature.

These five different situations in the stress-temperature space occur for a quite simple situation in the load-temperature space, i.e. a constant applied load and an increasing-decreasing temperature (see Fig. I.3-1). The situation would be more complex in a real structure where the load varies during the fire. Yet even the simple situation in the load-temperature space considered in this example leads to an important number of configurations in the stress-temperature space, due to the development of thermal stresses in the section. This example shows the variety and complexity of situations that a material model must be able to capture when it is used to model a structural element.

I.3.2.2. *Implications for concrete constitutive models*

Tests on concrete have shown that the mechanical behavior depends on the path in the stress-temperature space; transient creep strain or LITS have been introduced to account for this dependency. The simple example treated in this section shows that it is essential for concrete models to take into account this dependency, because various situations in the stress-temperature space arise in structural elements even when simple situations in the load-temperature space are considered.

The eight possible situations in the stress-temperature space are plotted in Fig. I.3-4; the five different situations highlighted by the numerical example are present on this graph, in addition with three other possible situations that have not been discussed yet:

VI.   decreasing stress and constant temperature
VII.   constant stress and decreasing temperature
VIII.   increasing stress and decreasing temperature

Although they have not been observed in the simple example treated in this section, these three latter situations could arise in a structure subjected to fire.
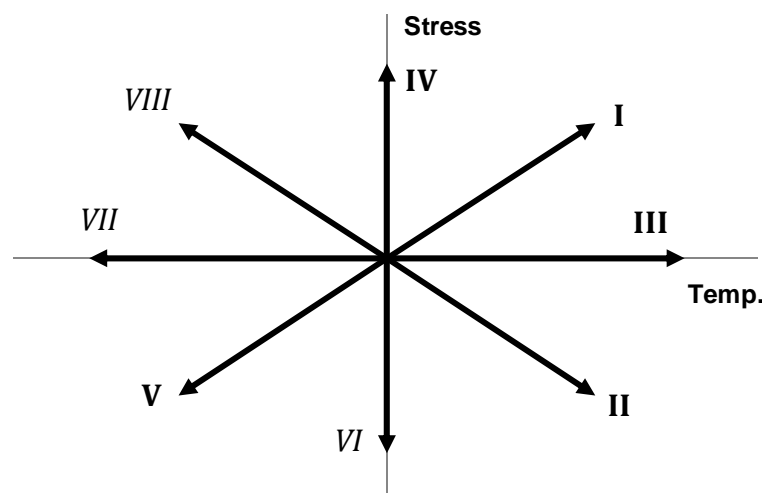
Fig. I.3-4: Different possible stress-temperature paths

According to experimental evidence, transient creep does not develop the same way in the eight situations depicted in Fig. I.3-4. Concrete models must properly handle the different

---

situations and their effect on the transient creep strain. These effects are summarized here below:

- Situation I: transient creep strain develops because the temperature increases under stress.
- Situation II: it is generally assumed (Li and Purkiss, 2005) that transient creep strain develops in the concrete material submitted to increasing temperature as long as the stress in the material remains in compression, even if the compressive stress is decreasing (in absolute value). It is very important to note that the transient creep strain is irrecoverable, and thus it is not recovered even if the compressive stress is decreasing.
- Situation III corresponds to transient tests, therefore transient creep strain develops in the material.
- Situation IV corresponds to steady-state tests, therefore no transient creep strain develops in the material.
- Situation V, VII and VIII: no transient creep strain develops under decreasing temperature.
- Situation VI, as situation IV, is in steady-state conditions; therefore no transient creep strain develops in the material.

In conclusion, as an implication of the fact that various stress-temperature paths develop in concrete structural members subjected to fire, proper modelling of transient creep strain is an important requirement for concrete models intended to be used for modelling of structural elements.

I.3.3.   A typical behavior of reinforced concrete slabs in fire: the membrane action

I.3.3.1.   *Description of the problem*

The development of membrane forces in concrete slabs can significantly enhance their load-carrying capacity, compared to the load-carrying capacity estimated from considering only flexural behavior (Bailey, 2001). A series of fire tests have been performed in 1995-1996 on full-scale steel concrete composite building at the Building Research Establishment laboratory Cardington, U. K., in which some of the steel beams supporting the composite floor system were left unprotected (Bailey, et al., 1999). Tests results show that the stability of the building structures was maintained during the fire even though the temperatures in the unprotected steel beams exceeded 1150°C and high vertical displacements of the floor were observed (Bailey, 2004). The fire resistance of the composite floor was largely higher compared to the resistance predicted by design methods based on flexural behavior. The reason of the excellent fire behavior of the composite building in Cardington full-scale tests is the mechanism of membrane action that developed in the composite floor slab (Wang, 1996). Following the Cardington tests, other full-scale fire tests have confirmed that membrane action can be efficiently used in composite floor slabs to sustain the applied load under fire (Zhao, et al., 2008; Vassart, et al., 2011).

Membrane action results from the development of in-plane forces within the depth of concrete floor slabs. Tensile membrane action can develop in two-way spanning floor slabs that are vertically supported even if they have no horizontal restraint. In this case, the applied vertical load is sustained by tensile membrane action occurring in the centre of the slab, which has to be reinforced accordingly, whereas a ring of compressive membrane forces develops around the perimeter of the slab to ensure the horizontal equilibrium. This behavior leads to large displacements as vertical loads are equilibrated by in-plane forces; therefore tensile membrane action cannot be used under normal working conditions. However, under accidental loads such as fire, this behavior can be mobilized and lead to certain robustness of the building structure, provided it is designed correctly (Bailey, 2004).

Compared to the prescriptive approach for the fire design of composite buildings, a performance-based approach that takes into account the tensile membrane action may allow for a significant reduction of building costs. The designer may ensure the structural stability of the building in fire by applying thermal protection to only those structural elements within the building which need to retain their strength and stiffness for the tensile membrane action to develop. This approach allows for reducing significantly the thermal protection on the steel members, leading to important cost-saving in terms of material and fixing time, see the picture from Franssen, et al. (2010) in Fig. I.3-5.

Fig. I.3-5: Building designed to take advantage of tensile membrane action in accidental fire situation (ArcelorMittal, Belgium)

On the other hand, compressive membrane action has been used for a long time in the design of structures using materials with low tensile strength and comparatively large compressive strength such as stone, masonry or concrete. Opposite to tensile membrane action, compressive membrane action can be used in concrete structures at ambient temperature, through the design of appropriate structure shapes such as arches or vaults; see

for instance the Pantheon's vaulted roof in Rome, Fig. I.3-6, dated from 1st century B.C. (picture taken from http://arpc167.epfl.ch/alice/WP_2011_S3/lenherr/archives/2233). The vertical applied loads are transmitted by the structure through in-plane compressive forces. At the supports, the horizontal components of these compressive forces must be equilibrated; they can be equilibrated by tie beams acting in tension, or by abutments or flying buttress in cathedrals. As a result, the designers have often taken advantage of compressive membrane action for buildings in materials such as stone, masonry or concrete under normal working conditions.

However, when exposed to fire, the behavior may change from compressive membrane action to flexural mode in building structures. The development of flexion in the structure is partly due to the thermal gradients that develop across the section of the structural members, but the change from compressive membrane action to flexural mode mostly arises when proper horizontal supports are not maintained during the fire. This is the case, for instance, if the tie beams designed to equilibrate the horizontal forces at the base of the arch structure are left unprotected; temperature increase in these tie beams leads to a lack of horizontal support for the structure. As a result, the compressive membrane action cannot be mobilized anymore; it is replaced by a flexural behavior, leading to an important decrease in the load bearing capacity of the structure compared to the load bearing capacity at ambient temperature.

Fire may thus induce a change in the structural behavior of concrete and composite buildings, from flexural behavior to tensile membrane action or from compressive membrane action to flexural behavior. As a result, the analysis of the tensile and the compressive membrane action behavior in concrete and composite buildings in accidental fire situations is an important issue in structural fire engineering. In the following, an example is provided for the two types of building structures discussed here, i.e. a structure in which tensile membrane action develops in fire and a structure designed to take advantage of compressive membrane action at ambient temperature.

Fig. I.3-6: Pantheon's vaulted roof, Rome

I.3.3.2. Tensile membrane action: Ulster large-scale fire test

This section presents the experimental behavior of a steel-concrete composite floor subjected to natural fire; it will be shown that tensile membrane action developed in this floor during the fire. The full-scale fire test of the steel-concrete composite floor was conducted by the University of Ulster on 27 February 2010 in Ireland. The work was supported by the Research Fund for Coal and Steel and six partners were involved in this project, among which the University of Liege (Vassart, et al., 2011).

The full-scale composite floor, made of cellular steel beams connected to composite slabs, was tested under natural fire, see Fig. I.3-7 and Fig. I.3-8. The two central secondary beams were left unprotected. All the beam sections (protected and unprotected) and the slab were instrumented in order to measure the evolution of temperatures and displacements during the fire. The compartment covers an area of 15 m by 9 m with a floor to soffit distance of 3 m. The surrounding walls of the compartment were made of normal weight concrete block works with three 3 x 1.5 m openings in the front wall. The surrounding walls were not fixed to the composite floor at the top which allowed vertical movement of the floor without interaction with the walls. All the columns and solid beams on the opening side were protected for a standard fire of two hours using 20 mm thick fibre boards. The surrounding cellular beams were also protected using ceramic fibres.

Fig. I.3-7: Inside view of the compartment before the test

Fig. I.3-8: Fire test and structural elements after the fire

The slab was made of 51 mm deep profile of the Kingspan Multideck 50 type with a concrete cover of 69 mm on the profile, which makes a total depth of 120 mm. The average cube strength was 54.8 N/mm2 at 28 days. A steel mesh of 10 mm with a spacing of 200 mm in each direction made of S500 steel was used as reinforcement. It was located at a vertical distance of 40 mm above the steel sheets. The slab was fixed on all steel beams by means of steel studs welded on the upper flanges (full connexion). All connections from secondary beams to main beams and from beams to columns are simple connections. Horizontal bracing was provided in 4 positions leaving the slab completely free of external horizontal restraint.

The applied load of 3.25 kN/m^2 was achieved using 44 sandbags of 1 ton evenly positioned over the floor plate. The fire load of 700 MJ/m² was achieved using 45 standard (1m x 1m x 0.5m high) wood cribs, comprising 50 mm x 50 mm x 1000 mm wooden battens, positioned evenly around the compartment, yielding a fire load was 40 kg of wood per square metre of ground area.

The temperature in the compartment was recorded during the test, see Fig. I.3-9. As the central cellular beams were unprotected, their temperature increased rapidly, leading to an important decrease in steel strength and stiffness. As a result, web post buckling occurred in these beams due to the vertical shear forces induced by each web post combined with the longitudinal restraint provided by the concrete slab, see Fig. I.3-10. The slab lost the support made by the central cellular beams, due to web post buckling of these beams, and tensile membrane action began to develop in the composite floor system (Fig. I.3-11). The central vertical deflection of the slab reached more than 0.75 m but the structure was able to sustain the applied load. Although the fire was more intense and of longer duration that assumed in the initial studies, the structure survived the total duration of the fire until complete burnout.

The numerical analysis of this fire test requires an advanced constitutive model for concrete. The concrete model should be able to capture the material behavior when the structural behavior changes from flexural behavior to tensile membrane action. This change in the load bearing mode induces significant unloading and reloading in different parts of the structure. Tensile membrane action leads to important deflections in the structure as can be seen in Fig. I.3-11 and the material models should be sufficiently robust. In addition, as the fire test was conducted under natural fire, the structural behavior has to be properly captured during the cooling phase also. These different aspects lead to severe requirements in terms of constitutive models. The numerical analysis of the Ulster fire test will be performed in Chapter V using the original concrete model developed in the present thesis, in order to validate the ability of the model to be used in structural fire engineering applications.
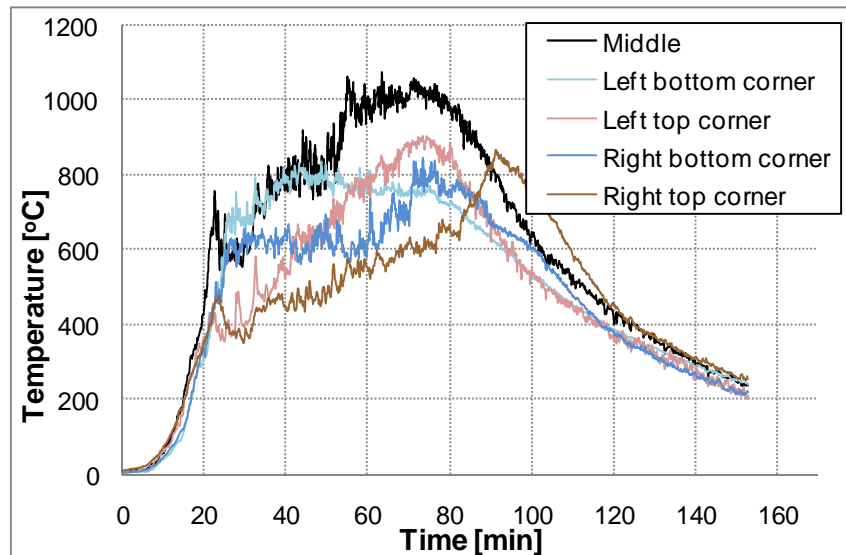
Fig. I.3-9: Measured temperatures in the compartment

Fig. I.3-10: Web post buckling in the unprotected cellular beams

Fig. I.3-11: Deflection of the slab developing tensile membrane action

I.3.3.3. *Compressive membrane action: a shell roof in fire*

This section presents a study case that was analyzed on a request by *Ingénieurs Conseils en Bâtiments* (ICB), Luxemburg, in the framework of a concrete building rehabilitation. This practical example illustrates the case of a building structure designed to take advantage of compressive membrane action at ambient temperature but which load bearing mode could change to flexural behavior under fire, if the necessary measures are not taken in terms of thermal protection.

The study case is the fire resistance analysis of a roof structure made of two shells side by side and shown in Fig. I.3-12. The span of one shell is 15.10 m whereas the height between the keystone and the support of the shell is 2.60 m. The length of the building is 27.00 m. The shells are made of reinforced concrete and their thickness varies from 160 mm (side) to 100 mm (center). The horizontal forces at the base of the shells are equilibrated by steel tie beams distributed every 4.50 m. The tie beams are steel cables of 35 mm diameter. Cupolas of dimensions 1.50 m by 1.00 m are distributed in the roof every 4.50 m in the direction of their length. It was requested to analyze the fire resistance of the structure in the situation of ISO fire in one or the two compartments.
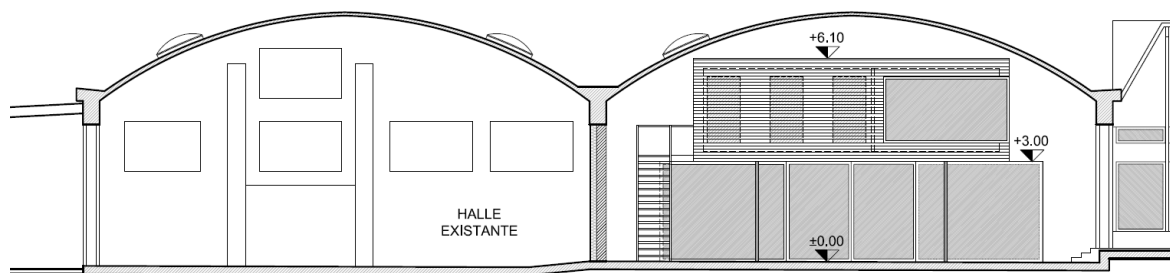
Fig. I.3-12: Elevation view of the structure

When the structure is loaded at ambient temperature, compressive membrane action develops in the concrete shells and the horizontal forces are equilibrated by tensile axial forces in the tie beams. However in fire situation, heating of these tie beams leads to a change in the load bearing mode; the structure develops a flexural behavior because the compressive membrane action cannot be mobilized without the restraint brought by the tie beams. As a result, the fire resistance of the building structure depicted in Fig. I.3-12 is very dependent on the thermal protection applied to the tie beams. Numerical analysis of this study case requires an advanced concrete model; this numerical analysis using the original concrete model developed in this work will be presented in Chapter V and this analysis will serve to highlight the capabilities of the model.

I.3.3.4. *Implications for concrete constitutive models*

As was shown in this section, membrane action is a very efficient load bearing mode for concrete structures. At elevated temperature, proper modelling of membrane action is of prime importance. Indeed, tensile membrane action can be mobilized in a fire-exposed structure that was designed considering flexural behavior under normal working conditions. In this case, tensile membrane action can dramatically improve the fire behavior of the structure, provide robustness in accidental situations, and lead to important cost-saving in

terms of material and fixing time. At the opposite, compressive membrane action is often used in the design of concrete structures under normal working conditions, because concrete strength is significantly higher in compression than in tension. Yet in fire situation, the structural behavior can change from compressive membrane action to flexural mode if proper thermal insulation is not applied to the structural elements that sustain the horizontal forces.

The structural behaviors observed in this section have implications for the concrete models that are used in structural fire engineering. These concrete models must be able to capture the transitions from flexural behavior to tensile membrane behavior and from compressive membrane behavior to flexural behavior that result from exposure to elevated temperature. These transitions, in terms of global strength mode of the structure, imply transitions from compression to tension, or tension to compression, in terms of stresses in the material. Therefore the concrete models must properly handle the unloading stiffness, the development of permanent strains, and the unilateral effect. In addition, modelling large-scale structures in fire, as presented in this section, implies certain requirements in terms of numerical robustness of the constitutive models.

I.4. Conclusion

The purpose of this chapter was to clarify the objectives of this research work, by establishing the requirements of a concrete constitutive model intended to be used for the simulation of structures in fire. First, the material behavior at ambient and elevated temperatures has been reviewed based on experimental data published in the literature. Then, a few up-to-date applications in the field of structural fire engineering have been presented; these applications have highlighted important features that are required for the material models to be used in this field.

Based on the review of the concrete behavior at ambient temperature, the main mechanical phenomena that arise in loaded concrete can be summarized as follows:

- Non linear behavior in tension and in compression;
- Dramatically lower strength in tension than in compression;
- Softening behavior after the peak stress;
- Volumetric expansion under compressive loading (dilatancy);
- Degradation of the elastic properties that appears during unloading;
- Development of inelastic (permanent) strains that appears during unloading;
- Strength and ductility increase under multiaxial compression (confinement effect);
- Stiffness recovery after crack closure (unilateral effect).

Based on the review of the concrete behavior at elevated temperature, the main phenomena observed in concrete subjected to applied temperature and load can be summarized as follows:

- Evolution of the mechanical properties during heating;
- Development of (partly irreversible) free thermal strains;
- Influence of the applied stress during heating (i.e., influence of the path in the stress-temperature space) that can be accounted for by the transient creep strain or by the Load Induced Thermal Strain;
- Spalling phenomenon.

The phenomena listed here above should be properly captured by concrete constitutive models. The original model developed in this study aims to capture these phenomena, except for the spalling phenomenon which is not taken into account because the mass transfers and phase changes phenomena, which have to be modeled to capture spalling (Majorana, et al., 2010), are considered beyond the scope of this study.

Based on the presentation of real applications and research topics in structural fire engineering, we have insisted on the following requirements for concrete models:

- In order to allow for analyses of building structures under natural fire, the evolution laws for the mechanical properties must also be available during and after the cooling phase of the fire (residual properties), and the non-recoverability of transient creep strain must be captured in the model.
- Due to the development of complex and different stress-strain-temperature histories in structural elements subjected to fire, the models must properly take into account

the concrete dependency on the stress-temperature path. In particular the transient creep strain must be adequately captured for every situation of stress-temperature history.

- As large-scale structural behaviors may change during fire from flexural mode to membrane action (or reverse), concrete models must properly capture the unloading features and the unilateral effect that characterize the material.

- Finally, concrete models must be sufficiently robust to be used for large-scale numerical simulations.

As a conclusion, this chapter has allowed to define the requirements for a concrete constitutive model intended to be used for structural fire engineering applications. In the next chapter, a state of the art of the existing concrete models is presented and discussed on basis of the ability of the models to fulfill the requirements exposed in the present section. Then, in the following chapters, an original model is developed using the present requirements as guidelines. Constant reference to the phenomena highlighted in this section is made to verify the ability of the model to capture the concrete behavior and its relevance as regards to the objectives of this thesis.

CHAPTER II - STATE OF THE ART OF CONCRETE CONSTITUTIVE MODELS

The objective of this chapter is to review the state of the art of constitutive models developed for concrete. A literature review is thus performed and several theories and models are presented. In addition, this chapter aims to take decisions regarding the assumptions to adopt for the model that is developed in the next chapters; at the end of this chapter, the general theoretical framework and the main assumptions of our model are drawn based on the analysis of the literature review.

Several research works have been conducted in the last decades to derive uniaxial constitutive models for concrete at elevated temperature. Uniaxial models are used for modelling linear structural members such as beams and columns. A significant part of the research efforts focuses on the phenomenon of transient creep strain; this phenomenon, which develops in fire-exposed concrete, has implications on the structural behavior and therefore it has to be accurately taken into account in the constitutive models. In this chapter, the most important models for transient creep strain are reviewed and compared, and their ability to fulfill the requirements defined in the previous chapter is discussed. Then, conclusions are drawn regarding the assumptions to be used for the development of a new model for transient creep strain.

Different approaches have been followed in the literature to model the mechanical behavior of concrete under multiaxial stress states. These different approaches are defined, at ambient temperature, and two of them are presented in details: the plasticity theory and the damage theory. The plasticity theory and the damage theory offer a theoretical framework to tackle the concrete modelling issue; yet none of these theories, used alone, allows for capturing all the phenomena discussed in the previous chapter. Therefore, recent research on concrete modelling at ambient temperature has focused on models coupling plasticity and damage. At elevated temperature, very few research works have coupled plasticity and damage theories and the extension of plasticity-damage models to incorporate the effects of high temperature is still a challenging issue. It is also noteworthy that, under multiaxial stress states, the temperature dependency is not clearly established for some of the mechanical properties used to model the concrete behavior, due to a lack of experimental data.

II.1. Uniaxial constitutive models of concrete and transient creep strain

This section reviews the research works on constitutive modelling of concrete under uniaxial stress states at elevated temperature. Since the mid-seventies, different models have been proposed that incorporate the phenomenon of transient creep, which develops in concrete heated under load. As was shown in the previous chapter, proper modelling of this phenomenon is a critical requirement for concrete models intended to be used in structural fire engineering. Hence special attention is given in this section to the existing transient creep models.

II.1.1.   Introduction on transient creep modelling

The phenomenon of transient creep strain has been described in the previous chapter: the transient creep strain is the difference in strain between concrete that is heated under load and concrete that is loaded at elevated temperature; this strain develops during first-time heating and is irrecoverable (Anderberg and Thelandersson, 1976). The fact that transient creep does not depend on time makes the term "transient creep" quite improper, but this term has imposed itself in the literature.

It is well-admitted in literature that transient creep has to be considered in any fire analysis involving concrete in compression (Khoury, et al., 1985a-b; Li and Purkiss, 2005); any stress analysis of heated concrete which ignores transient creep will provide erroneous results (Schrefler, et al., 2002). For instance, the effect of not including transient creep strain in a stress-strain model can be shown to produce erroneous unsafe results for the behavior of columns heated on three sides, in fire (Purkiss, 1996).

Since the pioneering works on uniaxial concrete models at high temperature (Anderberg and Thelandersson, 1976; Schneider, 1985), a number of analytical models capable of predicting transient creep strain have been developed in the literature. Based on these transient creep models, authors have developed uniaxial concrete models at elevated temperature that integrate explicitly a term for transient creep strain; the most important models are presented in Section II.1.2.

Another approach consists in including implicitly the transient creep strain in the stress-mechanical strain relationship; this is the case, for example, in the current Eurocode 2 (EC2) model (European Committee for Standardization, 2004b). In the latter approach, there is no explicit term for transient creep strain. This phenomenon is included but it is implicitly considered in the mechanical strain term. As this approach was adopted in the current EC2 model, which has proved for many years to yield quite satisfactory results when modelling

experimental tests made on concrete structural elements in fire, the necessity of taking transient creep into account by an explicit term in the strain decomposition has been questioned (Franssen, 2005a). But it should be noted that these tests mostly consist in simple structural elements subjected to standard fire, thus considering only the heating phase. The capability of implicit transient creep model, such as the EC2 model, to accurately represent the response of concrete elements subjected to natural fire, including the cooling phase, has not been demonstrated to the author's knowledge. Recent research (Law and Gillie, 2008) have shown that considering the transient creep term implicitly can have important implications on the Young modulus calculation of concrete during cooling. For a simplified pure concrete column consisting of a single member pinned at both end, which was uniformly heated and then cooled back down to ambient temperature, it was shown by numerical calculations that the response during cooling was significantly different using an explicit or an implicit model of transient creep strain. Indeed for this non loaded and axially restrained column, implicit models slowly released the stresses during cooling and were only pulled into tension when the temperature was close to returning to ambient, whereas explicit models were unable to recover the strains and rapidly progressed into tension. However, the implication on the behavior of a complete structure is still a pending question. The implicit model of EC2 is presented in Section II.1.3 and it is discussed whether an implicit model may fulfill the requirements for concrete models defined in Chapter I, considering the applications of structural fire engineering.

II.1.2.   Review of the uniaxial concrete models with an explicit term for transient creep

II.1.2.1.   *Different strain components in heated concrete*

As explained in Chapter I, a common approach in concrete modelling (Schneider, 1988; Li and Purkiss, 2005) consists in dividing the macroscopically measurable strains in heated concrete (i.e. the total strains) into individual strain components according to Eq. II.1-1:

$$\varepsilon_{tot} = \varepsilon_{th} + \varepsilon_{\sigma} + \varepsilon_{tr} + \varepsilon_{cr} \qquad \text{Eq. II.1-1}$$

where ε_{tot} is the total strain, ε_{th} the free thermal strain, ε_{σ} the instantaneous stress-related strain, ε_{tr} the transient creep strain and ε_{cr} the basic creep strain. The instantaneous stress-related strain can in turn be divided in elastic and plastic strains $\varepsilon_{\sigma} = \varepsilon_{el} + \varepsilon_{p}$, with ε_{el} the elastic strain and ε_{p} the plastic strain.

Following the approach expressed by Eq. II.1-1, the uniaxial constitutive relationships for concrete at elevated temperature require explicit relationships for the calculation of free thermal strain, instantaneous stress-related strain, transient creep strain and basic creep strain. These relationships may depend on the applied stress and temperature, the stress-temperature history, and a set of material parameters to be determined.

Basic creep, defined as the additional strain that develops when only time is changing with all other conditions such as stress and temperature being constant, is generally omitted

for the structural calculation of building structures in the fire situation. Indeed in fire situation, this basic creep strain is often very small compared to the other strains in concrete due to the short period of the fire (Li and Purkiss, 2005). Therefore this term is not addressed further in this work.

Relationships for the calculation of free thermal strain are given in the literature. It is generally admitted that free thermal strain is a nonlinear function of temperature (Schneider, 1982). The nonlinearity results from the different thermal response between the aggregates and the cementitious matrix and from the chemo-physical changes of the aggregates at elevated temperature (Purkiss, 1996).The free thermal strain can be calculated as a function of the thermal expansion coefficient α, which depends on the temperature, according to Eq. II.1-2 (de Borst and Peeters, 1989). Other authors have proposed formulas that directly give free thermal strain as a function of temperature, as expressed by Eq. II.1-3 (Franssen, 1987; Schneider, 1988). The latter approach has been adopted in Eurocode 2. As the type of aggregate has a significant influence on free thermal strain, different functions $\psi(T)$ have been adopted for siliceous and calcareous aggregates in EC2. Different coefficients of thermal expansion α are also defined for concrete with siliceous or carbonate aggregates (Youssef and Moftah, 2007).

$$\dot{\varepsilon}_{th} = \alpha(T)\dot{T}$$

Eq. II.1-2

$$\dot{\varepsilon}_{th} = \psi(T)$$

Eq. II.1-3

The response to steady state tests gives experimental data of the relationships between instantaneous stress-related strain ε_σ and stress σ, as shown in Chapter I. The instantaneous stress-strain curves at elevated temperature can thus be modeled based on the test results. Authors use a set of parameters, such as the compressive and tensile strength and the strain at peak stress, to model the experimental curves; the temperature dependency of these parameters has been discussed in the previous chapter.

As opposite to instantaneous stress-related strain, transient creep strain cannot be measured directly. Transient creep strain is obtained experimentally as the difference between the total strains obtained from transient tests and from steady-state tests. Experimental data have shown that transient creep strain develops during first-time heating and is irrecoverable; it was also shown that this strain depends on the temperature and on the stress applied during heating.

II.1.2.2. *General characteristics of transient creep models*

Different authors have proposed analytical models for transient creep strains. In most of these models, the transient creep strain is linearly proportional to the applied stress and increases with temperature but not linearly (Anderberg and Thelandersson, 1976; Terro, 1998). In Anderberg and Thelandersson's model, transient creep strain was assumed to be proportional to the applied stress and to free thermal strain, and to depend on the type of aggregate (siliceous or carbonate). Yet, it is thought that the origins of transient creep are in the cement paste (de Borst and Peeters, 1989; Law and Gillie, 2008) and free thermal strain of

concrete is dominated by that of the aggregate (Khoury, et al., 1985); therefore transient creep strain is probably physically independent from free thermal expansion. An additional evidence of the absence of link between transient creep strain and free thermal strain is the fact that a lightweight concrete with zero free thermal strain develops the same transient creep strain as a normal weight concrete (Law and Gillie, 2008). Nielsen, et al. (2002) proposed a modification to the Anderberg and Thelandersson's formulation of transient creep strain in which transient creep strain is linearly proportional to temperature instead of free thermal strain. In Diederichs model (1987 cited in Li and Purkiss, 2005), transient creep strain is proportional to the applied stress and to a third order function of temperature obtained by experimental data fitting. In Schneider's model (1985), the transient creep strain is also a function of the initial stress before heating, in addition to the applied stress, the temperature and the temperature dependent concrete modulus of elasticity and strength.

Other authors refer to Load Induced Thermal Strain (LITS) instead of transient creep strain. LITS is the sum of different strain components in heated concrete; it consists of transitional thermal creep, drying creep, basic creep, and changes in elastic strains that are caused by the change in elastic modulus as temperature increases (Law and Gillie, 2008). Transient creep refers to the sum of transitional thermal creep and drying creep; it is by far the largest component of LITS (Terro, 1998). Terro used the experimental results of Khoury, et al. (1985) to develop an empirical formula by data fitting for the Load Induced Thermal Strain. In Terro's empirical formula, LITS is assumed to be a linear function of applied stress and a nonlinear function of the temperature; the model also accounted for the effect of the volume fraction of aggregates on the transient creep strain.

The main features of the transient creep models cited in this section are presented in Section II.1.2.3. This state of the art is partly based on recent reviews published in the literature (Li and Purkiss, 2005; Youssef and Moftah, 2007; Law and Gillie, 2008).

II.1.2.3. *Transient creep models in the literature*

In Anderberg and Thelandersson's model (1976), the transient creep strain rate $\dot{\varepsilon}_{tr}$ is proportional to the free thermal strain rate $\dot{\varepsilon}_{th}$, according to Eq. II.1-4. This relationship is valid until temperatures of about 500°C; beyond this temperature, Anderberg proposes the relationship of Eq. II.1-5 to take into account the observed accelerated temperature effect on the transient creep strain.

$$\dot{\varepsilon}_{tr} = k_2 \frac{\sigma}{f_{c,20}} \dot{\varepsilon}_{th} \quad ; \quad T \leq 500°C \qquad \text{Eq. II.1-4}$$

$$\dot{\varepsilon}_{tr} = 0.1 \times 10^{-3} \frac{\sigma}{f_{c,20}} \dot{T} \quad ; \quad 500°C \leq T \leq 800°C \qquad \text{Eq. II.1-5}$$

In the above equations, k_2 is a (constant) parameter depending on the kind of aggregate and concrete mix, σ is the applied stress, $f_{c,20}$ is the compressive strength at ambient temperature, $\dot{\varepsilon}_{th}$ and $\dot{T}$ are the free thermal strain rate and temperature rate. On the basis of

experimental tests (Anderberg and Thelandersson, 1976), k_2 is found to vary from 1.8 to 2.35 for quartzite aggregate concrete.

Anderberg and Thelandersson's model is thus a relatively simple model with only one parameter and in which the transient creep strain is linearly proportional to the applied stress. An important assumption is that transient creep strain is proportional to free thermal strain, which seems to be a controversial assumption. Note that the transient creep strain is assumed to be the same for loading and unloading as long as the stress is in compression (Li and Purkiss, 2005). In tension, the transient creep strain has not been investigated by the authors due to its unimportance in structural analysis.

The model by Nielsen, et al. (2002) differs from Anderberg and Thelandersson's by the fact that the transient creep strain rate $\dot{\varepsilon}_{tr}$ is linearly proportional to temperature rate $\dot{T}$, instead of free thermal strain rate. Nielsen, et al. use a constant parameter $\beta = 0.38 \times 10^{-4}$ and one single equation for the full temperature range, see Eq. II.1-6. This model is a totally generic model, with no material parameter.

$$\dot{\varepsilon}_{tr} = \beta \frac{\sigma}{f_{c,20}} \dot{T} \qquad\qquad \text{Eq. II.1-6}$$

However, assuming a linear proportionality of transient creep strain rate with temperature rate does not reflect experimental observations of the temperature dependency of transient creep strain beyond 500°C-600°C. Nielsen's model was further improved (Pierce, et al., 2004) by using a bi-linear expression of β, thus considering transient creep strain a nonlinear function of the temperature, see Eq. II.1-7. Simultaneously, three parameters were introduced in the model for consideration of the aggregate type.

$$\beta = 0.01 \times \begin{cases} 2\, A \times \bar{T} + B & ; \quad 0 \leq \bar{T} \leq \bar{T}^* \\ 2\, C\left(\bar{T} - \bar{T}^*\right) + 2\, A \times \bar{T} + B & ; \bar{T} \geq \bar{T}^* \end{cases} \qquad \text{Eq. II.1-7}$$

In Eq. II.1-7, $\bar{T}$ is the normalized temperature defined as $\bar{T} = (T - 20)/100$, $\bar{T}^* = 4.5$ is a dimensionless transition temperature between the two expressions, which corresponds to a temperature of 470°C, and A, B and C are parameters. Based on comparison with experimental data, the authors proposed two sets of values for the parameters A, B and C, in order to describe a lower curve ($A = 0.06\%$, $B = 0.15\%$, $C = 1.00\%$) and an upper curve ($A = 0.04\%$, $B = 0.10\%$, $C = 0.70\%$). The authors state that the use of two parabolic expressions captures the rather abrupt change in behavior detected experimentally around the transition temperature. On the other hand, the model keeps a relative simplicity as the number of parameters is limited and the dependence in the applied stress level is proportional.

In Schneider's model (1988), the transient creep strain component also includes basic creep strains, in addition with transitional thermal creep and drying creep. The transient creep strain component depends on the applied stress and temperature. The transient creep also depends on the elastic modulus at elevated temperature, which depends on the initial stress applied before heating in Schneider's model. Finally, the transient creep strain depends on the

moisture content and type of aggregates. Schneider's model for transient creep strain is given by Eq. II.1-8.

$$\varepsilon_{tr,cr} = \frac{\Phi}{E_{20} \times f(T) \times g(\sigma,T)} \, \sigma \qquad \text{Eq. II.1-8}$$

In Eq. II.1-8, $\varepsilon_{tr,cr}$ is the transient creep strain component considered by Schneider, E_{20} is the elastic modulus at ambient temperature, $f(T)$ is a function that accounts for the temperature-dependency of the concrete modulus, $g(\sigma,T)$ is a function that accounts for the increase in elasticity due to the pre-applied stress, Φ is an empirical creep function and σ is the applied stress.

The function $f(T)$ is derived from experimental data on the evolution of elastic modulus with temperature, as shown in the previous chapter. The function $g(\sigma,T)$ is given by Schneider, see Eq. II.1-9.

$$g(\sigma,T) = \begin{cases} 1.0 + \dfrac{\sigma_{ci}}{f_{c,20}} \times \dfrac{(T-20)}{100} & ; \quad \dfrac{\sigma_{ci}}{f_{c,20}} \leq 0.3 \\[3mm] 1.0 + 0.3 \times \dfrac{(T-20)}{100} & ; \quad \dfrac{\sigma_{ci}}{f_{c,20}} > 0.3 \end{cases} \qquad \text{Eq. II.1-9}$$

The term σ_{ci} in Eq. II.1-9 refers to the initial compressive stress generated by external forces before the concrete is heated, whereas $f_{c,20}$ refers to the compressive strength at ambient temperature.

The creep function Φ is given by Eq. II.1-10.

$$\Phi = \begin{cases} g\,\varphi + \dfrac{\sigma}{f_{c,20}} \times \dfrac{(T-20)}{100} & ; \quad \dfrac{\sigma}{f_{c,20}} \leq 0.3 \\[3mm] g\,\varphi + 0.3 \times \dfrac{(T-20)}{100} & ; \quad \dfrac{\sigma}{f_{c,20}} > 0.3 \end{cases} \qquad \text{Eq. II.1-10}$$

where the function φ is given by Eq. II.1-11.

$$\varphi = C_1 \tanh \gamma_w (T-20) + C_2 \tanh \gamma_0 \left(T - T_g\right) + C_3 \qquad \text{Eq. II.1-11}$$

The term γ_w accounts for the moisture content w in % by weight, see Eq. II.1-12, whereas γ_0, T_g, C_1, C_2, C_3 are constant defined by Schneider for different types of concrete. The values of the constant γ_0, T_g, C_1, C_2, C_3 are respectively 0.0075 /°C, 700 °C, 2.60 [-], 1.40 [-], 1.40 [-] for quartzite concrete; 0.0075 /°C, 650 °C, 2.60 [-], 2.40 [-], 2.40 [-] for limestone concrete; 0.0075 /°C, 600 °C, 2.60 [-], 3.00 [-], 3.00 [-] for lightweight concrete (Schneider, 1988). However in more recent publication, Schneider gives slightly modified values for these constant based on ongoing research results: 0.0075 /°C, 800 °C, 2.50 [-], 0.70 [-], 0.70 [-] for quartzite concrete; 0.0075 /°C, 700 °C, 2.50 [-], 1.40 [-], 1.40 [-] for

limestone concrete; 0.0075 /°C, 600 °C, 2.50 [-], 3.00 [-], 2.90 [-] for lightweight concrete (Schneider, et al., 2008).

$$\gamma_w = (0.3w + 2.2) \times 10^{-3}$$ Eq. II.1-12

By taking into account the effect of the load history before heating on the deformation response to a change in stress and temperature increase, Schneider (1988) aims at incorporating the effect of concrete memory in its model. In recent research, Schneider has extended his theory to take into account the effect of the load history during heating on the deformation response of concrete (Schneider, et al., 2008; Schneider and Schneider, 2009).

Schneider's model is more complex and comprises an important number of parameters compared with the other models of transient creep strain. In this model, the relationships between transient creep strain and both temperature and applied stress are non linear.

The predictions of the presented models of transient creep strain are compared with experimental data for quartzite concrete specimens subjected to applied stress ratios α equal to 0.10, 0.30 and 0.45, where α is defined as the ratio of the stress applied during heating on the compressive strength at ambient temperature, see Fig. II.1-1. Experimental data of transient creep strain (TCS) are obtained by measuring total strains during first time heating of the concrete specimens under applied stress ratio α, and by subtracting from the total strains the free thermal strain and the instantaneous stress-related strain obtained from steady-state tests (Schneider, 1988).

In Fig. II.1-1, the curve related to Anderberg and Thelandersson's model has been obtained using the value 2.35 for the constant k_2 and the EC2 formula for computing the free thermal strain ε_{th}; it would have been more consistent to use Anderberg's formula for the free thermal strain calculation but the author was unable to obtain the expression of this formula. In Pearce's model, the values of the three constants A, B, C were taken as the upper curve values. In Schneider's model, the parameters for quartzite concrete were considered with a moisture content by weight $w = 3\%$, and the elastic modulus was computed according to the formulas given in a recent publication (Schneider, et al., 2008).

The relationship between transient creep strain and temperature is nonlinear, especially beyond temperature of 500°C. Therefore, the linear relationship proposed by Nielsen cannot accurately follow the trend observed in the test results beyond this temperature; the other models are nonlinear with temperature. Schneider's model gives lower values compared to the other models; the predictions of this model agree reasonably with the test results. The models by Anderberg and by Pearce both consider a transition temperature around which an accelerated temperature effect on the transient creep strain is observed. Although this is confirmed by experimental data, the model by Pearce seems to overestimates this effect for the tested concrete mix.
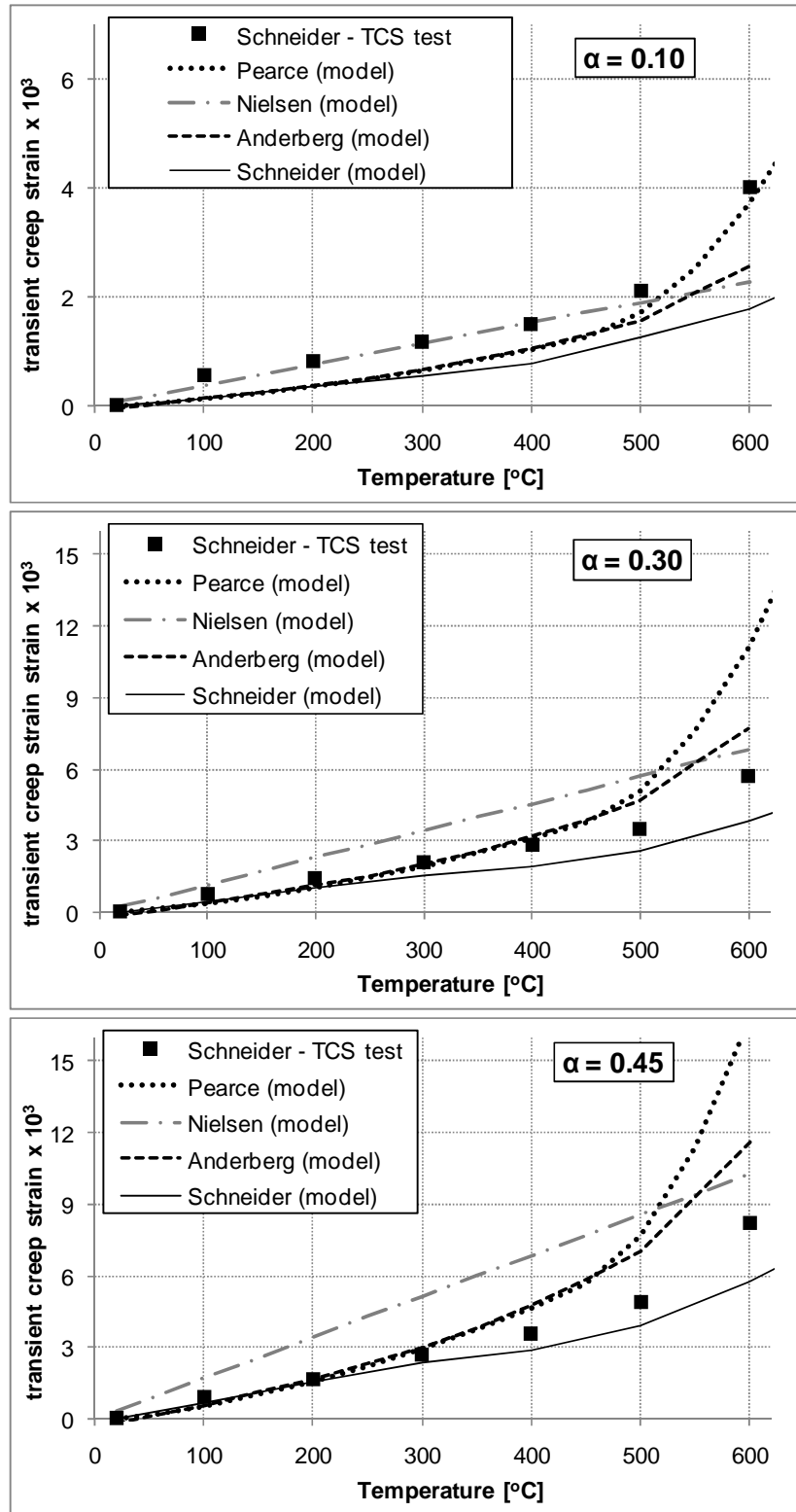
Fig. II.1-1: Comparison between experimental data of TCS (Schneider, 1988) and prediction of different models published in the literature

Terro (1998) developed a model for Load Induced Thermal Strain based on the experimental results obtained at Imperial College (Khoury, et al., 1985); the LITS model by Terro is a function of temperature T, stress level during heating σ and percent aggregate content by volume V_a. It is important to notice that the expression of LITS given by Terro

cannot be compared directly with the expressions of transient creep strain given by other authors, as LITS include additional strain components compared to transient creep strain.

The LITS model by Terro assumes a linear relationship between LITS and applied stress, and a nonlinear dependency on the temperature. The model is based on a "Master" LITS curve normalized for values corresponding to an applied stress ratio $\sigma/f_{c,20}$ of 0.3, see Eq. II.1-13.

$$LITS\left(T,\sigma=0.3\,f_{c,20}\right)=\left(A_0+A_1\,T+A_2\,T^2+A_3\,T^3+A_4\,T^4\right)\times10^{-6} \qquad \text{Eq. II.1-13}$$

Eq. II.1-13 stands for concrete with carbonate and lightweight aggregates; for concrete with gravel siliceous aggregate, a different Master curve was introduced, see Eq. II.1-14. The type of aggregate is thus a parameter in Terro's LITS model.

$$LITS\left(T,\sigma=0.3\,f_{c,20}\right)=1.48\times10^{-6}\left(\begin{array}{c}B_0+B_1\,T+B_2\,T^2\\+B_3\,T^3+B_4\,T^4+B_5\,T^5\end{array}\right) \qquad \text{Eq. II.1-14}$$

The values of the adimensional parameters are as follows: $A_0=-43.87$, $A_1=2.73$, $A_2=6.35\times10^{-2}$, $A_3=-2.19\times10^{-4}$, $A_4=2.77\times10^{-7}$, $B_0=-1098.50$, $B_1=39.21$, $B_2=-0.43$, $B_3=2.44\times10^{-3}$, $B_4=-6.27\times10^{-6}$, $B_5=5.95\times10^{-9}$.

For stress ratios different from 0.3, LITS is determined using Eq. II.1-15, which expresses a linear dependency of LITS on the applied stress ratio.

$$LITS\left(T,\sigma\right)=LITS\left(T,\sigma=0.3\,f_{c,20}\right)\times\left(0.032+3.226\,\frac{\sigma}{f_{c,20}}\right) \qquad \text{Eq. II.1-15}$$

The Master curves given in Eq. II.1-13 and Eq. II.1-14 apply for concrete containing 65% aggregate content by volume. For different aggregate content by volume, the LITS is calculated according to Eq. II.1-16. The effect of aggregate content on LITS is assumed to be linear and similar in magnitude to the effect on basic creep.

$$LITS\left(T,\sigma\right)\big|_{V_a}=LITS\left(T,\sigma\right)\big|_{65\%}\times\left(\frac{V_a}{0.65}\right) \qquad \text{Eq. II.1-16}$$

The equations given by Terro for calculation of LITS apply to temperatures up to 590°C; the author gives no indication for temperatures above this value.

The predictions of Terro's model are compared with experimental data of LITS (Persson, 2003) for concrete specimens subjected to applied stress ratios α of 0.167, 0.33 and 0.50, see Fig. II.1-2. Experimental data of LITS are obtained by measuring total strains during first time heating of the concrete specimens under applied stress ratio α, and by subtracting the free thermal strain and the initial elastic strain from the total strains. Carbonate aggregates were considered in Terro's model with an aggregate content of 65%.

The experimentally obtained LITS is higher (in absolute value) than transient creep strain, which is consistent with the definition of these two strain components: LITS includes,

in addition with transient creep strain, basic creep strain and changes in elastic strains. It can be seen that the model by Terro succeeds in capturing the LITS experimentally obtained by Persson.
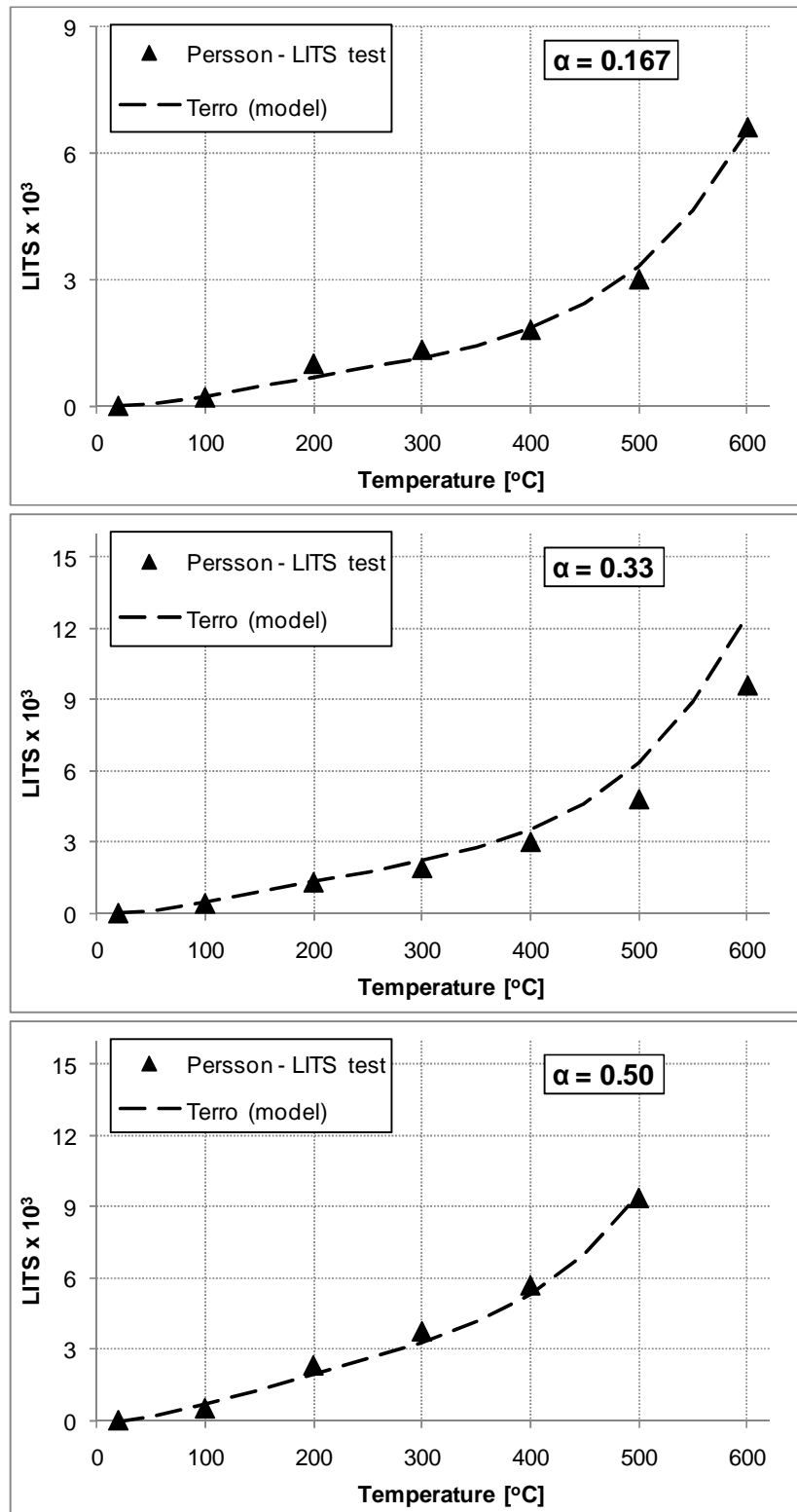
Fig. II.1-2: Comparison between experimental data of LITS (Persson, 2003) and prediction of Terro's model

II.1.3. A concrete model that implicitly incorporates transient creep: the Eurocode 2 model

In the current Eurocode 2 model (European Committee for Standardization, 2004b) no analytical model is given for the calculation of transient creep strain. It is stated in section 3.2.1 of EC2 that: "Numerical values on strength and deformation properties given in this section are based on steady state as well as transient state tests and sometimes a combination of both. As creep effects are not explicitly considered, the material models in this Eurocode are applicable for heating rates between 2 and 50 K/min. For heating rates outside the above range, the reliability of the strength and deformation properties shall be demonstrated explicitly."

The strength and deformation properties given in the Eurocode are partly based on transient state tests and although the transient creep effects are not explicitly considered, the model is applicable to transient situations. Indeed, transient creep effects have been implicitly incorporated in the Eurocode model. The division of the macroscopically measurable strains in heated concrete into individual strain components is done in the EC2 according to Eq. II.1-17:

$$\varepsilon_{tot} = \varepsilon_{th} + \varepsilon_m + \varepsilon_{cr}$$

Eq. II.1-17

where ε_m is the mechanical strain. From Eq. II.1-1 and Eq. II.1-17 it is clear that the mechanical strain is the sum of the instantaneous stress-related strain and the transient creep strain.

In implicit models, the stress is directly related to the mechanical strain, without calculation of the transient creep strain. In the EC2 model, for instance, the relationship at a given temperature T between the stress and the mechanical strain is given for the ascending branch by Eq. II.1-18.

$$\frac{\sigma}{f_{c,T}} = \frac{3\,\varepsilon_m}{\varepsilon_{c1}\left(2 + \left(\varepsilon_m/\varepsilon_{c1}\right)^3\right)}$$

Eq. II.1-18

with $f_{c,T}$ and ε_{c1} the temperature-dependent compressive strength and peak stress strain (PSS). In this relationship, the value of the peak stress strain accounts for the transient creep strain. Indeed the peak stress strain given in the EC2 corresponds to the upper limit (maximum value) of the peak stress strain given in the previous ENV version of Eurocode 2 (European Committee for Standardization, 1995). In the ENV version of EC2, the user had the choice between a lower limit, an upper limit and a recommended average value; the upper limit allowed for considering implicitly the transient creep strain (Franssen, 2005a).

The relationship of Eq. II.1-18 is plotted at 500°C in Fig. II.1-3, next to the relationship of ENV using the lower limit of the peak stress strain. These two models are compared with experimental data of the instantaneous stress-strain relationship at 500°C; obtained by Schneider (1988) as a result of a steady-state test. The ENV model with lower limit of PSS agrees with the experimental curve of the instantaneous stress-strain relationship, which

shows that this model does not include transient creep strain. As there was no additional strain component in the ENV model for consideration of transient creep strain, the code was modified and it was proposed in the current version of Eurocode that the upper limit would be the sole recommended value for the peak stress strain to be used in the stress strain model, therefore including implicitly the transient creep strain in the model. The difference in strain between the EC2 model and the ENV model with lower limit of PSS aims at capturing the experimentally observed difference in strain between transient tests and steady-state tests, i.e. the transient creep strain.
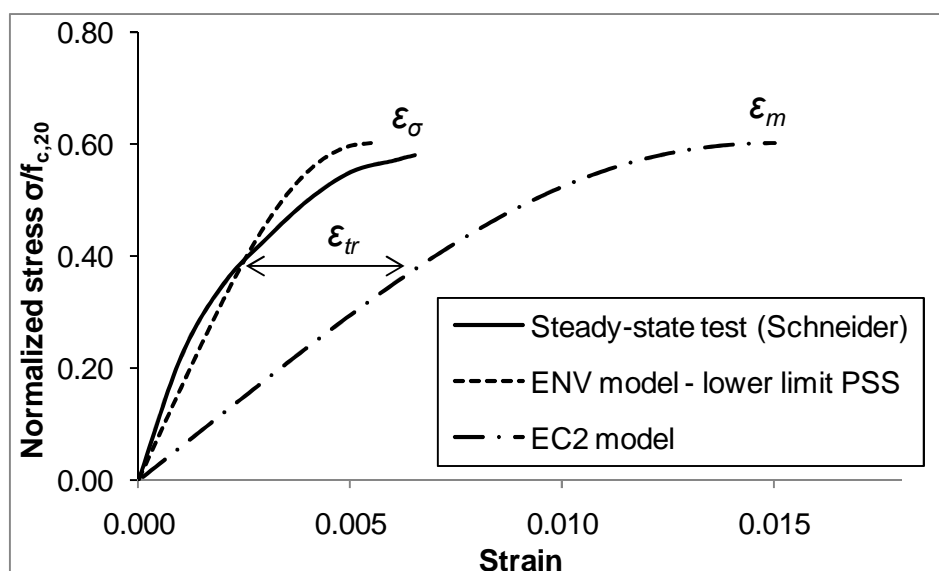
Fig. II.1-3 : Comparison at 500°C between the EC2 model, the ENV model with lower limit of PSS and experimental data of steady-state tests (Schneider, 1988)

II.1.4. Discussion on the existing models

II.1.4.1. *Implicit and explicit approaches*

A number of research works have been conducted to develop constitutive models for concrete in the uniaxial situation. In these works, different approaches have been adopted to handle the phenomenon of transient creep strain. Most researchers have proposed models with an explicit term for transient creep strain in the total strain decomposition; however in the Eurocode 2 and in other published models (Franssen, 1987; Franssen, 1997) it was decided to propose a model that incorporates implicitly the transient creep strain in the mechanical strain term. In order to make a choice between these two approaches, it is necessary to analyze the implications of these two types of models on the numerical simulation of the response of a structure in fire.

The use of an implicit transient creep model does not allow for capturing some of the phenomena described in Chapter I. This is due to two inherent limitations of these implicit models, compared to explicit models.

Firstly, the mechanical strain given by implicit models for a given stress-temperature state is the same, whether concrete has been heated and then loaded at constant temperature or

loaded and then heated under constant stress and this is known not to correspond to experimental evidence. In the tests made to derive the constitutive models, either the temperature or the stress is constant, whereas the other variable is increased. It is important to notice that, in real structures, the transient creep strain depends not only on temperature and stress but also on the stress-temperature path followed by the material. As a result, in explicit models, the relationship between the stress and the mechanical strain is not univocal at a given temperature, because the transient creep strain that is explicitly computed depends on the stress-temperature path. However in implicit models, the stress is directly associated to the mechanical strain, without calculating the transient creep strain; as a consequence the relationship between the stress and the mechanical strain is univocal at a given temperature.

This first limitation of implicit transient creep models is not compatible with the requirement established in Chapter I when studying the stress-temperature paths in a structural element. Indeed it was shown that the stress-temperature paths in structural elements are complex and that these paths induce different effects in terms of transient creep strain. Implicit models reproduce correctly the behavior of concrete only in a very particular situation, when the temperature increases and the stress is constant, and this situation is not so common, even in a simple element subjected to the heating phase of a fire. This is even more the case during the cooling phase of the fire. It is thus preferable to utilize an explicit model for the sake of precision of the stress and stiffness calculated at the local level, i.e. in every point of integration considered in the structure.

The second limitation of implicit transient creep models is about the elastic modulus that is used for unloading at elevated temperature. Constitutive models that include implicitly the transient creep strain recover this transient creep strain during unloading and/or cooling. This is because, at a given temperature, the elastic modulus used for unloading is taken as the initial tangent of the constitutive curve in terms of ($\varepsilon_m; \sigma$), see Fig. II.1-4. In explicit models, the transient creep strain is not recovered during unloading and/or cooling and the modulus for unloading at a given temperature is taken as the initial tangent to the instantaneous stress-strain curve. This influence of the type of transient creep model on the unloading stiffness was highlighted by the numerical example of Law and Gillie (2008) discussed in Section II.1.1.

This second limitation of implicit transient creep models has also important implications on the structural behavior assessed by numerical simulations, especially when natural fires are considered. In this case, the structural response is assessed during the cooling phase of the fire; however the concrete behavior is not captured properly by implicit models during cooling because the transient creep strain is implicitly recovered in these models. Proper modelling of the structural response during cooling requires an explicit computation of transient creep strain.
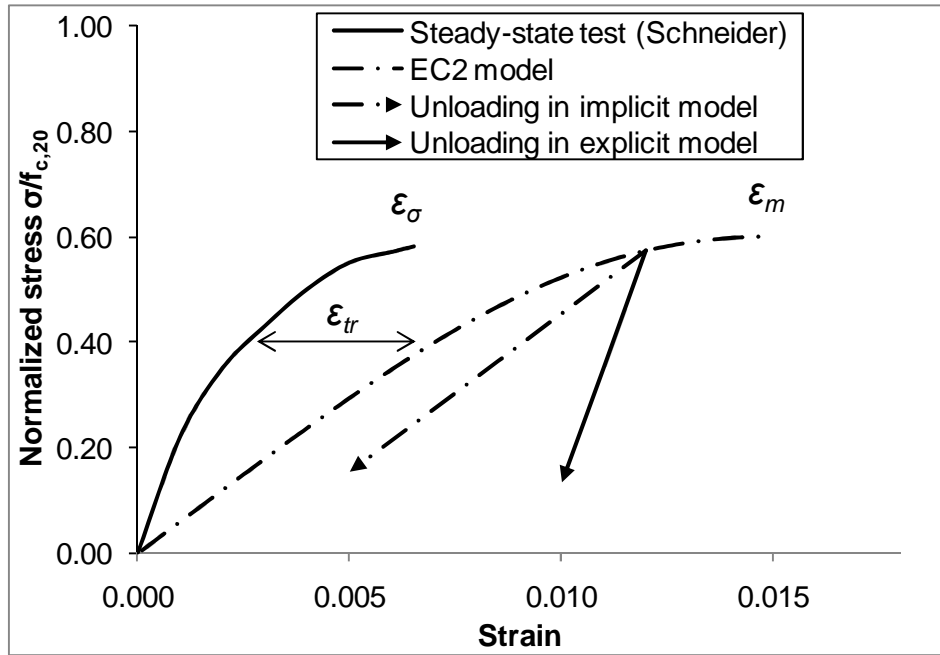
Fig. II.1-4: The transient creep strain is treated as permanent strain by explicit models but it is recovered by implicit models

Despite the limitations of implicit models, the current EC2 model, which treats the transient creep strain implicitly, is widely used and accepted by regulators for practical applications in structural fire engineering. It has been used for many years for structural fire calculations, usually based on prescriptive approach based on the standard ISO fire. It is a fact that, as long as concrete columns are checked for fire resistance during the heating phase only, or that the calculations concerns structural elements in which the steel reinforcement has predominant effect compared with the concrete part, the EC2 has proved to yield quite satisfactory results, which to the author's opinion could partially explain why the explicit concrete models have not imposed themselves instead of the EC2.

However, performance-based design is now more and more used for assessing the fire resistance of structures. In a performance-based approach, the aim is to model the response of a real structure subjected to a real fire scenario. A more realistic representation of the fire will be used that comprises not only a heating phase but also a cooling phase during which the temperature of the fire is decreasing back to ambient temperature, as explained in Chapter I. The influence of such realistic fire scenarios in the evaluation of the fire resistance is a key issue in the performance-based approach, as presented for example for concrete-filled hollow structural section columns (Fike and Kodur, 2009). Although the limitations of implicit models such as the EC2 model were not considered as significant when following prescriptive design, these limitations could lead to inappropriate results when a performance-based design including the cooling phase is performed, for the reasons mentioned in this section.

II.1.4.2. *Parameters influencing the transient creep strain*

Among the models that include an explicit term for transient creep strain, different assumptions have been adopted in the literature, leading to transient creep models with various numbers of parameters. The complexity degree of a model, and the number of

parameters involved, is the result of a compromise between the requirements in terms of accuracy and reliability, on the one hand, and the requirements in terms of practical applicability for structural fire engineers, on the other hand.

Based on the literature review, it can be concluded that the linear relationship of transient creep strain with applied stress, and the non linear relationship with temperature, are recurrent hypothesis. Indeed assuming a linear relationship with temperature does not reproduce the experimental observations, and this assumption was abandoned by Nielsen when its model was improved (Pearce, et al., 2004). At the opposite, the approximately linear dependency of transient creep strain with applied stress has been highlighted by experimental tests (Khoury, et al., 1985) and this assumption has been adopted in most of the models presented in the literature. Another recurrent assumption that appears in the models is the influence of the aggregate type. These conclusions on the assumptions made by different authors will be considered in the present work, when developing the original concrete model.

II.2. Multiaxial constitutive models of concrete

This section reviews the research works on constitutive modelling of concrete under multiaxial stress states. Multiaxial models for concrete are required for modelling of structures or structural components such as concrete slabs, joint elements, pressure vessels or tunnels. At ambient temperature, different strategies have been presented in the literature to model the multiaxial mechanical behavior of concrete; a state of the art of these strategies is presented in this section. The present work is particularly interested in two theories: the plasticity theory and the damage theory. The theoretical framework of the plasticity and damage theories is given and their application to concrete modelling is discussed. As will be shown, plasticity models are well adapted for capturing some of the phenomena discussed in the previous chapter, such as concrete dilatancy, whereas damage models are particularly suitable for modelling others, such as stiffness degradation and unilateral effect. As a result, constitutive models coupling plasticity and damage at ambient temperature have recently been presented to encompass the advantages of both theories; the main features of these plasticity-damage models are presented in this section.

Due to the high complexity of the many phenomena involved, the extension of plasticity-damage models to incorporate the effects of temperature is still a challenging issue. At elevated temperatures, proper temperature-dependent relationships for the parameters must be defined. In addition, the transient creep strain must be included in the model. This section presents a state of the art on the plasticity-damage models at high temperatures and on the extension of transient creep models to multiaxial stress states.

II.2.1. General review

II.2.1.1. *Introduction*

Concrete behavior has been discussed in Chapter I. Concrete is a non-linear material which exhibits microcrack growth and plastic flow (Ortiz, 1985). From a phenomenological point of view, in terms of mechanical behavior concrete notably presents a non-symmetric behavior in tension and compression with respect to stiffness degradation, strain softening, pressure sensitivity and volumetric dilatancy.

Different mechanics theories have been adopted by researchers to capture the mechanical behavior of concrete, e.g. plasticity theory, continuum damage theory, microplane theory, fracture mechanics, embedded finite element method and extended finite element method. The efficiency of a theory for modelling concrete behavior depends on the objectives of the model; here, the characteristics of the different class of models are briefly discussed and confronted with the requirements defined in Chapter I.

II.2.1.2. _Continuum vs. discrete modelling of concrete fracture_

Before starting to describe the different theories for modelling of concrete behavior, an important distinction must be done between two fundamentally different approaches for the description of failure processes in materials: the continuum modelling and the discrete modelling (Sluys and Berends, 1998). Discrete crack models are intended to simulate the initiation and propagation of dominant cracks. In contrast, continuum models aim at capturing the deterioration process in concrete through a constitutive relationship; these models are based on the assumption that it is not necessary to individually model the cracks in a concrete structure because, due to the concrete heterogeneity and the presence of reinforcement, many small cracks develop in the structure and dominant cracks only appear later in the loading process (de Borst, et al., 2004).

In continuum models the failure process is assumed to be distributed over an area that belongs to a sampling point in a numerically integrated finite element; this failure process is translated into a deterioration of the current stiffness and strength at that integration point (Feenstra and de Borst, 1995; de Borst, et al., 2004). This approach is called "smeared crack", because the non-linearities due to cracking are smeared over the integration points; the damaged material is considered to be a continuum in which the notions of stress and strain apply. The evolution of cracking is governed by certain internal parameters which are updated in the sampling point upon progressive cracking. The well-known consequence of the "smeared crack" approach for modelling materials with softening behavior is the localization which results in mesh-dependent solutions; it is necessary to introduce an internal length scale in the problem to specify the size of the failure process zone (Sluys and Berendts, 1998). Different techniques have been proposed to overcome this issue, such as nonlocal models or gradient models.

In discrete models, cracking is described as a discrete phenomenon. Different techniques can be adopted for modelling the failure in a discontinuous manner in the material. For instance, interface (zero-thickness) elements are placed between two adjacent solid finite elements and the cracks are modeled by discontinuous displacements along the interface elements. Discrete constitutive models are required to relate the cohesive stresses and relative displacements in the crack zone. However a disadvantage of discrete interface models is that either the localization zone should be predefined, or sophisticated automated mesh regeneration techniques must be employed to update the mesh topology of the structure during the cracking process (Oliver, et al., 2008). These limitations are hardly compatible with practical applications in structural fire engineering. In recent research (Pandolfi and Ortiz, 2002), it was proposed to use a fixed mesh with cohesive interface surfaces surrounding all the elements to overcome these difficulties; yet this technique may result in mesh alignment sensitivity as the cracks are forced to propagate along element boundaries. Another type of discrete models has thus been developed in order to allow for capturing arbitrary crack propagation with fixed finite element meshes without loss of mesh objectivity, resulting in the so-called Embedded Finite Element Method (E-FEM) (Dvorkin, et al., 1990; Sluys and Berends, 1998) and the Extended Finite Element Method (X-FEM) (Belytschko, et al., 2001). In this class of models, the discontinuity that represents the crack is incorporated in the shape functions of the finite element, independently of the boundaries of the element. The

discontinuity may consist in a jump in the displacement field (strong discontinuity) or it may be formulated in the displacement gradient field or strain field (weak discontinuity).

II.2.1.3. Review of the principal theories applied to concrete

Fracture mechanics belongs to the discrete crack modelling approach. Linear elastic fracture mechanics (LEFM) is based on the assumption that the material, which contains a singularity (the crack), remains linear elastic. Stress intensity factors are defined in the neighborhood of the crack to simulate the near-tip singularity (Belytschko and Black, 1999). The stress intensity factors depend on the crack mode; mode I refers to opening, mode II to forward shear and mode III to tearing or out-of-plane shear, see Fig. II.2-1 (Pivonka, et al., 2004). Linear elastic fracture mechanics is well adapted for modelling brittle materials, in which the response is linear elastic up to the maximum stress and then suddenly reaches failure through the propagation of a dominant crack. However, concrete is a quasi-brittle material which exhibits non-linearity before the maximum stress. As LEFM cannot account for the non-linear behavior of concrete, non-linear fracture mechanics (NLFM) has been developed. Non-linear fracture mechanics applied to concrete assumes that an initial crack begins to propagate at the proportional limit in the stress-strain response and continues to propagate in a stable manner up to the peak stress (Shah, et al., 1995). Yet, as fracture mechanics has been developed in the first place for capturing the propagation of one dominant crack, which occurs from a pre-existing crack-like flaw, it is not well adapted to describe the behavior of an entire reinforced concrete structure. In a reinforced concrete structure, the crack propagation is influenced by the heterogeneous character of concrete and the presence of steel rebars, leading to crack branching or crack arrest followed by crack nucleation and growth at other locations (de Borst, et al., 2004). Furthermore, a lot of smeared micro-cracks develop in concrete before the appearance of macro-cracks, and the geometry and location of these microcracks is difficult to predict. As a result, fracture mechanics does not appear as an adapted theory for modeling concrete mechanical behavior in structural applications (Wu, et al., 2006).
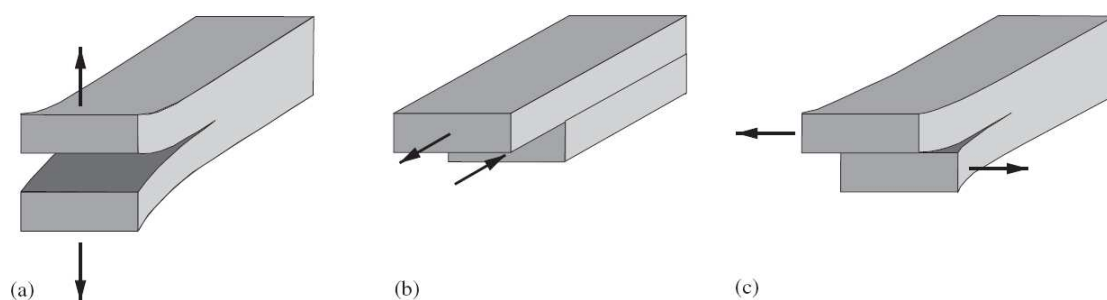
Fig. II.2-1: Crack modes: (a) mode I opening; (b) mode II shear; (c) mode III tearing (from Pivonka, et al., 2004)

Continuum damage mechanics (CDM) is commonly used for modelling concrete behavior; damage models rely on the assumption that the degradation due to micro-cracking can be taken into account through the variations of the elastic properties. Therefore damage models are particularly suitable for description of stiffness degradation and unilateral effect in concrete (Wu, et al., 2006). Continuum damage mechanics can be formulated within the

framework of thermodynamics of irreversible processes with internal variables, to derive consistent constitutive models that preserve the consistency with respect to conservation and evolution principles and that are suitable for many engineering problems (Richard, et al., 2010). Extensive research work has been performed on concrete modelling in the framework of CDM, in which damage is considered as an isotropic (e.g. Mazars, 1984; Lee and Fenves, 1998; Wu, et al., 2006; Grassl and Jirasek, 2006; Richard, et al., 2010) or an anisotropic process (e.g. Ortiz, 1985; Carol, et al., 2001a-b; Desmorat, et al., 2007; Voyiadjis, et al., 2008; Abu Al-Rub and Voyiadjis, 2009). Although continuum damage mechanics provides many advantages for modelling concrete, it is not suitable for capturing some important observed phenomena such as irreversible deformations and inelastic volumetric expansion (dilatancy) in compression. Therefore CDM has been used in combination with plasticity theory in recent research to encompass the advantages of the two approaches in a single constitutive model.

Plasticity theory offers a very interesting framework for modelling concrete because, on the one hand, this theory is nowadays theoretically consolidated and computationally efficient (Wu, et al., 2006) and, on the other hand, it is suitable for capturing the phenomena of dilatancy, permanent strain and hardening and softening behavior of the material (Feenstra and de Borst, 1996; Lee and Fenves, 1998). The split of strains into elastic and plastic parts within the plasticity theory allows for convenient modelling of the inelastic deformations in concrete. Plasticity models are characterized by the definition of a plasticity yield surface, hardening-softening law and plastic flow rule. The plasticity yield surface defines the level of stress from where plastic deformations exist. The hardening-softening law governs the evolution and changes in yield surface during the plastic deformation. The plastic flow rule defines the size of the increment of plastic deformation as well as its direction. As continuum damage mechanics, plasticity theory is formulated at the continuum level in the framework of thermodynamics of irreversible processes with internal variables. Many researchers have used plasticity theory alone to model the concrete behavior (William and Warnke, 1974; Onate, et al., 1993; Feenstra and de Borst, 1996; Grassl, et al., 2002; Li and Crouch, 2010). The published models frequently use non-associative flow rules in order to capture the dilatancy in compression, and work or strain hardening to model the hardening and softening of the material. However, plasticity models are unable to address the process of damage due to microcracks growth, and therefore they fail to reproduce some of the phenomena observed in experiments such as the stiffness degradation and unilateral effect (Wu, et al., 2006). To overcome this limitation, an efficient strategy consists in enriching plasticity theory by damage components.

Application of the microplane modelling approach to concrete modelling has been proposed recently (Bazant, et al., 2000) to overcome disadvantages of other approaches such as plasticity models. In plasticity models, the constitutive relationships are formulated directly in terms of stress and strain tensors and their invariants, but this approach leads to difficulties when applied to concrete because of the various behavioral characteristics of this material depending on its stress states. In the microplane model, the constitutive law is formulated in terms of vectors rather than tensors; this constitutive law gives a relation between the stress and strain components on a plane of any orientation in the material microstructure, called the microplane. This allows for facilitating physical interpretation of stress components. The

description of the concrete behaviors under various stress states is performed by combining the microscopic stress–strain relations defined in multi-oriented microplanes. However, the authors recognize (Bazant, et al., 2000) that the microplane model induces an increase in computational work and storage requirements by a factor 10 compared to the classical plasticity models, due to the need to deal with stress components on all the microplanes. In addition, it was noted (Park and Kim, 2005) that microplane models might not allow for capturing exactly the specific strength of concrete as various stress–strain relations defined in the multi-oriented microplanes are used for calculation of the macroscopic stress. These shortcomings are considered as incompatible with the requirements defined in this thesis.

The Embedded Finite Element Method and the Extended Finite Element Method allow for incorporating kinematic discontinuities due to cracking. The motivation to develop E-FEM and X-FEM was to overcome the limitations of the discrete crack approach and the smeared crack approach. The advantage of these methods over the discrete crack models is that they do not need continuous change in topology to follow the crack propagation. The advantage over the smeared crack models is that they can deal with distorted mesh without causing deterioration of the results (Dvorkin, et al., 1990). Nevertheless, it has been noted that the use of continuum constitutive models, based on smeared crack theory, remains appealing for applications with large scale concrete structures and multi-cracked concrete elements because continuum models, by considering the damaged material as a continuum in which the notions of stress and strain apply, manage to integrate local phenomena in a pragmatic and robust manner (Feenstra and de Borst, 1996; Richard, et al., 2010).

II.2.1.4. *Plastic-damage models for concrete*

Based on the present review, it is found that combination of the plasticity theory with the damage theory may result in a very efficient strategy for modeling the mechanical behavior of concrete. Plastic-damage models offer a convenient framework to capture the concrete behavior while, in addition, they benefit from the advantages of continuum constitutive models. These models can address the main phenomena observed in experimental tests on concrete, described in Chapter I. Finally, plastic-damage models rely on the well consolidated theories of plasticity and continuum damage mechanics, and many research works have been done to provide efficient computational tools for implementation of these theories in finite element codes.

Constitutive models for concrete at ambient temperature based on plastic-damage formulation have been proposed by several authors. These models usually combine stress-based plasticity with either isotropic or anisotropic damage. Models coupling plasticity with anisotropic damage address the characterization of the concrete damage behavior with different microcracking in different directions (Meschke, et al., 1998; Voyiadjis, et al., 2008). However, modeling anisotropic damage in concrete is complex; see for instance the works of Carol et al. (2001a-b). It has been noted by several authors that the applicability to structural analysis of anisotropic damage models for concrete is not straightforward due to the inherent complexities of the required numerical algorithms (Grassl and Jirasek, 2006; Wu, et al., 2006). As a consequence, isotropic damage has been widely used for concrete (Lee and Fenves, 1998; Krätzig and Pölling, 2004; Grassl and Jirasek, 2006). The isotropic damage

process can be characterized by one scalar, several scalars or a tensor. Yet, the one-scalar damage models are not adapted for concrete even when modelling damage as an isotropic process. The use of different scalars to capture the damage process in concrete (Mazars, 1984; Lee and Fenves, 1998) is consistent with the experimental observation of different damage mechanisms developing in tension and in compression; a minimum of two scalar variables is necessary to describe these different damage mechanisms. Some authors have proposed a fourth-order damage tensor to characterize the state of isotropic damage in concrete (Ju, 1990; Wu, et al., 2006), showing that a fourth-order tensor is required to capture the unilateral effect. In conclusion, even for isotropic damage, proper description of the damage state in concrete requires a fourth-order tensor based on two scalar variables.

Among the published plastic-damage models, stress-based plasticity is formulated either in the effective stress space (Lee and Fenves, 1998; Wu, et al., 2006; Grassl and Jirasek, 2006) or in the nominal (damaged) stress space (Lubliner, et al., 1989; Krätzig and Pölling, 2004). Effective stress $\bar{\sigma}$ is meant as the average micro-level stress applied to the undamaged volume of the material whereas nominal stress σ is meant as the macro-level stress and is defined as force divided by the total area, see Fig. II.2-2.
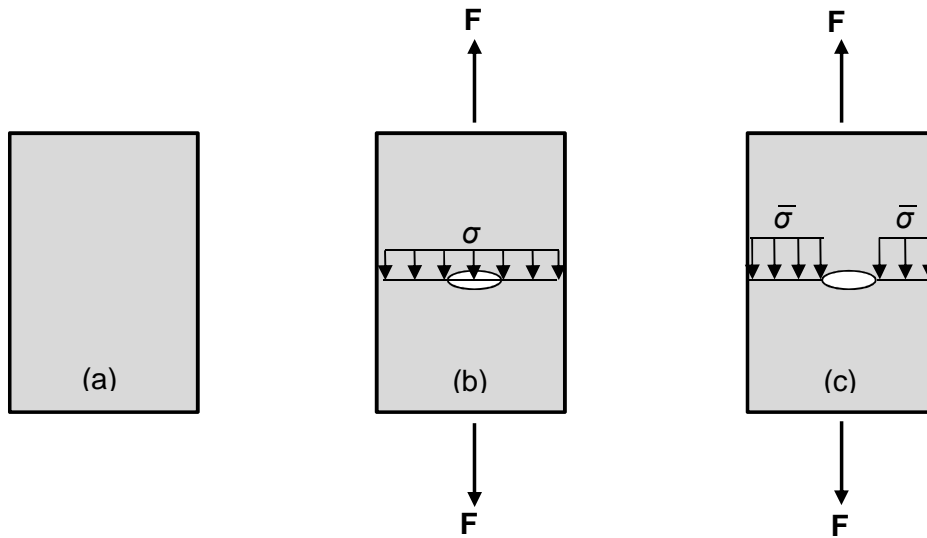
Fig. II.2-2: Schematic representation of nominal and effective stress. (a) Virgin material; (b) Nominal stress; (c) Effective stress applied to the undamaged part of the material

Formulation of the plastic response in the effective stress space relies on the assumption that plastic flow occurs in the undamaged material micro-bounds by means of effective quantities (Ju, 1989). It has been shown recently that local uniqueness is always guaranteed for the plastic-damage models with plasticity formulated in the effective stress space, whereas local uniqueness requires severe restriction when plasticity is formulated in the nominal stress space (Grassl and Jirasek, 2006). Besides, other authors have noted that plastic-damage models formulated in the effective stress space are numerically more stable and attractive compared with models formulated in the nominal stress space (Abu Al-Rub and Voyiadjis, 2009). Formulation of the plastic response in the effective stress space allows for decoupling the plastic part from the damage part in the computation process; computation of the plastic response then constitutes a standard elastoplastic problem in the effective stress space.

As a conclusion, the approach that has been adopted in the present research is the combination of stress-based plasticity formulated in the effective stress space and isotropic damage. In the following parts of this chapter, the theoretical background is given for the plasticity theory and the damage theory applied to concrete modelling. Then, the strategy for coupling of these two theories is presented for the particular case of stress-based plasticity formulated in the effective stress space and isotropic damage. Finally, Section II.2.5 addresses the extension of plastic-damage models to incorporate the effects of high temperature and transient creep.

II.2.2.   Plasticity models

The theoretical background of plasticity theory is presented in this section. First, the concept of plasticity is introduced, with the three cornerstones of this theory which are the initial yield surface, the hardening law and the flow rule; this first part makes recurrent references to the works of Simo and Hughes (1998). Then, the application of plasticity theory to concrete modelling is discussed based on a literature review.

II.2.2.1. *General theory in a one-dimensional context*

To introduce the concept of plasticity, we examine the mechanical response of the one-dimensional frictional device presented by Simo and Hugues (1998) and illustrated in Fig. II.2-3. It is assumed that the device, which is initially of unit length and unit area, consists of a spring, with elastic constant E, and a Coulomb friction element, with constant $\sigma_Y > 0$. The applied stress (force) and the total strain (change in length) in the device are noted σ and ε, respectively.

From Fig. II.2-3, it can be stated that the total strain ε is the sum of two parts: the elastic strain ε_{el}, developed by the spring, and the plastic strain ε_p, developed by the friction device; this is expressed by Eq. II.2-1.

$$\varepsilon = \varepsilon_{el} + \varepsilon_p \qquad\qquad \text{Eq. II.2-1}$$
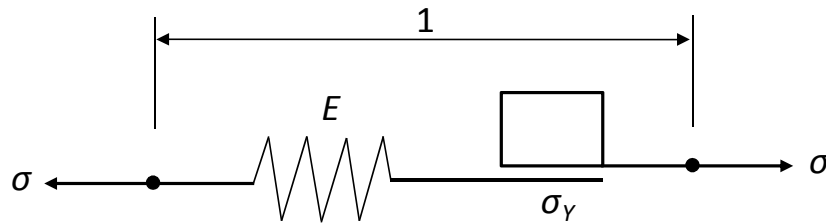
Fig. II.2-3: One-dimensional frictional device illustrating rate-independent plasticity (Simo and Hugues, 1998)

The applied stress is equilibrated by the stress on the spring, see Eq. II.2-2, with upper bound corresponding to the constant σ_Y characterizing the friction device.

$$\sigma = E\,\varepsilon_{el} = E\left(\varepsilon - \varepsilon_p\right) \quad ; \quad \left|\sigma\right| \leq \sigma_Y \qquad\qquad \text{Eq. II.2-2}$$
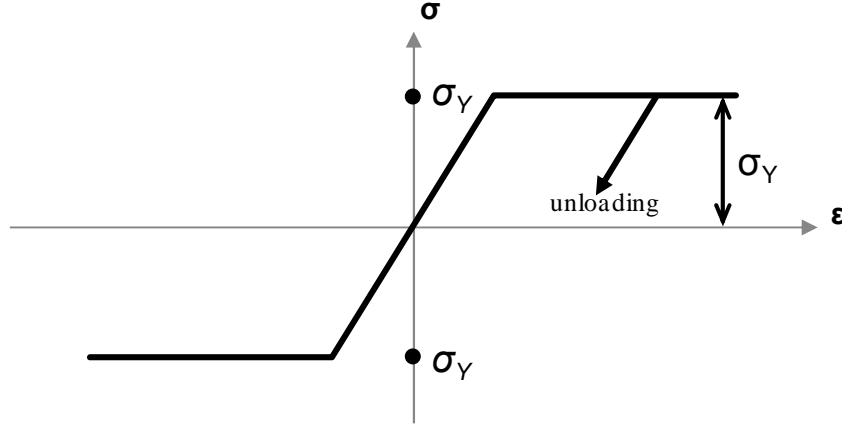
Fig. II.2-4: Stress-strain relationship for the one-dimensional elastic-friction model

The mechanical response of the elastic friction model is schematized in Fig. II.2-4. As the stress on the system cannot be greater in absolute value than $\sigma_Y > 0$, it results that the admissible stresses are constrained to lie in a certain closed interval $[-\sigma_Y; \sigma_Y]$. This condition on the stress is referred to as the yield condition and the boundary of the closed interval, which reduces to two points $\{-\sigma_Y; \sigma_Y\}$ in the present one-dimensional model, is called the yield surface. The yield condition is written in Eq. II.2-3.

$$f(\sigma) := |\sigma| - \sigma_Y \leq 0 \qquad \text{Eq. II.2-3}$$

If the absolute value σ of the applied stress is lower than the constant of the friction device σ_Y, i.e. if the stress is not on the yield surface, no change in plastic strain takes place; the instantaneous response of the device is elastic, see Eq. II.2-4.

$$f(\sigma) < 0 \Rightarrow \dot{\sigma} = E(\dot{\varepsilon} - \dot{\varepsilon}_p) = E\dot{\varepsilon} \qquad \text{Eq. II.2-4}$$

A change in the plastic strain ε_p arises only if the stress is on the yield surface. Indeed when the applied stress σ reaches the constant of the frictional device σ_Y, this device experiences slip in the direction of the applied stress. The evolution of the plastic strain is then governed by Eq. II.2-5, named flow rule, where $\gamma \geq 0$ is the slip rate.

$$\dot{\varepsilon}_p = \gamma \, sign(\sigma) \qquad \text{Eq. II.2-5}$$

The flow rule of Eq. II.2-5 can be used to describe the evolution of the plastic strain for any admissible stress state σ provided that γ and σ satisfy with the physical requirements that the stress must be admissible and that the plastic flow can take place only if the stress is on the yield surface. These requirements result in the conditions of Eq. II.2-6, which are referred to as Kuhn-Tucker conditions.

$$\gamma \geq 0, \quad f(\sigma) \leq 0, \quad \gamma f(\sigma) = 0 \qquad \text{Eq. II.2-6}$$

In addition, a condition is introduced to express the physical requirement that a change in plastic strain (i.e., $\gamma > 0$) can only arise if the stress point σ "persists" on the yield surface. This condition, called consistency condition and given by Eq. II.2-7, allows for determining the actual value of the slip rate γ.

$$\gamma \dot{f}(\sigma) = 0$$
<div align="right">Eq. II.2-7</div>

The plasticity model can be further enriched by introducing the concept of hardening. In strain hardening plasticity, the stress varies simultaneously with the plastic strain in the device; therefore the yield surface varies with the amount of plastic flow in the system. Depending on the behavior that is represented, the yield surface can expand (hardening) or be reduced (softening) with the amount of plastic flow.

Hardening (or softening) is introduced in plasticity models by incorporating hardening variables into the yield condition. The evolution of these hardening variables during the plastic deformation process is governed by hardening laws. For instance, a yield condition with isotropic linear hardening is given by Eq. II.2-8, where $E_p \geq 0$ is a constant called plastic modulus and κ is the internal hardening variable that depends on the amount of plastic flow. Isotropic linear softening is similarly described using $E_p < 0$. The internal variable κ can be written for instance in terms of the equivalent plastic strain, see Eq. II.2-9.

$$f(\sigma, \kappa) := |\sigma| - |\sigma_Y + E_p \, \kappa| \leq 0, \quad \kappa \geq 0$$
<div align="right">Eq. II.2-8</div>

$$\dot{\kappa} = |\dot{\varepsilon}_p|$$
<div align="right">Eq. II.2-9</div>

In the situation described by Eq. II.2-8, the location of the center of the yield surface does not vary with the amount of plastic flow; to introduce such variation in the model, an additional internal variable must be introduced in the equation of the yield condition to capture kinematic hardening.

II.2.2.2. *General theory in a three-dimensional context*

In a three-dimensional context, the strains and stresses are represented by second order symmetric tensors (i.e., symmetric matrixes). We consider the standard basis $\{\underline{e}_1, \underline{e}_2, \underline{e}_3\}$. Adopting the assumption of small strains, the strain tensor $\underline{\underline{\varepsilon}}$ is defined by Eq. II.2-10, with $\underline{u} = (u_1, u_2, u_3)$ the displacement field, which is a first order tensor (i.e., a vector), $\underline{\nabla} = \dfrac{\partial}{\partial x_i} \underline{e}_i$ the vector differential operator and $\otimes$ the tensorial product.

$$\underline{\underline{\varepsilon}} = \frac{1}{2}\left[\underline{\nabla} \otimes \underline{u} + \left(\underline{\nabla} \otimes \underline{u} \right)^T \right]$$
<div align="right">Eq. II.2-10</div>

This equation can be rewritten in terms of components in the standard basis. The displacement field vector is given by $\underline{u} = u_i \, \underline{e}_i$ and the strain tensor is given by Eq. II.2-11, with $i, j = 1, 2, 3$.

$$\underline{\underline{\varepsilon}} = \frac{1}{2}\left[\frac{\partial u_i}{\partial x_j} + \frac{\partial u_j}{\partial x_i}\right] \underline{e}_i \otimes \underline{e}_j \qquad \text{Eq. II.2-11}$$

The stress tensor is denoted by Eq. II.2-12.

$$\underline{\underline{\sigma}} = \sigma_{ij}\,\underline{e}_i \otimes \underline{e}_j \qquad \text{Eq. II.2-12}$$

Using these notations, the plasticity theory can be generalized to the three-dimensional setting. The total strain tensor $\underline{\underline{\varepsilon}}$ is assumed to be the sum of an elastic strain tensor $\underline{\underline{\varepsilon}}_{el}$ and a plastic strain tensor $\underline{\underline{\varepsilon}}_p$ according to $\underline{\underline{\varepsilon}} = \underline{\underline{\varepsilon}}_{el} + \underline{\underline{\varepsilon}}_p$. The stress tensor $\underline{\underline{\sigma}}$ is related to the elastic strain $\underline{\underline{\varepsilon}}_{el}$ by means of a stored-energy function W according to Eq. II.2-13 (Simo and Hugues, 1998).

$$\underline{\underline{\sigma}} = \frac{\partial W}{\partial \underline{\underline{\varepsilon}}_{el}} \qquad \text{Eq. II.2-13}$$

For linearized elasticity, W is a quadratic form of the elastic strain, thus given by Eq. II.2-14 where $\underline{\underline{C}}_0$ is the fourth order tensor of elastic moduli, which is assumed constant.

$$W = \frac{1}{2}\underline{\underline{\varepsilon}}_{el} : \underline{\underline{C}}_0 : \underline{\underline{\varepsilon}}_{el} \qquad \text{Eq. II.2-14}$$

The above equations imply that the stress tensor is obtained by Eq. II.2-15.

$$\underline{\underline{\sigma}} = \underline{\underline{C}}_0 : \left(\underline{\underline{\varepsilon}} - \underline{\underline{\varepsilon}}_p\right) \qquad \text{Eq. II.2-15}$$

The developments above are consistent with the general framework of thermodynamics of irreversible processes with internal variables. Indeed we consider the expression of the rate of dissipation per unit volume $\mathcal{D}$ given by Eq. II.2-16.

$$\mathcal{D} = \underline{\underline{\sigma}} : \underline{\dot{\underline{\varepsilon}}} - \rho\,\dot{\psi} \geq 0 \qquad \text{Eq. II.2-16}$$

In this equation, ρ is the density (specific mass) and ψ is the Helmholtz free energy per unit mass which depends on the internal state variables of the system. For a material that responds to the plasticity theory with hardening, the free energy per unit mass ψ can be written as a function of the elastic strain $\underline{\underline{\varepsilon}}_{el}$ and additional internal variables κ_i used to capture the inelastic strains that develop in the material. After performing the time derivation of the free energy per unit mass $\psi\left(\underline{\underline{\varepsilon}}_{el}, \kappa_i\right)$, the rate of dissipation per unit volume is evaluated by Eq. II.2-17.

$$\mathcal{D} = \left(\underline{\underline{\sigma}} - \rho\frac{\partial \psi}{\partial \underline{\underline{\varepsilon}}_{el}}\right) : \underline{\dot{\underline{\varepsilon}}}_{el} + \underline{\underline{\sigma}} : \underline{\dot{\underline{\varepsilon}}}_p - \rho\frac{\partial \psi}{\partial \kappa_i}\dot{\kappa}_i \geq 0 \qquad \text{Eq. II.2-17}$$

Referring to the standard thermodynamic arguments (Coleman and Gurtin, 1967), since the dissipation must always be non-negative, in particular for an elastic behavior ($\dot{\underline{\varepsilon}}_p = 0$ and $\dot{\kappa}_i = 0$), the stress tensor is given by Eq. II.2-18.

$$\underline{\underline{\sigma}} = \rho \frac{\partial \psi}{\partial \underline{\underline{\varepsilon}}_{el}}$$
Eq. II.2-18

The expression of Eq. II.2-18 is similar to Eq. II.2-13 where the stored-energy function $W = \rho \psi$ is the free energy per unit volume.

The three basic functions that define the plasticity theory, i.e. the initial yield surface, the hardening rule and the plastic flow rule, are respectively defined by Eq. II.2-19, Eq. II.2-20 and Eq. II.2-21 in the three dimensional context (Simo and Hugues, 1998). In these equations, $\underline{\underline{q}}$ are internal variables which are functions of $(\underline{\underline{\varepsilon}}_p, \kappa_i)$, $\underline{h}$ and $\underline{r}$ are prescribed functions which define the type of hardening and the direction of plastic flow, and $\gamma \geq 0$ is the consistency parameter which is determined using the Kuhn-Tucker conditions and the consistency condition as established previously for the one dimensional context.

$$f\left(\underline{\underline{\sigma}}, \underline{q}\right) = 0$$
Eq. II.2-19

$$\dot{\underline{q}} = -\gamma \underline{h}\left(\underline{\underline{\sigma}}, \underline{q}\right)$$
Eq. II.2-20

$$\dot{\underline{\varepsilon}}_p = \gamma \underline{r}\left(\underline{\underline{\sigma}}, \underline{q}\right)$$
Eq. II.2-21

Finally, the tensor of tangent elastoplastic modulus is given by Eq. II.2-22.

$$\underline{\underline{\underline{C}}}^{ep} = \begin{cases} \underline{\underline{\underline{C}}}_0 & \text{if } \gamma = 0 \\ \underline{\underline{\underline{C}}}_0 - \dfrac{\underline{\underline{\underline{C}}}_0 : \underline{r} \otimes \underline{\underline{\underline{C}}}_0 : \partial_\sigma f}{\partial_\sigma f : \underline{\underline{\underline{C}}}_0 : \underline{r} + \partial_q f \cdot \underline{h}} & \text{if } \gamma > 0 \end{cases}$$
Eq. II.2-22

During a numerical calculation by the finite element method of a structure made of plastic material, the numerical integration of the constitutive law $\dot{\underline{\underline{\sigma}}} = \underline{\underline{\underline{C}}}^{ep} : \dot{\underline{\underline{\varepsilon}}}$ is required. This integration necessarily requires a step-by-step algorithmic method since the tensor $\underline{\underline{\underline{C}}}^{ep}$ is not constant, due to the hardening term and the normal to the yield surface $\partial_\sigma f$ which changes with the stress. The tensor of tangent elastoplastic modulus given by Eq. II.2-22 is generally nonsymmetric, except in the case for which the flow rule is given by the expression of Eq. II.2-23. This case has special significance and is called an associative flow rule.

$$\underline{r}\left(\underline{\underline{\sigma}}, \underline{q}\right) = \partial_\sigma f\left(\underline{\underline{\sigma}}, \underline{q}\right)$$
Eq. II.2-23

Note that the second order symmetric tensors of stress and strain can be rewritten as vectors with six components, as expressed by Eq. II.2-24.

$$\begin{aligned}\underline{\varepsilon} &= \left(\varepsilon_{xx}, \varepsilon_{yy}, \varepsilon_{zz}, \varepsilon_{xy}, \varepsilon_{xz}, \varepsilon_{yz}\right)^T \\ \underline{\sigma} &= \left(\sigma_{xx}, \sigma_{yy}, \sigma_{zz}, \sigma_{xy}, \sigma_{xz}, \sigma_{yz}\right)^T\end{aligned} \qquad \text{Eq. II.2-24}$$

II.2.2.3. *Plasticity model for concrete – Yield surface*

The plasticity theory can be used for modelling of concrete material provided proper functions are adopted to describe the yield surface, hardening rule and plastic flow.

The yield surface should capture the experimental behavior of concrete presented in Chapter I. Concrete is a pressure-sensitivity material with a dramatically lower strength in tension than in compression (Jirasek and Bazant, 2002); therefore the yield surface of concrete should be non-symmetric in tension and compression and should reflect the increase in ductility and strength induced by confinement. Proper description of the effect of confinement is important as such a situation arises, for instance, in concrete columns with a large amount of transverse reinforcement (stirrups). In addition, proper yield surface for concrete material should capture other experimentally observed phenomena. For instance, it should capture the decrease in maximum tensile stress that can be transmitted by the material, compared with the uniaxial tensile strength, when the tensile loading in one direction is combined with compression in one or two perpendicular directions, i.e. in pure shear.

Numerous yield surfaces have been published in the literature to characterize the behavior of different materials. In this section, a few theories are presented and their application to concrete is discussed. For an isotropic material, the yield criterion must depend only on the set of the three principal stresses, $F\left(\sigma_{ij}\right) = F\left(\sigma_1, \sigma_2, \sigma_3\right) = 0$, or the three stress invariants, $F\left(\sigma_{ij}\right) = F\left(I_\sigma, II_\sigma, III_\sigma\right) = 0$. As a reminder, the three stress invariants are given by Eq. II.2-25.

$$I_\sigma = \sigma_{ii} = Tr\left(\underline{\sigma}\right) \quad ; \quad II_\sigma = \frac{1}{2}\left(\sigma_{ij}\sigma_{ji} - \sigma_{ii}\sigma_{jj}\right) \quad ; \quad III_\sigma = \det \underline{\sigma} \qquad \text{Eq. II.2-25}$$

The hydrostatic stress tensor $\underline{p}$ is related to the first stress invariant I_σ by $\underline{p} = (1/3) I_\sigma \underline{1}$, with $\underline{1}$ the identity tensor. This hydrostatic stress tensor tends to change the volume of the stressed body whereas the deviatoric stress tensor, given by Eq. II.2-26, tends to distort the stressed body.

$$\underline{s} = \underline{\sigma} - \frac{1}{3} Tr\left(\underline{\sigma}\right) \underline{1} \qquad \text{Eq. II.2-26}$$

For geometric interpretation, the Haigh-Westergaard coordinates are used here, i.e., the hydrostatic stress invariant ξ, the deviatoric stress invariant ρ, and the deviatoric polar angle θ, see Eq. II.2-27. The Haigh-Westergaard coordinates span a cylindrical coordinate system of the stress space, see Fig. II.2-5.

$$\xi = \frac{1}{\sqrt{3}} I_\sigma$$

$$\rho = \sqrt{2 J_2} \quad ; \quad J_2 = \frac{1}{2} s_{ij} s_{ji}$$

<div style="text-align:right">Eq. II.2-27</div>

$$\cos 3\theta = \frac{3\sqrt{3}}{2} \frac{J_3}{J_2^{3/2}} \quad ; \quad J_3 = \frac{1}{3} s_{ij} s_{jk} s_{ki}$$
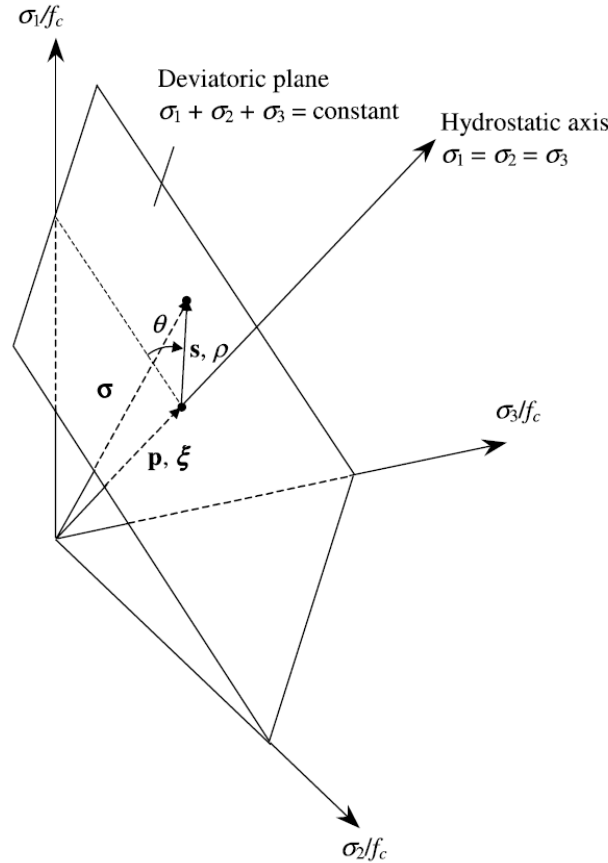
Fig. II.2-5: Haigh-Westergaard coordinates (from Grassl, et al., 2002)

a) <u>Von Mises yield surface</u>

The criterion established by Von Mises (1913) is an isotropic criterion based on the second deviatoric stress invariant ρ. Its physical interpretation is that the behavior of the material becomes plastic when the elastic shear energy reaches a threshold value. It delimits the deviatoric stress by the uniaxial compressive strength f_c in the form:

$$f\left(\underline{\underline{\sigma}}\right) = \rho - \sqrt{\frac{2}{3}} f_c = 0$$

<div style="text-align:right">Eq. II.2-28</div>

In the space of the principal stresses, the yield surface is represented by a cylinder with infinite length, see Fig. II.2-6. When projected in the biaxial stress space, it is an ellipse symmetric with respect to the origin of the principal stress plane, see Fig. II.2-7. This one-parameter criterion infers that the compressive and tensile strength are equal because of lack

of pressure-sensitivity. So, it cannot be used as failure envelope for concrete because it would not properly capture the tensile part of the actual failure envelope.

In the compressive quadrant, the Von Mises criterion could be accepted as an approximation of the failure envelope of concrete. However this criterion, as it includes only the second deviatoric stress invariant, is intended for the description of material in which the failure is by slip between dislocation planes (mode II of failure). Therefore, it is valid for many ductile metals but, for concrete, a model including the effect of the hydrostatic component of stresses should probably be preferred. Indeed in concrete, the cohesive properties have also a preponderant part, together with slip properties. This hydrostatic effect can be considered by the introduction of the first stress tensor invariant ξ within the yield surface model. An example of model combining both ξ and ρ is the Drucker-Prager model.
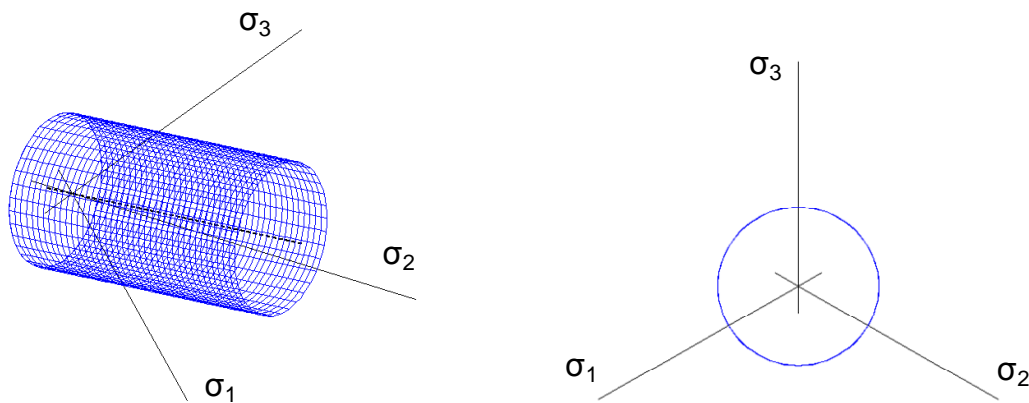
Fig. II.2-6: Von Mises failure surface plotted in the 3D stress space (left) and in the deviatoric plane (right) (picture V. Papanikolaou ©)
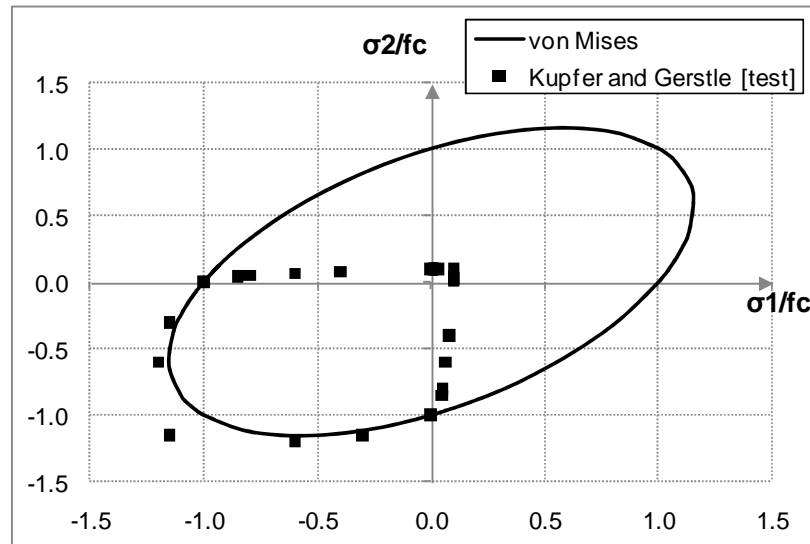
Fig. II.2-7: Biaxial failure envelope resulting from Von Mises yield criterion in the normalized principal stress plane, compared with test data (Kupfer and Gerstle, 1973)

b) Drucker-Prager yield surface

The Drucker-Prager yield surface (1952) is commonly used for cohesive granular material such as soil or concrete. It includes the hydrostatic effect on the yield behavior. In the principal stress space, it is represented by a circular cone with its central axis as the line of hydrostatic stress, see Fig. II.2-8. The deviatoric sections of the Drucker-Prager criterion have a circular shape. This criterion delimits the deviatoric stress by a linear combination of the cohesive and frictional strength in the form of Eq. II.2-29, where A and B denote two material parameters.

$$f\left(\underline{\sigma}\right) = \rho + \sqrt{6}\, A\xi - \sqrt{2}\, B = 0 \qquad \text{Eq. II.2-29}$$

The parameters A and B can be related to the internal friction angle ϕ_c along a triaxial compression path and to the internal cohesion c. When projected in the biaxial stress space, it can be an ellipse, parabola or hyperbola depending on the parameters values.
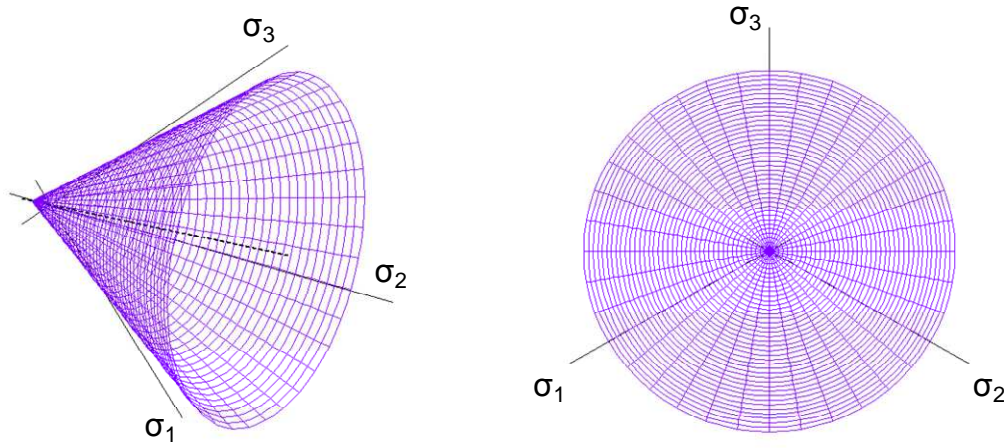
Fig. II.2-8: Drucker-Prager failure surface plotted in the 3D stress space (left) and in the deviatoric plane (right) (picture V. Papanikolaou ©)

Owing to the two parameters A and B, it is possible to match the criterion to two characteristics strength values. For instance, to obtain a quite reasonable approximation of the actual failure envelope in the quadrants that correspond to biaxial tension and to tension-compression, the two parameters are matched to the peak stresses under uniaxial compression f_c and uniaxial tension f_t by choosing the set of values (1) given by Eq. II.2-30. In this case, the intersection of the Drucker-Prager cone with the biaxial stress plane is a hyperbola and the equibiaxial strength becomes infinite (Jirasek and Bazant, 2002), see Fig. II.2-9.

$$A = \frac{1}{\sqrt{3}}\frac{f_c - f_t}{f_c + f_t} \quad ; \quad B = \frac{2}{\sqrt{3}}\frac{f_c f_t}{f_c + f_t} \qquad \text{Eq. II.2-30}$$

On the other hand, a good description in the biaxial compression range can be obtained by matching the uniaxial and equibiaxial compressive strengths f_b with the set of values (2), see Eq. II.2-31. Experimental data on equibiaxial stress tests suggest that the equibiaxial compressive strength f_b is approximately equal to 1.15-1.20 times the uniaxial

compressive strength f_c for usual concrete (Feenstra and de Borst, 1996). The corresponding biaxial failure envelope is an ellipse that succeeds in capturing the actual failure envelope in compression, but not in tension. This failure envelope has been used in the literature as the compressive part of a multi-surface plasticity criterion for concrete, in combination with the Rankine cutoff in tension (Feenstra and de Borst, 1996).

$$A = \frac{1}{\sqrt{3}} \frac{f_b - f_c}{2f_b - f_c} \quad ; \quad B = \frac{1}{\sqrt{3}} \frac{f_b f_c}{2f_b - f_c} \qquad \text{Eq. II.2-31}$$

A disadvantage of the Drucker-Prager yield surface is that it is not closed along the first invariant and therefore it does not allow for modelling the apparition of plasticity for high levels of hydrostatic pressures. As a result, this criterion should not be used for applications in triaxial tests with high confinement (Jason, et al., 2006).
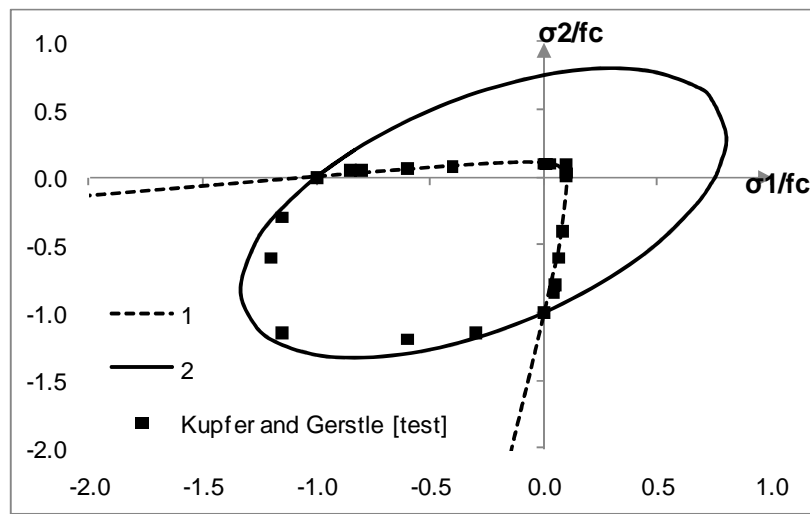
Fig. II.2-9: Biaxial failure envelope resulting from Drucker-Prager yield criterion plotted in the normalized principal stress plane. 1: with the parameters matched to the peak stresses under uniaxial compression and uniaxial tension. 2: with the parameters matched to the uniaxial and equibiaxial compressive strengths.

c) Rankine yield surface

The Rankine criterion states that yielding arises when the maximum principal stress reaches a pre-defined yield stress; it can be expressed as $f(\underline{\sigma}) = \sigma_1(\underline{\sigma}) - f_t = 0$. This criterion can be used for modelling of smeared tensile cracking in concrete (Jirasek and Bazant, 2002).

Rankine yield surface is represented in the stress space by a pyramid made up of three distinct planes, see Fig. II.2-10. The deviatoric section of Rankine yield surface has a triangular shape, which approximately corresponds to the concrete experimental behavior at low compressive hydrostatic pressure (Jirasek and Bazant, 2002).

This criterion is not adapted for capturing the behavior of concrete in compression; however it can be used in association with another yield surface, to model the tensile behavior of concrete. Yet, the experiments have shown that the maximum tensile stress that can be

transmitted by the material decreases with respect to the uniaxial tensile strength when tensile loading in one direction is combined with compression in one or two perpendicular directions; this effect cannot be taken into account using Rankine criterion.
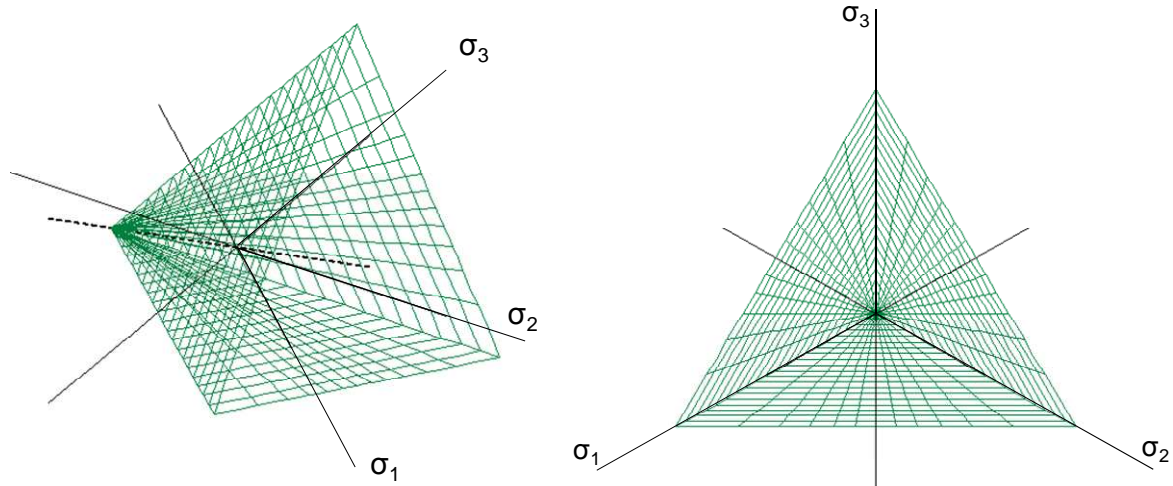
Fig. II.2-10: Rankine failure surface plotted in the 3D stress space (left) and in the deviatoric plane (right) (picture V. Papanikolaou ©)

d) The Menetrey and Willam triaxial failure criterion

Many other failure criteria have been proposed in the literature to capture the behavior of concrete, with different number of parameters and different degree of complexity, e.g. the four-parameters criterion by Ottosen (1977) or the five-parameters criterion by Willam and Warnke (1974). This section presents the triaxial failure criterion by Menetrey and Willam (1995). While the Von Mises and Drucker-Prager criteria respectively include one and two parameters, the Menetrey and Willam criterion is a generalized three-parameters criterion. Owing to the three parameters, the model can be adjusted such that it exactly reproduces the strength in uniaxial tension, uniaxial compression and biaxial compression, see Fig. II.2-11.
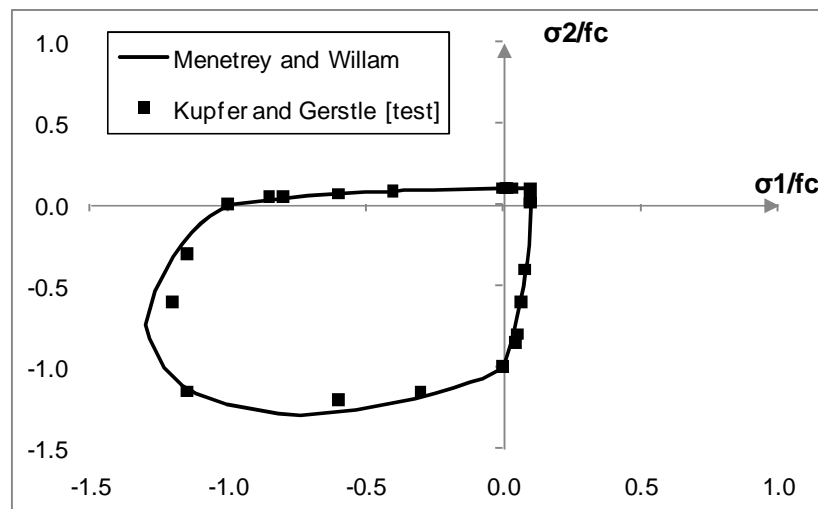
Fig. II.2-11: Biaxial failure envelope resulting from Menetrey and Willam triaxial failure criterion, with e = 0.52, plotted in the normalized principal stress plane

The Menetrey and Willam failure criterion can be written in a generalized form that allows particularizing the criterion to the Von Mises, the Drucker-Prager or the Rankine criteria, for adapted values of the parameters. The representations of the Menetrey and Willam failure criterion in the stress space and in the deviatoric plane are plotted in Fig. II.2-12.

The Menetrey and Willam triaxial failure criterion offers several advantages. It captures with a good accuracy the biaxial and triaxial strength of concrete. It has only three parameters: the uniaxial strength data in tension and compression, which are easily determined from experiments, and an eccentricity parameter e, which influences the hydrostatic compressive region. The criterion can be expressed as a function of the three stress invariants formulated in terms of the Haigh-Westergaard coordinates, for easy geometric representation. The described surface is smooth and convex in stress space provided the eccentricity parameter is chosen in the range $0.5 < e \leq 1$, except for the vertex located at the point of equitriaxial extension, see Fig. II.2-12. Due to its advantages this criterion has been used as the yield criterion in different plastic models for concrete recently published in the literature (Grassl, et al., 2002; Cervenka and Papanikolaou, 2008).
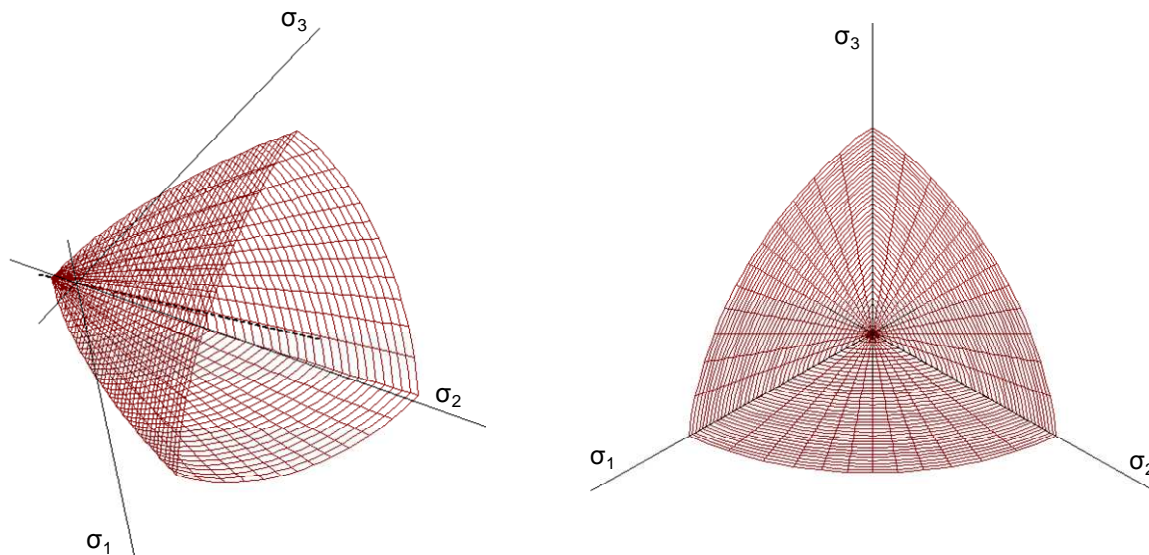
Fig. II.2-12: Menetrey and Willam failure surface plotted in the 3D stress space (left) and in the deviatoric plane (right) (picture V. Papanikolaou ©)

e) <u>Composite yield surface</u>

As concrete presents a highly non symmetric behavior in tension and in compression, a multi-surface yield criterion can be used instead of a unique yield surface criterion to capture the behavior of concrete under different load paths. The underlining idea is that different yield surfaces are used to capture the different mechanisms associated to tension and compression. For instance, a criterion which limits the maximum principal stress, well adapted for the description of a fragile behavior characteristic of the concrete behavior in tension, can be coupled to a "ductile" criterion limiting the deviatoric stress, well adapted to capture the plastic behavior of concrete in compression.

A multi-surface model for concrete combining the Drucker-Prager criterion with the Rankine cutoff in tension has been proposed by Feenstra and de Borst (1996). In this case, the

two parameters *A* and *B* in the Drucker-Prager criterion are matched to the uniaxial and equibiaxial compressive strengths. The resulting composite yield surface is plotted in Fig. II.2-13, and compared with the Menetrey and Willam yield surface and with biaxial strength envelope test data by Kupfer and Gerstle. When a multi-surface yield criterion made of two yield surfaces is considered, the criterion is given by Eq. II.2-32.

$$\begin{cases} f_1\left(\underline{\underline{\sigma}}\right) \leq 0 \\ f_2\left(\underline{\underline{\sigma}}\right) \leq 0 \end{cases}$$

Eq. II.2-32
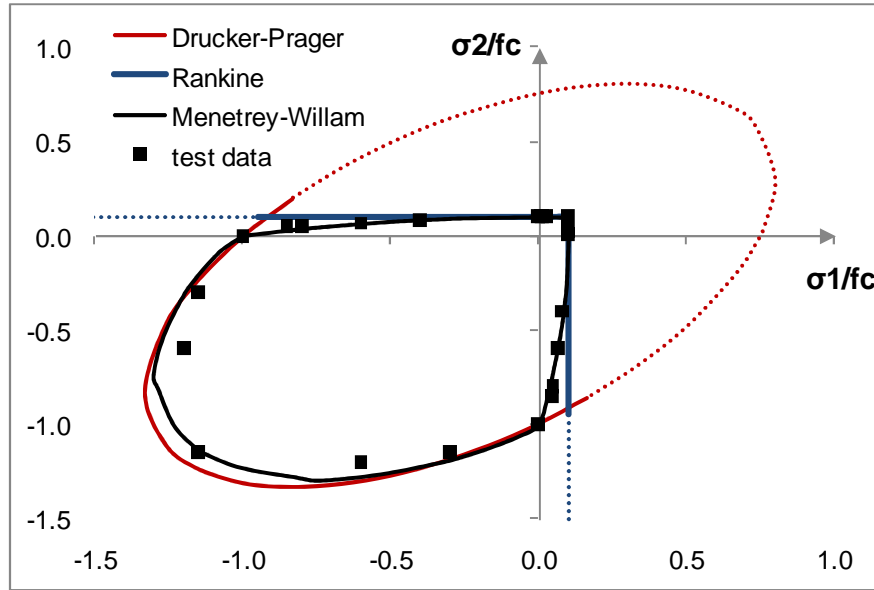
Fig. II.2-13: Biaxial failure envelopes resulting from a composite Rankine-Drucker Prager yield criterion (Feenstra and de Borst, 1996) and from the Menetrey-Willam (1995) criterion, compared with test data from Kupfer and Gerstle (1973)

The main advantage of using multi-surface yield theory for concrete is the ability to handle the different physical mechanisms that develop in tension and in compression with a dedicated yield surface. However, a disadvantage of this method is the difficulty to handle the "corners" of the composite yield surface, at the points where both surfaces intersect: where the surface is discontinuous (non-smooth), the direction of the plastic flow is hard to evaluate. Multi-surface yield criteria have nevertheless been adopted by numerous authors (Feenstra and de Borst, 1996; Nechnech, et al., 2002; de Sa and Benboudjema, 2011) for concrete modelling due to their convenience in capturing separately the tensile and compressive phenomena.

II.2.2.4. *Plasticity model for concrete – Flow rule and Hardening/Softening*

The evolution of the plastic strain rate is given by a plastic flow rule as expressed by Eq. II.2-33, with $\gamma \geq 0$ the consistency parameter that defines the length of plastic flow and $\underline{\underline{r}}$ a prescribed function that defines the direction of plastic flow. The evolution of the plastic

strain must satisfy with the Kuhn-Tucker conditions given by Eq. II.2-6. The consistency parameter γ is often referred to as plastic multiplier $\dot{\lambda}$ in the literature.

$$\dot{\underline{\underline{\varepsilon}}}_p = \gamma \, \underline{\underline{r}}\left(\underline{\underline{\sigma}}, \underline{\underline{q}}\right) = \dot{\lambda} \, \underline{\underline{r}}\left(\underline{\underline{\sigma}}, \underline{\underline{q}}\right) \qquad \text{Eq. II.2-33}$$

The consistency parameter can be determined using the consistency condition, given by Eq. II.1-7, provided the direction $\underline{r}$ and the hardening rules are known.

The value of the direction $\underline{r}$ is defined as a function of the material state, represented by the stress state $\underline{\underline{\sigma}}$ and the hardening variables. A plastic potential g dependent on the stress tensor and the hardening variables is generally used, leading to Eq. II.2-34.

$$\dot{\underline{\underline{\varepsilon}}}_p = \dot{\lambda} \, \frac{\partial g\left(\underline{\underline{\sigma}}, \underline{\underline{q}}\right)}{\partial \underline{\underline{\sigma}}} \qquad \text{Eq. II.2-34}$$

The flow rule is said associated when $\partial_\sigma g$ is collinear to $\partial_\sigma f$. In this case, the plastic flow is normal to the yield surface in the stress space. On the opposite, the flow rule is said non associated when $\partial_\sigma g$ has a different direction than $\partial_\sigma f$. Associated flow rules are well adapted for materials such as metals in which the failure is due to slip between dislocation planes (mode II of failure) and therefore induces no volumetric variation. However for concrete type materials, a non associated flow rule should be preferred because the plastic deformation is accompanied by volumetric variations: $tr\left(\dot{\underline{\underline{\varepsilon}}}_p\right) \neq 0$ (Lemaitre, et al., 2009).

In case of multi-surface plasticity, a different plastic potential g_i is introduced for each yield function f_i. The evolution of the plastic strain rate is determined by Koiter's rule (Koiter, 1953), which allows for a summation of the plastic strain of each yield function according to Eq. II.2-35. In this equation, $\dot{\lambda}_i$ represents the plastic multiplier associated to the plastic potential g_i.

$$\dot{\underline{\underline{\varepsilon}}}_p = \sum_{i=1}^{n} \dot{\lambda}_i \, \frac{\partial g_i}{\partial \underline{\underline{\sigma}}} \qquad \text{Eq. II.2-35}$$

In the two-surface model proposed by Feenstra and de Borst (1996), they suggest to use an associated flow rule in tension, i.e. $g_t = f_t$, and a non associated flow rule in compression, $g_c \neq f_c$. The suggested plastic potential in compression is such that the compressive plastic flow is associated in the deviatoric plane but its volumetric part uses a dilatancy coefficient different from the coefficient of internal friction.

Hardening or softening of the yield surfaces are driven by the internal variables κ_i. In the model by Feenstra and de Borst, the Drucker-Prager surface evolves by isotropic hardening followed by softening, whereas the Rankine surface evolves by isotropic softening. The hardening variable κ_1 is introduced in the Drucker-Prager surface equation for modelling

the behavior in compression, while another hardening variable, κ_2, is introduced in the Rankine surface equation for modelling the behavior in tension. The two hardening variables are defined by Eq. II.2-36, where ς_{12} and ς_{21} are constant parameters describing the coupling between the two plastic mechanisms. Due to a lack of experimental data, the authors recommend to set $\varsigma_{12} = \varsigma_{21} = 0$, thus decoupling the softening mechanism in tension from the hardening-softening mechanism in compression.

$$\dot{\kappa}_1 = \dot{\lambda}_1 + \varsigma_{12}\,\dot{\lambda}_2$$
$$\dot{\kappa}_2 = \varsigma_{21}\,\dot{\lambda}_1 + \dot{\lambda}_2$$

Eq. II.2-36

Assuming that the mechanisms in tension and compression are decoupled, the hardening variables κ_1 and κ_2 can be interpreted as effective plastic strains in the sense of the work hardening hypothesis, adapted for non associated flow (Jirasek and Bazant, 2002). Indeed after setting $\varsigma_{12} = \varsigma_{21} = 0$ in Eq. II.2-36, the hardening variables are given by Eq. II.2-37, with g_1 the plastic potential that defines the flow rule for the compressive mechanism and f_t the uniaxial tensile yield strength.

$$\dot{\kappa}_1 = \frac{\underline{\underline{\sigma}} : \underline{\underline{\dot{\varepsilon}}}_{p1}}{g_1} \quad ; \quad \dot{\kappa}_2 = \frac{\underline{\underline{\sigma}} : \underline{\underline{\dot{\varepsilon}}}_{p2}}{f_t}$$

Eq. II.2-37

As a result, under uniaxial tension κ_2 is equal to the plastic strain in the direction of applied stress, whereas under uniaxial compression κ_1 is proportional to the plastic strain in the direction of applied stress. Owing to this interpretation of the hardening variables, the hardening laws may be identified from uniaxial stress-strain curves.

II.2.3.   Damage models

Concrete subjected to external and/or thermal loads develops microcracking, which results in a modification of its mechanical properties. The damage models offer a convenient framework for taking into account the influence of microcracking on the mechanical behavior of concrete at the macroscopic level. The theoretical background of damage theory is presented in the first part of this section. Then, an example of its application to concrete modelling is given in the second part.

II.2.3.1. *Theoretical background of continuum damage mechanics*

The damage theory relies on the consideration of internal variables (scalar or tensor) that describe the state of damage of the material. In the isotropic case, the micro-crack state of the material is considered homogeneous in all directions. The isotropic damage of the material due to microcracking is modeled in the simplest case by a single scalar internal variable called damage variable *D*, which ranges from 0 for the undamaged material to 1 for completely damaged material. However in some cases, proper modelling of the isotropic state of damage of the material may require several scalars, for instance when the material behavior is non

symmetric in tension and in compression. When particular phenomena have to be captured, such as the unilateral effect in concrete, proper description of the isotropic state of damage may even require the use of a tensor (Ju, 1990). For anisotropic materials, a tensor is automatically required for modelling the anisotropic damage state due to the influence of the orientation of micro-defects.

In damage theory, a distinction is made between the damaged and the undamaged parts of the material. Before any damage develops in the material, the material is in its virgin state and the damaged and undamaged parts coincide. Then, damage progressively growths and it is considered that this damage reduces the volume of the material that sustains the applied load, i.e. the undamaged part of the material. The distinction between the damaged and undamaged parts of the material leads to the definition of the effective stress $\bar{\underline{\sigma}}$, which applies to the undamaged part of the material A_{und}, see Fig. II.2-2. Hence, effective stress is meant as the average micro-level stress applied to the undamaged volume of the material whereas nominal stress $\underline{\underline{\sigma}}$ is meant as the macro-level stress and is defined as external force $\underline{F}_{ext}$ divided by the total area A_{tot}. These considerations lead to Eq. II.2-38.

$$\underline{F}_{ext} = \underline{\underline{\sigma}} \times A_{tot} = \bar{\underline{\sigma}} \times A_{und}$$
Eq. II.2-38

In the undamaged part of the material, the elastic theory applies, which leads to the effective stress-strain relationship of Eq. II.2-39. In this equation, the effective stress tensor is directly related to the strain tensor by the elastic stiffness of the undamaged material $\underline{\underline{C}}_0$.

$$\bar{\underline{\sigma}} = \underline{\underline{C}}_0 : \underline{\underline{\varepsilon}}$$
Eq. II.2-39

In the simplest isotropic case, the state of damage is described by a single scalar D. This damage variable D may be defined in terms of degradation of the Young's modulus of the material, see Eq. II.2-40, where $\underline{\underline{C}}$ is the current material stiffness tensor (Nechnech, et al., 2002). Meanwhile, the damage variable D is also a measure of the ratio between the damaged surface and the total surface of the material, see Eq. II.2-41.

$$\underline{\underline{C}} = (1 - D)\underline{\underline{C}}_0$$
Eq. II.2-40

$$A_{und} = (1 - D) A_{tot}$$
Eq. II.2-41

As a result, the relationship between the apparent and effective stress tensors is given by Eq. II.2-42. This leads to the definition of the nominal stress-strain relationship of Eq. II.2-43.

$$\underline{\underline{\sigma}} = (1 - D)\bar{\underline{\sigma}}$$
Eq. II.2-42

$$\underline{\underline{\sigma}} = (1 - D) \underline{\underline{C}}_0 : \underline{\underline{\varepsilon}}$$
Eq. II.2-43

The damage theory relies on the general framework of thermodynamics of irreversible processes with internal variables. We consider a deformable body under a static loading and

subjected to progressive damage, and we assume that it is an isothermal process. The elastic energy $\mathcal{U}$ per unit volume of the body is a function of the elastic strain tensor $\underline{\underline{\varepsilon}}$ and an internal damage variable D, according to Eq. II.2-44. In this equation, $\mathcal{U}_0$ is the elastic energy of the virgin (undamaged) material; for linearized elasticity, it is given by Eq. II.2-45.

$$\mathcal{U}\left(\underline{\underline{\varepsilon}}, D\right) = (1-D)\ \mathcal{U}_0\left(\underline{\underline{\varepsilon}}\right) \qquad \text{Eq. II.2-44}$$

$$\mathcal{U}_0\left(\underline{\underline{\varepsilon}}\right) = \frac{1}{2}\underline{\underline{\varepsilon}} : \underline{\underline{\underline{C}}}_0 : \underline{\underline{\varepsilon}} \qquad \text{Eq. II.2-45}$$

The Helmholtz free energy per unit volume $\rho\psi$ can be taken equal to the elastic energy per unit volume $\mathcal{U}$. The rate of dissipation per unit volume $\mathcal{D}$ is then given by Eq. II.2-46 (Grassl and Jirasek, 2006).

$$\mathcal{D} = \underline{\underline{\sigma}} : \underline{\underline{\dot{\varepsilon}}} - \rho\dot{\psi} \geq 0 \qquad \text{Eq. II.2-46}$$

After performing the time derivation of the free energy per unit mass $\psi\left(\underline{\underline{\varepsilon}}, D\right)$, the rate of dissipation per unit volume is evaluated by Eq. II.2-47.

$$\mathcal{D} = \left(\underline{\underline{\sigma}} - \rho\frac{\partial\psi}{\partial\underline{\underline{\varepsilon}}}\right) : \underline{\underline{\dot{\varepsilon}}} - \rho\frac{\partial\psi}{\partial D}\dot{D} \geq 0 \qquad \text{Eq. II.2-47}$$

The stress tensor is then obtained by Eq. II.2-48, whereas the non negativity of the dissipation leads to the condition of Eq. II.2-49 on the damage process.

$$\underline{\underline{\sigma}} = \rho\frac{\partial\psi}{\partial\underline{\underline{\varepsilon}}} = (1-D)\underline{\underline{\underline{C}}}_0 : \underline{\underline{\varepsilon}} \qquad \text{Eq. II.2-48}$$

$$-\rho\frac{\partial\psi}{\partial D}\dot{D} \geq 0 \qquad \text{Eq. II.2-49}$$

The term $-\rho\,\partial\psi/\partial D$ is referred to as the dissipative force conjugate to the damage variable, or damage energy release rate (Grassl and Jirasek, 2006). It represents the amount of dissipated internal energy required for generating unit of damage; therefore it is a measure of damage susceptibility. The physical interpretation of Eq. II.2-49 is that the damage process reduces the internal energy of a system. As the damage energy release rate is always nonnegative, the condition of Eq. II.2-49 turns into $\dot{D} \geq 0$, i.e. the damage variable D cannot decrease.

The different models developed in the framework of the continuum damage theory are characterized by the number of variables used to describe the state of damage, the definition of the damage criterion used to describe the initial domain of elasticity, and the evolution laws of these damage variables and damage surface. A connection can be made with the theory of plasticity, as the damage criterion can be interpreted as a yield criterion, the evolution law of

the damage variables as a plastic flow rule and the evolution law of the damage surface as a hardening law.

The damage criteria can be based on different variables of the model. For modelling of concrete, several damage criteria have been proposed in the literature, based on the equivalent strain (Mazars, 1984), on the stress (Ortiz, 1985) or on the damage energy release rate (Ju, 1989; Wu, et al., 2006). Other authors used empirically defined damage criteria (Faria, et al., 1998; Comi and Perego, 2001); however these two empirical models fail to reproduce the concrete behavior under certain stress states, and moreover the model by Comi and Perego requires many parameters with not very clear physical meaning.

As in plasticity theory, when a stress point in the principal stress space is on the current damage surface, two configurations are possible in terms of damage evolution. One may be unloading or neutral loading, thus leading to no evolution of damage, $\dot{D} = 0$. The other is loading, accompanied by the evolution of damage and defined as $\dot{D} > 0$ (Tao and Phillips, 2005).

In the next section, the model by Mazars (1984) is presented as an example of application of damage theory to concrete.

II.2.3.2. *Mazars model*

The stress-strain relationship considered in Mazars model is given by Eq. II.2-50, with E_0 the initial Young modulus and v the Poisson's ratio.

$$\underline{\underline{\sigma}} = (1-D)\,\underline{\underline{C}}_0 : \underline{\underline{\varepsilon}} \quad \leftrightarrow \quad \sigma_{ij} = (1-D)\frac{E_0}{1+v_0}\left(\varepsilon_{ij} + \frac{v}{1-2v}\varepsilon_{kk}\delta_{ij}\right) \qquad \text{Eq. II.2-50}$$

In Mazars model, the non symmetric behavior of concrete in tension and compression is taken into account by the definition of two damage variables; the damage variable D that appears in Eq. II.2-50 is composed of two components as will be shown below.

Mazars assumes that microcracking is created by extension of the concrete material. Therefore, the evolution of damage is driven by the amount of extension experienced by the material during the mechanical loading. Damage develops in the material when the amount of extension in one of the principal strain directions overreaches a certain threshold. This amount of extension is characterized by a variable called equivalent strain and given by Eq. II.2-51. In this equation, $\langle x \rangle_+$ is the Macauley bracket that refers to the positive part of x, i.e. $\langle x \rangle_+ = 0$ if $x < 0$ and $\langle x \rangle_+ = x$ if $x \geq 0$; and ε_i are the principal strains.

$$\tilde{\varepsilon} = \sqrt{\langle \varepsilon_1 \rangle_+^2 + \langle \varepsilon_2 \rangle_+^2 + \langle \varepsilon_3 \rangle_+^2} = \sqrt{\sum_{i=1}^{3}\left(\langle \varepsilon_i \rangle_+\right)^2} \qquad \text{Eq. II.2-51}$$

The damage variable D and the damage criterion are function of this equivalent strain variable. The main advantage of the concept of extension expressed by an equivalent strain is the characterization of a triaxial state by reference to a uniaxial state; this allows for capturing

the results of uniaxial tension test. The damage criterion is given by Eq. II.2-52, where $\kappa(D)$ is the threshold of damage growth.

$$f(\tilde{\varepsilon}, D) = \tilde{\varepsilon} - \kappa(D)$$ Eq. II.2-52

The initial threshold of damage can be related to the peak stress of the material in uniaxial tension f_t as follows: $\kappa_0 = f_t/E_0$. In the course of loading, $\kappa(D)$ takes the maximum value of the equivalent strain $\tilde{\varepsilon}$ ever reached during the loading history.

The damage surface evolution is governed by the evolution of the damage threshold $\kappa(D)$. The damage evolution is also governed by a function of $\kappa(D)$; as $\kappa(D)$ is calculated from $\tilde{\varepsilon}$, the evolution of damage is driven by the equivalent strain $\tilde{\varepsilon}$, which is a measure of the amount of extension.

Because of the differences in the mechanical behavior of concrete in compression and in tension, the description of damage relies on two distinct scalars governed by their evolution law. In tension, the micro-cracks that lead to damage growths in concrete are perpendicular to the applied stress; this first type of damage is called by Mazars *direct damage* and is written as D_t. In compression, the micro-cracks are parallel to the applied stress. These micro-cracks are due to an extension of the material in the transversal direction by Poisson effect; this second type of damage is called *transmitted damage* and is written as D_c. The evolution laws of the damage variables D_t and D_c with the damage threshold $\kappa(D)$ are given by Eq. II.2-53 and Eq. II.2-54. The parameters A_t, B_t, A_c and B_c are characteristics of the material.

$$D_t = 1 - \frac{\kappa_0(1-A_t)}{\kappa} - \frac{A_t}{\exp\left[B_t(\kappa-\kappa_0)\right]}$$ Eq. II.2-53

$$D_c = 1 - \frac{\kappa_0(1-A_c)}{\kappa} - \frac{A_c}{\exp\left[B_c(\kappa-\kappa_0)\right]}$$ Eq. II.2-54

The damage parameter D is defined as a linear combination of the *direct damage* in tension and the *transmitted damage* in compression, $D = \alpha_t D_t + \alpha_c D_c$. The weighting coefficients α_t and α_c, that appear in the latter expression, depend on the stress state; they define the relative importance of tension and compression in the damage process. The condition $\alpha_t + \alpha_c = 1$ has to be verified. The expression of these weighting coefficients is given by Mazars as functions of the principal values of the strains $\underline{\underline{\varepsilon}}^+$ and $\underline{\underline{\varepsilon}}^-$ due to positive and negative stresses. In uniaxial tension, $\alpha_t = 1$, whereas in uniaxial compression $\alpha_c = 1$. Hence, D_t and D_c can be obtained separately from uniaxial tests.

Mazars model contains seven parameters. The Young's modulus E_0 and Poisson's ratio ν can be measured from a uniaxial compression test. The parameters related to damage in tension (f_t, A_t, B_t) can be provided by a direct tensile test or three-point bend test. The

parameters related to damage in compression (A_c, B_c) can be fitted from the response of the material to uniaxial compression.

II.2.4. Coupling plasticity and damage

The last two sections have presented the theoretical backgrounds of the plasticity and the damage theories and have given some information about their application to concrete modelling. The present section is interested in the coupling between these two theories. Indeed, models based on a plastic-damage formulation are better adapted to capture the different phenomena (e.g. permanent strains, degradation of stiffness, etc) exhibited by concrete material, compared with plasticity models and damage models, see Fig. II.2-14. This section focuses on the combination of stress-based plasticity formulated in the effective stress space and isotropic damage for the reasons mentioned at the end of the general review, see Section II.2.1.4.
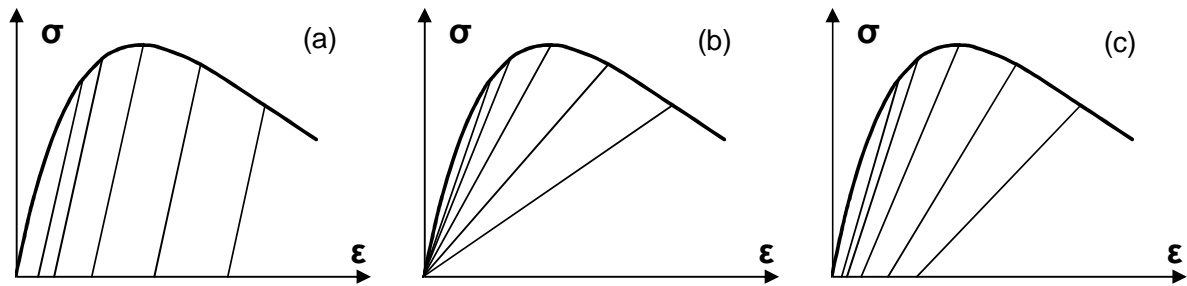
Fig. II.2-14: Uniaxial stress-strain behavior for a model based on (a) plasticity theory,
(b) damage theory, (c) coupled plastic-damage theory

Several recently published concrete models have adopted a plastic-damage formulation with stress-based plasticity in the effective stress space and isotropic damage.

The models published in the literature notably differ by the type of coupling between plasticity and damage. Indeed, plasticity and damage may be driven by the same internal variables or the evolution of these two phenomena may be driven separately using different internal variables. In the latter case, different thresholds are defined for each of these phenomena. The choice of governing the evolutions of plasticity and damage with different internal variables relies on the assumption that the physical mechanisms of interaction between damage and plastic strains, if they exist, are too complicated to be modeled by a single phenomenological approach. In the model by Wu, et al. (2006), the evolution of plasticity is driven by the equivalent plastic strains under uniaxial tension and compression whereas the evolution of damage is driven by the damage energy release rates (DERRs); in addition with the yield criteria, two damage criteria are defined with their damage thresholds. This approach gives a lot of flexibility in the modelling, as for instance it allows for developing degradation of the elastic properties without developing irreversible strains or vice versa; however, this approach implies a large number of parameters. By using the same internal variables to govern the evolution of plasticity and damage, and consequently the same threshold for the two phenomena, the number of parameters can be reduced. The models that use a single set of internal variables for driving plasticity and damage make the implicit

assumption that the two phenomena are caused by the same physical mechanisms at the microscopic level. These physical mechanisms at the microscopic level can thus be represented by a single set of macroscopic variables, which are used to model all the phenomenological aspects of the behavior (irreversible strains, degradation of the elastic properties, unilateral effect, etc). Although the validity of this assumption may be questioned for concrete, it has been adopted in several models proposed in the literature (Grassl and Jirasek, 2006; Nechnech, et al., 2002; Matallah and La Borderie, 2009) due to the resulting simplicity of the model and the limited number of parameters. In these models, damage is linked to the evolution of the plastic strains.

Different formulations of the stress-strain relationships have been used in the plastic-damage models. An interesting approach is based on the formulation of Eq. II.2-55. This formulation has been adopted by different researchers (Grassl and Jirasek, 2006; Nechnech, et al., 2002; Wu, et al., 2006), although these researchers have used different formulations to represent the isotropic damage: the term D in Eq. II.2-55 has a different signification in each of these models. In the model of Grassl and Jirasek (2006), the term D is a single scalar. In the model of Nechnech, et al. (2002), the term D is a single scalar calculated from two scalar damage variables (one for tension and one for compression), and a third scalar parameter is used to capture the unilateral effect. In the model of Wu, et al. (2006), the term D is a fourth-order tensor based on two scalar damage variables. A fourth-order tensor is indeed required for representing the state of isotropic damage in concrete; the cost for not using a tensor is an additional scalar parameter necessary for the representation of the unilateral effect.

$$\underline{\underline{\sigma}} = \left(1 - D\right) \, \underline{\underline{\underline{C}}}_0 : \left(\underline{\underline{\varepsilon}} - \underline{\underline{\varepsilon}}_p\right) \qquad \text{Eq. II.2-55}$$

The formulation of Eq. II.2-55 can be derived from thermodynamic considerations using the Helmholtz free energy per unit volume given by Eq. II.2-56 (Grassl and Jirasek, 2006).

$$\rho\psi = \left(1 - D\right) \frac{1}{2} \left(\underline{\underline{\varepsilon}} - \underline{\underline{\varepsilon}}_p\right) : \underline{\underline{\underline{C}}}_0 : \left(\underline{\underline{\varepsilon}} - \underline{\underline{\varepsilon}}_p\right) \qquad \text{Eq. II.2-56}$$

Other authors have suggested different formulations of the stress-strain relationship. For instance, the damage variable can be taken as a multiplier of the plastic strain tensor (Matallah and La Borderie, 2009), as expressed by Eq. II.2-57. This formulation relies on the assumption that the stresses cannot be affected by plastic strains if damage is not activated and inversely; therefore the stress expression is function of the combined variable $D\,\underline{\underline{\varepsilon}}_p$. This assumption is consistent with the assumption made by the authors in terms of coupling between plasticity and damage, as discussed here above; indeed they assume that damage is linked to the evolution of plastic strains. The isotropic damage is represented by a single scalar and an additional parameter to describe the unilateral effect. An advantage of the formulation by Matallah and La Borderie is the fact that the anisotropy of the plastic strain tensor naturally induces damage anisotropy, due to the fact that the isotropic damage variable is multiplied by the plastic strains tensor. However, this formulation contains several disadvantages. The physical interpretation of the effective stresses, as stresses applied to the undamaged part of material, is not valid in this case. More important, the degradation of the

elastic properties of the material is not represented during unloading of the material, as the damage term is not applied to the elastic stiffness tensor.

$$\underline{\underline{\sigma}} = \underline{\underline{C}}_0 : \left(\underline{\underline{\varepsilon}} - D\, \underline{\underline{\varepsilon}}_p \right)$$

Eq. II.2-57

In the model by Richard, et al. (2010), the total strain tensor is decomposed in deviatoric and hydrostatic parts. The underlining idea is that the cracked behavior in concrete can be separated into frictional sliding, modeled by the deviatoric part of the model, and cracks opening and closing, modeled by the hydrostatic strain part. The scalar damage variable affects the deviatoric total strain tensor and the positive part of the hydrostatic total strain tensor; this decomposition allows for capturing partially the unilateral effect. In this model, damage evolution is driven by total strains, which induces difficulties when stress passes from compression to tension: damage is only activated when the total strain becomes positive again. Another inconvenient of the model is related to the formulation of yield criterion in nominal stresses, which implies computational difficulties. In order to avoid a double iteration process, the authors propose to circumvent this difficulty by computing the damage variable based on the trial elastic stress instead of the nominal (converged) stress.

Different yield criteria have been used in the plastic-damage models. Several authors used a unique yield function, e.g. the model by Grassl and Jirasek (2006) uses a yield function based on the failure criterion by Menetrey and Willam (1995), whereas the model by Wu, et al. (2006) uses the yield function proposed by Lee and Fenves (1998). Other authors have adopted multi-surface yield criteria, e.g. Nechnech, et al. (2002) uses a criterion combining Rankine and Drucker Prager yield functions.

As a conclusion, the development of a constitutive model for concrete based on a plastic-damage formulation is based on a set of assumptions and strategic choices. It has been said that isotropic damage is preferred to anisotropic damage in this work, for reasons related to the applicability to structural analysis. In the present work, stress-based plasticity is formulated in the effective stress space rather than in the nominal stress space, as several authors have shown that this former option is more stable and attractive (Grassl and Jirasek, 2006; Abu Al-Rub and Voyiadjis, 2009); computation of the plastic response then constitutes a standard elastoplastic problem in the effective stress space. Then, strategic assumptions are to be made about other important points, such as the type of coupling between plasticity and damage, the internal variables that are used to govern the evolution equations, the formulation of the relationship between nominal stress and total strain, the variables used to represent the isotropic state of damage, the yield criteria.

Based on the review presented in this chapter, it is decided to use the same internal variables for the plastic and damage phenomena, in order to limit the number of parameters in the model; these internal variables are based on plastic quantities. Therefore, there is no specific threshold for damage: this phenomenon starts to develop simultaneously with plastic strains. The model is developed following the stress-strain relationship of Eq. II.2-55, adopted by many other researchers for its convenience and physical interpretation in terms of effective and nominal stresses. This approach is very convenient for solving the plastic problem in the effective stress space using, for instance, a return-mapping algorithm (implicit scheme), and

then updating the damage variables using the values of the internal plastic variables determined at the end of the plastic problem (explicit scheme). In the model, the isotropic state of damage is represented by a fourth-order tensor based on two scalars, as a tensor is needed for proper representation of the asymmetric behavior in tension-compression and the unilateral effect. Owing to this tensor, modelling of the unilateral effect does not require an additional parameter, as is the case for instance in the model of Nechnech, et al. (2002). Finally, in the present work, it was decided to adopt a multi-surface yield function because the underlining concept of this theory is justified for concrete, in which different mechanisms develop in tension and in compression. In addition, this approach offers more flexibility in the modelling of the hardening laws compared with a single yield criterion, in which the choice of the hardening variables is more complex. The multi-surface criteria based on Rankine and Drucker Prager functions seem a good choice as its applicability for modelling of concrete has been well established and computationally efficient algorithms have been developed (Feenstra and de Borst, 1996).

The different assumptions have been summarized in Table II.2-1. Once these strategic choices have been made, it remains to develop the equations of the model; this work is presented in Chapters III and IV.

Options	Decision	Justification
Damage: Isotropic VS Anisotropic	Isotropic damage	Simplifying assumption for easier applicability to structural analysis
Plasticity formulation: Effective VS Nominal stress space	Plasticity formulated in the effective stress space	Local uniqueness, numerical stability, formulation of a standard elastoplastic problem (Grassl and Jirasek, 2006; Abu Al-Rub and Voyiadjis, 2009)
Coupling between plasticity and damage: Same VS Different internal variables	Plasticity and damage driven by the same internal variables; no specific threshold for damage	Limitation of the number of parameters in the model
Stress-strain relationship	"(1-D)" formulation (Eq. II.2-55)	Convenience in the numerical process, physical interpretation of effective and nominal quantities
(Isotropic) damage variables: Scalar(s) VS Tensor	4th order tensor with two damage scalars	Necessary for capturing isotropic damage in concrete including asymmetry tension-compression and unilateral effect (Ju, 1990; Wu, et al., 2006)
Yield criteria: Single VS Multiple yield surface	Multi-surface yield criteria (Rankine in tension and Drucker-Prager in compression)	Flexibility and consistency for concrete in which different mechanisms develop in tension and compression

Table II.2-1: Main assumptions for the plastic-damage model developed in the thesis

II.2.5. Extension to high temperatures

II.2.5.1. *General overview*

Different authors have worked on the development of concrete models at high temperatures. A model based on the plasticity theory has been developed by Khennane and Baker (1992); the proposed thermo-plasticity model is intended for modelling of concrete under biaxial stress states but it does not include the effect of degradation of the elastic properties. Another example of concrete model based on thermo-plasticity theory has been proposed by Heinfling (1998). This latter contribution notably takes into account the increasing temperature sensitivity of compressive strength to hydrostatic pressure and it introduces in the constitutive model a characteristic length depending on the size of the finite elements for regularization of the model, adopting Hillerborg's method (Hillerborg, et al., 1976). Other authors have developed concrete models at high temperatures based on the damage theory (Gawin, et al., 2004; Baker and de Borst, 2005). These two damage models use a thermal damage parameter to capture the degradation of Young modulus with temperature; this thermal damage parameter can be defined by Eq. II.2-58. The interpretation of this degradation as damage is justified by the fact that it is irreversible.

$$\Lambda(T) = 1 - \frac{E(T)}{E_{20}} \qquad \text{Eq. II.2-58}$$

The first application of plastic-damage model for concrete at high temperatures, to the author's knowledge, is due to Nechnech (2000; Nechnech, et al., 2002). Nechnech incorporated the effect of transient creep in his model using Anderberg's formula. The notion of thermal damage is also introduced to account for the temperature variation of the elastic modulus. Plasticity is formulated in the effective stress space and the isotropic state of damage is modeled by means of two damage scalars. This contribution has highlighted the interest of plastic-damage models for concrete at high temperature. However, the modeling of damage by two scalars did not allow for capturing the unilateral effect; the author had to introduce an additional parameter in his model to get around this limitation. Besides, the model was only developed in two dimensions and its applicability for practical applications of structural fire engineering has not been demonstrated. Since then, plastic-damage models for concrete at high temperatures have been proposed by Luccioni, et al. (2003) and by de Sa and Benboudjema (2011). In the former, a thermal damage parameter measures the deterioration produced by high temperatures and this thermal damage is introduced in the expressions of the plastic threshold and the mechanical damage threshold to incorporate the temperature effects. In the latter, the influence of different modeling assumptions for the concrete mechanical model is investigated, such as the consideration of the transient creep or the use of isotropic or orthotropic damage. de Sa and Benboudjema do not use a thermal damage parameter but they directly incorporate the temperature-dependency of Young modulus through a temperature-dependent expression of $E(T)$ to be considered in the expression of the stiffness tensor.

The analyses at ambient temperature presented in the previous sections have lead to the choice of a plastic-damage model for modeling the mechanical behavior of concrete. In the following, we will thus give an insight into the developments to introduce in plastic-damage models for generalization to high temperatures.

At high temperatures, the plastic-damage models have to be modified to take into account the thermal strains, the transient creep strains and the evolution of the mechanical properties with temperature. As for the uniaxial situation, the macroscopically measurable strains in heated concrete (i.e. the total strains) are divided into individual strain components according to Eq. II.2-59.

$$\underline{\underline{\varepsilon}}_{tot} = \underline{\underline{\varepsilon}}_{th} + \underline{\underline{\varepsilon}}_{tr} + \underline{\underline{\varepsilon}}_{\sigma} \qquad \text{Eq. II.2-59}$$

In this equation, $\underline{\underline{\varepsilon}}_{tot}$ is the total strain tensor, $\underline{\underline{\varepsilon}}_{th}$ the free thermal strain tensor, $\underline{\underline{\varepsilon}}_{tr}$ the transient creep strain tensor and $\underline{\underline{\varepsilon}}_{\sigma}$ the instantaneous stress-related strain tensor. This latter term can in turn be divided in elastic and plastic strains tensors: $\underline{\underline{\varepsilon}}_{\sigma} = \underline{\underline{\varepsilon}}_{el} + \underline{\underline{\varepsilon}}_{p}$, with $\underline{\underline{\varepsilon}}_{el}$ the elastic strain tensor and $\underline{\underline{\varepsilon}}_{p}$ the plastic strain tensor.

The expressions of the free thermal strain and the transient creep strain, established for the uniaxial situation, have to be extended to the multiaxial situation. Then, the constitutive relationship between the instantaneous stress-related strain tensor $\underline{\underline{\varepsilon}}_{\sigma}$ and the stress tensor $\underline{\underline{\sigma}}$ has to be derived by extension of the plastic-damage model for accounting for the temperature-dependency of the mechanical properties.

II.2.5.2. *Multiaxial model for free thermal strain*

In the multiaxial situation, several authors have proposed to extend the expression of the free thermal strain as a function of the temperature-dependent thermal expansion coefficient α according to Eq. II.2-60 (de Borst and Peeters, 1989; Khennane and Baker, 1992; de Sa and Benboudjema, 2011). In this equation, $\underline{1}$ is the second order identity tensor; free thermal strain is thus assumed to be isotropic.

$$\underline{\dot{\underline{\varepsilon}}}_{th} = \alpha(T) \times \dot{T} \times \underline{\underline{1}} \qquad \text{Eq. II.2-60}$$

The other approach for modelling of free thermal strain, which consists in using an expression directly depending on the temperature, can be extended to high temperatures based on a similar assumption; this leads to Eq. II.2-61. This latter approach has been followed in the Eurocode (European Committee for Standardization, 2004b), in which different functions $\psi(T)$ are given for siliceous and calcareous aggregates.

$$\underline{\dot{\underline{\varepsilon}}}_{th} = \psi(T) \times \underline{\underline{1}} \qquad \text{Eq. II.2-61}$$

II.2.5.3. *Multiaxial model for transient creep strain*

In a one-dimensional context, the literature review has shown that the transient creep strain rate is assumed by most researchers as proportional to the applied stress. Generalization of the transient creep strain formula to a multiaxial stress state has been proposed based on the assumption that the linear proportionality between the transient creep strain rate and the stress is maintained, and assuming that the process of transient creep does not induce anisotropy (de Borst and Peeters, 1989; Khennane and Baker, 1992). Hence, the transient creep strain rate tensor is given by Eq. II.2-62 (de Borst and Peeters, 1989), with $k(T)$ a parameter used to model the non linear relationship between the transient creep strain rate and temperature rate and $\underline{\underline{H}}$ a fourth-order tensor.

$$\dot{\underline{\varepsilon}}_{tr} = \left(k(T) \times \dot{T}\right) \underline{\underline{H}} : \underline{\sigma} \qquad \text{Eq. II.2-62}$$

As the process of transient creep is assumed isotropic, de Borst and Peeters proposed that the tensor $\underline{\underline{H}}$ be given by Eq. II.2-63. In this expression, δ_{ij} is the Kronecker symbol and γ an additional material parameter. Based on the multiaxial data from Thelandersson (1987), it is suggested that γ has approximately the same value as Poisson's ratio ν. The strategy described by Eq. II.2-62 and Eq. II.2-63 has been adopted by many researchers for generalizing the transient creep strain calculation to a multiaxial stress state (Khennane and Baker, 1992; Nechnech, 2000; Gawin, et al., 2004; de Sa and Benboudjema, 2011).

$$H_{ijkl} = -\gamma \delta_{ij} \delta_{kl} + 0.5(1+\gamma)\left(\delta_{ik} \delta_{jl} + \delta_{il} \delta_{jk}\right) \qquad \text{Eq. II.2-63}$$

When damage is considered in the model, it is generally assumed that the transient creep strain calculation, given by Eq. II.2-62, considers the effective stress tensor and not the nominal stress tensor, since the mechanism of transient creep occurs only in the undamaged part of the material (Nechnech, et al., 2002; de Sa and Benboudjema, 2011).

Another formulation has been proposed by Thelandersson (1987) for extending its transient creep strain formula to a multiaxial situation. This formulation is based on a decomposition of the transient creep strain rate into a deviatoric part and a volumetric part. However, it was noted by de Borst and Peeters (1989) that it is possible to relate their formulation with Thelandersson's by adopting given values for the parameters that appear in the two formulas.

II.2.5.4. *Temperature-dependency of the plastic-damage model*

Based on the considerations at ambient temperature, it is admitted that the instantaneous stress-related strain tensor $\underline{\varepsilon}_{\sigma}$ is related to the stress tensor $\underline{\sigma}$ by means of the constitutive relationship of Eq. II.2-64.

$$\underline{\sigma} = (1-D) \, \underline{\underline{C}}_0 : \left(\underline{\varepsilon}_{\sigma} - \underline{\varepsilon}_P\right) \qquad \text{Eq. II.2-64}$$

However, this latter expression has to be extended to take into account the effects of high temperatures. Generalization of the constitutive model to high temperatures requires proper description of the temperature-dependency of the material properties. This temperature-dependency has been discussed in Chapter I. For instance, the elastic modulus is reduced by exposure to high temperatures (Schneider, 1985); this elastic modulus is used for calculation of the fourth order initial stiffness tensor $\underline{\underline{C}}_0$ that appears in Eq. II.2-64. The evolutions of the mechanical properties with temperature have to be incorporated within the equations that describe the plastic part and the damage part of the constitutive model.

The plastic part of the constitutive relationship expressed by Eq. II.2-64 is modified by incorporating the temperature-dependency of the mechanical properties into the expressions of the yield criteria and the hardening functions. Considering for instance the Rankine yield surface given by Eq. II.2-65, it is clear that the variation of the uniaxial tensile strength $f_t(T)$ with temperature induces a modification of the surface. The expression of a multi-surface yield criterion at high temperatures is thus given by Eq. II.2-66, in which hardening is considered through the set of internal variables $\underline{q}$ functions of $\left(\underline{\underline{\varepsilon}}_p, \kappa_i \right)$.

$$f\left(\underline{\sigma}\right) = \sigma_1\left(\underline{\sigma}\right) - f_t(T) = 0 \qquad \text{Eq. II.2-65}$$

$$\begin{cases} f_1\left(\underline{\sigma},\underline{q},T\right) \le 0 \\ f_2\left(\underline{\sigma},\underline{q},T\right) \le 0 \end{cases} \qquad \text{Eq. II.2-66}$$

The damage part of the model is also affected by temperature. In general, the effects of elevated temperatures induce a modification of the damage threshold and a modification of the evolution laws of the damage variables. Yet in the plastic-damage model considered in this work, the evolution of damage is driven by the same internal variables as plasticity. As a result, the effects of high temperatures on the damage part of the model only affect the evolution laws of the damage variables, as there is no specific damage threshold.

The models thus require proper temperature-dependent evolution laws for the material properties. However, it was said in the previous chapter that the experimental data for some of these properties at high temperatures is scarce or presents a significant scatter, e.g. Poisson's ratio and the crack energy. As a result of this lack of experimental data, these parameters are sometimes considered as independent of temperature in numerical applications (Nechnech, 2000; Nechnech, et al., 2002).

II.3. Conclusion

The present chapter aims to review the models developed in the literature for capturing the mechanical behavior of concrete at ambient and at elevated temperature. The first part of the chapter dealt with the modelling of the concrete uniaxial behavior at elevated temperature; this study allowed for introducing the strain decomposition in heated concrete and to discuss on the modelling of transient creep phenomenon. The second part of the chapter focused on the representation of the concrete behavior under multiaxial stress states; it presented different modelling approaches and studied two of them in more details, the plasticity and damage theories.

The objective of this state of the art was to present the theoretical frameworks, the assumptions and the modelling techniques that are used by researchers in the field of concrete modelling. These modelling tools have been confronted with the requirements, defined in Chapter I, which have to be met by the original model presented in this thesis. This analysis has lead to the conclusions described here below.

Based on the review of the uniaxial concrete models at elevated temperature, the following conclusions are drawn:

-   It is convenient to divide the total strain into individual strain components.
-   Transient creep strain should be one of these strain components. Indeed, concrete models that incorporate implicitly the effects of transient creep into another strain component, e.g. in a mechanical strain term, fail to capture the dependency in the stress-temperature path and the unloading stiffness. These limitations of implicit models are incompatible with the requirements for a concrete model used in a performance-based environment. As a result, it is necessary to use an explicit term for transient creep in the model.
-   The instantaneous stress-related strain (ISRS) is another strain component. The relationship between ISRS and stress is experimentally obtained by steady-state test; this relationship is thus univocal at a given temperature.
-   The transient creep strain calculation should depend on the stress-temperature path.
-   The transient creep strain term should be irrecoverable at both temperature and stress decrease.
-   The transient creep strain rate can be assumed as linearly proportional to the applied stress.
-   The transient creep strain rate can be assumed to depend on temperature but not linearly.
-   For practical applications, the number of parameters in the model should be limited to a minimum; however it is generally assumed that transient creep strain depends on the type of aggregate (siliceous or calcareous).

Based on the review of the multiaxial models for concrete, the following conclusions are drawn:

- Among the different theories that have been applied to the modelling of concrete in multiaxial stress states, the continuum constitutive models based on smeared crack approach offer a pragmatic and robust framework for applications with large scale concrete structures and multi-cracked concrete elements.

- Models based on the plasticity theory are well adapted for capturing the phenomena of dilatancy, permanent strain and hardening and softening behavior in concrete. Models based on the damage theory are particularly suitable for description of stiffness degradation and unilateral effect. In this thesis, it is decided to combine the capabilities of the two theories by developing a coupled plastic-damage model.

- The non linear behavior of concrete, which is due to the development of plastic strains and damage, is assumed to be completely governed by the plastic internal variables. Therefore the evolution of damage is linked to the development of plastic strains; the model does not require any damage threshold and the number of parameters is thus limited.

- Assuming that plastic flow occurs in the undamaged material micro-bounds by means of effective quantities, stress-based plasticity is formulated in the effective stress space rather than the nominal stress space.

- Isotropic damage is chosen rather than anisotropic damage.

- The isotropic state of damage is described by a fourth-order tensor that contains two damage scalar variables.

- As concrete exhibits different failure mechanisms in tension and in compression, modelling of these behaviors with different yield functions is consistent. Therefore a multi-surface yield criterion is preferred to a single surface criterion. Combination of a Drucker-Prager yield surface in compression and a Rankine yield surface in tension has been successfully adopted for modelling of concrete.

- Non associated plasticity should be considered in the plastic flow rule in compression in order to capture the dilatancy effect.

The conclusions made at the end of this chapter are used as guidelines in the development of the original model that is presented in the two following chapters.

CHAPTER III - TRANSIENT CREEP STRAIN
IN A UNIAXIAL CONSTITUTIVE MODEL

In this chapter, an original model is developed for capturing the concrete thermo-mechanical behavior in uniaxial stress state. This model includes an explicit term for transient creep strain; hence, the concrete model takes into account the stress-temperature path. The transient creep model that is developed encompasses the most widely accepted characteristics of transient creep, which have been summarized at the end of the previous chapter. The uniaxial concrete model is based on the present implicit model of Eurocode 2 and it is calibrated to yield the same results in the situation of transient test; therefore it can be seen as a new formulation of the present Eurocode 2 concrete model that incorporates an explicit term for transient creep.

The development of the model and its implementation in a finite elements software are presented in the first part of this chapter. Then, the model is validated against experimental data to validate its ability to capture the concrete behavior at high temperatures and to meet the requirements defined in the previous chapters.

III.1. Objectives and assumptions

In the former chapter, the comparative discussion about the explicit and implicit approaches for modelling transient creep strain in concrete has led to the conclusion that explicit models must be employed, in line with the performance-based design requirements. Concrete models that include implicitly the transient creep strain, such as the current Eurocode 2 model (European Committee for Standardization, 2004b), have inherent limitations that prevent them from accurately representing the mechanical strains that develop in concrete members subjected to fire. Namely, implicit models are not able to capture properly the actual unloading stiffness at elevated temperatures and they fail to take into account the dependency of the strain on the stress-temperature path.

It has been shown (Schneider, 1988, Khoury, et al., 1985a) that the amount of transient creep may depend significantly on the type of concrete (mostly, the type and relative content of aggregates). It is possible to determine precisely the properties of a well defined type of concrete to be used in well defined conditions, usually for a very important project, e.g. the concrete vessel for a nuclear reactor that will be subjected to a well defined fire scenario. For more general applications, generic properties of concrete have to be established. Generic properties are used in research projects, for instance, when the mechanical behavior of two structural systems has to be compared, with no reference to a particular concrete mix. Generic properties are also needed at the preliminary stage of a design, when no information is yet available on the particular mix that will be used. Generic properties are also required for determining the fire resistance of an element in a small project, where the cost to conduct experimental tests would be by far outweigh the budget allocated for the design studies of the building (Gernay and Franssen, 2012).

The constitutive model of Eurocode 2 has imposed itself as one of the most widely used generic models in the last decade, in Europe and beyond. It has been proposed by a draft committee comprising several European experts, has proved to yield quite satisfactory results when applied to structural calculations (although most applications where under ISO fire, which means under constantly increasing temperature) and it is well accepted by authorities and regulators. It was estimated that, if there is a chance to see a breakthrough in the utilization of explicit models, this could not be achieved by selecting one of the various particular models presented up to now, each with its own characteristics and some requiring particular tests to characterize different concrete mixes, but rather by proposing an explicit model that would yield the same results as the present Eurocode implicit model when used in the situation of transient test. This model could then be seen as a new formulation of the Eurocode model and be called Explicit Transient Creep Eurocode model (ETC Eurocode model). It should of course encompass the most widely accepted characteristics of transient creep, and capture properly the transient creep strain observed in experimental tests.

In agreement with the assumptions adopted by most of the presented models, the transient creep strain rate in the ETC model would be linearly proportional to the applied stress and nonlinearly proportional to the temperature increase rate. The ETC model would not contain any material parameter, except for the type of aggregate. The objective is to capture the phenomenon of transient creep strain with the minimum number of parameter; generic models should be preferred in structural fire engineering for the reasons explained previously. However, the current Eurocode 2 concrete model has already introduced the type of aggregate as a parameter, since the relationship between compressive strength and temperature is different for siliceous and calcareous concrete in the Eurocode. Considering that the ETC model is based on the present Eurocode model, and that the transient creep strain dependence on the type of aggregate has been highlighted by most of the authors in the literature, it seems justified to incorporate this parameter in the ETC model.

Concrete has a memory and concrete models have been developed in the literature to take into account the effect of the load history before heating (Schneider, 1988) and during heating (Schneider, et al., 2008; Schneider and Schneider, 2009) on the deformation response to a change in stress and temperature increase. However, this effect has not been taken into account in the present thesis because of uncertainties on the hypothesis to be made for considering the load history during heating on the basis of experimental tests in which only the load level before heating was considered (with the load level maintained constant during heating). In a real section subjected to fire, the temperature starts to increase in the peripheral part of the section before any temperature variation in the central part of the section. As a result, thermal stresses develop and the applied stresses on the central part of the section vary before heating of this central part, see Section I.3.2. The time that corresponds to the beginning of heating is different for each point of the section and the applied stress is affected by the thermal gradients. Therefore, the concept of load level applied before heating is difficultly applicable to structural applications. It is noted that this effect has also been neglected by many other authors, as shown in Chapter II.

III.2. Explicit Transient Creep Model

III.2.1. Development of the model

For the development of the uniaxial concrete model, the total strain is assumed to be made of individual strain components according to Eq. III.2-1. In this equation, ε_{tot} is the total strain, ε_{th} the free thermal strain, ε_σ the instantaneous stress-related strain and ε_{tr} the transient creep strain. The instantaneous stress-related strain can in turn be divided in elastic and plastic strains: $\varepsilon_\sigma = \varepsilon_{el} + \varepsilon_p$.

$$\varepsilon_{tot} = \varepsilon_{th} + \varepsilon_\sigma + \varepsilon_{tr} \qquad \text{Eq. III.2-1}$$

III.2.1.1. Transient creep strain

Adopting the assumptions of linear proportionality to applied stress and nonlinear proportionality to temperature rate, the transient creep strain rate can be expressed by an expression of the form of Eq. III.2-2. The function $\phi(T)$ is a nonlinear function of temperature that expresses the transient creep dependency in temperature; this function depends on the type of aggregate (siliceous or calcareous). The material parameter $f_{c,20}$ is the uniaxial compressive strength at ambient temperature and σ denotes the applied stress.

$$\dot{\varepsilon}_{tr} = \dot{\phi}(T) \times \frac{\sigma}{f_{c,20}} \qquad \text{Eq. III.2-2}$$

The transient creep strain rate given by Eq. III.2-2 has to be integrated over a finite time (or temperature) step. The stress at the beginning and at the end of the time step are respectively denoted by $\sigma^{(s)}$ and $\sigma^{(s+\Delta s)}$. The development in Taylor's series of the stress in the neighborhood of the stress $\sigma^{(s)}$ is given by Eq. III.2-3, where the variable time is noted by τ. In this equation, the notation $O(\Delta\tau)^2$ denotes the terms that are at least of the second order in $\Delta\tau$.

$$\sigma = \sigma^{(s)} + \frac{\partial\sigma}{\partial\tau}\Delta\tau + O(\Delta\tau)^2 \qquad \text{Eq. III.2-3}$$

The rate form of the transient creep strain equation can be rewritten according to Eq. III.2-4, where the second order terms have been neglected in the development of the stress. Due to this latter assumption, the precision of the calculation depends on the size of the time step. In this equation, the total derivative D_τ has been employed for the function $\phi(T)$ as this function is an implicit function of time τ: $\phi(T(\tau))$.

$$\frac{D\varepsilon_{tr}}{D\tau} = \frac{D\phi(T)}{D\tau} \times \frac{1}{f_{c,20}} \left(\sigma^{(s)} + \frac{\partial\sigma}{\partial\tau}\Delta\tau \right)$$

<div align="right">Eq. III.2-4</div>

In fact, the value of the function $\phi(T)$ is known at every time step as the temperature evolution is considered as a data in the mechanical problem. Therefore, while incrementing from time step s to time step $s+\Delta s$, the increment in the function $\phi(T)$ can be computed exactly by: $\Delta\phi(T) = \phi(T^{s+\Delta s}) - \phi(T^s)$.

The evaluation of the term in parenthesis in Eq. III.2-4 during the increment from time step s to time step $s+\Delta s$ depends on the strategy that is adopted for the numerical integration. In an explicit numerical scheme, the stress is taken at the beginning of the time step, thus neglecting the variation of the stress during the time step. Accordingly, it is assumed that $\partial\sigma/\partial\tau = 0$. On the opposite, in an implicit numerical scheme, the stress is taken at the end of the time step. This implies an iterative process as the (converged) stress at the end of the time step is not known when the transient creep strain is evaluated. In such implicit scheme, the term $(\partial\sigma/\partial\tau)\Delta\tau$ is thus computed to converge to the value of the increment in stress $\Delta\sigma$, defined as $\Delta\sigma = \sigma^{(s+\Delta s)} - \sigma^{(s)}$. In this case, the increment in transient creep strain only depends on the stress at the end of the time step. Finally, an intermediate strategy would consider the stress $\sigma^{(s+\beta\Delta s)}$ at an intermediate time $s+\beta\Delta s$, with $0 \le \beta \le 1$ and with $\sigma^{(s+\beta\Delta s)}$ given by Eq. III.2-5.

$$\sigma^{(s+\beta\Delta s)} = \sigma^{(s)} + \beta\Delta\sigma$$

<div align="right">Eq. III.2-5</div>

The linearized expression of the stress between two time steps can thus be rewritten according to Eq. III.2-5 (de Borst and Peeters, 1989). This equation corresponds to an explicit numerical scheme for $\beta = 0$ and an implicit numerical scheme for $\beta = 1$.

Finally, the increment in transient creep strain between time steps s and $s+\Delta s$ can be evaluated using Eq. III.2-6. As the stress has been linearized, the precision of this formulation depends on the size of the time step. Besides, an additional assumption has to be made in order to chose the value of the parameter β. This assumption will be discussed when presenting the numerical implementation of the model.

$$\Delta\varepsilon_{tr} = \Delta\phi(T) \times \frac{1}{f_{c,20}} \left(\sigma^{(s)} + \beta\Delta\sigma \right)$$

<div align="right">Eq. III.2-6</div>

The transient creep strain is thus computed according to the incremental expression of Eq. III.2-6. In this equation, it remains to define the expression of the nonlinear function $\phi(T)$; the developments made to derive this function are detailed here below.

An important assumption of the new concrete model is that it is calibrated to give the same response as the current Eurocode 2 model in the situation of transient test. In the Eurocode 2 model, the total strain is divided into free thermal strain and mechanical strain: $\varepsilon_{tot} = \varepsilon_{th} + \varepsilon_m$. By comparing this latter expression with Eq. III.2-1, it is clear that the

mechanical strain is the sum of the instantaneous stress-related strain and the transient creep strain. According to our assumption, the equality can be written in the situation of transient test, see Eq. III.2-7; this equation expresses the equality between, on the one hand, the mechanical strain of the Eurocode 2 model ε_m^{EC2} and, on the other hand, the sum of the instantaneous stress-related strain and the transient creep strain of the ETC model in the situation of transient test (TT) ε_σ^{TT} and ε_{tr}^{TT}.

$$\varepsilon_\sigma^{TT} + \varepsilon_{tr}^{TT} = \varepsilon_m^{EC2} \qquad \text{Eq. III.2-7}$$

By definition, a transient test corresponds to the situation in which the temperature is increased from ambient temperature T_{20} until final temperature T_f under constant applied compressive stress σ^*. Therefore the transient creep strain term ε_{tr}^{TT} in Eq. III.2-7, written in the situation of transient test, is given by Eq. III.2-8:

$$\varepsilon_{tr}^{TT} = \left[\phi(T_f) - \phi(T_{20}) \right] \times \frac{\sigma^*}{f_{c,20}} \qquad \text{Eq. III.2-8}$$

The instantaneous stress-related strain term ε_σ is experimentally obtained by steady-state test, as was shown in the Chapter II. In the ETC model, the instantaneous stress-strain relationship $\sigma - \varepsilon_\sigma$ is thus calibrated on the experimental response of the concrete material subjected to steady-state test. In particular, the tangent to the instantaneous stress-strain curve at zero stress is calibrated on the initial stiffness of the material subjected to steady-state test. A good indication of values of this initial stiffness is given by the initial tangent to the ENV curves in the prestandard of Eurocode 2 (European Committee for Standardization, 1995) using the lower limit of the peak stress strain (PSS), $\varepsilon_{c1,\min}$, since the ENV relationship with $\varepsilon_{c1,\min}$ is based (Franssen, 1987) on steady-state tests made by Schneider (1982). This initial tangent to the ENV curves is given by: $E_{\text{ENV}} = (3f_{c,T})/(2\varepsilon_{c1,\min})$, with $f_{c,T}$ the temperature-dependent compressive strength.

The instantaneous stress-strain relationship is used to characterize the concrete behavior under steady-state conditions and therefore it is univocal at a given temperature; indeed the dependency in the stress-temperature path is handled by the transient creep strain term in the ETC model. As a result, the instantaneous stress-related strain in the transient test situation ε_σ^{TT}, which appears in Eq. III.2-7, is known once the instantaneous stress-strain relationship $\sigma - \varepsilon_\sigma$ is defined.

The mechanical strain in the Eurocode 2 model is given by Eq. III.2-9. In this equation, $\varepsilon_{c1,EC2}$ is the PSS given by the Eurocode 2 (which corresponds to the upper limit in the previous ENV version of Eurocode). The initial tangent to the Eurocode 2 curve is given by: $E_{\text{EC2}} = (3f_{c,T})/(2\varepsilon_{c1,EC2})$.

$$\frac{\sigma}{f_{c,T}} = \frac{3\,\varepsilon_m^{EC2}}{\varepsilon_{c1,EC2}\left(2+\left(\varepsilon_m^{EC2}\big/\varepsilon_{c1,EC2}\right)^3\right)}$$

Eq. III.2-9

Based on the developments above, it is now possible to derive the function $\phi(T)$. Assuming that the function $\phi(T)$ is null at 20°C and replacing Eq. III.2-8 into Eq. III.2-7 which expresses the equality in the situation of transient test, it holds:

$$\phi(T_f) = \frac{\varepsilon_m^{EC2} - \varepsilon_\sigma^{TT}}{\sigma^*\big/f_{c,20}}$$

Eq. III.2-10

Eq. III.2-10 denotes the fact that, at a given temperature, the difference between the mechanical strain and the instantaneous stress-related strain, i.e. the transient creep strain, linearly increases with the applied stress; the proportionality factor being the function $\phi(T)$. This function only depends on temperature; it is independent on the applied stress. In particular, Eq. III.2-10 can thus be expressed for a very small value of the applied compressive stress σ^*. When the applied compressive stress σ^* tends to zero, the concrete behavior is linear elastic; the mechanical strain and the instantaneous stress-related strain are then given by Eq. III.2-11.

$$\varepsilon_m^{EC2} = \frac{\sigma^*}{E_{EC2}} \quad ; \quad \varepsilon_\sigma^{TT} = \frac{\sigma^*}{E_{ENV}}$$

Eq. III.2-11

After inserting Eq. III.2-11 into Eq. III.2-10, and replacing E_{EC2} and E_{ENV} by their expressions, the function $\phi(T)$ is finally obtained, see Eq. III.2-12.

$$\phi(T) = \frac{2}{3} \frac{\varepsilon_{c1,EC2} - \varepsilon_{c1,min}}{f_{c,T}\big/f_{c,20}}$$

Eq. III.2-12

The function $\phi(T)$ is a growing function of temperature that is not reversible during cooling, as each of its components $\varepsilon_{c1,EC2}$; $\varepsilon_{c1,min}$; $f_{c,T}\big/f_{c,20}$ is irrecoverable. This is in line with the definition of transient creep that is not recovered during the cooling phase. The components of the function $\phi(T)$ are all given in the EC2 and ENV. As the value of the temperature-dependent compressive strength $f_{c,T}$ given in the Eurocode 2 depends on the type of aggregate (siliceous or calcareous), the function $\phi(T)$ and consequently the transient creep strain ε_{tr} also depend on the type of aggregate. The values of the function $\phi(T)$ are given in Table III.2-1, with the values of the different parameters of Eq. III.2-12.

T(°C)	$\varepsilon_{c1,min}$	$\varepsilon_{c1,EC2}$	Siliceous aggregates		Calcareous aggregates	
			$f_{c,T}/f_{c,20}$	ϕ	$f_{c,T}/f_{c,20}$	ϕ
20	0.0025	0.0025	1.00	0.0000	1.00	0.0000
100	0.0025	0.0040	1.00	0.0010	1.00	0.0010
200	0.0030	0.0055	0.95	0.0018	0.97	0.0017
300	0.0040	0.0070	0.85	0.0024	0.91	0.0022
400	0.0045	0.0100	0.75	0.0049	0.85	0.0043
500	0.0055	0.0150	0.60	0.0106	0.74	0.0086
600	0.0065	0.0250	0.45	0.0274	0.60	0.0206
700	0.0075	0.0250	0.30	0.0389	0.43	0.0271
800	0.0085	0.0250	0.15	0.0733	0.27	0.0407
900	0.0100	0.0250	0.08	0.1250	0.15	0.0667
1000	0.0100	0.0250	0.04	0.2500	0.06	0.1667

Table III.2-1: Function $\phi(T)$ and parameters used for its calculation

Fig. III.2-1 compares the transient creep strain of the present model with experimental data of transient creep strain and with different models given in the literature and discussed in Chapter II. The transient tests have been conducted on siliceous concrete specimens first subjected to uniaxial compressive stresses equal to $0.10 \times f_{c,20}$, $0.30 \times f_{c,20}$ and $0.45 \times f_{c,20}$, and then heated at a constant rate. The experimental data include results published by Schneider (1988) and more recently by Annerel (2010). This latter author provides results up to 400°C for traditional vibrated concrete with siliceous aggregates under a compressive load level of 0.30. Note that the vertical scale is not the same on the three graphs for more readability of the results obtained under a compressive stress level of 0.10. It can be seen that the present ETC model is reasonably close to the other models and to experimental data, and that the increase in transient creep strain with temperature is correctly reproduced by the ETC model. The quantitative discrepancy between experimental results and the model could be expected since the ETC concrete model is a generic model, for the reasons explained previously, and consequently it cannot be calibrated to capture exactly the behavior of the particular concrete mixes used in the experiments of Fig. III.2-1.
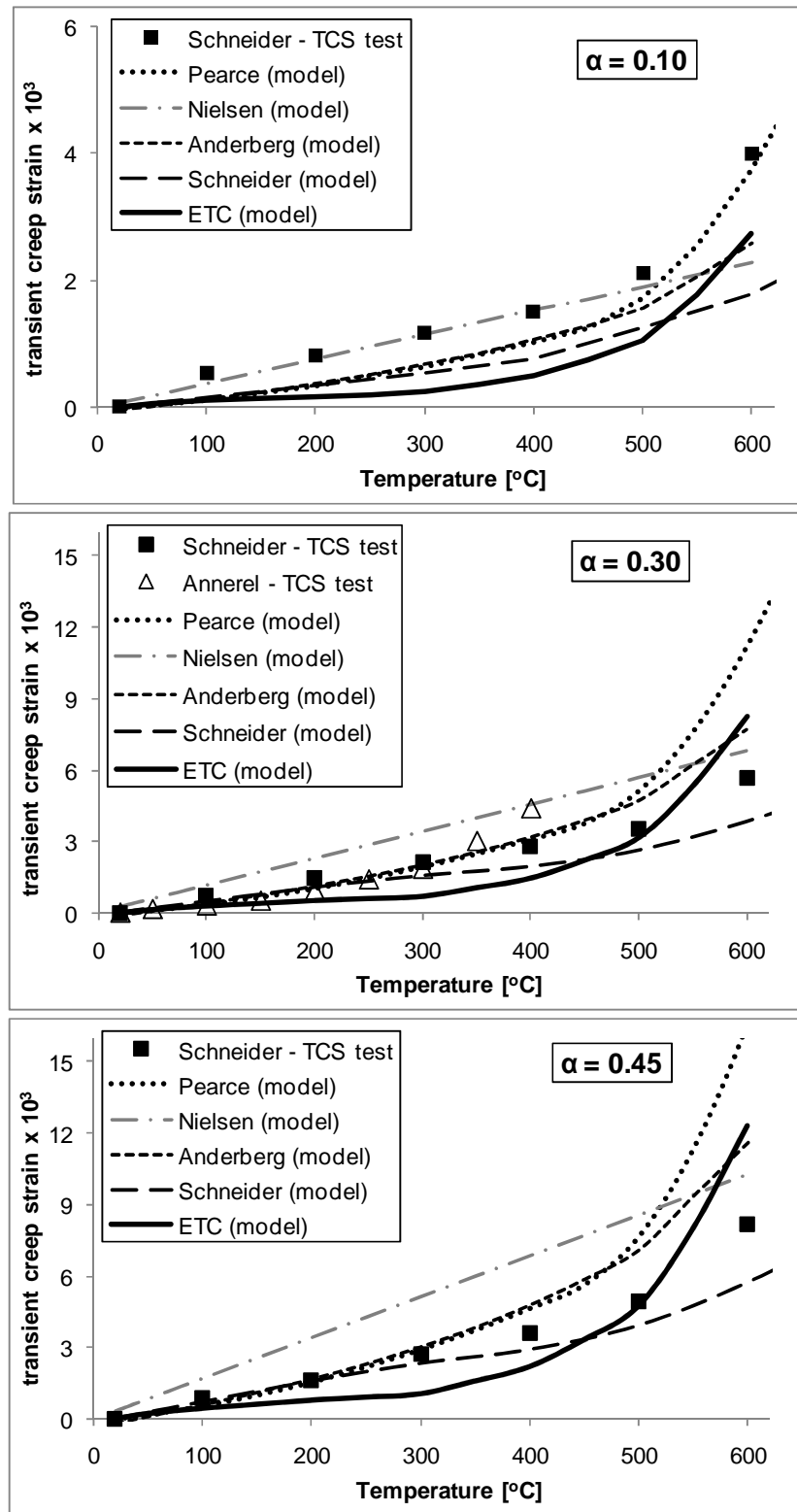
Fig. III.2-1: Comparison of the ETC transient creep model with different published models and with experimental data

III.2.1.2. *Instantaneous stress-related strain in compression*

The instantaneous stress-strain relationship of the model, i.e. the curve $\sigma = f(\varepsilon_\sigma, T)$, is derived to capture the experimental behavior in the situation of steady-state test. On the other hand, this relationship can be obtained from the above developments by inserting Eq. III.2-8 into the expression of Eq. III.2-7 characterizing the transient test situation; this leads to Eq. III.2-13. As mentioned previously, the instantaneous stress-strain relationship is independent of the stress-temperature path; therefore the expression written in the situation of transient test can be extended to every situation and ε_σ^{TT} has been replaced by ε_σ in Eq. III.2-13.

$$\varepsilon_\sigma(T,\sigma) = \varepsilon_m^{EC2}(T,\sigma) - \phi(T) \times \frac{\sigma}{f_{c,20}} \qquad \text{Eq. III.2-13}$$

The instantaneous stress-strain relationship of the model, given by Eq. III.2-13, is not exactly equal to the ENV relationship because the transient creep has been considered as linearly stress dependent. However, the initial stiffness of the new relationship is exactly equal to the ENV elastic modulus, see Fig. III.2-2. In Fig. III.2-2, the instantaneous stress-strain relationship of the ETC model is plotted at 500°C next to the relationship of ENV with lower limit of PSS and the relationship of Eurocode 2; experimental data of steady-state test at 500°C (Schneider, 1985) are also given on the graph.
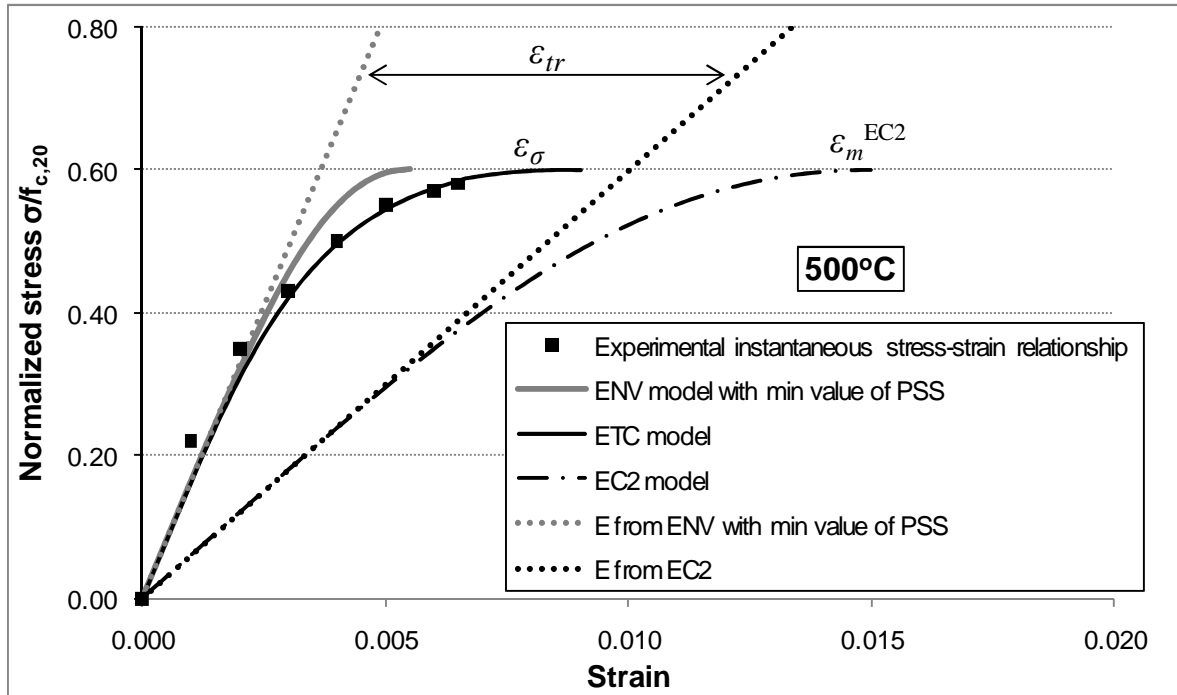
Fig. III.2-2: Comparison at 500°C of ENV, ETC and EC2 models with experimental data of steady-state tests from Schneider (1985)

It can be seen in Fig. III.2-2 that the instantaneous stress-strain relationship of the ETC model and the relationship of the ENV model are intended to capture the concrete behavior in steady-state test; the initial stiffness of the material in steady-state conditions is accurately captured by these models. On the contrary, the EC2 relationship aims at capturing the

concrete behavior in transient test. The difference between the ETC curve and the EC2 curve is the transient creep strain that develops in the situation of transient test, and is given by Eq. III.2-8.

In the explicit transient creep formulation (ETC) of the model, the constitutive relationship is thus expressed in terms of the instantaneous stress-related strain, in order to treat the transient creep effects separately from the elastic and plastic effects. The relationship between the instantaneous stress-related strain and the stress is given by Eq. III.2-13. Using Eq. III.2-9 to eliminate the mechanical strain from Eq. III.2-13, the instantaneous stress-strain relationship can be rewritten as Eq. III.2-14. This latter equation theoretically allows for computing the stress once the instantaneous stress-related strain ε_σ is known; however it is not straightforward to extract the stress σ from Eq. III.2-14.

$$\frac{\sigma}{f_{c,T}} = \frac{3\left(\varepsilon_\sigma + \phi(T) \times \left(\sigma / f_{c,20}\right)\right)}{\varepsilon_{c1,EC2}\left(2 + \left(\frac{\varepsilon_\sigma + \phi(T) \times \left(\sigma / f_{c,20}\right)}{\varepsilon_{c1,EC2}}\right)^3\right)} \qquad \text{Eq. III.2-14}$$

An algorithmic strategy can be implemented to solve the instantaneous stress-strain relationship of Eq. III.2-14 iteratively. To derive the tangent modulus of the stress-strain relationship of Eq. III.2-14, a change of variable is performed, see Eq. III.2-15. The tangent modulus can then be expressed as a function of the new variable derivative of stress.

$$\xi = \varepsilon_\sigma + \phi(T) \times \left(\sigma / f_{c,20}\right) \quad ; \quad \frac{d\sigma}{d\varepsilon_\sigma} = \frac{d\sigma}{d\xi}\frac{d\xi}{d\varepsilon_\sigma} = \frac{d\sigma}{d\xi}\frac{1}{1 - \dfrac{\phi(T)}{f_{c,20}}\dfrac{d\sigma}{d\xi}} \qquad \text{Eq. III.2-15}$$

After inserting the new variable ξ into Eq. III.2-14, the term $d\sigma/d\xi$ can be calculated. Finally, the tangent modulus is found after a few manipulations, see Eq. III.2-16. It can be verified that the ETC initial stiffness (elastic modulus) E_{ETC}, obtained by replacing ε_σ and σ by zero (and thus $\xi = 0$) in Eq. III.2-16, is equal to the ENV elastic modulus with the minimum value of PSS, see Eq. III.2-17.

$$\frac{d\sigma}{d\varepsilon_\sigma} = \frac{6\,f_{c,T}\left[1 - \left(\xi/\varepsilon_{c1,EC2}\right)^3\right]}{\varepsilon_{c1,EC2}\left[2 + \left(\xi/\varepsilon_{c1,EC2}\right)^3\right]^2 - 6\,\phi\,\dfrac{f_{c,T}}{f_{c,20}}\left[1 - \left(\xi/\varepsilon_{c1,EC2}\right)^3\right]} \qquad \text{Eq. III.2-16}$$

$$E_{ETC} = \frac{6\,f_{c,T}}{\varepsilon_{c1,EC2} \times 4 - 6\,\phi\,\dfrac{f_{c,T}}{f_{c,20}}} = \frac{3\,f_{c,T}}{2\,\varepsilon_{c1,min}} \qquad \text{Eq. III.2-17}$$

Eq. III.2-14 and Eq. III.2-16 can be used in the model to calculate the stress and the tangent modulus, once the instantaneous stress-related strain is known. However for the sake of convenience, it is chosen to derive a direct relationship $\sigma = f\left(\varepsilon_\sigma, T\right)$ that approximates the

instantaneous stress-strain relationship of Eq. III.2-14, rather than solving this latter equation iteratively. This decision was partly taken to allow for an easier generalization of the model in three dimensions. Another reason for this decision is the will to keep the simplicity of the formulation of the Eurocode model. It is found that it is possible to fit reasonably the implicit relationship of Eq. III.2-14 using a direct relationship of the same form as the current Eurocode model, provided proper values are used for the parameters and coefficients. Therefore, the direct relationship is developed according to Eq. III.2-18, which has the same generic form as the current EC2 model given by Eq. III.2-9.

$$\frac{\sigma}{f_{c,T}} = \frac{n\,\varepsilon_\sigma}{\varepsilon_{c1,ETC}\left[(n-1)+\left(\dfrac{\varepsilon_\sigma}{\varepsilon_{c1,ETC}}\right)^n\right]}$$

Eq. III.2-18

In the latter equation, n is a coefficient to be determined and $\varepsilon_{c1,ETC}(T)$ is the PSS for the ETC relationship, given by Eq. III.2-19.

$$\varepsilon_{c1,ETC} = \varepsilon_{c1,EC2} - \phi\frac{f_{c,T}}{f_{c,20}} = \frac{2\,\varepsilon_{c1,min}+\varepsilon_{c1,EC2}}{3}$$

Eq. III.2-19

The parameter n is chosen to obtain the best possible correlation between Eq. III.2-18 and Eq. III.2-14 which describes the curve obtained as the difference between the EC2 relationship and the transient creep strain in the situation of transient test. It was chosen to use a single value of n for all temperatures. Good correlation in the range of temperatures from 100°C and 1100°C is obtained using $n = 2$. In Fig. III.2-3, the instantaneous stress-strain relationships of Eq. III.2-14 and Eq. III.2-18 are plotted for three different temperatures using $n = 2$ and it can be seen that the direct form of Eq. III.2-18 is a good approximation of the implicit form of Eq. III.2-14. In the present model, the instantaneous stress-strain relationship is thus taken as the relationship of Eq. III.2-18 with $n = 2$.
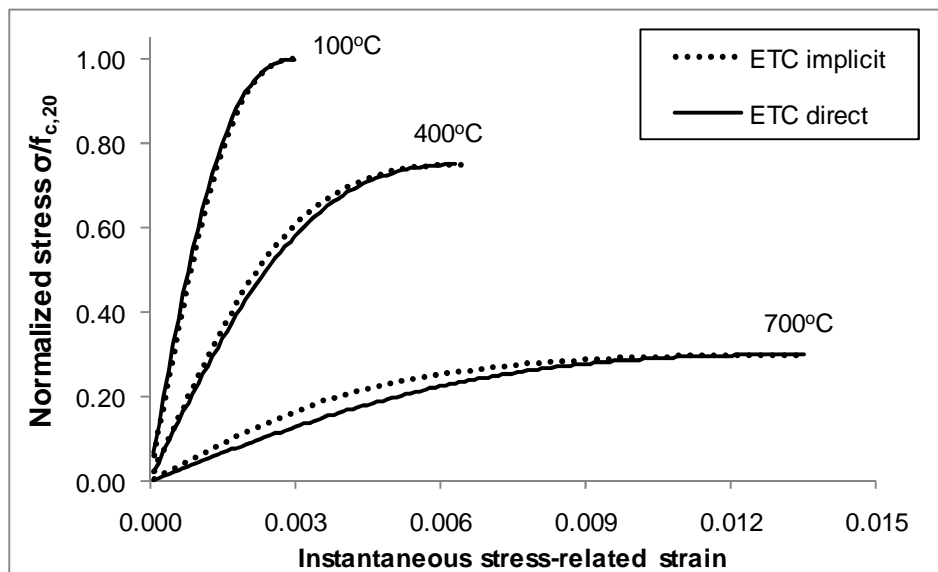
Fig. III.2-3: A direct instantaneous stress-strain relationship (Eq. III.2-18) is used instead of the implicit relationship of Eq. III.2-14

The ETC tangent modulus and the ETC initial stiffness (elastic modulus) are obtained directly by derivation of Eq. III.2-18. Using $n = 2$, the ETC tangent modulus is given by Eq. III.2-20 whereas the ETC initial stiffness is given by Eq. III.2-21.

$$E_t = \frac{d\sigma}{d\varepsilon_\sigma} = \frac{2\,f_{c,T}\left[1-\left(\varepsilon_\sigma/\varepsilon_{c1,ETC}\right)^2\right]}{\varepsilon_{c1,ETC}\left[1+\left(\varepsilon_\sigma/\varepsilon_{c1,ETC}\right)^2\right]^2}$$

Eq. III.2-20

$$E_{ETC} = \frac{2\,f_{c,T}}{\varepsilon_{c1,ETC}}$$

Eq. III.2-21

The evolution of the ETC initial stiffness (i.e. the elastic modulus) of Eq. III.2-21 with temperature is compared with the experimental data presented in Chapter I, see Fig. III.2-4. The evolution of the EC2 initial stiffness with temperature is also plotted on the graph. The results of the ETC model reasonably agree with experimental results, although the decrease in the initial stiffness with temperature is a bit overestimated by the model for temperatures between 300 °C and 500 °C. However, the EC2 model fails to capture the actual degradation of stiffness due to temperature; the decrease in the initial stiffness with temperature is largely overestimated by the EC2 model, due to the implicit consideration of transient creep strain in the EC2 model.
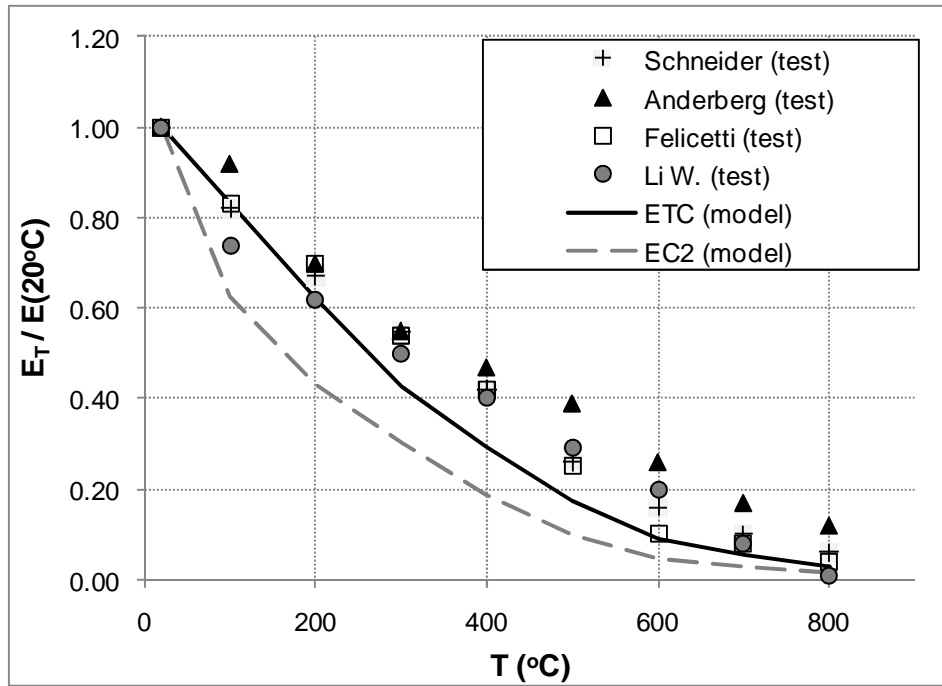
Fig. III.2-4: Evolution of the concrete elastic modulus with temperature: comparison between ETC model, EC2 model and experimental data

The descending branch of the instantaneous stress-strain relationship is needed for numerical reasons when modelling structures. It is made of two 3rd order polynomials from point $\left(\varepsilon_{c1,ETC}; f_{c,T}\right)$ until point $\left(\varepsilon_{c0,ETC}; 0\right)$ (Franssen, 1987). The relationship between the

ultimate strain at 0 stress of the ETC concrete model $\varepsilon_{c0,\text{ETC}}$ and the ultimate strain at 0 stress of the Eurocode 2 concrete model $\varepsilon_{c0,\text{EC2}}$ is given by Eq. III.2-22.

$$\varepsilon_{c0,\text{ETC}} = \varepsilon_{c0,\text{EC2}} - \left(\varepsilon_{c1,\text{EC2}} - \varepsilon_{c1,\text{ETC}}\right)$$

Eq. III.2-22

The values of the PSS for the ETC relationship $\varepsilon_{c1,\text{ETC}}(T)$ and the ultimate strain at 0 stress of the ETC concrete model $\varepsilon_{c0,\text{ETC}}(T)$ are given in Table III.2-2.

T(°C)	20	100	200	300	400	500	600	700	800	900
$\varepsilon_{c1,\text{ETC}}$	0.0025	0.0030	0.0038	0.0050	0.0063	0.0087	0.0127	0.0133	0.0140	0.0150
$\varepsilon_{c0,\text{ETC}}$	0.0200	0.0215	0.0233	0.0255	0.0263	0.0263	0.0227	0.0258	0.0290	0.0325

Table III.2-2: PSS and ultimate strain for the ETC relationship

The slope of the descending branch at the point where the sign of the concavity of the curve changes is noted E_{dscb}. This is the slope at the point of transition from the first to the second 3$^{\text{rd}}$ order polynomial. The value of E_{dscb} is given by Eq. III.2-23.

$$E_{dscb} = 2\frac{f_{c,T}}{\varepsilon_{c0,\text{ETC}} - \varepsilon_{c1,\text{ETC}}}$$

Eq. III.2-23

The stress σ and the tangent modulus E_t in the descending branch are calculated using Eq. III.2-24 to Eq. III.2-27. Note that these equations are presented here below for $\varepsilon_\sigma > 0$ in compression. In the implementation of the model, it has been assumed that $\varepsilon_\sigma < 0$ in compression and the sign of the equations have been adapted accordingly.

$$\varepsilon^* = \varepsilon_\sigma - \varepsilon_{c1,\text{ETC}} - f_{c,T}/E_{dscb} \quad ; \quad \sigma^* = E_{dscb}\, \varepsilon^*$$

Eq. III.2-24

If $\varepsilon^* \leq 0$;

$$\sigma = \frac{f_{c,T}}{2} - \sigma^*\left(\frac{\sigma^*}{2f_{c,T}} + 1\right)$$

$$E_t = -E_{dscb}\left(\frac{\sigma^*}{f_{c,T}} + 1\right)$$

Eq. III.2-25

If $0 < \varepsilon^* \leq f_{c,T}/E_{dscb}$;

$$\sigma = \frac{f_{c,T}}{2} + \sigma^*\left(\frac{\sigma^*}{2f_{c,T}} - 1\right)$$

$$E_t = E_{dscb}\left(\frac{\sigma^*}{f_{c,T}} - 1\right)$$

Eq. III.2-26

If $f_{c,T}/E_{dscb} < \varepsilon^*$;

$$\sigma = 0$$
$$E_t = 0$$

Eq. III.2-27

Chap. III – Transient creep strain in a uniaxial model

110

The instantaneous stress-strain relationship of the ETC model in compression is illustrated in Fig. III.2-5.
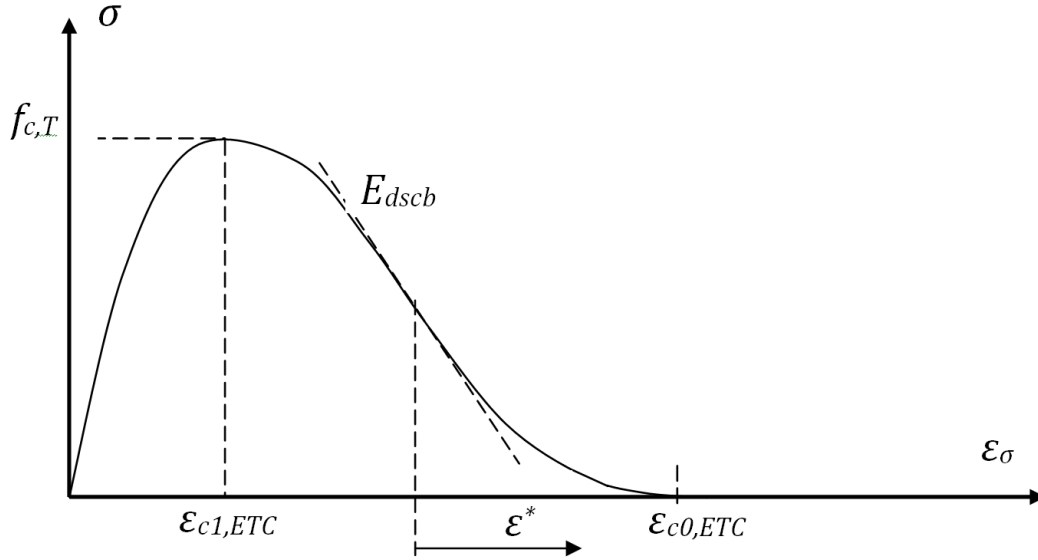
Fig. III.2-5: ETC instantaneous stress-strain relationship in compression

If concrete has been loaded in compression and, in a later stage, the instantaneous stress-related strain decreases, the unloading is made according to a plasticity model. This means that the path is a linear decrease from the point of maximum compressive strain in the loading curve parallel to the tangent at the origin in an $\varepsilon_\sigma - \sigma$ plane, see Fig. III.2-6.
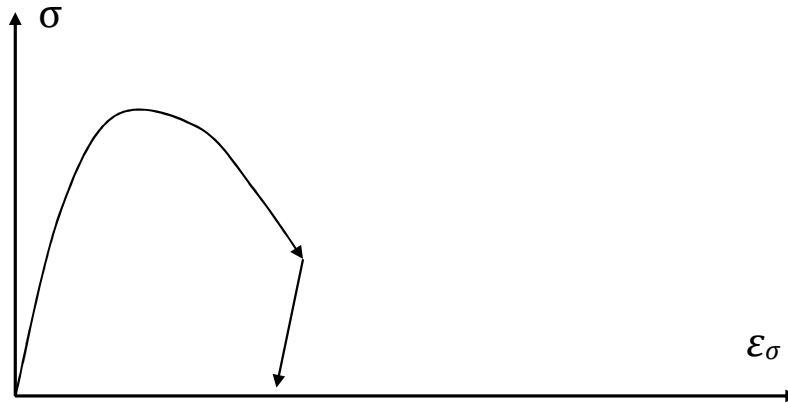
Fig. III.2-6: Unloading in compression with a plasticity model

III.2.1.3. *Instantaneous stress-related strain in tension*

In tension, the cracking behaviour of concrete is described by a smeared-crack model, which means that neither the opening of the individual cracks nor the spacing between different cracks is present in the model. The stress-strain relationship is made of a second order ascending branch and a descending branch made of two curves, each of them being a third order function of the strain (Franssen, 1987). The ascending branch is characterized by the tensile strength $f_{t,T}$, and the modulus at the origin E_{ETC}. The strain at peak stress is noted $\varepsilon_{t1,ETC}$ and is given by $\varepsilon_{t1,ETC} = 2 f_{t,T} / E_{\text{ETC}}$. The stress σ and the tangent modulus E_t are

given by Eq. III.2-28 and Eq. III.2-29, for $\varepsilon_\sigma \leq \varepsilon_{t1,ETC}$. Note that the equations here below are presented for $\varepsilon_\sigma > 0$ in tension.

$$\sigma = E_{\text{ETC}}\, \varepsilon_\sigma \left(1 - \frac{E_{\text{ETC}}\, \varepsilon_\sigma}{4\, f_{t,T}} \right) \qquad \text{Eq. III.2-28}$$

$$E_t = E_{\text{ETC}} \left(1 - \frac{E_{\text{ETC}}\, \varepsilon_\sigma}{2\, f_{t,T}} \right) \qquad \text{Eq. III.2-29}$$

The descending branch is characterized by the point $\left(\varepsilon_{t1,ETC}; f_{t,T} \right)$ and the slope of the descending branch at the point where the sign of the concavity of the curve changes E_{dscb}. The value of E_{dscb} in tension is the same as the value in compression. The stress σ and the tangent modulus E_t in the descending branch are calculated using Eq. III.2-30 to Eq. III.2-33.

$$\varepsilon^* = \varepsilon_\sigma - \varepsilon_{t1,ETC} - f_{t,T}/E_{dscb} \quad ; \quad \sigma^* = E_{dscb}\varepsilon^* \qquad \text{Eq. III.2-30}$$

If $\varepsilon^* \leq 0$;
$$\sigma = \frac{f_{t,T}}{2} - \sigma^* \left(\frac{\sigma^*}{2 f_{t,T}} + 1 \right)$$
$$E_t = -E_{dscb} \left(\frac{\sigma^*}{f_{t,T}} + 1 \right)$$
$\qquad \text{Eq. III.2-31}$

If $0 < \varepsilon^* \leq f_{t,T}/E_{dscb}$;
$$\sigma = \frac{f_{t,T}}{2} + \sigma^* \left(\frac{\sigma^*}{2 f_{t,T}} - 1 \right)$$
$$E_t = E_{dscb} \left(\frac{\sigma^*}{f_{t,T}} - 1 \right)$$
$\qquad \text{Eq. III.2-32}$

If $f_{t,T}/E_{dscb} < \varepsilon^*$;
$$\sigma = 0$$
$$E_t = 0$$
$\qquad \text{Eq. III.2-33}$

The instantaneous stress-strain relationship of the ETC model in tension is illustrated in Fig. III.2-7.

The PSS in tension is given by: $\varepsilon_{t1,ETC} = 2 f_{t,T}/E_{\text{ETC}} = \left(f_{t,T}/f_{c,T} \right) \times \varepsilon_{c1,ETC}$. Therefore the PSS in tension is proportional to the PSS in compression, the proportionality factor being the ratio between the tensile and the compressive strength at high temperature. Similarly, after a few developments the ultimate strain at 0 stress in tension $\varepsilon_{t0,ETC}$ can be obtained as a function of the ultimate strain at 0 stress in compression $\varepsilon_{c0,ETC}$, see Eq. III.2-34.

$$\varepsilon_{t0,ETC} = \varepsilon_{t1,ETC} + 2\frac{f_{t,T}}{E_{dscb}} = \frac{f_{t,T}}{f_{c,T}} \times \varepsilon_{c0,ETC} \qquad \text{Eq. III.2-34}$$
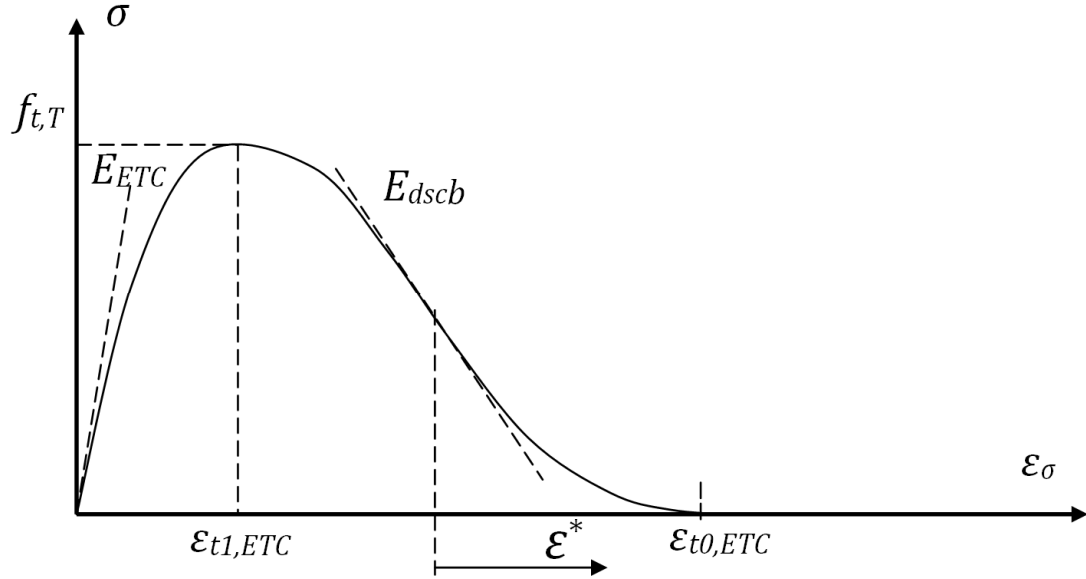
Fig. III.2-7: ETC instantaneous stress-strain relationship in tension

If concrete has been loaded in tension and, in a later stage, the strain decreases, the unloading is made according to a damage model. This means that the path is a linear decrease from the point of maximum tensile strain in the loading curve to the point of origin in the stress-strain diagram plane, see Fig. III.2-8.
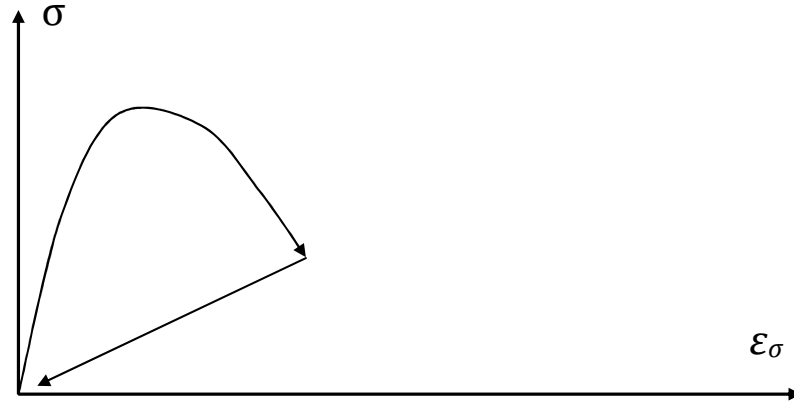
Fig. III.2-8: Unloading in tension with a damage model

III.2.1.4. *Free thermal strain*

The free thermal strain is determined according to Eurocode 2 (European Committee for Standardization, 2004b). The formula depends on the type of aggregate: siliceous aggregates (Eq. III.2-35) or calcareous aggregates (Eq. III.2-36).

$$
\begin{aligned}
\varepsilon_{th}\left(T\right) &= -1.8\times10^{-4} + 9\times10^{-6}\,T + 2.3\times10^{-11}\,T^3 &&; 20°C \leq T \leq 700°C \\
\varepsilon_{th}\left(T\right) &= 14\times10^{-3} &&; 700°C < T \leq 1200°C
\end{aligned}
\qquad \text{Eq. III.2-35}
$$

$$
\begin{aligned}
\varepsilon_{th}\left(T\right) &= -1.2\times10^{-4} + 6\times10^{-6}\,T + 1.4\times10^{-11}\,T^3 &&; 20°C \leq T \leq 805°C \\
\varepsilon_{th}\left(T\right) &= 12\times10^{-3} &&; 805°C < T \leq 1200°C
\end{aligned}
\qquad \text{Eq. III.2-36}
$$

This formula expresses the free thermal strain as a nonlinear function of temperature, see Fig. III.2-9. The free thermal strain of concrete is partly irreversible; a residual dilatation or residual contraction is observed after cooling down to ambient temperature depending on the maximum temperature reached in the material. The value of the residual free thermal strain as a function of the maximum temperature is taken from experimental tests made by Schneider and presented in Table I.2-1.
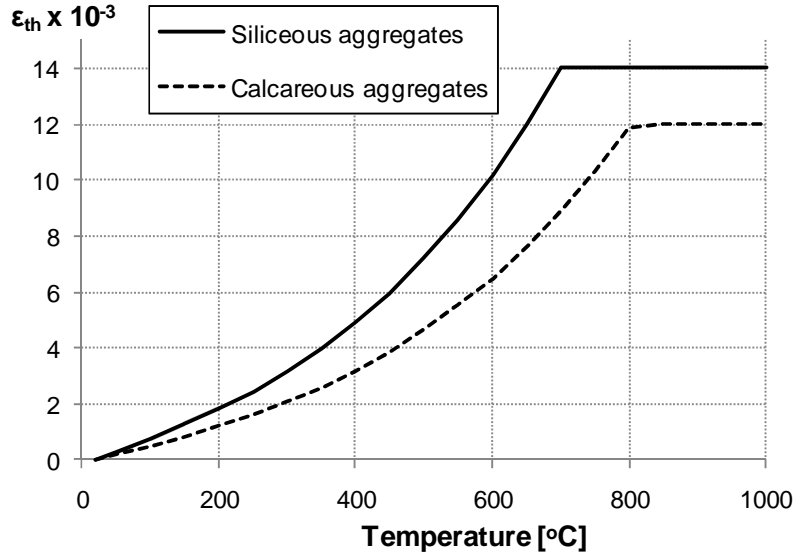
Fig. III.2-9: Free thermal strain

III.2.2. Implementation in a finite elements software

This section presents the procedure for implementation of the Explicit Transient Creep uniaxial concrete model in a finite elements code. Let us assume that at time step s the finite element code has converged, which means that the local state of equilibrium of the material is completely defined everywhere in the structure or, in terms of numerical modeling, at every integration point, i.e. the value of $\left\{\varepsilon_{tot}^{(s)}; \varepsilon_{th}^{(s)}; \varepsilon_p^{(s)}; \varepsilon_{tr}^{(s)}\right\}$ and $\left\{\sigma^{(s)}\right\}$ is known. The values of the displacements at the nodes are also defined. Then suppose that, from time step s to time step $s+1$, the variation of the nodes displacements calculated by the finite element code produce an increment in total strain, that is noted $\Delta\varepsilon_{tot}$. The problem is to update to time step $s+1$ the basic variables describing the local state of the material in a manner that is consistent with the constitutive law. This process should also yield the tangent modulus of the constitutive law, to be used by the finite element code in the iteration process. It is assumed that the temperatures are known, as a result of a thermal analysis that has been performed previous to the mechanical analysis.

The total strain $\varepsilon_{tot}^{(s+1)} = \varepsilon_{tot}^{(s)} + \Delta\varepsilon_{tot}$ is calculated straightforwardly (some codes even give the total displacement, and strain, as a primary result).

The free thermal strain is a direct function of the temperature: $\varepsilon_{th}^{(s+1)} = f\left(T^{(s+1)}\right)$. For all points of integration, computation of the free thermal strain at time step $s+1$ is thus

performed primarily, apart from the iterative resolution of the equilibrium at this time step. When entering into the material law during the iterative resolution of the equilibrium, the free thermal strain is subtracted from the total strain, which allows writing the material law in term of the mechanical strain.

In the ETC model, it was decided to extract the transient creep strain computation from the iterative resolution of the equilibrium in a time step. For all points of integration, the transient creep strain is thus evaluated at the same time as the free thermal strain, before entering into the material law. This assumption allows for treating the transient creep effects separately from the elastic and plastic effects, i.e. the transient creep calculation is decoupled from the integration of the constitutive law of the material. The aim is to obtain a direct constitutive relationship in terms of the instantaneous stress-related strain instead of the mechanical strain.

At the beginning of the time step, the stress at the equilibrium is not known. Consequently, it was decided to calculate the transient creep strain as a function of the stress at the previous time step $\sigma^{(s)}$ (explicit numerical scheme). This assumption is required to avoid an additional iterative process for the calculation of the transient creep strain. It was considered by the author that this assumption was valid for the structural applications for which the model is developed, and that the additional complexity and CPU time required to include the transient creep calculation into the integration of the material law were not justified for these applications. According to this assumption, using Eq. III.2-6 with $\beta = 0$, the transient creep strain at time step $s+1$ is computed by Eq. III.2-37.

$$\varepsilon_{tr}^{(s+1)} = \varepsilon_{tr}^{(s)} + \left[\phi\left(T^{(s+1)}\right) - \phi\left(T^{(s)}\right) \right] \frac{\sigma^{(s)}}{f_{c,20}} \qquad \text{Eq. III.2-37}$$

However, certain conditions are applied to the computation of transient creep strain using Eq. III.2-37, in order to take into account properly the influence of the stress-temperature path on the transient creep strain calculation. Between time step s and time step $s+1$, there is an increment in transient creep strain calculated by Eq. III.2-37 if and only if the three following conditions are fulfilled:

    i.   The temperature at time step $s+1$ exceeds the maximum temperature reached previously in the history of the material (first-time temperature increase);

    ii.   The converged stress at time step s is a compressive stress;

    iii.   The tangent modulus of the material at time step s is positive, i.e., the material is in the ascending branch of the stress-strain relationship.

The first condition is consistent with the physical definition of transient creep, as this phenomenon only develops in concrete that is first-time heated under stress; if the temperature has decreased or remained constant between time steps s and $s+1$, there cannot be any variation of transient creep strain. As the function $\phi(T)$ is growing with temperature, the transient creep term can only increase. It is assumed that no transient creep develops in tension; this assumption, expressed by the second condition, is based on the fact that no experimental data is available on this phenomenon under tensile stress state. This assumption

should be confirmed by future research; however it is clear that the concrete behavior in tension is less important than in compression. Finally, the third condition expresses the assumption that there is no increment in transient creep strain in the material which exhibits its softening behavior after the peak stress in compression. This assumption is also based on a lack of experimental data, due to the incompatibility between the transient test procedure and the characterization of post-peak behavior. Indeed, transient tests are stress-controlled by definition, as the applied stress has to remain constant during the test.

Transient creep strain is irreversible at both stress and temperature decrease. It is very clear that, at temperature decrease, there is no variation of transient creep strain; however, there can be an increment in transient creep strain at stress decrease. Using the three conditions explained here above, no distinction is made between the situation of heating under increasing compressive stress and the situation of heating under decreasing compressive stress. At stress decrease, additional transient creep strain is assumed to develop in the material submitted to increasing temperature as long as the stress in the material remains in compression. This assumption is confirmed by experimental results that will be presented in Section III.3.1 (Fig. III.3-2). By assumption, the increase in transient creep strain that develops in the concrete material submitted to (first-time) increase in temperature and submitted to given compressive stress is the same for loading and unloading. As noted by Li and Purkiss (2005), this assumption was also adopted by Anderberg and Thelandersson (1976).

As the thermal strain and the transient creep strain have been calculated at the beginning of the time step, the material law is written in term of the instantaneous stress-related strain in the ETC model. The instantaneous stress-related strain at time step $s+1$ is computed by Eq. III.2-38.

$$\varepsilon_\sigma^{(s+1)} = \varepsilon_{tot}^{(s+1)} - \varepsilon_{th}^{(s+1)} - \varepsilon_{tr}^{(s+1)}$$
<div align="right">Eq. III.2-38</div>

The stress $\sigma^{(s+1)}$ at time step $s+1$ can then be computed using the ETC constitutive relationship (written in instantaneous stress-related strain) of Eq. III.2-18.

Actually, solving the equilibrium of the structure is an iterative process and the increment in total strain produced by the finite element code is updated several times at each time step. Namely, the code produces an increment in total strain $\Delta\varepsilon_{tot}^{(i+1)}$ at every iteration during a time step. The total strain at iteration $i+1$ of time step $s+1$ is then given by $\varepsilon_{tot}^{(i+1)} = \varepsilon_{tot}^{(s)} + \Delta\varepsilon_{tot}^{(i+1)}$. As a consequence, the value of the instantaneous stress-related strain at time step $s+1$ has also to be updated at every iteration, according to Eq. III.2-39. However, the values of the free thermal strain and the transient creep strain do not change during the iteration process; these two strain components are only computed once at the beginning of each time step.

$$\varepsilon_\sigma^{(i+1)} = \varepsilon_{tot}^{(i+1)} - \varepsilon_{th}^{(s+1)} - \varepsilon_{tr}^{(s+1)}$$
<div align="right">Eq. III.2-39</div>

Finally, the stress $\sigma^{(i+1)}$ at iteration $i+1$ of time step $s+1$ is computed as a function of the instantaneous stress-related strain $\varepsilon_\sigma^{(i+1)}$ and the temperature at time step $s+1$, using Eq. III.2-40.

$$\sigma^{(i+1)} = \frac{2 \times f_{c,T}\left(T^{(s+1)}\right) \times \varepsilon_\sigma^{(i+1)}}{\varepsilon_{c1,\text{ETC}}\left(T^{(s+1)}\right) \times \left[1 + \left(\dfrac{\varepsilon_\sigma^{(i+1)}}{\varepsilon_{c1,\text{ETC}}\left(T^{(s+1)}\right)}\right)^2\right]}$$

Eq. III.2-40

The implementation procedure for the ETC concrete material law in the non linear software SAFIR (Franssen, 2005b) is schematized in Fig. III.2-10. The following notation has been used: $\underline{f}_{\text{ext}}$ is the vector of the external nodal forces, $\Delta\underline{f}$ is a given increment of force between time step s and time step $s+1$, T is the temperature (which has been calculated for every time step before the beginning of the mechanical calculation), $\underline{r}^{(i+1)}$ is the residual force after $i+1$ iterations, $\underline{f}_{\text{int}}$ is the vector of the internal forces, $\Delta\underline{u}$ is the increment of displacement corresponding to $\Delta\underline{f}$, $\underline{\underline{K}}^{(i+1)}$ is the stiffness matrix, $\underline{\underline{B}}$ is the matrix linking deformations and nodal displacements and $\underline{\underline{D}}_t$ is the tangent stiffness matrix of the non linear material law.

III.2.3. Characteristics of the ETC model

The Explicit Transient Creep concrete model developed in this chapter presents the following characteristics:

- The ETC model has the same generic form as the current EC2 implicit model;
- All the parameters in the ETC model derive from parameters of the EC2 or the ENV standard codes;
- The ETC initial stiffness is close to the elastic modulus of ENV with lower limit of the PSS, which leads to an accurate representation of the elastic modulus of the material;
- The transient creep strain calculated with the ETC model reasonably agrees with experimental data and other models found in the literature;
- The instantaneous stress-strain relationship considered in the ETC model agrees with experimental data obtained by steady-state tests;
- The mechanical stress-strain relationship obtained with the ETC model for a material first-time heated under constant stress (transient tests) is calibrated to yield the same results as the present version of EC2.

Therefore, the ETC model can be seen as a new formulation of the EC2 model that includes an explicit term for transient creep.

step $= 0$

$$\boxed{\textbf{STEP = STEP + 1}}$$

$$\underline{f}_{\text{ext}}^{(s+1)} = \underline{f}_{\text{ext}}^{(s)} + \Delta\underline{f}$$

For all IP =>

$$T^{(s+1)} = \text{data}$$

Mechanical properties at $T^{(s+1)}$

$$\underline{\varepsilon}_{th}^{(s+1)} = f\left(T^{(s+1)}\right)$$

$$\underline{\varepsilon}_{tr}^{(s+1)} = f\left(\underline{\sigma}^{(s)}, T^{(s+1)}\right)$$

iter $= 0$

$$\boxed{\textbf{ITER = ITER + 1}}$$

$$\underline{r}^{(i+1)} = \underline{f}_{\text{ext}} - \underline{f}_{\text{int}}^{(i)}$$

$$\Delta\underline{u}^{(i+1)} = \left(\underline{\underline{K}}^{(i)}\right)^{-1} \underline{r}^{(i+1)}$$

$$\Delta\underline{u}_{\text{tot}}^{(i+1)} = \Delta\underline{u}_{\text{tot}}^{(i)} + \Delta\underline{u}^{(i+1)}$$

$$\Delta\underline{\varepsilon}^{(i+1)} = \underline{\underline{B}}\,\Delta\underline{u}_{tot}^{(i+1)}$$

$$\underline{\varepsilon}_{\sigma}^{(i+1)} = \underline{\varepsilon}_{tot}^{(i+1)} - \underline{\varepsilon}_{th}^{(s+1)} - \underline{\varepsilon}_{tr}^{(s+1)}$$

For all IP =>

$$\boxed{\begin{array}{c} \text{MATERIAL LAW} \\ \underline{\sigma}^{(i+1)} = f\left(\underline{\varepsilon}_{\sigma}^{(i+1)}, T^{(s+1)}\right) \\ \rightarrow \underline{\sigma}^{(i+1)}\,,\ \underline{\underline{D}}_{t}^{(i+1)} \end{array}}$$

$$\underline{\underline{K}}^{(i+1)} = \int\limits_{V} \underline{\underline{B}}^{\,t}\ \underline{\underline{D}}_{t}^{(i+1)}\ \underline{\underline{B}}\ dV$$

$$\underline{f}_{\text{int}}^{(i+1)} = \int\limits_{V} \underline{\underline{B}}^{\,t}\ \underline{\sigma}^{(i+1)}\,dV$$

No ◇ **Convergence?**

Yes

For all IP =>

$$\underline{\sigma}^{(s+1)} = \underline{\sigma}^{(i+1)}\,,\ \underline{\varepsilon}_{p}^{(s+1)} = \underline{\varepsilon}_{p}^{(i+1)}$$
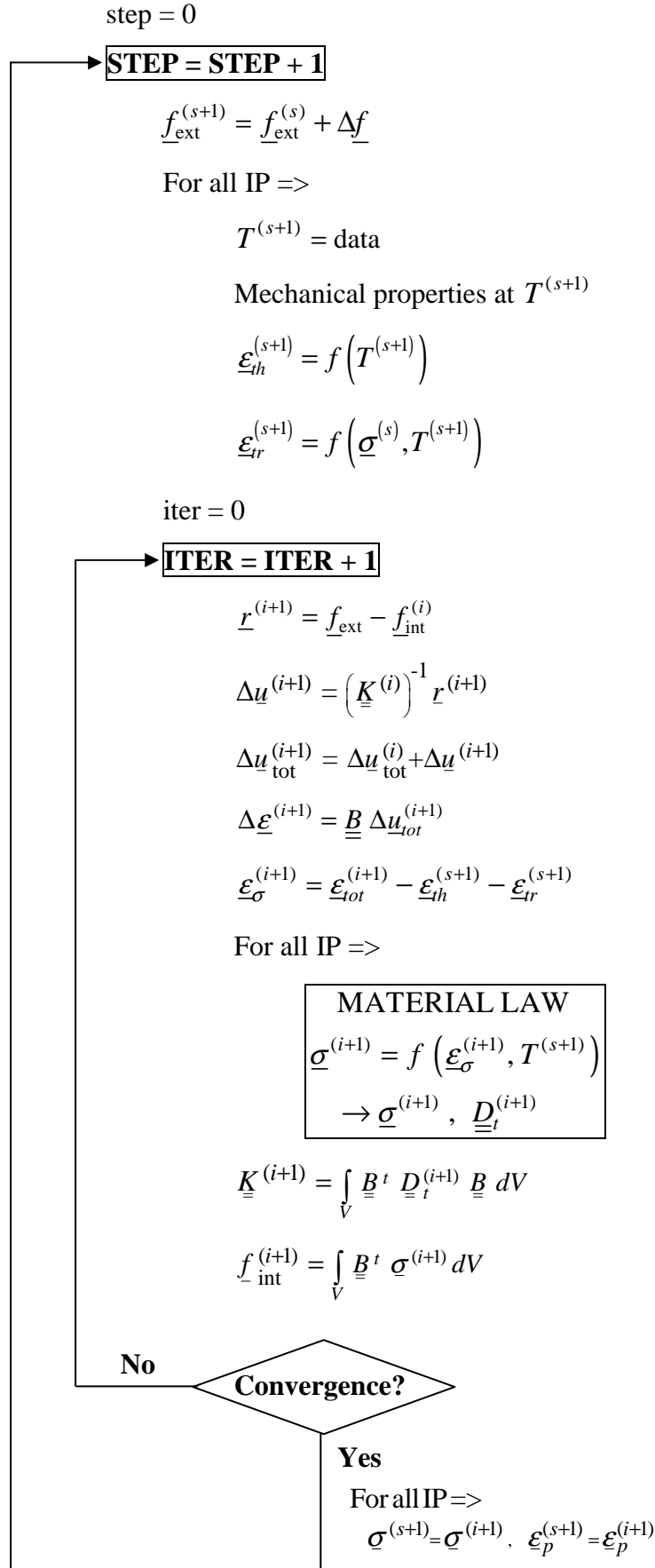
Fig. III.2-10: Implementation of the ETC concrete model in a finite elements software

III.3. Validation of the ETC model

III.3.1. Experimental validation at the material level for unsteady temperatures and loads

The ETC model is validated at the material level by comparison between experimental results and computed values of the mechanical strains developed by concrete specimens subjected to unsteady temperatures and loads. The considered experiments are taken from Schneider, et al. (2008). The specimens are axially unrestrained cylinders with 80 mm diameter and 300 mm height, made of siliceous concrete. In all cases, the temperature is constantly increasing at a rate of 2°C/min. The compressive strength at 20°C is 38 MPa. The numerical calculations are performed with the software SAFIR (Franssen, 2005b) where the ETC model has been implemented. Beam finite elements are used for modeling the specimens.

The concrete cylinders are subjected to different stress-time relationships, which can be expressed as stress-temperature relationships because the temperature is increasing at constant heating rate. The stress-temperature relationships for the three considered tests are plotted in the left part of Fig. III.3-1 to Fig. III.3-3. The aim of these tests is to highlight the influence of the explicit consideration of transient creep strain on the mechanical strain calculation. The mechanical strains computed using the ETC model and the EC2 implicit model are compared to the measured results, see the right part of Fig. III.3-1 to Fig. III.3-3. The observations are put in relation with the theoretical considerations expressed in Chapter I, Section I.3.2.2, about the different stress-temperature paths illustrated in Fig. III.3-4.

The test of Fig. III.3-1 corresponds to Situation I of Fig. III.3-4, i.e. simultaneously increasing stress and increasing temperature. This first test is close to a transient test, as the specimen is heated under compressive stress, although in this case the compressive stress is not constant but it is slowly increasing. As the EC2 model has been developed based on transient test results, the results obtained with the EC2 model agree with the experimental results. It can also be seen that the results obtained with the ETC model almost coincide with the results obtained with the EC2 model. Therefore, this first test allows verifying that, in the situations where the EC2 model was able to capture properly the concrete behavior, the ETC model yields the same results as the EC2 model.
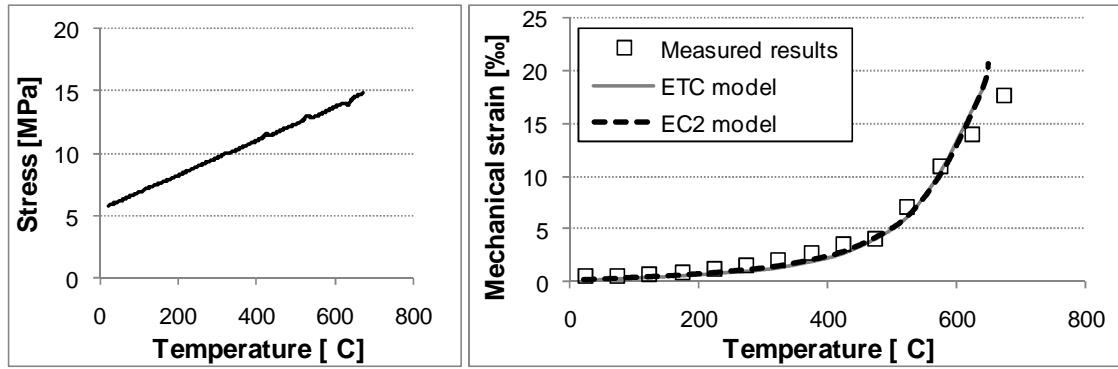
Fig. III.3-1: Mechanical strain-temperature relationships: measured and computed results (a)
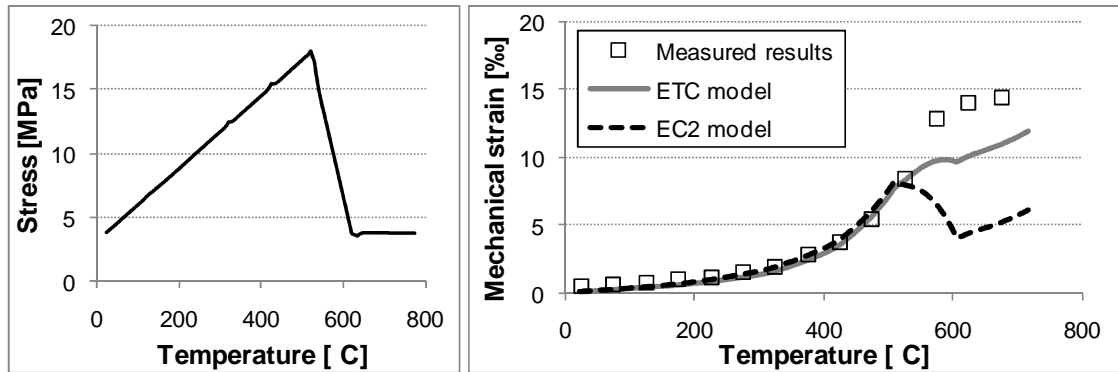
Fig. III.3-2: Mechanical strain-temperature relationships: measured and computed results (b)
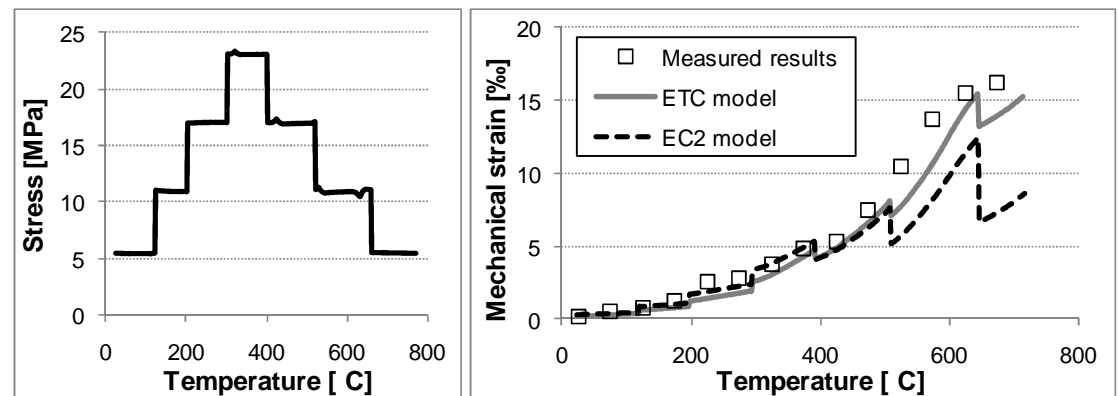
Fig. III.3-3: Mechanical strain-temperature relationships: measured and computed results (c)
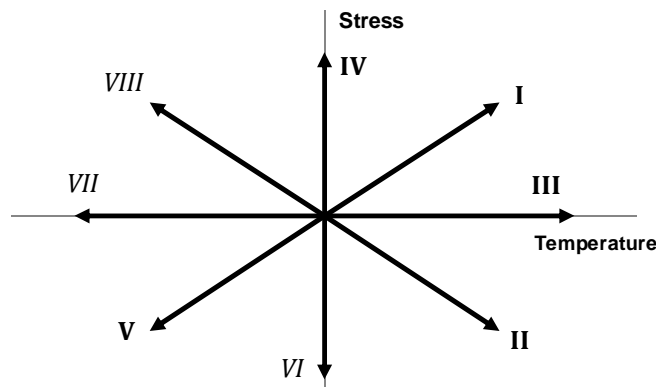
Fig. III.3-4: Different possible stress-temperature paths

The test of Fig. III.3-2 successively represents Situation I (increasing stress), Situation II (decreasing stress) and finally Situation III (constant stress) of Fig. III.3-4. At the beginning and until the peak stress, the difference between the two models is very small. Then, the stress rate becomes negative. During this second phase of the test (decreasing stress), the mechanical strain computed by the EC2 implicit model quickly decreases, because the transient creep strain is being recovered. On the contrary, the mechanical strain computed by the ETC model keeps on growing, though more and more slowly, because transient creep strain still develops in the material. The transient creep strain that continues to develop under increasing temperature and decreasing compressive stress counterbalances the elastic unloading due to the stress decrease. This increase in the mechanical strain under decreasing stress is also observed experimentally, which validates the assumption made in the model. The behavior predicted by the ETC model matches reasonably the measured behavior during this phase, whereas the EC2 model fails to capture this behavior. This confirms the fact that implicit models are not able to capture properly the actual unloading stiffness at elevated temperatures. At the end of the test, the stress is kept constant (Situation III) and both models predict exactly the same variation of the mechanical strain. The ETC model is able to capture qualitatively the experimental response during the three phases of the test, which is not the case for the EC2 model.

In the third test (Fig. III.3-3), the specimen is successively subjected to different constant stress levels while the temperature is increasing (Situation III). The transition between two stress levels is made by a "step", i.e. a quasi-instantaneous variation from one stress level to another. As these variations in stress are quasi-instantaneous, they occur at constant temperature; therefore they correspond to Situations IV and VI in Fig. III.3-4. At each stress step, the corresponding mechanical strain variations predicted by the two models are different. Implicit models such as the EC2 models amplify the effect of a stress step on the mechanical strain variation. Indeed, the transient creep strain considered in implicit models is suddenly increased or decreased together with the elastic strain. In explicit models, on the contrary, transient creep strain does not vary in such situations where the stress varies at constant temperature. It can be seen that the behavior predicted by the ETC model better matches the experimental behavior of the specimens, owing to a better modeling of the material stiffness at constant high temperature.

III.3.2. Unrestrained concrete column subjected to fire

An experimental fire test made in Japan on a centrally loaded concrete column (Schneider, et al., 1994) is simulated using the nonlinear finite element software SAFIR. Beam finite elements are used in the numerical simulation. A comparison between numerical results considering different concrete models and experimental data is performed. The column is 300 mm by 300 mm in cross section with a central hole of 100 mm diameter, see Fig. III.3-5. The siliceous concrete has a compressive strength of 55 MPa. Four 16 mm longitudinal rebars with 375 MPa yield strength steel are present with a cover of 40 mm. The simply supported column is submitted to a load of 677 kN and then exposed to Japanese standard fire temperature-time curve (Japanese Industrial Standards, 1969) during

180 minutes. Then, the element was allowed to cool down. The deformation behavior is presented in Fig. III.3-6.
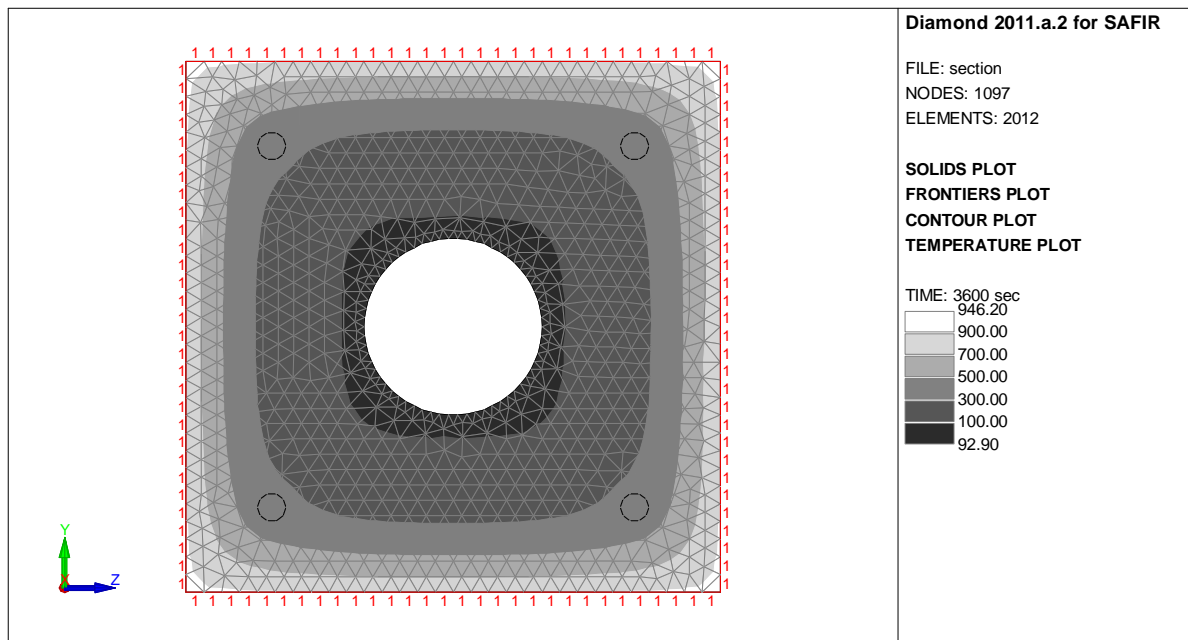
Fig. III.3-5: Column cross section and temperature distribution after 1 hour
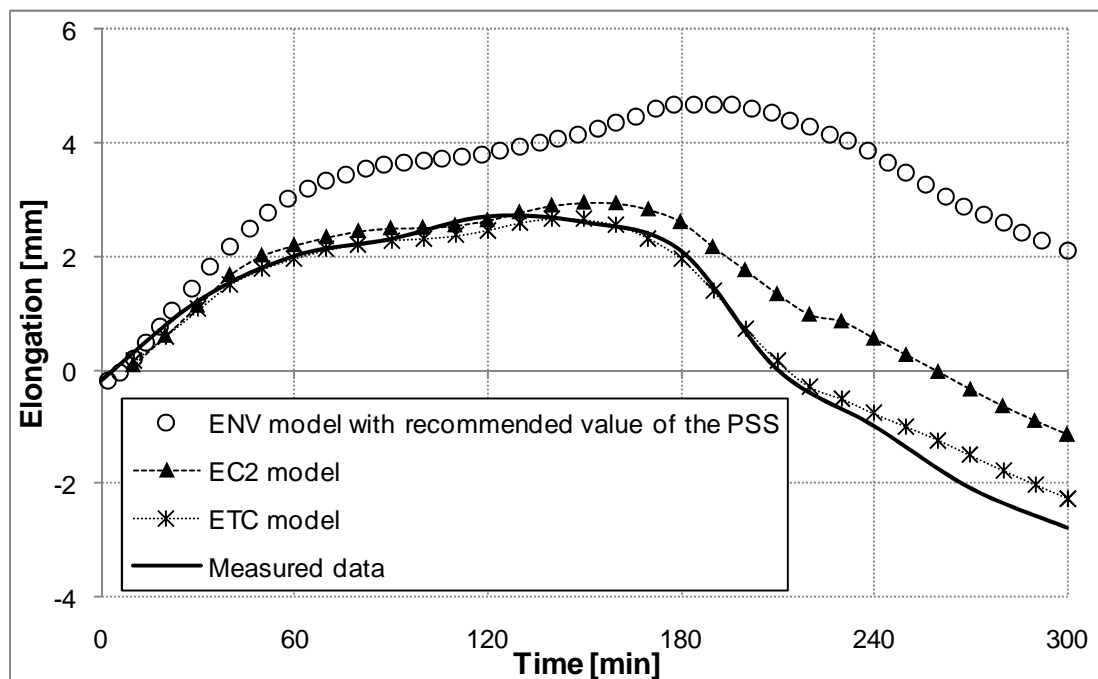
Fig. III.3-6: Comparison between measured and computed results on a concrete column subjected to natural fire

Based on the results plotted in Fig. III.3-6, the following observations can be made:

▪ The ENV model (European Committee for Standardization, 1995) with recommended value of the peak stress strain (PSS) leads to too large elongations, because of a highly underestimated transient creep strain. This model had been

found to be by far too stiff and has been removed when transforming the Eurocode from an ENV to an EN.

- The ETC model and the EC2 model lead to comparable results during approximately the first 140 minutes of heating. Beyond 140 minutes, the behavior predicted by the ETC model tends to differ from the behavior predicted by the EC2 model; the effects of the explicit consideration of transient creep strain on the structural behavior become notable. The ETC model matches better than the EC2 model the actual behavior of the structure.

- The difference between the behaviors predicted by the ETC and the EC2 models is particularly significant during the cooling phase. Measured data showed an important decrease of the elongation, due to a progressive decrease of thermal strain coupled with a very limited recovery of mechanical strain. Indeed, mechanical strain is mostly composed of permanent strain. This behavior is well represented with the ETC model owing to the explicit consideration of transient creep. The EC2 model, on the contrary, implicitly recovers the transient creep strain, leading to an underestimated final shortening of the column.

III.3.3. Axially restrained concrete columns subjected to heating and cooling

In a real building, restraint forces and moments typically appear in the structural elements subjected to fire due to the connection with the rest of the structure. It is expected that the influence of the transient creep strain in the explicit model compared to the implicit model will be even more pronounced for restrained fire-exposed structures than for simply supported fire-exposed structures. For instance, in an axially restrained concrete column subjected to fire, the restraint force first increases due to thermal expansion and then decreases when the mechanical strain in compression exceeds (in absolute value) the thermal elongation strain. During the contraction phase of the column, when the load is progressively transferred from the fire-exposed column to the rest of the structure, the computation of the concrete material unloading stiffness is a key issue for the validity of the simulation of the structural behavior. The use of a concrete model that includes an explicit term for transient creep strain is thus necessary for statically indeterminate structures, also during the heating phase of the fire. To illustrate these assertions, the following example deals with the numerical analysis of reinforced concrete columns with axial restraint.

III.3.3.1. *Numerical simulation of the tests*

A series of experimental tests made at South China University of Technology on axially restrained concrete columns (Wu, et al., 2010) is simulated using the nonlinear finite element software SAFIR. The experimental data are compared with the computed results obtained respectively with the EC2 concrete model and the ETC concrete model. The columns are all 2340 mm length, see Fig. III.3-7, but only their central part is exposed to fire on a length of 1650 mm. Two different cross sections are used in the tests, either T-shape or L-shape cross sections, see Fig. III.3-8; these sections are 250 mm wide and 250 mm deep. The C30 siliceous concrete cross sections are reinforced with 12 longitudinal steel bars of HRB400

(hot rolled ribbed bar of 400 MPa grade) with a diameter of 10 mm and a concrete cover of 25 mm. The columns are axially restrained using a restraining beam. The columns are initially concentrically loaded and then subjected to the standard ISO-834 fire on all sides. Two different levels of axial restraint and two different levels of load are considered for each shape of cross section, which leads to eight different cases, see Table III.3-1. The fire was stopped when approximately 50% of the working load was transferred from the column to the restraining beam, i.e. after a time varying between 90 and 105 min depending on the case, followed by a cooling phase.
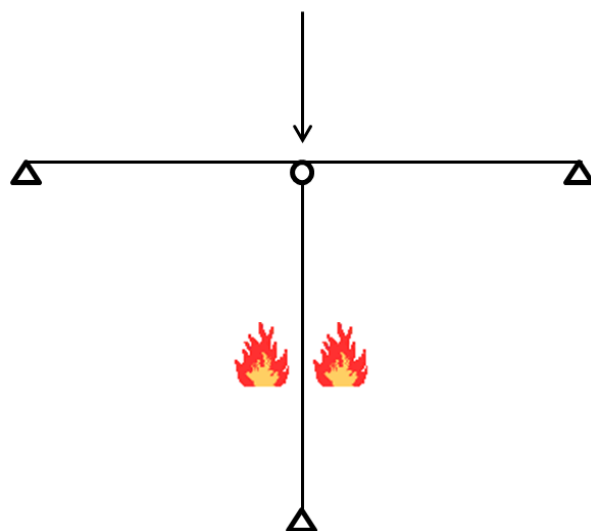
Fig. III.3-7: Schematic elevation view of the column and the restraining beam
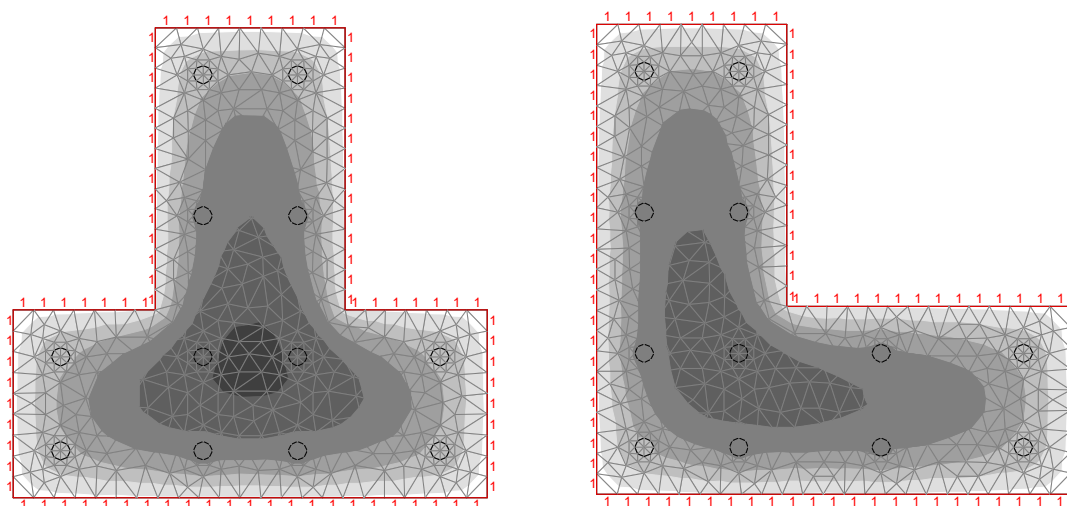
Fig. III.3-8: T-shape and L-shape cross sections

Column no.	Load [kN]	Axial restraint [MN/m]
RCT11	271	34.5
RCT12	272	51.9
RCT21	375	34.5
RCT22	377	51.9
RCL11	292	34.5
RCL12	285	51.9
RCL21	382	34.5
RCL22	380	51.9

Table III.3-1: Applied load and axial restraint for the fire tests

Thermal parameters for concrete and steel recommended by EC2 were used in the heat transfer analysis by SAFIR. Note that, in the original paper by Wu, et al. (2010) presenting the tests, the thermal analysis of the tests has also been performed using the thermal parameters from the EC2 and the software SAFIR and the simulations showed good agreement with the measured temperatures in the section. For the structural analysis performed for this thesis, initial eccentricity of 3 mm was introduced as it is the same value used by Wu, et al. to perform the numerical simulation of their tests. No buckling phenomenon was observed during the tests. After the fire tests, minor spalling of concrete was observed for several columns; however, accidental spalling was not considered in the numerical simulations. The mechanical law for the steel reinforcement was taken from Eurocode. It should be noted that no creep is explicitly considered in the relationships for steel reinforcement, which is an important assumption as the creep of the steel reinforcement is known to have an effect on stress and strain state in reinforced concrete frames when temperature in reinforcement bars exceeds 400°C (Williams-Leir, 1983; Bratina, et al., 2007), as is the case here. The axial restraint is modeled by a linear elastic spring connected to the top of the beam in the numerical simulations. The stiffness of the spring remains unchanged during the simulations, which can be justified by the fact that the maximum displacement at the center of the restraining beam is only about 13 mm (Wu, et al., 2010) and therefore the axial restraint stiffness can be considered as constant. The deformation behavior and the evolution of the axial load for the eight experiments is presented in Fig. III.3-9 and Fig. III.3-10.

Fig. III.3-9: Comparison between measured and computed results – T-shape

Axial displacement-time relationships   Axial force-time relationships
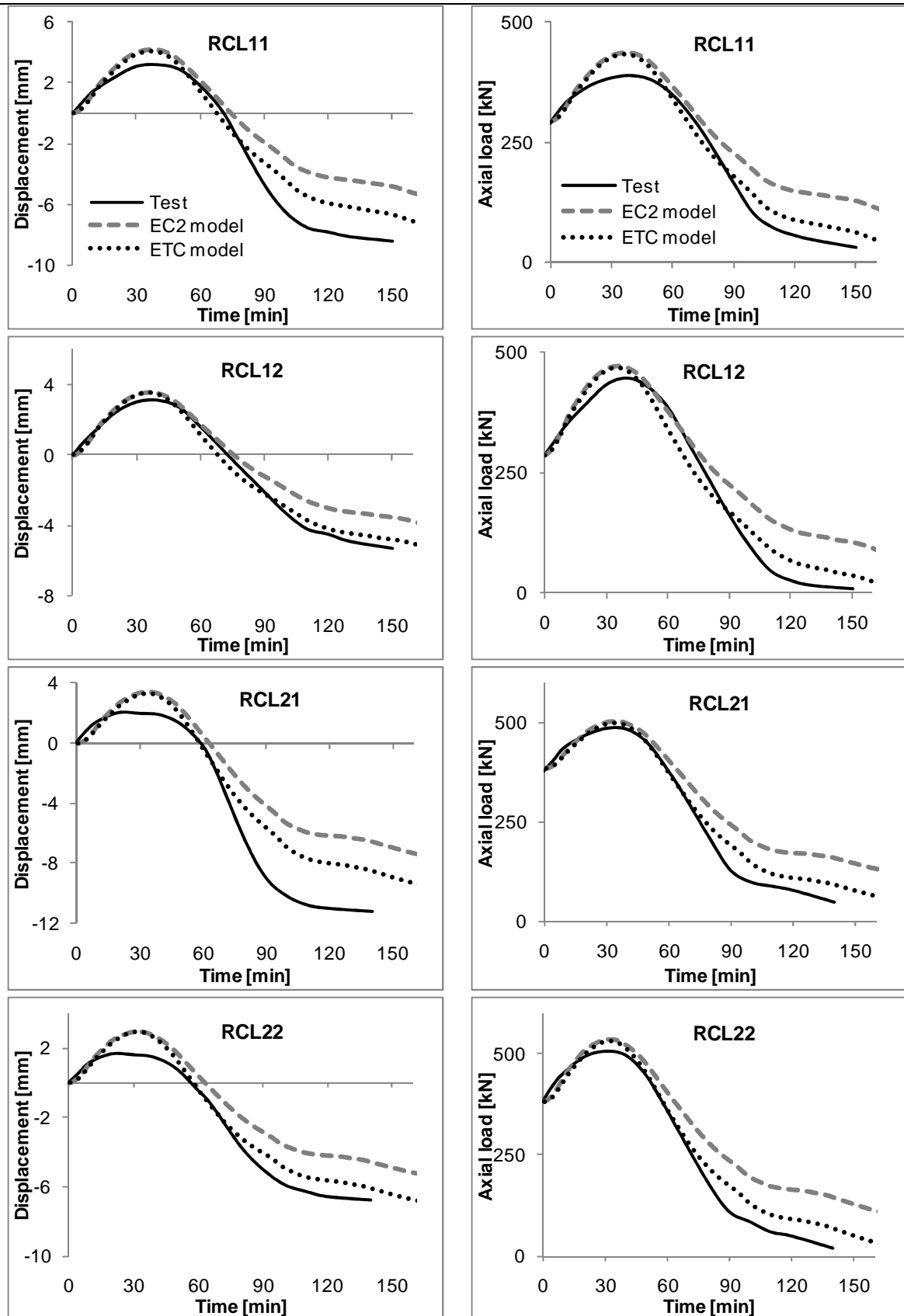
Fig. III.3-10: Comparison between measured and computed results – L-shape

The ETC model and the EC2 model lead to comparable results during the expanding phase of the column. Then during the contracting phase, the behavior predicted by the ETC model tends to differ from the behavior predicted by the EC2 model; the effect of the explicit consideration of transient creep on the structural behavior becomes notable. In these experiments, the contracting phase (decrease in displacement) is associated with unloading of the column (decrease in axial load) because of the axial restraint. It has been shown previously at the material level that the ETC model is better than the EC2 model to capture the concrete behavior under stress (or load) decrease, see Fig. III.3-2 and Fig. III.3-3. This is confirmed at the structural level by the experiments of Fig. III.3-9 and Fig. III.3-10, as it can be seen that the ETC model matches better than the EC2 model the actual behavior of the structure for all eight experiments.

In the last part of the experiments, the fire is stopped and the temperatures are thus decreasing in the compartment. During this cooling phase, the vertical displacement at the top of the column decreases (shortening) because part of the thermal elongation is recovered due to the cooling of the column and because the concrete does not recover its mechanical properties. As a consequence, the axial load continues to decrease during the cooling phase. Because of the combination of two effects, the load decrease and the temperature decrease, the difference between the behaviors predicted by the ETC and the EC2 models is particularly significant during this cooling phase. In the EC2 model, the transient creep strain that is implicitly considered is recovered during unloading and cooling, whereas the ETC model allows for a better modeling of the column behavior in unloading and cooling situations owing to the explicit term for transient creep strain.

III.3.3.2. *Practical significance of the results*

It is interesting to give a further insight into the practical significance of the results presented here. It has been shown that the effect of the transient creep strain model on the global behavior of the columns is significant as the estimation of the residual axial load sustained by the columns at the end of the fire can differ by up to 25% of the initial applied load depending on the transient creep strain model that is used for the calculation. In the following, it is explained how the results given by the Eurocode model are unconservative, due to the overestimation of the residual axial load that are sustained by the columns.

In a prescriptive approach, the columns are checked for fire resistance when subjected to standard fire (such as the ISO fire), in which only the heating phase is considered. However in a performance-based approach, it can be very important to model the cooling phase of the fire too as explained in Section I.3.1.

Similarly in a prescriptive approach, the structural member should be given a failure criterion beyond which it is considered that the collapse has been reached. In such approach, one cannot accept the levels of load decrease obtained in the simulations plotted in Fig. III.3-9 and Fig. III.3-10, in which load decrease of up to 90% are observed, because the failure criterion would have been reached much before. Yet in a performance-based approach, the structural fire engineers do not consider the structural members as isolated of the rest of the structure but aim to model the actual behavior of the entire structure. Indeed, if the structure is properly design, it may have a certain robustness that allows for a redistribution of the forces

during the fire. In a robust structure, the fact that one of the structural elements is not able to sustain the applied load any more does not automatically imply the collapse of the entire structure.

In the experiment presented here, the column is axially restrained and it is considered that the applied vertical load can shift to the members that provide axial restraint after the column displacement goes back to the initial equilibrium state and the column experiences shortening. In a real building, this would correspond to a situation where the structure is able to redistribute the load initially supported by the column to the other columns through horizontal elements. For instance, let us consider the hypothetical structure of Fig. III.3-11 and let us assume that a localized fire is attacking the central column. If the structure is sufficiently robust, the load that was supported by the central column can be redistributed to the other columns through the beam. In this case, the collapse of the central column, that can be considered as the time when the column is not able to support the initial applied load any more, does not automatically imply the collapse of the entire structure. The discussion would be the same for instance if the fire had developed in the entire compartment but that the central column, that had less strength in reserve, had reached collapse before the other columns.

It is clear that if the evolution of the axial load in the central column is not properly evaluated, the additional load redistributed to the rest of the structure could be underestimated or overestimated. Finally, this could lead to a wrong estimation of the global fire resistance of the structure. The constitutive model that is used for the concrete material, and especially the type of transient creep strain model, could thus have an implication on the estimation of the global fire resistance of a structure. It has been shown, based on the experiments presented in Fig. III.3-9 and Fig. III.3-10, that the numerical results obtained using the EC2 model systematically underestimate the decrease in the axial load for axially restrained columns subjected to natural fire. Therefore, the results given by the EC2 model are unconservative as they lead to the underestimation of the additional load redistributed to the structure, which obviously has an impact on the fire resistance of the structure.
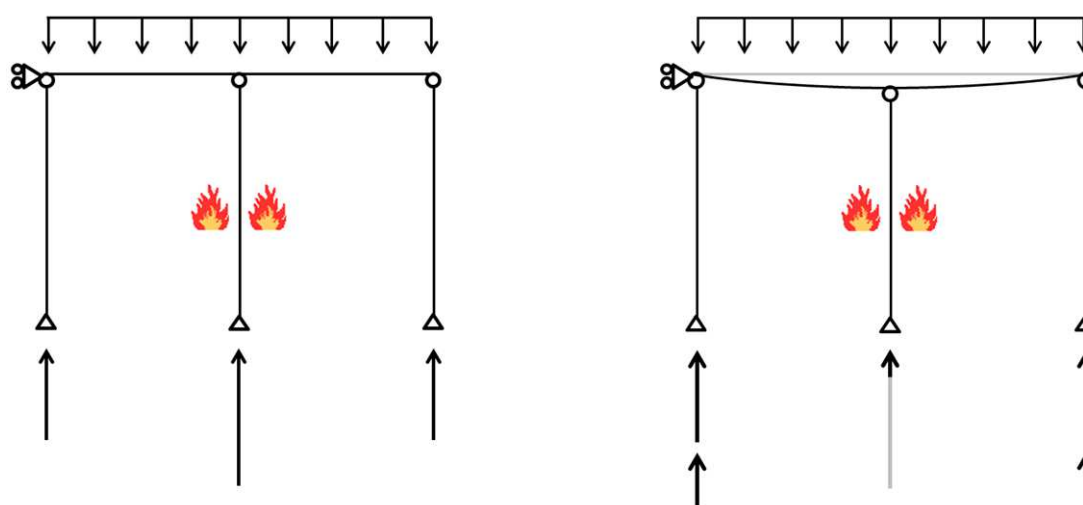
Fig. III.3-11: Redistribution of forces in a robust structure subjected to localized fire. Left: at the beginning of the fire; Right: at the end of the fire.

Simplified models such as Eurocode 2 are well adapted for prescriptive approaches in which isolated structural members are considered, i.e. for analyzing the behavior of statically determinate structural members subjected to the heating phase of a fire. However, the fire engineer should be careful when using such simplified constitutive models in analyses including statically indeterminate structural members or including the cooling phase of a fire, as these simplified models have not been validated for these applications. When it comes to performance-based design, more accurate models should be used, and notably the transient creep strain should be properly modeled with an explicit term.

III.4. Conclusion

This chapter has presented a new model for the mechanical behavior of concrete at high temperature and under uniaxial stress state. This new concrete model is a generic model with an explicit term for transient creep strain. It requires no additional material parameter compared with the current implicit model of Eurocode 2 and it yields the same results as the Eurocode 2 model in the situation where the temperature is increasing under constant applied stress. This calibration on the current Eurocode 2 model is an important aspect of the new model as the Eurocode 2 model has been widely used in the last decade and is well accepted by authorities and regulators for real building design. However, the current Eurocode 2 model includes implicitly the transient creep strain and this has been shown to lead to several limitations for capturing the concrete behavior in situations characteristic of a performance-based design. Owing to its explicit consideration of transient creep strain, the new concrete model succeeds in capturing the concrete behavior in these complex situations. Namely, the new model is able to capture the dependency in the stress-temperature path and the unloading stiffness at high temperature. The new concrete model can thus be seen as an explicit formulation of the Eurocode 2 model, developed for extending the domain of applicability of the Eurocode model from prescriptive design to performance-based design.

The next chapter deals with the development of a concrete model for multiaxial stress state; the uniaxial transient creep strain model presented in this chapter will be extended to multiaxial stress state for incorporation in the multiaxial model.

CHAPTER IV - DEVELOPMENT OF A MULTIAXIAL CONSTITUTIVE MODEL FOR CONCRETE AT ELEVATED TEMPERATURE

This chapter presents a new constitutive model for the mechanical behavior of concrete at high temperature under multiaxial stress state. This model is based on the assumptions adopted as a result of the literature review analysis presented in Chapter II. Namely, the model is developed within the theoretical framework of continuum constitutive models based on smeared crack approach and it relies on a coupled plastic-damage theory. The plastic-damage constitutive model that is derived is a full three dimensional model; it can be used for any multiaxial stress state. At high temperature, the multiaxial model includes the generalization of the uniaxial transient creep model presented in the previous chapter.

The development of the model is described in the first part of the chapter, considering ambient temperature. Then, the extension of the model to take into account high temperatures is presented, with special emphasis on the multiaxial transient creep strain model and the evolution of the material properties with temperature. Finally, the last part of this chapter gives an insight into the numerical implementation of the model in a finite elements software. The validation of the model and its application to practical examples are presented in the next chapter.

IV.1. Plastic-damage model

IV.1.1. Constitutive law

Following the strain decomposition principle, the total strain is assumed to be made of individual strain components according to Eq. IV.1-1. In this equation, $\underline{\underline{\varepsilon}}_{tot}$ is the total strain tensor, $\underline{\underline{\varepsilon}}_{th}$ the free thermal strain tensor, $\underline{\underline{\varepsilon}}_{\sigma}$ the instantaneous stress-related strain tensor and $\underline{\underline{\varepsilon}}_{tr}$ the transient creep strain tensor.

$$\underline{\underline{\varepsilon}}_{tot} = \underline{\underline{\varepsilon}}_{th} + \underline{\underline{\varepsilon}}_{\sigma} + \underline{\underline{\varepsilon}}_{tr} \qquad \text{Eq. IV.1-1}$$

In the concrete constitutive model developed here, the free thermal strain and the transient creep strain are thus treated separately from the instantaneous stress-related strain. The constitutive model that expresses the relationship between the instantaneous stress-related strain and the stress is presented first. The generalization of the transient creep strain and free thermal strain models to multiaxial stress states will be described in Section IV.2.

It has been shown in the previous chapters that permanent strains develop in concrete subjected to stress upon a certain stress level; the instantaneous stress-related strain is thus divided into an elastic part and a plastic part according to Eq. IV.1-2. In this equation, $\underline{\underline{\varepsilon}}_{el}$ is the elastic strain tensor and $\underline{\underline{\varepsilon}}_{p}$ is the plastic strain tensor.

$$\underline{\underline{\varepsilon}}_{\sigma} = \underline{\underline{\varepsilon}}_{el} + \underline{\underline{\varepsilon}}_{p} \qquad \text{Eq. IV.1-2}$$

Another important property of concrete that has to be reproduced by the model is the degradation of the elastic properties of the material when it is subjected to stress upon a certain stress level. Therefore, isotropic damage is introduced in the model using a fourth-order isotropic damage tensor $\underline{\underline{D}}$. Accordingly with the assumptions retained at the end of Chapter II, the instantaneous stress-related strain tensor $\underline{\underline{\varepsilon}}_{\sigma}$ is related to the stress tensor $\underline{\underline{\sigma}}$ by means of the constitutive relationship of Eq. IV.1-3. In this equation, $\underline{\underline{I}}$ is the fourth-order identity tensor and $\underline{\underline{C}}_{0}$ is the fourth-order isotropic linear-elastic stiffness tensor.

$$\underline{\underline{\sigma}} = \left(\underline{\underline{I}} - \underline{\underline{D}} \right) : \underline{\underline{C}}_{0} : \left(\underline{\underline{\varepsilon}}_{\sigma} - \underline{\underline{\varepsilon}}_{p} \right) \qquad \text{Eq. IV.1-3}$$

The stress tensor that appears in Eq. IV.1-3 is the nominal (i.e. apparent) stress tensor; the nominal stress is meant as the macro-level stress and is defined as force divided by the total area. However, it has been assumed that the characterization of plastic response of concrete can be formulated in the effective stress space with no reference to any damage. Defining the effective stress tensor $\underline{\underline{\bar{\sigma}}}$ as the tensor of the average micro-level stress applied

to the undamaged volume of the material and considering that the plastic behavior occurs in the undamaged material, the constitutive relationship in the effective stress space can be written following the classical elastoplastic behavior, see Eq. IV.1-4.

$$\bar{\underline{\underline{\sigma}}} = \underline{\underline{\underline{C}}}_0 : \left(\underline{\underline{\varepsilon}}_\sigma - \underline{\underline{\varepsilon}}_p \right)$$

Eq. IV.1-4

Computation of the plastic response using Eq. IV.1-4 can be performed following the standard approach for elastoplasticity in the effective stress space; this computation yields the effective stress tensor and plastic internal variables. Then, the fourth-order damage tensor is used to map the effective stress tensor $\bar{\underline{\underline{\sigma}}}$ into the nominal stress tensor $\underline{\underline{\sigma}}$ according to Eq. IV.1-5.

$$\underline{\underline{\sigma}} = \left(\underline{\underline{\underline{I}}} - \underline{\underline{\underline{D}}} \right) : \bar{\underline{\underline{\sigma}}}$$

Eq. IV.1-5

The fourth-order damage tensor allows for a proper description of the isotropic state of damage in concrete. The use of such tensor is required for modeling the stiffness recovery in concrete when the situation changes from tension to compression. As the damage mechanisms that develop in concrete are different in tension and in compression, a damage scalar internal variable d_t is considered for modelling of tensile damage and a damage scalar internal variable d_c is considered for modeling of compressive damage. The damage tensor is calculated from these two damage scalars using Eq. IV.1-6, which is based on the research works by Wu, et al. (2006).

$$\underline{\underline{\underline{D}}} = d_t \, \underline{\underline{\underline{P}}}^+ + d_c \, \underline{\underline{\underline{P}}}^-$$

Eq. IV.1-6

In this latter equation, $\underline{\underline{\underline{P}}}^+$ and $\underline{\underline{\underline{P}}}^-$ are the fourth-order projection tensors calculated according to Eq. IV.1-7:

$$\underline{\underline{\underline{P}}}^+ = \sum_i H\left(\bar{\sigma}_i \right) \left(\underline{\underline{p}}_{ii} \otimes \underline{\underline{p}}_{ii} \right), \quad \underline{\underline{\underline{P}}}^- = \underline{\underline{\underline{I}}} - \underline{\underline{\underline{P}}}^+$$

Eq. IV.1-7

where $H\left(\bar{\sigma}_i \right)$ is the Heaviside function computed for the ith eigenvalue $\bar{\sigma}_i$ of $\bar{\underline{\underline{\sigma}}}$, see Eq. IV.1-8, and the second-order tensor $\underline{\underline{p}}_{ii}$ is defined by Eq. IV.1-9, with $\underline{n}_i$ the ith normalized eigenvector corresponding to $\bar{\sigma}_i$.

$$H\left(\bar{\sigma}_i \right) = \begin{cases} 0 & if \ \bar{\sigma}_i < 0 \\ 1 & if \ \bar{\sigma}_i \geq 0 \end{cases}$$

Eq. IV.1-8

$$\underline{\underline{p}}_{ij} = \underline{\underline{p}}_{ji} = \frac{1}{2} \left(\underline{n}_i \otimes \underline{n}_j + \underline{n}_j \otimes \underline{n}_i \right)$$

Eq. IV.1-9

The fourth-order projection tensors are built to allow for a decomposition of the effective stress tensor $\overline{\underline{\sigma}}$ into positive and negative components according to Eq. IV.1-10.

$$\overline{\underline{\sigma}}^{+} = \underline{\underline{P}}^{+} : \overline{\underline{\sigma}} \ , \qquad \overline{\underline{\sigma}}^{-} = \overline{\underline{\sigma}} - \overline{\underline{\sigma}}^{+} = \underline{\underline{P}}^{-} : \overline{\underline{\sigma}}$$
<div align="right">Eq. IV.1-10</div>

Consequently, the tensile damage scalar d_t only affects the positive part of the effective stress tensor whereas the compressive damage scalar d_c only affects the negative part of the effective stress tensor, see Eq. IV.1-11. When the stress state in the material changes from tension to compression, the effect of the tensile damage scalar d_t on the macroscopic behavior disappear, which corresponds physically to the closure of the tensile cracks. This representation of the state of damage allows for capturing properly the unilateral effect in concrete, as can be seen in Fig. IV.1-1; in this figure, the model response to a unilateral test is compared with experimental data given by Ramtani (1990).

$$\underline{\sigma} = \left(1 - d_t\right) \overline{\underline{\sigma}}^{+} + \left(1 - d_c\right) \overline{\underline{\sigma}}^{-}$$
<div align="right">Eq. IV.1-11</div>

In the following, the equations of the model are detailed. First, the equations are given for defining the plastic response in the effective stress space; then, the evolution laws of damage variables are defined.
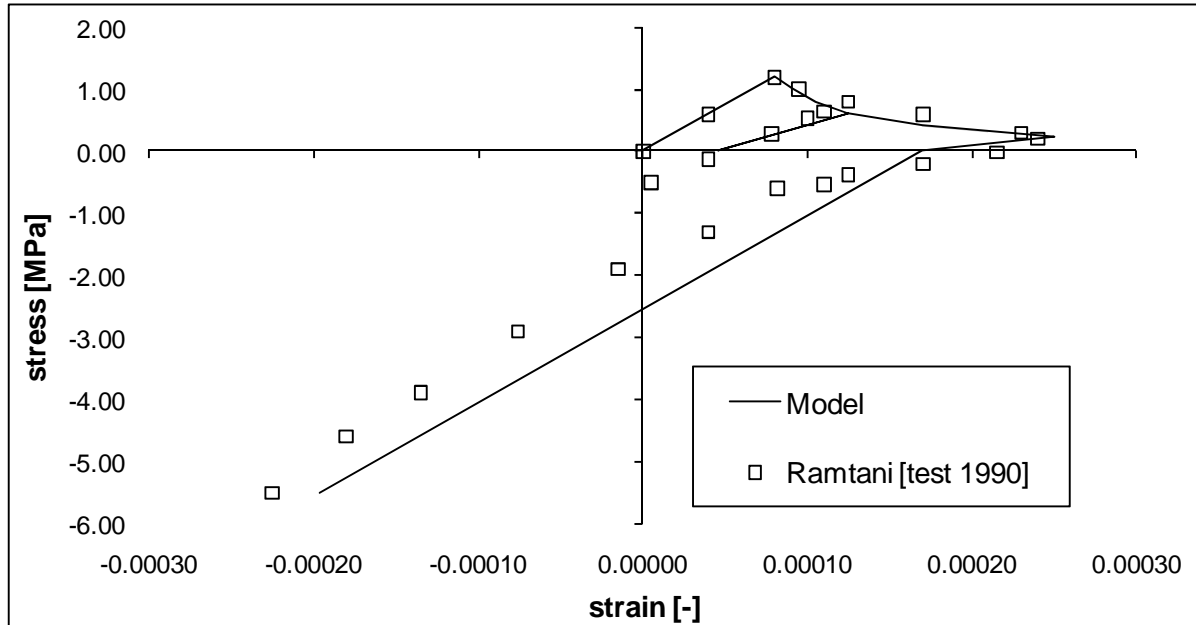
Fig. IV.1-1: Unilateral effect in concrete

IV.1.2. Plastic theory

The equations defining the plastic response are established in the effective stress space, i.e. in terms of effective quantities.

IV.1.2.1. *Multi-surface yield criterion*

As was established at the end of Chapter II, the yield criterion that is adopted consists in a multi-surface yield criterion based on a Rankine (principal stress) yield function to limit the tensile stresses and a Drucker-Prager yield contour for compression. This assumption relies on the experimental observation that, in concrete, different failure mechanisms develop in tension and in compression.

The Rankine yield function F_t is given by Eq. IV.1-12, where $\bar{\sigma}_I$ is the maximum principal effective stress and $\bar{\tau}_t$ is the tensile hardening function depending on the tensile hardening parameter κ_t. Hardening in tension is assumed to be driven only by the tensile hardening parameter κ_t; therefore the dependency of the Rankine yield function F_t in the internal variables $\underline{\underline{q}}$ simply comes down to a dependency in a single scalar variable that characterize the evolution of plasticity in tension.

$$F_t\left(\underline{\underline{\bar{\sigma}}},\underline{\underline{q}}\right) = \bar{\sigma}_I - \bar{\tau}_t\left(\kappa_t\right) \qquad \text{Eq. IV.1-12}$$

The Drucker-Prager yield function F_c is given by Eq. IV.1-13:

$$F_c\left(\underline{\underline{\bar{\sigma}}},\underline{\underline{q}}\right) = \sqrt{3\bar{J}_2} + \alpha\,\bar{I}_1 - (1-\alpha)\,\bar{\tau}_c\left(\kappa_c\right) \qquad \text{Eq. IV.1-13}$$

In this latter equation, $\bar{I}_1$ is the trace (first invariant) of the effective stress tensor, $\bar{J}_2$ is the second invariant of the deviatoric effective stress tensor, $\bar{\tau}_c$ is the compressive hardening function depending on the compressive hardening parameter κ_c and α is a material parameter (coefficient of internal friction) defined by Eq. IV.1-14. In Eq. IV.1-14, f_c and f_b respectively represent the uniaxial and biaxial compressive strength of the material.

$$\alpha = \frac{f_b - f_c}{2f_b - f_c} \qquad \text{Eq. IV.1-14}$$

The invariants $\bar{I}_1$ and $\bar{J}_2$ are given by Eq. IV.1-15.

$$\begin{aligned} \bar{I}_1 &= \bar{\sigma}_{11} + \bar{\sigma}_{22} + \bar{\sigma}_{33} \\ \bar{J}_2 &= \frac{1}{6}\left[\left(\bar{\sigma}_{11} - \bar{\sigma}_{22}\right)^2 + \left(\bar{\sigma}_{22} - \bar{\sigma}_{33}\right)^2 + \left(\bar{\sigma}_{33} - \bar{\sigma}_{11}\right)^2 + 6\left(\bar{\sigma}_{12}^2 + \bar{\sigma}_{13}^2 + \bar{\sigma}_{23}^2\right)\right] \end{aligned} \qquad \text{Eq. IV.1-15}$$

Similarly to the tensile case, hardening of the Drucker-Prager yield surface in compression is assumed to be driven only by the compressive hardening parameter κ_c.

The multi-surface yield criterion is then given by Eq. IV.1-16:

$$\begin{cases} F_t\left(\underline{\overline{\sigma}}, \kappa_t\right) \leq 0 \\ F_c\left(\underline{\overline{\sigma}}, \kappa_c\right) \leq 0 \end{cases}$$

Eq. IV.1-16

The multi-surface yield criterion that results from the combination of Rankine yield function and Drucker-Prager yield function is plotted in the two-dimensional stress space, i.e. assuming that $\sigma_{III} = 0$, in Fig. IV.1-2. The limit yield function is obtained for the maximum values of the hardening functions $\overline{\tau}_t$ and $\overline{\tau}_c$; this limit yield function agrees with experimental data of the biaxial failure envelope given by Kupfer and Gerstle (1973) and presented in Chapter I. The yield function experiences isotropic hardening/softening driven by the hardening functions $\overline{\tau}_t$ and $\overline{\tau}_c$; the value of the yield function for a current value of these hardening functions is also plotted in Fig. IV.1-2.
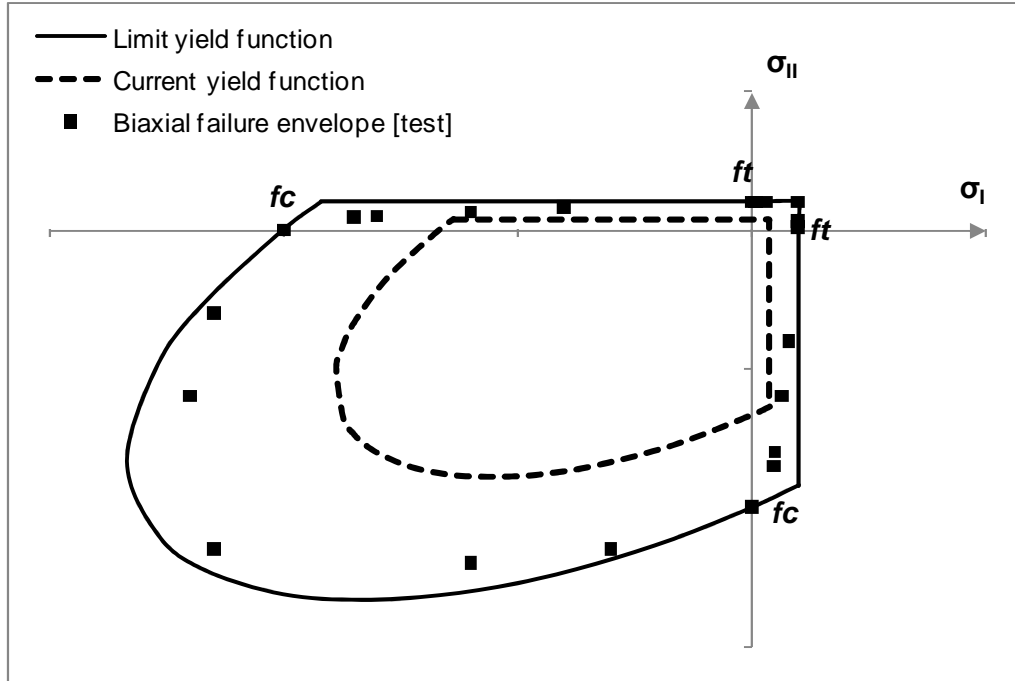
Fig. IV.1-2: Multi-surface yield criterion plotted in the two-dimensional principal stress space (assuming $\sigma_{III} = 0$)

IV.1.2.2. *Plastic flow rules*

The yield conditions, in general written as $F_t\left(\underline{\overline{\sigma}}, \kappa_t\right) = 0$ and/or $F_c\left(\underline{\overline{\sigma}}, \kappa_c\right) = 0$, define the stress states for which the material exhibits plastic flow. Plastic flow rules have to be postulated to govern the evolution of plastic flow when the effective stress state reaches the yield surfaces.

In tension, an associated flow rule is used, which means that the plastic flow is normal to the yield surface in the effective stress space, see Eq. IV.1-17. Therefore, the plastic potential in tension G_t is equal to the plastic yield function. In this equation, $\underline{\dot{\varepsilon}}_p^t$ denotes the

tensile plastic strain rate tensor whereas the parameter $\dot{\lambda}_t$ is called plastic multiplier in tension and defines the length of the tensile plastic flow.

$$\underline{\dot{\underline{\varepsilon}}}_p^t = \dot{\lambda}_t \frac{\partial G_t}{\partial \overline{\underline{\sigma}}} = \dot{\lambda}_t \frac{\partial F_t}{\partial \overline{\underline{\sigma}}} \qquad \text{Eq. IV.1-17}$$

In compression, a non-associated flow rule is adopted to capture the dilatancy phenomenon that develops in concrete. Indeed, concrete is a frictional material in which plastic deformation in compression is accompanied by volumetric variation. As a result, the plastic flow is not normal to the yield surface in the effective stress space; it is given by Eq. IV.1-18. In this equation, $\dot{\lambda}_c$ is the plastic multiplier in compression and G_c is the plastic potential in compression.

$$\underline{\dot{\underline{\varepsilon}}}_p^c = \dot{\lambda}_c \frac{\partial G_c}{\partial \overline{\underline{\sigma}}} \qquad \text{Eq. IV.1-18}$$

The plastic potential G_c is given by Eq. IV.1-19, where α_g is a dilatancy parameter. The physical interpretation of Eq. IV.1-19 is that the compressive flow is associated in the deviatoric plane but its volumetric part uses a dilatancy coefficient α_g different from the coefficient of internal friction α (Feenstra and de Borst, 1996).

$$G_c = \sqrt{3\overline{J}_2} + \alpha_g \, \overline{I}_1 \qquad \text{Eq. IV.1-19}$$

According to Koiter's rule (1953), the total plastic strain rate tensor can be obtained as the sum of the tensile and the compressive plastic strain rate tensors, according to Eq. IV.1-20.

$$\underline{\dot{\underline{\varepsilon}}}_p = \dot{\lambda}_t \frac{\partial F_t}{\partial \overline{\underline{\sigma}}} + \dot{\lambda}_c \frac{\partial G_c}{\partial \overline{\underline{\sigma}}} \qquad \text{Eq. IV.1-20}$$

The plastic multipliers $\dot{\lambda}_t$ and $\dot{\lambda}_c$ can be determined using the Kuhn-Tucker conditions expressed by Eq. IV.1-21.

$$\dot{\lambda}_j \geq 0 , \quad F_j\left(\overline{\underline{\sigma}}, \kappa_j\right) \leq 0 , \quad \dot{\lambda}_j \, F_j\left(\overline{\underline{\sigma}}, \kappa_j\right) = 0 \quad \big| \quad j = t, c \qquad \text{Eq. IV.1-21}$$

In addition, $\dot{\lambda}_t$ and $\dot{\lambda}_c$ also satisfy with the consistency requirement of Eq. IV.1-22.

$$\dot{\lambda}_j \, \dot{F}_j\left(\overline{\underline{\sigma}}, \kappa_j\right) = 0 \quad \big| \quad j = t, c \qquad \text{Eq. IV.1-22}$$

IV.1.2.3. *Hardening variables*

The hardening variables κ_t and κ_c respectively govern the evolution of the Rankine and the Drucker-Prager yield surfaces; this evolution is made by isotropic hardening/softening. In fact, the hardening variables are the plastic internal variables that characterize the plastic state of the material; they can be considered as indicators of the degree

---

of yielding in the material and therefore are called accumulated plastic strains. These hardening variables can be related to the plastic multipliers. In their composite plasticity model, Feenstra and de Borst (1996) have suggested to use the rate equations of Eq. IV.1-23 to assess the evolution of the hardening variables. These relationships are based on a work-hardening hypothesis, which means that the hardening variables are determined by the inelastic work rate for the corresponding yield functions. In Eq. IV.1-23, ς_{12} and ς_{21} are constant parameters describing the coupling between the tensile and the compressive yielding mechanisms.

$$\begin{aligned} \dot{\kappa}_t &= \dot{\lambda}_t + \varsigma_{12}\, \dot{\lambda}_c \\ \dot{\kappa}_c &= \varsigma_{21}\, \dot{\lambda}_t + \dot{\lambda}_c \end{aligned}$$

Eq. IV.1-23

Due to a lack of experimental data, it is generally assumed that the yielding mechanisms in tension and in compression are decoupled, thus setting $\varsigma_{12} = \varsigma_{21} = 0$ in the applications (Feenstra and de Borst, 1996). In other words, if only one yielding mechanism is active, the other yield surface does not evolve. The hardening variables are thus given by Eq. IV.1-24.

$$\dot{\kappa}_t = \dot{\lambda}_t \geq 0, \quad \dot{\kappa}_c = \dot{\lambda}_c \geq 0$$

Eq. IV.1-24

Application of the work-hardening hypothesis ($\dot{W}^p = \overline{\overline{\sigma}} : \underline{\dot{\varepsilon}}_p$) with the assumption of decoupling between the tensile and the compressive yielding mechanisms leads to Eq. IV.1-25 for yielding in tension. In this equation, $\underline{n}_I$ is the normalized eigenvector corresponding to $\overline{\sigma}_I$. As a result, the hardening variable κ_t can be defined by Eq. IV.1-26. The interpretation of Eq. IV.1-26 is that this hardening variable can be seen as the effective plastic strain in the sense of work-hardening hypothesis (Jirasek and Bazant, 2002).

$$\dot{W}^p = \overline{\overline{\sigma}} : \underline{\dot{\varepsilon}}_p^t = \dot{\lambda}_t\, \overline{\overline{\sigma}} : \frac{\partial F_t}{\partial \overline{\overline{\sigma}}} = \dot{\lambda}_t\, \overline{\overline{\sigma}} : \left(\underline{n}_I \otimes \underline{n}_I \right) = \dot{\lambda}_t\, \overline{\sigma}_I = \dot{\lambda}_t\, \overline{\tau}_t$$

Eq. IV.1-25

$$\dot{\kappa}_t = \frac{\overline{\overline{\sigma}} : \underline{\dot{\varepsilon}}_p^t}{\overline{\tau}_t}$$

Eq. IV.1-26

Similar developments in compression lead to Eq. IV.1-27 and Eq. IV.1-28 (Jirasek and Bazant, 2002). As in tension, the hardening variable in compression given by Eq. IV.1-28 can be interpreted as the effective plastic strain according to the work-hardening hypothesis, although the formula in compression is adapted for non associated flow.

$$\dot{W}^p = \overline{\overline{\sigma}} : \underline{\dot{\varepsilon}}_p^c = \dot{\lambda}_c\, \overline{\overline{\sigma}} : \frac{\partial G_c}{\partial \overline{\overline{\sigma}}} = \dot{\lambda}_t\, G_c$$

Eq. IV.1-27

$$\dot{\kappa}_c = \frac{\overline{\overline{\sigma}} : \underline{\dot{\varepsilon}}_p^c}{G_c}$$

Eq. IV.1-28

The rate equations of the hardening variables can be expressed in the uniaxial case to give a more direct interpretation of these variables. Under uniaxial tension in direction x, the Rankine yield function is given by $F_t = \bar{\sigma}_x - \bar{\tau}_t(\kappa_t)$, with $\bar{\sigma}_x$ the effective applied stress. We have $\bar{\sigma}_x = \bar{\tau}_t(\kappa_t)$ during the yielding process under uniaxial tension and the tensile hardening function $\bar{\tau}_t$ has thus the meaning of current uniaxial tensile yield stress in the effective stress space. The rate equation Eq. IV.1-26 for calculation of the tensile hardening parameter turns into Eq. IV.1-29. In the uniaxial case, the tensile hardening parameter is thus equal to the plastic strain in the direction of applied stress. As a result, it is possible to identify the hardening law in tension from the stress-strain curve in uniaxial tension.

$$\dot{\kappa}_t = \frac{\bar{\underline{\underline{\sigma}}} : \dot{\underline{\underline{\varepsilon}}}_p^t}{\bar{\tau}_t} = \frac{\bar{\sigma}_x \, \dot{\varepsilon}_{p,x}^t}{\bar{\tau}_t} = \dot{\varepsilon}_{p,x}^t \qquad \text{Eq. IV.1-29}$$

Under uniaxial compression in direction x, the Drucker-Prager yield function is given by Eq. IV.1-30. As a result, we have $|\bar{\sigma}_x| = \bar{\tau}_c(\kappa_c)$ during the yielding process, with $\bar{\sigma}_x < 0$ the effective stress in uniaxial compression. Therefore the compressive hardening function $\bar{\tau}_c$ stands for the current uniaxial compressive yield stress in the effective stress space.

$$F_c\left(\bar{\underline{\underline{\sigma}}}, \underline{\underline{q}}\right) = \sqrt{3\bar{J}_2} + \alpha \bar{I}_1 - (1-\alpha)\,\bar{\tau}_c(\kappa_c) = |\bar{\sigma}_x| - \alpha|\bar{\sigma}_x| - (1-\alpha)\,\bar{\tau}_c(\kappa_c) \qquad \text{Eq. IV.1-30}$$

Under uniaxial compression in direction x, the plastic potential G_c is given by $G_c = (1-\alpha_g)|\bar{\sigma}_x|$. As a result, the rate equation Eq. IV.1-28 for calculation of the compressive hardening parameter turns into Eq. IV.1-31. In the uniaxial case, the compressive hardening parameter is thus proportional to the plastic strain in the direction of applied stress. As a result, it is possible to identify the hardening law in compression from the stress-strain curve in uniaxial compression.

$$\dot{\kappa}_c = \frac{\bar{\underline{\underline{\sigma}}} : \dot{\underline{\underline{\varepsilon}}}_p^c}{G_c} = \frac{-|\bar{\sigma}_x| \, \dot{\varepsilon}_p^c}{(1-\alpha_g)|\bar{\sigma}_x|} = \frac{\dot{\varepsilon}_{p,x}^c}{\alpha_g - 1} \qquad \text{Eq. IV.1-31}$$

IV.1.2.4. Hardening laws

It remains to determine the hardening laws in the effective stress space for calculation of $\bar{\tau}_t$ and $\bar{\tau}_c$ as a function of the hardening variables. It has been shown that the hardening functions $\bar{\tau}_t$ and $\bar{\tau}_c$ have the meaning of current uniaxial tensile and compressive strength of the material. However, these functions are written in the effective stress space and therefore they cannot be determined by direct identification with the experimental uniaxial stress-strain curves, which are in the nominal (apparent) stress space. Based on Eq. IV.1-11, the relationship between the effective and the nominal hardening functions in uniaxial tension is obtained according to Eq. IV.1-32. In this equation, τ_t is the tensile hardening function in the nominal stress space; therefore this function can be directly identified to the current uniaxial

tensile strength of the material. Similarly, in uniaxial compression the relationship is given by Eq. IV.1-33.

$$\tau_t(\kappa_t) = (1 - d_t)\bar{\tau}_t(\kappa_t) \qquad\qquad \text{Eq. IV.1-32}$$

$$\tau_c(\kappa_c) = (1 - d_c)\bar{\tau}_c(\kappa_c) \qquad\qquad \text{Eq. IV.1-33}$$

In uniaxial tension, the response in nominal (i.e. apparent) stress is elastic until peak stress, followed by a material softening until failure. It is assumed here that the tensile behavior of concrete is driven by the damage mechanism. In other words, it is assumed that the softening response of the material in tension is due to the development of microcracks that progressively reduce the volume of the undamaged material. Although plastic strains develop in tension, it is assumed that they do not lead to softening of the material. Consequently, the tensile hardening law in the effective stress space presents a horizontal plateau, see Eq. IV.1-34, and the apparent softening that is observed experimentally in concrete is only driven by the evolution of the tensile damage parameter d_t. In Eq. IV.1-34, the parameter f_t is the uniaxial tensile strength (i.e. peak stress). In fact, the meaning of Eq. IV.1-34 is that there is no variation of the Rankine yield surface in the effective stress space. This definition of the effective and the nominal tensile hardening laws leads to the uniaxial tensile responses in the nominal and in the effective stress space plotted in Fig. IV.1-3.

$$\bar{\tau}_t(\kappa_t) = f_t \qquad\qquad \text{Eq. IV.1-34}$$
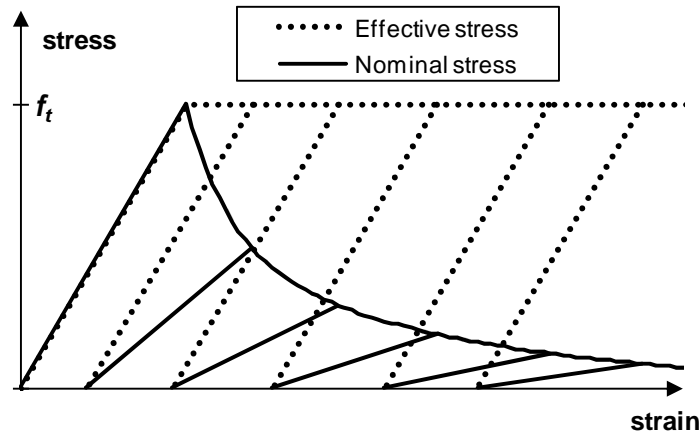
Fig. IV.1-3: Uniaxial tensile response in the effective and nominal stress spaces

In uniaxial compression, the concrete behavior presents first an elastic domain until the compressive limit of elasticity f_{c0}, followed by a hardening branch until the stress reaches the compressive strength f_c and finally a softening branch until failure. The hardening law in nominal stress should reflect this behavior. To be consistent with the developments presented in the previous chapter for concrete under uniaxial stress state, the compressive hardening law in the nominal stress space is expressed following the same formulation as the ascending branch of the instantaneous stress-strain relationship of the Explicit Transient Creep (ETC) Eurocode model, see Eq. IV.1-35. The compressive hardening law of Eq. IV.1-35 adequately

captures the experimental response of concrete in uniaxial compression. In this equation, κ_{c1} is the accumulated plastic strain in compression at peak stress, such that $\tau_c(\kappa_{c1}) = f_c$.

$$\tau_c(\kappa_c) = f_{c0} + \frac{2(f_c - f_{c0})\kappa_c}{\kappa_{c1}\left(1 + \left(\dfrac{\kappa_c}{\kappa_{c1}}\right)^2\right)} \qquad if \ \kappa_c \leq \kappa_{c1} \qquad \qquad \text{Eq. IV.1-35}$$

The apparent softening law is calibrated on experimental data. The mathematical expression is derived in order to ensure continuous differentiability between the hardening and softening branches at peak stress. Finally, the relationship in apparent stress for the softening branch is given by Eq. IV.1-36, where b_c is a model parameter to be determined.

$$\tau_c(\kappa_c) = f_c\left(1 + b_c(\kappa_c - \kappa_{c1})\right)\exp\left(-b_c(\kappa_c - \kappa_{c1})\right) \qquad if \ \kappa_c \geq \kappa_{c1} \qquad \text{Eq. IV.1-36}$$

The expression of the compressive hardening function in the effective stress space $\bar{\tau}_c$ can be determined by inserting Eq. IV.1-35 and Eq. IV.1-36 into Eq. IV.1-33, once the expression of the compressive damage parameter d_c has been established. The expressions of the compressive hardening laws in the nominal ($\tau_c(\kappa_c)$) and in the effective ($\bar{\tau}_c(\kappa_c)$) stress space lead to the uniaxial compressive response in nominal and effective stress plotted in Fig. IV.1-4.
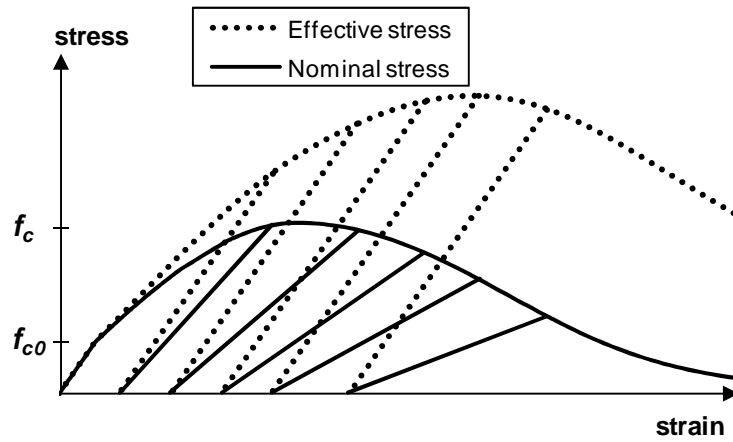
Fig. IV.1-4: Uniaxial compressive response in the effective and nominal stress spaces

IV.1.3. Damage theory

An important assumption concerns the selection of the internal variables that are used for driving the damage mechanism. In this model, it has been assumed that the evolution of damage in concrete is driven by the plastic internal variables. This assumption implies that the physical mechanisms that lead to the development of irreversible strains and to the degradation of the elastic properties are related, which can be controversial. Recent investigations by Poinard, et al. (2010), presented in Chapter I, have shown that the concrete behavior can change from a cohesive-brittle behavior governed by damage phenomena at low

confinement to that of a granular material governed by plasticity at high confinement; this observation tends to demonstrate that the damage and plastic mechanisms in concrete have different physical origins. Yet, the level of confinement reached in the experiment of Poinard, et al. (higher than 150 MPa) is beyond the scope of this research and, for stress levels typical of structural fire engineering applications, the concrete behavior can be captured by models in which plasticity and damage are driven by the same internal variables (Grassl and Jirasek, 2006; Nechnech, et al., 2002; Matallah and La Borderie, 2009). The use of same internal variables for driving plasticity and damage in concrete constitutive models is convenient because it reduces the number of parameters in the model.

The plastic internal variables that drive the yield flow and the hardening process are the accumulated plastic strains κ_t and κ_c; these plastic internal variables are also used to drive the evolution of damage as it is assumed that plasticity and damage phenomena are coupled. Accordingly, damage is initiated at the same time as permanent strains, and the process of material non-linearity in concrete consists in both damage and plasticity developing simultaneously. Evolution laws are postulated for the damage variables in order to describe the growth of microcracks in the material. Several authors have noted that the damage evolution as a function of the plastic strain is of an exponential form (Lee and Fenves, 1998; Matallah and La Borderie, 2009; de Sa and Benboudjema, 2011); therefore an exponential formulation is adopted here. The evolution laws for tensile and compressive damage are calibrated on the experimental uniaxial stress-strain curves in tension and compression using Eq. IV.1-37 and Eq. IV.1-38.

$$\tau_t\left(\kappa_t\right)=\left(1-d_t\left(\kappa_t\right)\right)\overline{\tau}_t\left(\kappa_t\right) \qquad \text{Eq. IV.1-37}$$

$$\tau_c\left(\kappa_c\right)=\left(1-d_c\left(\kappa_c\right)\right)\overline{\tau}_c\left(\kappa_c\right) \qquad \text{Eq. IV.1-38}$$

In tension, the evolution law for tensile damage is derived to yield the proper softening response of concrete in tension, see Fig. IV.1-3. The evolution law is thus given by a combination of exponentials according to Eq. IV.1-39; this combination of exponentials results from a numerical calibration on experimental data. In this equation, a_t is a non dimensional model parameter to be determined.

$$d_t\left(\kappa_t\right)=1-\left[\frac{1}{2}\exp\left(-a_t\ \kappa_t\right)+\frac{1}{2}\exp\left(-6\,a_t\ \kappa_t\right)\right] \qquad \text{Eq. IV.1-39}$$

In compression, the hardening law has directly been derived in nominal stress based on the apparent behavior of concrete in uniaxial compression, see Eq. IV.1-35 and Eq. IV.1-36. Therefore the evolution law for compressive damage is calibrated to yield the degradation of the elastic stiffness experimentally observed during uniaxial compression test with unloading-reloading, see Fig. IV.1-4. The evolution law for compressive damage is given by Eq. IV.1-40, with a_c a non dimensional model parameter to be determined.

$$d_c\left(\kappa_c\right)=1-\exp\left(-a_c\ \kappa_c\right) \qquad \text{Eq. IV.1-40}$$

IV.1.4.   Identification of the parameters

IV.1.4.1. *Model parameters*

The evolution laws of the model contain a series of non dimensional model parameters: a_c, b_c, a_t and κ_{c1}. In the following, these model parameters are formulated in terms of material parameters that can be identified by experimental tests.

Model parameter κ_{c1}

The parameter κ_{c1} is the accumulated plastic strain in compression at peak stress. Under uniaxial compression, the accumulated plastic strain κ_c is proportional to the plastic strain in the direction of applied stress, see Eq. IV.1-31. Writing this equation at peak stress leads to the expression of Eq. IV.1-41, with $\tilde{\varepsilon}_p^c < 0$ the plastic strain at peak stress under uniaxial compression.

$$\kappa_{c1} = \tilde{\varepsilon}_p^c \big/ \left(\alpha_g - 1 \right) \qquad\qquad \text{Eq. IV.1-41}$$

The parameter $\tilde{\varepsilon}_p^c$ can be expressed as a function of the (instantaneous stress-related) strain at peak stress under uniaxial compression ε_{c1}, which is a material parameter often given in absolute value ($\varepsilon_{c1} > 0$), and the elastic strain at peak stress under uniaxial compression $\tilde{\varepsilon}_{el} < 0$: $\tilde{\varepsilon}_p^c = -\left(\varepsilon_{c1} - \left| \tilde{\varepsilon}_{el} \right| \right)$. After introducing the damage at peak stress under uniaxial compression $\tilde{d}_c$ as an additional material parameter, the parameter $\tilde{\varepsilon}_p^c$ is finally given by Eq. IV.1-42. In this equation, $E = 2\, f_c / \varepsilon_{c1}$ is the initial stiffness (elastic modulus) according to the ETC constitutive relationship, which is generalized here to the multiaxial situation.

$$\tilde{\varepsilon}_p^c = -\left(\varepsilon_{c1} - \frac{f_c}{E\left(1 - \tilde{d}_c\right)} \right) = -\varepsilon_{c1}\left(\left(1 - 2\tilde{d}_c\right) \big/ \left(2 - 2\tilde{d}_c\right) \right) \qquad \text{Eq. IV.1-42}$$

After inserting Eq. IV.1-42 into Eq. IV.1-41, the expression of the model parameter κ_{c1} is obtained as a function of the strain and damage at peak stress under uniaxial compression ε_{c1} and $\tilde{d}_c$, and the dilatancy parameter α_g, see Eq. IV.1-43.

$$\kappa_{c1} = \frac{\varepsilon_{c1}\left(1 - 2\tilde{d}_c\right)}{\left(2 - 2\tilde{d}_c\right)\left(1 - \alpha_g\right)} \qquad\qquad \text{Eq. IV.1-43}$$

The accumulated plastic strain κ_c is always nonnegative. The dilatancy parameter α_g is lower than 1; experimental evidence such as the multiaxial compression tests (Kupfer, et al., 1969) suggest that this parameter has a value comprised between 0.20 and 0.30. Therefore, the non negativity of κ_c implies that the stiffness degradation of concrete in uniaxial

---

compression is lower than 0.50 at peak stress: $\tilde{d}_c < 0.50$. This condition is in line with the experimental observations, as identification from cyclic compression tests (Karsan and Jirsa, 1969) indicates values around 0.25.

Model parameter a_c

A non dimensional parameter a_c appears in the evolution law for compressive damage. This parameter can be expressed as a function of the material parameters that have been introduced here above; indeed rewriting Eq. IV.1-40 at peak stress for uniaxial compression leads to the expression of Eq. IV.1-44 for the parameter a_c.

$$a_c = -\ln\left(1-d_c\right)/\kappa_c = \frac{\ln\left(1-\tilde{d}_c\right)\left(\alpha_g-1\right)\left(2-2\tilde{d}_c\right)}{\varepsilon_{c1}\left(1-2\tilde{d}_c\right)} \qquad \text{Eq. IV.1-44}$$

Model parameter a_t

The model parameter a_t that appears in the evolution law for tensile damage is determined based on energetic considerations. As the evolution laws for the hardening variables rely on a work-hardening hypothesis, the total plastic work can be related to the energy dissipation of the material (Feenstra and de Borst, 1996). In tension, the concept of crack energy is often introduced in the constitutive laws for regularization of the model with regards to the mesh sensitivity on the global structural response (Hillerborg, et al., 1976). The concept of equivalent length is also introduced to define a representative dimension of the mesh size in which it is assumed that the crack energy is uniformly dissipated. The total (apparent) plastic work in tension can thus be expressed by Eq. IV.1-45, where $\bar{G}_t$ is the crack energy in tension in N.m/m², l_c is the characteristic length in m also referred to as the localization zone size and g_t is the crack energy density per unit volume in N.m/m³. The crack energy and the characteristic length are assumed as material properties; these material properties ensure the objectivity of the numerical simulation at the structural level.

$$\int_0^\infty \tau_t\left(\kappa_t\right) d\kappa_t = \frac{\bar{G}_t}{l_c} = g_t \qquad \text{Eq. IV.1-45}$$

Based on Eq. IV.1-45, the adimensional model parameter a_t that appears in the expression of the tensile damage evolution law can be calibrated on the material parameters $\bar{G}_t$ and l_c. Indeed, calculation of the first term in the equality leads to the expression of Eq. IV.1-46.

$$\int_0^\infty \tau_t\left(\kappa_t\right) d\kappa_t = \frac{f_t}{2}\left(\frac{1}{a_t} + \frac{1}{6\,a_t}\right) = \frac{7\,f_t}{12\,a_t} \qquad \text{Eq. IV.1-46}$$

The model parameter a_t is thus obtained as a function of the material parameters $\bar{G}_t$, l_c and f_t according to Eq. IV.1-47.

$$a_t = \frac{7\,f_t}{12\left(\bar{G}_t/l_c\right)}$$

Eq. IV.1-47

Model parameter b_c

Similar energetic considerations are made in compression for calculation of the parameter of the hardening law b_c. The crack energy in compression $\bar{G}_c$, in N.m/m², and the internal length l_c, in m, are introduced in the constitutive law; they are considered as material properties. The total (apparent) plastic work in compression is expressed by Eq. IV.1-48, with g_c the crack energy density per unit volume in N.m/m³.

$$\int_0^{\kappa_{c1}} \tau_c\left(\kappa_c\right) d\kappa_c + \int_{\kappa_{c1}}^{\kappa_c} \tau_c\left(\kappa_c\right) d\kappa_c = \frac{\bar{G}_c}{l_c} = g_c$$

Eq. IV.1-48

The left term of the sum in Eq. IV.1-48 refers to the crack energy density dissipated before the peak stress, during hardening of the material, whereas the right term of the sum represents the crack energy density dissipated after the peak stress, during softening of the material. After integration of Eq. IV.1-48, the expression of the parameter b_c as a function of the material parameters is obtained, see Eq. IV.1-49.

$$b_c = \frac{2\,f_c}{\left(\bar{G}_c/l_c\right) - f_{c0}\,\kappa_{c1} - \left(f_c - f_{c0}\right)\kappa_{c1}\,\ln 2}$$

Eq. IV.1-49

In the latter equation, the model parameter b_c is thus expressed as a function of the material parameters in compression f_c, f_{c0}, $\bar{G}_c$, l_c and κ_{c1}. However, the crack energy $\bar{G}_c$ and internal length l_c can be difficult to derive for practical applications. It can be more convenient to define an adimensional parameter x_c that represents, in uniaxial compression, the ratio between the crack energy dissipated before the peak stress and the total crack energy dissipated at failure. This adimensional material parameter, that ranges between 0 and 1, should then be seen as a direct measure of the ductility of concrete in compression; variation of this parameter from 0 to 1 allows for modeling different material behaviors from infinitely ductile behavior (horizontal plateau for $x_c = 0$) to perfectly brittle behavior (sudden failure at peak stress for $x_c = 1$). The interpretation of this adimensional parameter is thus straightforward and the advantage of using an adimensional parameter for practical applications is that no mistake can be made with the dimensions. The disadvantage of this approach is that, by replacing two parameters by one, some information is lost; namely in this case, the characteristic length is not addressed in compression. The adimensional material

parameter x_c is related to the other material parameters by the following relationship of Eq. IV.1-50.

$$x_c = \frac{\int_0^{\kappa_{c1}} \tau_c(\kappa_c)\, d\kappa_c}{\overline{G}_c / l_c} = \frac{f_{c0}\, \kappa_{c1} + (f_c - f_{c0})\, \kappa_{c1} \ln 2}{\overline{G}_c / l_c}$$

Eq. IV.1-50

For practical applications, x_c is considered as a material parameter and no reference are made any more to the crack energy $\overline{G}_c$ and internal length l_c in compression. Finally, the expression of the model parameter b_c as a function of x_c and the other material parameters is given by Eq. IV.1-51.

$$b_c = \frac{2\, f_c\, x_c}{(1 - x_c)\left[f_{c0}\, \kappa_{c1} + (f_c - f_{c0})\, \kappa_{c1} \ln 2 \right]}$$

Eq. IV.1-51

IV.1.4.2. *Material parameters and their phenomenological effect*

The model contains ten material parameters that are summarized in Table IV.1-1. These parameters can be obtained by three tests: uniaxial compression test until failure comprising one unloading-reloading at peak stress, biaxial compression test until peak stress, and uniaxial tension test until failure.

Parameter	Name	Units	Required test
ν	Poisson's ratio	[−]	Uniaxial compression
f_{c0}	Compr. limit of elasticity	[MPa]	Uniaxial compression
f_c	Uniaxial compr. strength	[MPa]	Uniaxial compression
ε_{c1}	Peak stress strain	[−]	Uniaxial compression
α_g	Dilatancy parameter	[−]	Uniaxial compression
x_c	Compr. dissipated energy	[−]	Uniaxial compression
$\tilde{d}_c$	Compr. damage at peak stress	[−]	Uniax. compr. + unloading
f_b	Biaxial compr. strength	[MPa]	Biaxial compression
f_t	Uniaxial tensile strength	[MPa]	Uniaxial tension
g_t	Tensile crack energy density	[MPa]	Uniaxial tension

Table IV.1-1: Material parameters

Parameters obtained from uniaxial tension test: f_t and g_t

In tension, the uniaxial tensile strength f_t corresponds to the peak stress in a uniaxial tension test, whereas the tensile crack energy density g_t is a measure of the ductility of the softening branch.

The tensile crack energy density g_t is the ratio between the crack energy in tension $\bar{G}_t$ and the characteristic length l_c. A formula has been given by the CEB-FIB (1990) for calculation of the crack energy in tension, in N.m/m², from the mean compressive strength of concrete $f_{cm} = f_c + 8\,\text{MPa}$ and the maximum size of aggregates d, see Eq. IV.1-52. The coefficient a_d is given in Table IV.1-2 for different maximum size of aggregates d. The objective when developing the empirical formula of Eq. IV.1-52 was to use only parameters generally known to the designer. This formula has been found to agree with experimental results (Hilsdorf and Brameshuber, 1991) and it has been widely used in literature (Feenstra and de Borst, 1996; Grassl and Jirasek, 2006). For concrete used in typical applications, Eq. IV.1-52 leads to a crack energy in tension $\bar{G}_t$ that ranges between 50 and 150 N.m/m².

$$\bar{G}_t = a_d . f_{cm}^{0.7}$$
Eq. IV.1-52

d [mm]	a_d
8	4
16	6
32	10

Table IV.1-2: Coefficient a_d for consideration of the effect of the maximum aggregate size on the tensile crack energy $\bar{G}_t$

The characteristic length in the model depends on the chosen element type, element size, element shape and integration scheme (Feenstra and de Borst, 1996). A very simple formula has been proposed for biaxial case (Rots, 1988), see Eq. IV.1-53. In this equation, A_e is the area of the element and α_l is a modification factor which is equal to 1 for quadratic elements and equal to $\sqrt{2}$ for linear elements. This formula gives good approximation for most practical applications.

$$l_c = \alpha_l . \sqrt{A_e}$$
Eq. IV.1-53

Fig. IV.1-5 presents the computed results obtained by modeling a uniaxial tension test with different values of the tensile crack energy density g_t, next to experimental data (Gopalaratnam and Shah, 1985). It can be seen that, at the macroscopic level, the tensile crack energy density allows for properly capturing the slope of the softening branch in tension. Identification of this parameter should be made by computing the values of $\bar{G}_t$ and l_c using Eq. IV.1-52 and Eq. IV.1-53, which allows for regularizing the constitutive law by means of a

characteristic length. For a given meshing, the tensile crack energy density can also be identified by calibration on the macroscopic response of the material as shown in Fig. IV.1-5. This latter method eliminates the dependency on the maximum aggregate size and it avoids the necessity of defining a characteristic length, but it does not allow for dealing with the issue of mesh sensitivity. Yet, the problem of mesh sensitivity has to be addressed in a way or another in constitutive models; this very complex problem requires specific and intensive investigation and it is only partly treated here, because it is considered beyond the scope of the present work. In the following, an example is given to illustrate the problem of localization and the regularization technique using the characteristic length parameter.
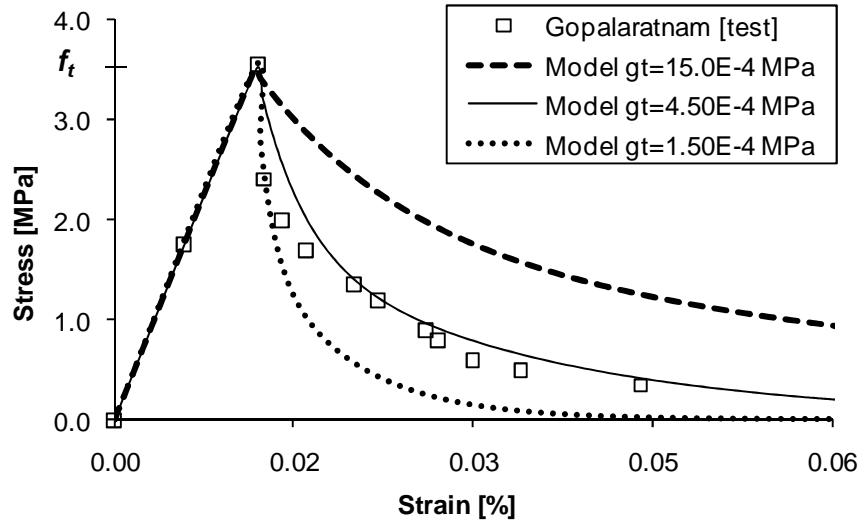
Fig. IV.1-5: Identification of the model parameters in a uniaxial tension test

To give a further understanding of the parameters $\bar{G}_t$, l_c and g_t, the problem of localization of the deformations in the numerical integration process is illustrated here by an academic example. We consider a 1.0 m side cube of plain concrete that is modeled using two different meshing: in the first case, a single cube-shaped three-dimensionnal finite element of 1.0 m side, see Fig. IV.1-6 left; in the second case, eight cube-shaped three-dimensionnal finite element of 0.5 m side, see Fig. IV.1-7 right. In order to provoke the localization of deformations in the second numerical model, the value of the tensile strength of the upper layer finite elements is defined as slightly different (-3%) to the value of the tensile strength of the lower layer finite elements.
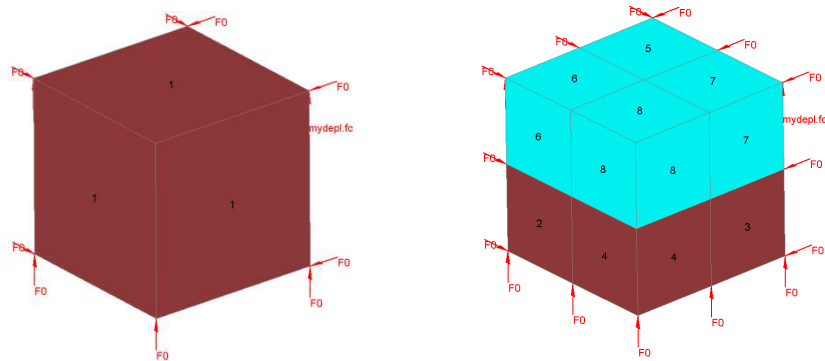
Fig. IV.1-6: Two different meshing for the 1.0 m side cube

The two cubes are subjected to uniaxial tensile loading; the force-displacement diagrams are plotted in Fig. IV.1-7. Three simulations have been performed:

- Simulation with the meshing of 1.0 m side and the value of the tensile crack energy density $g_t = g_{t,1} = 4.50 \times 10^{-4}$ MPa obtained by calibration on the experimental data;

- Simulation with the meshing 0.5 m side and the same value of the tensile crack energy density $g_t = g_{t,1}$ as in the previous simulation;

- Simulation with the meshing of 0.5 m side and a value of the tensile crack energy density $g_t = g_{t,2}$ modified for regularization of the force-displacement response. The value of $g_{t,2}$ is equal to 13.50×10^{-4} MPa.
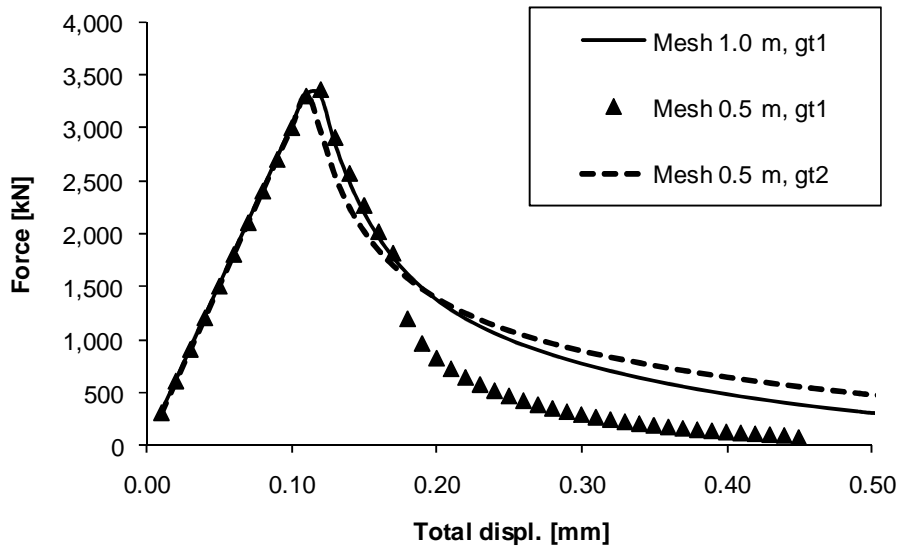
Fig. IV.1-7: Effect of localization on the numerical response and regularization with parameter g_t
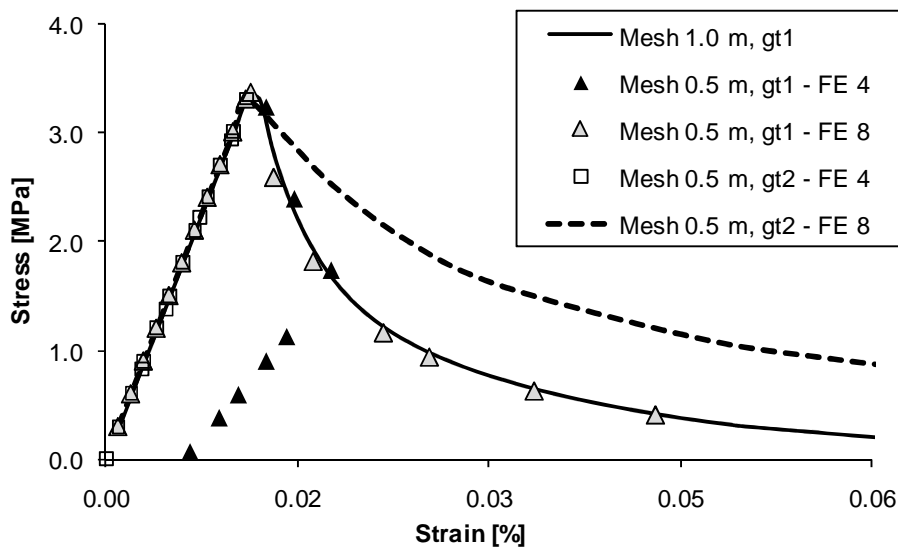
Fig. IV.1-8: The stress-strain responses highlight the localization of deformations in certain integration points and the unloading in others

The results show that the meshing has an influence on the post-peak response in terms of force-displacement. The numerical response obtained with the meshing of 0.5 m side is more brittle than the response obtained with the meshing of 1.0 m side when the material parameters are kept unchanged. However, it is possible to eliminate this mesh-dependency by modifying the tensile crack energy density parameter g_t. In fact, the parameter g_t must be adapted to the meshing to ensure that the crack energy in tension $\bar{G}_t$ remains constant, as this latter parameter depends on the material but is independent of the numerical model. As the parameter g_t is evaluated as $g_t = \bar{G}_t / l_c$, it is the role of the characteristic length l_c to take into account the effect of meshing to regularize the model.

The analysis of the paths in the stress-strain space followed by different integration points gives a better understanding of the localization phenomenon. In Fig. IV.1-8, the evolution of stresses and strains are plotted for the three simulations discussed here. When the mesh of 1.0 m side is used, the model comprises only one finite element and all the integration points have the same response in the stress-strain space. However with the meshing of 0.5 m side, different integration points show different responses in the stress-strain space; for this meshing, the stress-strain response is given in one integration point of the upper layer (FE 8), which has a slightly lower tensile strength compared with the lower layer, and in one integration point of the lower layer (FE 4). It can be seen that the integration point of the upper layer exhibits a softening behavior with large strains whereas the integration point of the lower layer exhibits elastic unloading. In the simulation with $g_t = g_{t,1}$, the unloading in the lower layer integration points does not appear directly after the peak stress; it arises when the applied force on the cube has been reduced by approximately 50% of the peak force. This bifurcation in the stress-strain response of certain integration points in the model explains the sudden change in the force-displacement diagram for this simulation. In the simulation with $g_t = g_{t,2}$, the unloading of the lower layer integration points arise directly after the peak stress, whereas the upper layer integration points exhibit a softening response that is more ductile compared with the simulation with 1.0 m size meshing. This higher ductility in the stress-strain space is due to the fact that $g_{t,2} > g_{t,1}$, since $l_{c,2} < l_{c,1}$. As a conclusion, due to the localization of the deformations in certain integration points, it was necessary to use a higher value of the tensile crack energy density g_t for the lower meshing size to eventually obtain the same response in the force-displacement space.

Parameters obtained from uniaxial compression test: ν, f_c, f_{c0} and ε_{c1}

Poisson's ratio ν, the uniaxial compressive strength f_c and the peak stress strain in uniaxial compression ε_{c1} are material parameters commonly used in concrete models, which have been discussed in Chapter I.

In uniaxial compression, the concrete response is linearly elastic up to the compressive limit of elasticity f_{c0}. Experimental results presented in Chapter I show that this compressive limit of elasticity has a value of approximately $0.30 \times f_c$.

Parameter obtained from uniaxial compression test: x_c

The compressive dissipated energy x_c is used for calibration of the softening response of concrete in compression. Fig. IV.1-9 presents the computed results obtained by modeling a uniaxial compression test with different values for the material parameter x_c, next to experimental data (Karsan and Jirsa, 1969). The parameter x_c allows for capturing the proper softening response; increasing this parameter leads to a more brittle behavior whereas decreasing this parameter leads to a more ductile behavior.
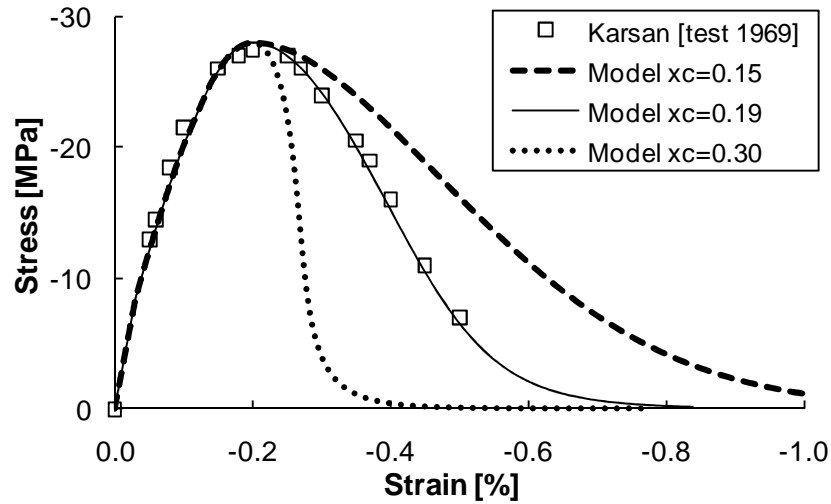
Fig. IV.1-9: Identification of the model parameter x_c in a uniaxial compression test

Parameter obtained from uniaxial compression test: $\tilde{d}_c$

The compressive damage at peak stress $\tilde{d}_c$ is used for calibration of the stiffness degradation of concrete in compression.
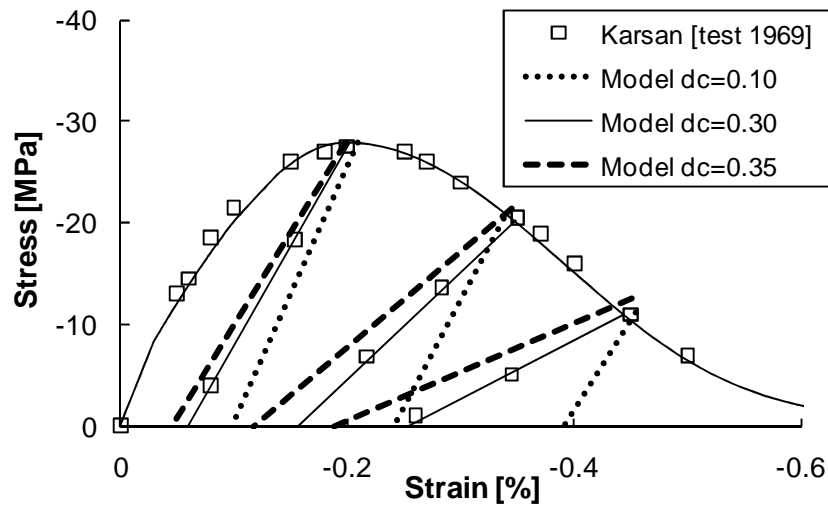
Fig. IV.1-10: Identification of the model parameter $\tilde{d}_c$ in a uniaxial compression test

The parameter $\tilde{d}_c$ is determined by means of a uniaxial compressive test with unloading at peak stress. Modification of the value of this parameter allows for an increase or a decrease in the relative importance of the damage process with respect to the plastic process in the model. For low values of this parameter, the plastic process prevails over the damage process in compression, which results in a significant development of plastic strains and relatively limited degradation of the elastic properties; on the contrary, for high values of this parameter (but lower than 0.50) the response is mostly driven by the damage process. Fig. IV.1-10 presents the computed results obtained by modeling a uniaxial compression test with different values for the material parameter $\tilde{d}_c$, next to experimental data (Karsan and Jirsa, 1969). Based on these experimental data, the value for the compressive damage at peak stress can be set to 0.30.

Parameter obtained from uniaxial compression test: α_g

The dilatancy parameter α_g allows capturing the dilatancy behavior of concrete subjected to compression. The value of this parameter can be established by measuring the volumetric strain developed by a concrete sample subjected to uniaxial compression. In uniaxial compression, the plastic strains in the three principal directions calculated using the compressive flow rule are given by Eq. IV.1-54.

$$\varepsilon_{p,x}^c = \left(\alpha_g - 1\right)\lambda_c \quad ; \quad \varepsilon_{p,y}^c = \varepsilon_{p,z}^c = \left(\alpha_g + 1/2\right)\lambda_c \qquad \text{Eq. IV.1-54}$$

The plastic volumetric strain is thus given by Eq. IV.1-55.

$$\varepsilon_{p,vol}^c = \varepsilon_{p,x}^c + \varepsilon_{p,y}^c + \varepsilon_{p,z}^c = 3\,\alpha_g\,\lambda_c \qquad \text{Eq. IV.1-55}$$

From this latter equation, it is clear that the dilatancy parameters α_g governs the plastic change of volume; the plastic volumetric strain is null for $\alpha_g = 0$, whereas the material exhibits a plastic dilatancy for $\alpha_g > 0$ and a plastic contractancy for $\alpha_g < 0$. The situation of $\alpha_g = 0$ corresponds to a purely deviatoric flow, i.e. the plastic deformation is exclusively due to slip and the material exhibits no plastic change of volume. As concrete experiences an increase of volume during plastic flow because of the asperities at the slip interface, the dilatancy parameter α_g is positive.

The (instantaneous stress related) volumetric strain is the sum of the elastic and plastic parts, see Eq. IV.1-56.

$$\varepsilon_{vol}^c = \varepsilon_{e,vol}^c + \varepsilon_{p,vol}^c = \sigma_x \left(\frac{1-2\nu}{E\left(1-d_c\right)}\right) + 3\,\alpha_g\,\lambda_c \qquad \text{Eq. IV.1-56}$$

From elasticity theory, the elastic volumetric strain is null for a Poisson's coefficient equal to 0.5. For concrete, Poisson's coefficient is lower than 0.5, leading to a reduction of volume of the specimen subjected to uniaxial compression in the elastic field. In uniaxial

compression, the elastic part of the volumetric strain is always negative and linearly increases, in absolute value, with the effective stress. However in the nominal stress space, the relationship between the elastic part of volumetric strain and the nominal stress is not linear due to the damage component. The plastic part of the volumetric strain is always positive and linearly increases with the plastic multiplier λ_c. As the total volumetric strain is the sum of the elastic and plastic parts, the sign of the total volumetric strain depends on the respective importance of the two parts. The volumetric strain is negative, dominated by the elastic part, for moderated stress levels, for which the behavior is almost linear elastic. Then, plastic strains start to develop which results in a decrease of the volumetric strain in absolute value. Finally for higher stress levels, the plastic part becomes dominant and the volumetric strain changes sign from negative to positive.

Fig. IV.1-11 presents the computed results obtained by modeling a uniaxial compression test with different values of the material parameter α_g, and comparison with experimental data (van Mier, 1984).
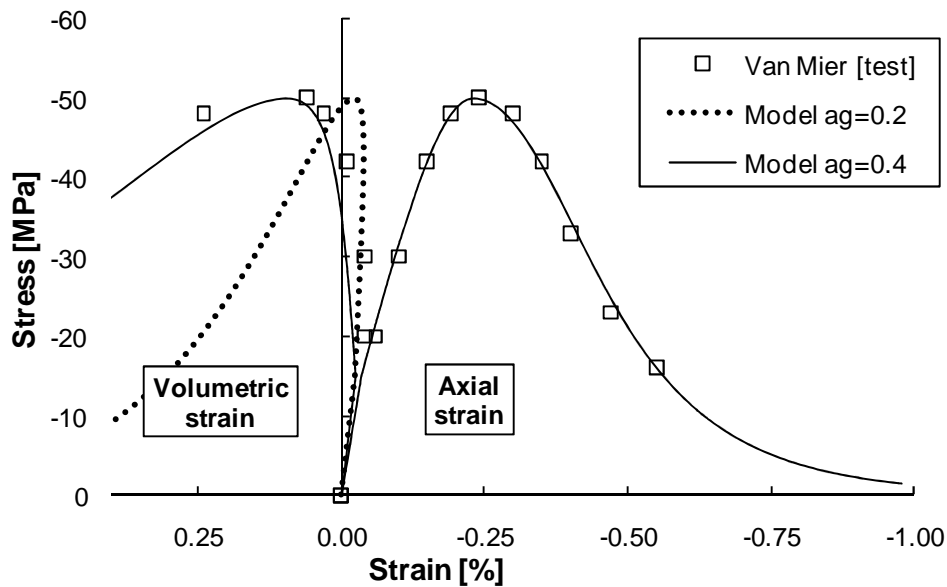
Fig. IV.1-11: Identification of the model parameter α_g in a uniaxial compression test

Parameter obtained from biaxial compression test: f_b

Finally, the biaxial compressive strength f_b is used for capturing properly the positive effect of compressive confinement on the concrete strength. Based on experimental data (Kupfer, et al., 1969), a strength increase of 16% in biaxial compression compared to uniaxial compression is generally considered (Grassl and Jirasek, 2006; Wu, et al., 2006), thus $f_b = 1.16 \times f_c$.

IV.1.5.   Thermodynamic aspects

In the present model, the evolution laws for the internal variables have been postulated and not derived from a dissipation potential. This is the usual procedure for non standard material models, such as the models with non associated flow rule (Grassl and Jirasek, 2006). Still, it has to be verified that the resulting model is thermodynamically admissible. Therefore the dissipation inequality has to be checked for the present model; the condition of nonnegative dissipation may lead to certain constraints on the model parameters.

IV.1.5.1. *Condition of nonnegative dissipation*

For the present type of damage-plastic model, the Helmholtz free energy per unit volume is given by Eq. IV.1-57.

$$\rho\,\psi\left(\underline{\underline{\varepsilon}},\underline{\varepsilon}_p,d_t,d_c\right)=\frac{1}{2}\left(\underline{\underline{\varepsilon}}-\underline{\varepsilon}_p\right):\left[\left(\underline{\underline{I}}-\underline{\underline{D}}\right):\underline{\underline{C}}_0\right]:\left(\underline{\underline{\varepsilon}}-\underline{\varepsilon}_p\right) \qquad \text{Eq. IV.1-57}$$

In this equation, ρ is the density (specific mass) and ψ is the Helmholtz free energy per unit mass which depends on the internal state variables of the system. In this part, isothermal processes are considered so that the temperature remains constant and is not explicitly listed among the state variables.

The rate of dissipation per unit volume $\mathcal{D}$ is then evaluated according to Eq. IV.1-58.

$$\mathcal{D}=\underline{\underline{\sigma}}:\underline{\dot{\underline{\varepsilon}}}-\rho\,\dot{\psi}=\left(\underline{\underline{\sigma}}-\rho\frac{\partial\psi}{\partial\underline{\underline{\varepsilon}}}\right):\underline{\dot{\underline{\varepsilon}}}-\rho\frac{\partial\psi}{\partial\underline{\varepsilon}_p}:\underline{\dot{\underline{\varepsilon}}}_p-\rho\frac{\partial\psi}{\partial d_t}\dot{d}_t-\rho\frac{\partial\psi}{\partial d_c}\dot{d}_c \qquad \text{Eq. IV.1-58}$$

Referring to the standard thermodynamics arguments (Coleman and Gurtin, 1967), the stress-strain equation is obtained by Eq. IV.1-59.

$$\underline{\underline{\sigma}}=\rho\frac{\partial\psi}{\partial\underline{\underline{\varepsilon}}}=\left(\underline{\underline{I}}-\underline{\underline{D}}\right):\underline{\underline{C}}_0:\left(\underline{\underline{\varepsilon}}-\underline{\varepsilon}_P\right) \qquad \text{Eq. IV.1-59}$$

The rate of dissipation per unit volume is then given by Eq. IV.1-60. To obtain the expression of Eq. IV.1-60, it must be noted that the dissipative thermodynamic force conjugate to the plastic strain is equal to the nominal stress, since we have: $-\rho\,\partial\psi/\partial\underline{\varepsilon}_P=\left(\underline{\underline{I}}-\underline{\underline{D}}\right):\underline{\underline{C}}_0:\left(\underline{\underline{\varepsilon}}-\underline{\varepsilon}_P\right)=\underline{\underline{\sigma}}$. The dissipative forces conjugate to the tensile and compressive damage variables are the tensile and compressive damage energy release rates (DERR), given by Eq. IV.1-61.

$$\mathcal{D}=-\rho\frac{\partial\psi}{\partial\underline{\varepsilon}_p}:\underline{\dot{\underline{\varepsilon}}}_p-\rho\frac{\partial\psi}{\partial d_t}\dot{d}_t-\rho\frac{\partial\psi}{\partial d_c}\dot{d}_c=\underline{\underline{\sigma}}:\underline{\dot{\underline{\varepsilon}}}_p+Y_t\,\dot{d}_t+Y_c\,\dot{d}_c \qquad \text{Eq. IV.1-60}$$

$$Y_t = -\rho \frac{\partial \psi}{\partial d_t} = \frac{1}{2}\left(\underline{\varepsilon} - \underline{\varepsilon}_p\right) : \left(\underline{\underline{P}}^+ : \underline{\underline{C}}_0\right) : \left(\underline{\varepsilon} - \underline{\varepsilon}_p\right)$$

$$Y_c = -\rho \frac{\partial \psi}{\partial d_c} = \frac{1}{2}\left(\underline{\varepsilon} - \underline{\varepsilon}_p\right) : \left(\underline{\underline{P}}^- : \underline{\underline{C}}_0\right) : \left(\underline{\varepsilon} - \underline{\varepsilon}_p\right)$$

<div style="text-align:right">Eq. IV.1-61</div>

The tensile and compressive damage energy release rates Y_t and Y_c can be related to the specific free energy of the undamaged material under the same elastic strain as the material which free energy is given by Eq. IV.1-57, as the damage variables do not affect these DERR.

The terms $\underline{\sigma} : \dot{\underline{\varepsilon}}_p$, $Y_t \, \dot{d}_t$ and $Y_c \, \dot{d}_c$ can be interpreted respectively as the plastic dissipation, the damage dissipation in tension and the damage dissipation in compression. Eq. IV.1-60 requires that the total dissipation be nonnegative. As the evolution of damage is in the present model related to the plastic flow, it is not necessarily required that the individual parts of dissipation are all nonnegative provided their sum is nonnegative. In the following, each of these terms is analyzed separately for more convenience; however it should be remembered that ensuring the non negativity of each of the terms is a sufficient but non-necessary condition for thermodynamic admissibility.

IV.1.5.2. *Damage dissipation*

The physical interpretation of the damage dissipation terms $Y_t \, \dot{d}_t$ and $Y_c \, \dot{d}_c$ is that the damage process reduces the internal energy of the system. From Eq. IV.1-61 it is clear that the DERR Y_t and Y_c are always nonnegative. Therefore, the condition of non negativity of the damage dissipation terms results in a condition of non negativity of the damage variable rates: $\dot{d}_t, \dot{d}_c \geq 0$. It is a physical requirement that the damage variables cannot decrease. This condition is satisfied using the damage evolution laws of Eq. IV.1-39 and Eq. IV.1-40 provided the accumulated plastic strains in tension and compression do not decrease, which is ensured by the Kuhn-Tucker condition (Eq. IV.1-21). As a result, the non negativity of the damage dissipation is satisfied in the model.

IV.1.5.3. *Plastic dissipation*

The plastic dissipation term can be rewritten using Eq. IV.1-62. Since $\dot{\lambda}_t, \dot{\lambda}_c \geq 0$ and all the terms of the tensor $\left(\underline{\underline{I}} - \underline{\underline{D}}\right)$ are non negative, the condition of non negativity of the plastic dissipation is satisfied if the products of the effective stress and the tensile (resp. compressive) plastic flow direction are nonnegative.

$$\mathscr{D}_p = \underline{\sigma} : \dot{\underline{\varepsilon}}_p = \dot{\lambda}_t \; \underline{\sigma} : \frac{\partial F_t}{\partial \underline{\overline{\sigma}}} + \dot{\lambda}_c \; \underline{\sigma} : \frac{\partial G_c}{\partial \underline{\overline{\sigma}}} = \dot{\lambda}_t \left(\underline{\underline{I}} - \underline{\underline{D}}\right) : \underline{\overline{\sigma}} : \frac{\partial F_t}{\partial \underline{\overline{\sigma}}} + \dot{\lambda}_c \left(\underline{\underline{I}} - \underline{\underline{D}}\right) : \underline{\overline{\sigma}} : \frac{\partial G_c}{\partial \underline{\overline{\sigma}}} \quad \text{Eq. IV.1-62}$$

In tension, the product of the effective stress and the tensile plastic flow direction is given by Eq. IV.1-63.

$$\underline{\underline{\sigma}} : \frac{\partial F_t}{\partial \underline{\underline{\sigma}}} = \underline{\underline{\sigma}} : \left(\underline{n}_I \otimes \underline{n}_I \right) = \bar{\sigma}_I \qquad \text{Eq. IV.1-63}$$

For all states that satisfy the yield condition $F_t \left(\underline{\underline{\sigma}}; \kappa_t \right) = \bar{\sigma}_I - \bar{\tau}_t \left(\kappa_t \right) = 0$, the product of Eq. IV.1-63 is thus equal to the effective tensile hardening function $\bar{\tau}_t \left(\kappa_t \right)$. As a result, non negativity of the plastic dissipation in tension is ensured provided the effective tensile hardening function $\bar{\tau}_t \left(\kappa_t \right)$ is nonnegative. This latter condition is automatically satisfied in the present model, see Eq. IV.1-34.

The product of the effective stress and the compressive plastic flow direction is given by Eq. IV.1-64.

$$\underline{\underline{\sigma}} : \frac{\partial G_c}{\partial \underline{\underline{\sigma}}} = \sqrt{3 \, \bar{J}_2} + \alpha_g \, \bar{I}_1 = G_c \qquad \text{Eq. IV.1-64}$$

In case of plastic dissipation in compression, the yield condition is satisfied: $F_c = 0$. Therefore, the condition of non negativity of the plastic dissipation in compression can be rewritten according to Eq. IV.1-65.

$$\sqrt{3 \bar{J}_2} + \alpha_g \, \bar{I}_1 \geq \sqrt{3 \bar{J}_2} + \alpha \, \bar{I}_1 - (1 - \alpha) \, \bar{\tau}_c \left(\kappa_c \right) \qquad \text{Eq. IV.1-65}$$

It can be seen that, in case of associated plasticity in compression ($\alpha_g = \alpha$), the condition of Eq. IV.1-65 simplifies to $(1 - \alpha) \, \bar{\tau}_c \left(\kappa_c \right) \geq 0$ and, as $\alpha \leq 1$ for $f_b \geq f_c / 2$ and thus for concrete where $f_b \geq f_c$, it remains to verify the non negativity of the effective compressive hardening function: $\bar{\tau}_c \left(\kappa_c \right) \geq 0$. This condition on the hardening function for associated plasticity in compression is equivalent to the condition found previously in tension. Thus, in case of associated plasticity, the non negativity of the plastic dissipation in compression would have been satisfied in the model. However, the present model considers non associated plasticity in compression ($\alpha_g \neq \alpha$); as a result analytical verification of Eq. IV.1-65 is not straightforward.

The condition of non negativity of the plastic dissipation in compression can be verified in particular cases. For instance in uniaxial compression, the scalar product of the effective stress and the compressive plastic flow direction gives $\sqrt{3 \bar{J}_2} + \alpha_g \, \bar{I}_1 = \left(1 - \alpha_g \right) |\sigma_{xx}| \geq 0$. The condition is satisfied provided that the dilatancy parameter $\alpha_g \leq 1$. For more complex load cases, it should be verified numerically that the total dissipation, comprising both the plastic and the damage dissipations, is nonnegative.

IV.2. Extension to high temperature

The division of the total strain tensor into individual strain components $\underline{\varepsilon}_{tot} = \underline{\varepsilon}_{th} + \underline{\varepsilon}_{\sigma} + \underline{\varepsilon}_{tr}$ has been adopted in the present model. In the previous section, a plastic-damage model has been developed for capturing the relationship between the instantaneous stress related strain tensor $\underline{\varepsilon}_{\sigma}$ and the stress tensor $\underline{\sigma}$ at ambient temperature. The present section presents the relationships for the calculation of the free thermal strain tensor $\underline{\varepsilon}_{th}$ and the transient creep strain tensor $\underline{\varepsilon}_{tr}$ under multiaxial stress states and the extension of the plastic damage model to high temperature.

IV.2.1. Multiaxial free thermal strain model

It has been said in Chapter III that the free thermal strain in uniaxial stress state was computed using the formula of Eurocode 2. This expression is generalized to the multiaxial stress state using the assumption of isotropy, see Eq. IV.2-1. In this equation, $\underline{1}$ is the second order identity tensor and $\varepsilon_{th}(T)$ is the free thermal strain given by Eurocode 2, which formula has been presented in Chapter III (Eq. III.2-35 and Eq. III.2-36).

$$\underline{\varepsilon}_{th}(T) = \varepsilon_{th}(T) \times \underline{1} \qquad \text{Eq. IV.2-1}$$

IV.2.2. Multiaxial transient creep strain model

The uniaxial transient creep strain model developed within the Explicit Transient Creep (ETC) model presented in Chapter III is generalized to multiaxial stress state. As a reminder, the transient creep strain rate in the ETC model is given by Eq. IV.2-2.

$$\dot{\varepsilon}_{tr} = \dot{\phi}(T) \times \frac{\sigma}{f_{c,20}} \qquad \text{Eq. IV.2-2}$$

Generalization of the transient creep strain formula to a multiaxial stress state is based on the assumption that the process of transient creep does not induce anisotropy. The formulation proposed by de Borst and Peeters (1989), which has been widely accepted in the literature (Khennane and Baker, 1992; Nechnech, et al., 2002; Gawin, et al., 2004; de Sa and Benboudjema, 2011), is adopted in the present work, see Eq. IV.2-3.

$$\dot{\underline{\varepsilon}}_{tr} = \dot{\phi}(T) \, \underline{\underline{H}} : \frac{\overline{\underline{\sigma}}^{-}}{f_{c,20}} \qquad \text{Eq. IV.2-3}$$

The tensor $\underline{\underline{H}}$ is given by Eq. IV.2-4, where δ_{ij} is the Kronecker symbol and the material parameter γ is taken equal to Poisson's ratio ν. The function $\phi(T)$ that appears in Eq. IV.2-3 has been defined in Chapter III.

$$H_{ijkl} = -\gamma\,\delta_{ij}\,\delta_{kl} + 0.5(1+\gamma)\left(\delta_{ik}\,\delta_{jl} + \delta_{il}\,\delta_{jk}\right) \qquad \text{Eq. IV.2-4}$$

The particularity of the formulation of Eq. IV.2-3 is that the calculation of the transient creep strain rate tensor is based on the negative part of the effective stress tensor. In models in which damage develops, it is consistent to use the effective stress rather than the nominal stress for calculation of transient creep strain because it can be assumed that the mechanism of transient creep occurs in the undamaged part of the material. In addition, it has been assumed in the ETC model that transient creep only develops under compressive stress; for this reason only the negative part of the effective stress tensor is considered in Eq. IV.2-3.

After integration over a finite time step, and adopting an explicit numerical scheme, the transient creep strain tensor can be computed using Eq. IV.2-5.

$$\underline{\underline{\varepsilon}}_{tr}^{(s+1)} = \underline{\underline{\varepsilon}}_{tr}^{(s)} + \left[\phi\left(T^{(s+1)}\right) - \phi\left(T^{(s)}\right)\right]\left[\underline{\underline{H}} : \frac{\left(\overline{\underline{\sigma}}^{-}\right)^{(s)}}{f_{c,20}}\right] \qquad \text{Eq. IV.2-5}$$

IV.2.3.   Material parameters

The constitutive relationship between the instantaneous stress-related strain tensor $\underline{\underline{\varepsilon}}_{\sigma}$ and the stress tensor $\underline{\underline{\sigma}}$ presented in the previous section is generalized to high temperature by incorporating in the model the temperature-dependency of the mechanical properties. In the plastic-damage model developed in the present work, the mechanical properties are captured by means of ten material parameters, see Table IV.1-1. Temperature-dependent evolution laws have to be derived for these material parameters to account for the thermo-mechanical degradation of concrete properties of strength and stiffness observed at high temperature and described in Chapter I.

IV.2.3.1. *Temperature dependency of the material parameters*

Uniaxial tensile strength

The evolution of the uniaxial tensile strength $f_{t,T}$ with temperature is taken from Eurocode 2 (European Committee for Standardization, 2004b). Evolution of this parameter with temperature results in a modification of the Rankine yield surface. This surface experiences isotropic contraction at high temperature due to the decrease of the tensile hardening function $\overline{\tau}_t$, which is equal to $f_{t,T}$, see Eq. IV.1-34.

Uniaxial compressive strength

The evolution of the uniaxial compressive strength $f_{c,T}$ with temperature is taken from Eurocode 2. Comparison between the Eurocode 2 model and experimental data presented in Chapter I (Abrams, 1971; Schneider, 1985) for siliceous concrete is presented in Fig. IV.2-1.

Compressive strength of concrete does not recover during cooling. According to Eurocode 4 part 1-2 (European Committee for Standardization, 2004c), an additional loss of 10% in compressive strength is considered during cooling from maximum to ambient temperature. This assumption prescribed by the Eurocode has been recently confirmed by an analysis based on hundreds of experimental results reported in the literature (Li and Franssen, 2011); in this analysis, it was shown that the additional reduction during cooling may be even higher than the 10% reduction considered in Eurocode 4. In fact, the residual strength of concrete after fire exposure depends on many parameters (Annerel, 2010) and its proper evaluation would probably require a more advanced model taking into account the effect of the different parameters, but the Eurocode formula has been adopted here because of its simplicity and its generic form and because it has the advantage of being a standard code formula. Consideration of the additional loss in compressive strength during cooling is of prime importance in the analysis of structures subjected to natural fire. Recent research based on numerical simulations have highlighted the possibility of collapse during or even after the cooling phase of a fire and one of the main mechanisms that lead to this type of failure is the additional loss of concrete strength during the cooling phase of the fire (Dimia, et al., 2011; Gernay and Dimia, 2011).
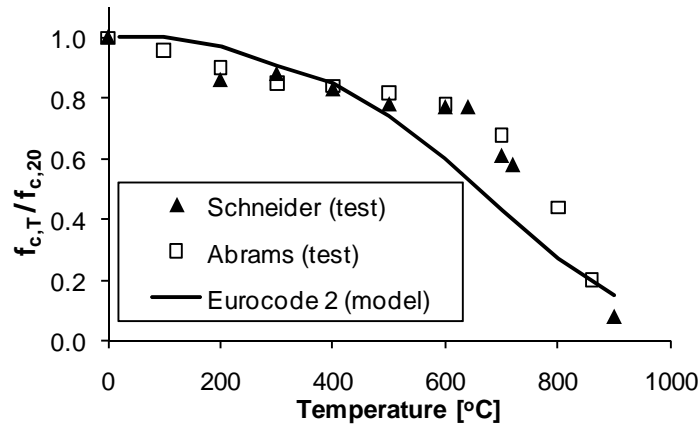
Fig. IV.2-1: Evolution of uniaxial compressive strength with temperature: comparison between model and experimental data (siliceous aggregates)

Peak stress strain

The peak stress strain in uniaxial compression ε_{c1} is calculated from parameters of the Eurocode, according to the formula derived in the ETC model, see Eq. IV.2-6.

$$\varepsilon_{c1} = \varepsilon_{c1,ETC} = \frac{2\,\varepsilon_{c1,min} + \varepsilon_{c1,EC2}}{3} \qquad \text{Eq. IV.2-6}$$

The evolution laws for $\varepsilon_{c1,min}$ and $\varepsilon_{c1,EC2}$ with temperature are given respectively in the ENV version of Eurocode (European Committee for Standardization, 1995) and in the present version. During cooling, the peak-stress strain ε_{c1} is considered as fixed to the value that prevailed at the maximum temperature, according to Eurocode 4.

Knowing the temperature-dependent relationships for the compressive strength $f_{c,T}$ and the peak stress strain ε_{c1}, the Young modulus E is calculated as $E = 2\,f_{c,T}/\varepsilon_{c1}$. In Chapter III, it has been shown that the Young modulus calculated by this formula agrees with experimental data, see Fig. III.2-4.

Poisson's ratio

It is experimentally observed that Poisson's ratio depends on temperature (Maréchal, 1970; Luccioni, et al., 2003). The concept of thermal damage has been proposed (Luccioni, et al., 2003) to take into account the deterioration of the concrete elastic properties due to high temperatures. By expressing the Young modulus and Poisson's ratio as functions of this thermal damage, it is possible to account for the temperature-dependency of these material parameters. However, the approach followed in the present model is different. Explicit temperature-dependent relationships have been adopted for the material properties because, to the author's opinion, this latter approach gives more flexibility compared with the thermal damage approach as it allows, for instance, adopting the relationships prescribed in the Eurocode for some of the material parameters. The temperature-dependent relationship for calculation of Young modulus has been presented above; following the same approach, it is thus necessary to take into account explicitly the temperature dependency of Poisson's ratio. Based on the experimental results presented in Chapter I, a bilinear relationship is adopted, see Eq. IV.2-7 and Fig. IV.2-2. The transition temperature T_ν is equal to 500°C.

$$
\begin{aligned}
\nu(T) &= \nu_{20}\left(0.2 + 0.8 \times \frac{T_\nu - T}{T_\nu - 20}\right) \quad ; \quad T \leq T_\nu \\
\nu(T) &= 0.2 \times \nu_{20} \quad\quad\quad\quad\quad\quad\quad ; \quad T > T_\nu
\end{aligned}
\qquad \text{Eq. IV.2-7}
$$
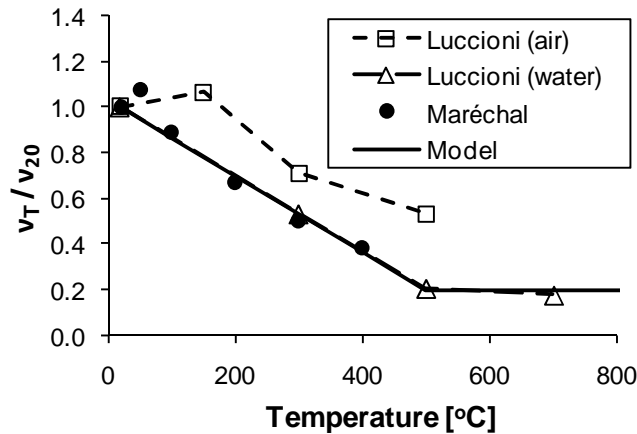
Fig. IV.2-2: Evolution of Poisson's ratio with temperature:
comparison between model and experimental data

Biaxial compressive strength

Experimental results indicate that the equibiaxial compressive strength $f_{b,T}$ decreases with temperature but, at a given temperature, the decrease in equibiaxial compressive strength is smaller than the decrease in uniaxial compressive strength $f_{c,T}$ (Ehm and Schneider, 1985); the ratio between these two parameters, equal to 1.16 at ambient temperature, should thus be adapted at high temperature. Adopting the notation $\beta = f_{b,T}/f_{c,T}$, the ratio between the coefficient β at high temperature and β_{20} at ambient temperature can be calculated using Eq. IV.2-8, where the transitions temperature $T_{\beta 1}$ and $T_{\beta 2}$ are respectively equal to 350°C and 750°C.

$$\begin{aligned}
\beta(T) &= \beta_{20} & &; \quad T \leq T_{\beta 1} \\
\beta(T) &= \beta_{20}\left(1+0.6\times\left(\frac{T-T_{\beta 1}}{T_{\beta 2}-T_{\beta 1}}\right)\right) & &; \quad T_{\beta 1} < T \leq T_{\beta 2} \\
\beta(T) &= 1.60\times\beta_{20} & &; \quad T_{\beta 2} < T
\end{aligned} \qquad \text{Eq. IV.2-8}$$

However, it should be noted that this relationship for the calculation of the ratio f_b/f_c at high temperature is based on a single set of experimental data. The proposed relationship suggests limiting the ratio by an horizontal plateau beyond 750°C as this temperature corresponds to the maximum temperature investigated during the experiments and the results should not be extrapolated beyond this limit, see Fig. IV.2-3.
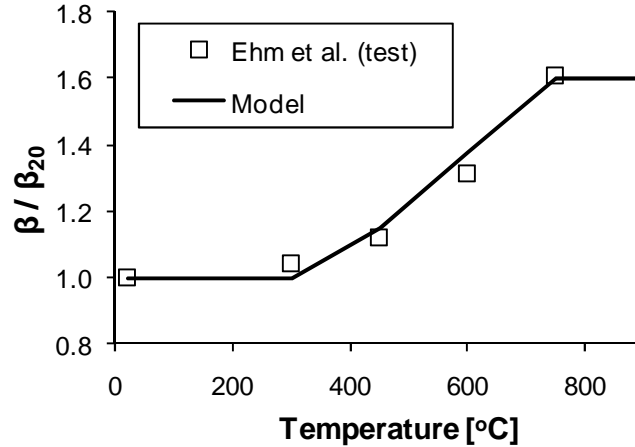
Fig. IV.2-3: Evolution of the ratio between equibiaxial strength and uniaxial strength in compression with temperature: comparison between model and experimental data

Compressive limit of elasticity

In uniaxial compression at ambient temperature, the concrete response is approximately linearly elastic up to a certain level and the compressive limit of elasticity f_{c0} has been introduced to model the limit of this elastic response. It is assumed that the approximately linear elastic concrete response in uniaxial compression for low stress levels remains proportionally unchanged at high temperature, i.e. the compressive limit of elasticity at high

temperature is always equal to 30% of the uniaxial compressive strength at high temperature: $f_{c0,T} = 0.30 \times f_{c,T}$.

Dilatancy parameter

The dilatancy parameter α_g that appears in the expression of the plastic potential in compression G_c is used to capture the volumetric dilatancy of the material. In the present model, it is assumed that the plastic potential in compression experiences isotropic contraction at high temperature with no modification in its shape; therefore it is assumed that the dilatancy parameter does not vary with temperature. This assumption is required because of a lack of experimental data on the evolution of this parameter with temperature.

Compressive damage at peak stress

The compressive damage at peak stress $\tilde{d}_c$ is calibrated from a uniaxial compression test with unloading at peak stress; it allows for capturing properly the degradation process in concrete under compression. This parameter deals with the process of mechanical damage in the material, as the degradation of elastic properties due to temperature, sometimes referred to as thermal damage, is already taken into account by means of the temperature-dependency of Young modulus and Poisson's ratio. As experimental data of cyclic tests in concrete at high temperature are very scarce, it is difficult to assess a possible temperature dependency in the process of mechanical damage. For this reason, it is assumed that the parameter $\tilde{d}_c$ does not vary with temperature.

Compressive dissipated energy

The adimensional parameter of compressive dissipated energy x_c represents, in uniaxial compression, the ratio between the crack energy dissipated before the peak stress and the total crack energy dissipated at failure. There is a lack of experimental data on the total crack energy dissipated at failure $\overline{G}_c$ for concrete in compression at high temperature so that it is difficult to assess the value of x_c at high temperature. In the present model, it is assumed that the parameter x_c is constant with temperature. This assumption means that, although the concrete response in uniaxial compression is modified with temperature, the ratio between the crack energy dissipated before the peak stress and the total crack energy dissipated at failure remains constant.

Tensile crack energy density

The tensile crack energy density g_t can be calculated from the tensile crack energy $\overline{G}_t(T)$ and the characteristic length l_c. Experimental results on the variation of $\overline{G}_t(T)$ with

temperature show a significant scatter depending on the test specimens and test methods, see Chapter I, so that it is difficult to derive a reliable model for the temperature dependency of this parameter based on the experimental data currently available. As a result, in the present model, the temperature-dependency of g_t was assumed based on mathematical considerations rather than on a physical basis. The tensile crack energy density g_t can be interpreted in terms of total plastic work, see Eq. IV.2-9; therefore it can be seen as the area under the tensile hardening function curve. At temperature increase, the uniaxial tensile strength $f_{t,T}$ decreases according to the law of Eurocode 2. In particular for temperatures beyond 600°C, $f_{t,T}$ is equal to 0. At these temperatures, it seems consistent to assume that the tensile crack energy density g_t is also equal to 0 as is implied by Eq. IV.2-9 or, in other words, as the area under the tensile hardening curve has become null. The tensile crack energy density must therefore vary with temperature and this variation is linked to the variation of the uniaxial tensile strength. By convenience, it was assumed that the tensile crack energy density g_t follows the same temperature dependency as the uniaxial tensile strength $f_{t,T}$ for every temperature.

$$g_t(T) = \int_0^\infty \tau_t(\kappa_t)\, d\kappa_t = \frac{7\, f_{t,T}}{12\, a_t}$$
Eq. IV.2-9

IV.2.3.2. Effect of temperature on the model parameters

The variations of the material parameters with temperature affect the model parameters a_c, b_c, a_t and κ_{c1} that are used in the equations of the model.

The model parameter a_c, given by Eq. IV.1-44 and used in the calculation of compressive damage, depends on the material parameters $\tilde{d}_c$, α_g and ε_{c1}. Due to the dependency in ε_{c1}, the model parameter a_c thus depends on temperature. This model parameter allows for imposing that, under isothermal conditions at a given temperature, the compressive damage under uniaxial compression is equal to $\tilde{d}_c$ at peak stress. As the parameter a_c varies with temperature during the calculation process, the evolution law for damage in compression must necessarily be rewritten in incremental form, see Eq. IV.2-10.

$$d_c^{(s+1)}\left(\kappa_c^{(s+1)}\right) = 1 - \exp\left(\ln\left(1 - d_c^{(s)}\right) - a_c^{(s+1)}\,\Delta\kappa_c\right)$$
Eq. IV.2-10

In this equation, *s* and *s+1* refer to the previous and current time step in the computation process and the increment in accumulated plastic strain in compression is: $\Delta\kappa_c = \kappa_c^{(s+1)} - \kappa_c^{(s)} \geq 0$. Using Eq. IV.2-10 it can be seen that, although a variation in temperature from time step *s* to *s+1* leads to a variation in the parameter a_c, there is no variation in the compressive damage parameter d_c if the accumulated plastic strain has not varied from time step *s* to *s+1* ($\Delta\kappa_c = 0$). This is consistent with the fact that d_c represents a mechanical damage; the concept of thermal damage has been handled separately by

introducing temperature-dependent relationships for the mechanical properties. Using the incremental form of the evolution law for damage in compression, the physical requirement of non negativity of the compressive damage increment is automatically satisfied.

The model parameters b_c and κ_{c1} also depend on temperature. These parameters are used in the hardening law in compression; they allow for capturing the temperature-dependency of the concrete response in compression by modifying the hardening law with temperature.

Finally, the model parameter a_t that appears in Eq. IV.2-9 does not depend on temperature as it has been assumed that the material parameters g_t and $f_{t,T}$ have the same temperature dependency. The crack energy density dissipated in tension g_t decreases with temperature following a relationship similar to that of $f_{t,T}$. The model parameter a_t allows for imposing that, under isothermal conditions at a given temperature, the crack energy dissipated in tension is equal to $g_t(T)$. As the model parameter a_t is constant with temperature, application of Eq. IV.1-39 in total form for the calculation of tensile damage ensures that the two conditions explained above for compressive damage are fulfilled. Namely, it ensures that an increment in temperature at constant value of the accumulated plastic strain in tension ($\Delta \kappa_t = 0$) does not lead to any variation of tensile damage and that the tensile damage rate is always positive or null.

IV.3. Numerical implementation

IV.3.1. General process

The present constitutive model has been implemented within the framework of the nonlinear finite element method. In the following, the Voigt notation has been used so that the second order symmetric tensors of stress and strain are rewritten as vectors with six components according to Eq. IV.3-1. Using this notation, the fourth order symmetric tensors are rewritten as second order tensors, i.e. into six-by-six-components matrix.

$$\underline{\varepsilon} = \left(\varepsilon_{xx}, \varepsilon_{yy}, \varepsilon_{zz}, \varepsilon_{xy}, \varepsilon_{xz}, \varepsilon_{yz} \right)^T$$
$$\underline{\sigma} = \left(\sigma_{xx}, \sigma_{yy}, \sigma_{zz}, \sigma_{xy}, \sigma_{xz}, \sigma_{yz} \right)^T$$

Eq. IV.3-1

Let us assume that at time step s the finite element code has converged, i.e. the values of the strains, stresses and internal variables are known at every integration point. The values of the displacements at the nodes are also defined. Then suppose that, from time step s to time step $s+1$, the variation of the displacements of the nodes calculated by the finite element code produce an increment in total strain, that is noted $\Delta \underline{\varepsilon}_{tot}$. Knowing the total strain at time step $s+1$ $\underline{\varepsilon}_{tot}^{(s+1)} = \underline{\varepsilon}_{tot}^{(s)} + \Delta \underline{\varepsilon}_{tot}$, the problem is to update the basic variables describing the local state of the material in a manner that is consistent with the constitutive law. This process should also yield the tangent modulus of the constitutive law, to be used by the finite element code in the iteration process. It is assumed that the temperatures are known, as a result of a thermal analysis that has been performed before the mechanical analysis. The general method presented in Chapter III for the uniaxial ETC model has been adapted to the multiaxial model.

First, for all integration points, one computes the mechanical properties, the free thermal strain and the transient creep strain at time step $s+1$. The free thermal strain vector $\underline{\varepsilon}_{th}^{(s+1)}$ and the transient creep strain vector $\underline{\varepsilon}_{tr}^{(s+1)}$ at time step $s+1$ are computed separately from the instantaneous stress-related strain.

The free thermal strain vector is computed using Eq. IV.3-2. The transient creep strain vector is computed using Eq. IV.3-3; however, the same conditions derived in Chapter III for the uniaxial case apply for computation of the transient creep strain in the multiaxial case. The first condition for having an increase in transient creep strain impose that the temperature at time step $s+1$ exceeds the maximum temperature reached previously in the history of the material. The second condition is related to the converged stress at time step s, which has to be a compressive stress. This condition is automatically fulfilled in the multiaxial case by considering only the negative part (compression) of the effective stress vector at time step s in the computation of the transient creep strain. The third condition can be expressed in terms

of the accumulated plastic strain in compression; namely, transient creep strain is assumed to develop only if $\kappa_c \leq \kappa_{c1}$.

The matrix $\underline{\underline{H}}$ that appears in Eq. IV.3-3 is given in Eq. IV.3-4, where the coefficient γ has been replaced by Poisson's ratio ν. The free thermal strain and transient creep strain are thus computed explicitly before entering into the iterative resolution of the equilibrium at the considered time step.

$$\underline{\varepsilon}_{th}^{(s+1)} = \varepsilon_{th}\left(T^{(s+1)}\right) \times \underline{1} \quad ; \quad \underline{1} = \{1,1,1,0,0,0\}^T \qquad \text{Eq. IV.3-2}$$

$$\underline{\varepsilon}_{tr}^{(s+1)} = \underline{\varepsilon}_{tr}^{(s)} + \left[\phi\left(T^{(s+1)}\right) - \phi\left(T^{(s)}\right)\right]\left[\underline{\underline{H}} \cdot \frac{\left(\overline{\sigma}^-\right)^{(s)}}{f_{c,20}}\right] \qquad \text{Eq. IV.3-3}$$

$$\underline{\underline{H}} = \begin{bmatrix} 1 & -\nu & -\nu & 0 & 0 & 0 \\ & 1 & -\nu & 0 & 0 & 0 \\ & & 1 & 0 & 0 & 0 \\ & & & 0.5(1+\nu) & 0 & 0 \\ & & & & 0.5(1+\nu) & 0 \\ & & & & & 0.5(1+\nu) \end{bmatrix} \qquad \text{Eq. IV.3-4}$$

Then, one enters into the iterative process to find the state of equilibrium of the structure at time step $s+1$. Resolution of the equilibrium in the structure at a given time step is an iterative process and the increment in total strain produced by the finite element code is updated several times at each time step. The increment in total strain from converged time step s to iteration $i+1$ of time step $s+1$ is noted $\Delta\underline{\varepsilon}_{tot}$ and the total strain at iteration $i+1$ of time step $s+1$ is given by: $\underline{\varepsilon}_{tot}^{(i+1)} = \underline{\varepsilon}_{tot}^{(s)} + \Delta\underline{\varepsilon}_{tot}$. Yet, the free thermal strain and the transient creep strain do not vary during the iteration process; they are only computed once at the beginning of the procedure. At iteration $i+1$, the instantaneous stress-related strain vector can thus be computed using Eq. IV.3-5.

$$\underline{\varepsilon}_{\sigma}^{(i+1)} = \underline{\varepsilon}_{tot}^{(i+1)} - \underline{\varepsilon}_{th}^{(s+1)} - \underline{\varepsilon}_{tr}^{(s+1)} \qquad \text{Eq. IV.3-5}$$

At each iteration, it is necessary to find the updated values of the stresses, the updated values of the internal variables and the tangent modulus corresponding to the instantaneous stress-related strain vector of Eq. IV.3-5, for all integration points. For the multiaxial constitutive model presented in this work, this operation requires an iterative process, so that there is a second level of iterations in the general algorithm. This second level of iterations, which deals with the material constitutive law, is called "internal iterations".

The general scheme of the numerical algorithm to solve the equilibrium of the structure at time step $s+1$ is illustrated in Fig. IV.3-1. The symbols that appear in this figure have been explained in Section III.2.2 when discussing the numerical implementation of the uniaxial concrete model.

$$\text{step} = 0$$

STEP = STEP + 1

$$\underline{f}_{\text{ext}}^{(s+1)} = \underline{f}_{\text{ext}}^{(s)} + \Delta\underline{f}$$

For all IP =>

$$T^{(s+1)} = \text{data}$$

Mechanical properties at $T^{(s+1)}$

$$\underline{\varepsilon}_{th}^{(s+1)} = \underline{\varphi}\left(T^{(s+1)}\right)$$

$$\underline{\varepsilon}_{tr}^{(s+1)} = \underline{\varphi}\left(\underline{\sigma}^{(s)}, T^{(s+1)}\right)$$

iter = 0

ITER = ITER + 1

$$\underline{r}^{(i+1)} = \underline{f}_{\text{ext}} - \underline{f}_{\text{int}}^{(i)}$$

$$\Delta\underline{u}^{(i+1)} = \left(\underline{\underline{K}}^{(i)}\right)^{-1}\underline{r}^{(i+1)}$$

$$\Delta\underline{u}_{\text{tot}}^{(i+1)} = \Delta\underline{u}_{\text{tot}}^{(i)} + \Delta\underline{u}^{(i+1)}$$

$$\Delta\underline{\varepsilon}_{tot} = \underline{\underline{B}}\,\Delta\underline{u}_{tot}^{(i+1)}$$

$$\underline{\varepsilon}_{\sigma}^{(i+1)} = \underline{\varepsilon}_{tot}^{(i+1)} - \underline{\varepsilon}_{th}^{(s+1)} - \underline{\varepsilon}_{tr}^{(s+1)}$$

For all IP =>

internal iterations
find $\underline{\sigma}^{(i+1)}$ and $\underline{\underline{D}}_t^{(i+1)}$

$$\underline{\underline{K}}^{(i+1)} = \int\limits_{V} \underline{\underline{B}}^{\,t}\,\underline{\underline{D}}_t^{(i+1)}\,\underline{\underline{B}}\,dV$$

$$\underline{f}_{\text{int}}^{(i+1)} = \int\limits_{V} \underline{\underline{B}}^{\,t}\,\underline{\sigma}^{(i+1)}\,dV$$

No ◇ **Convergence?**

Yes

For all IP =>

$$\underline{\sigma}^{(s+1)} = \underline{\sigma}^{(i+1)}, \quad \underline{\varepsilon}_p^{(s+1)} = \underline{\varepsilon}_p^{(i+1)}$$
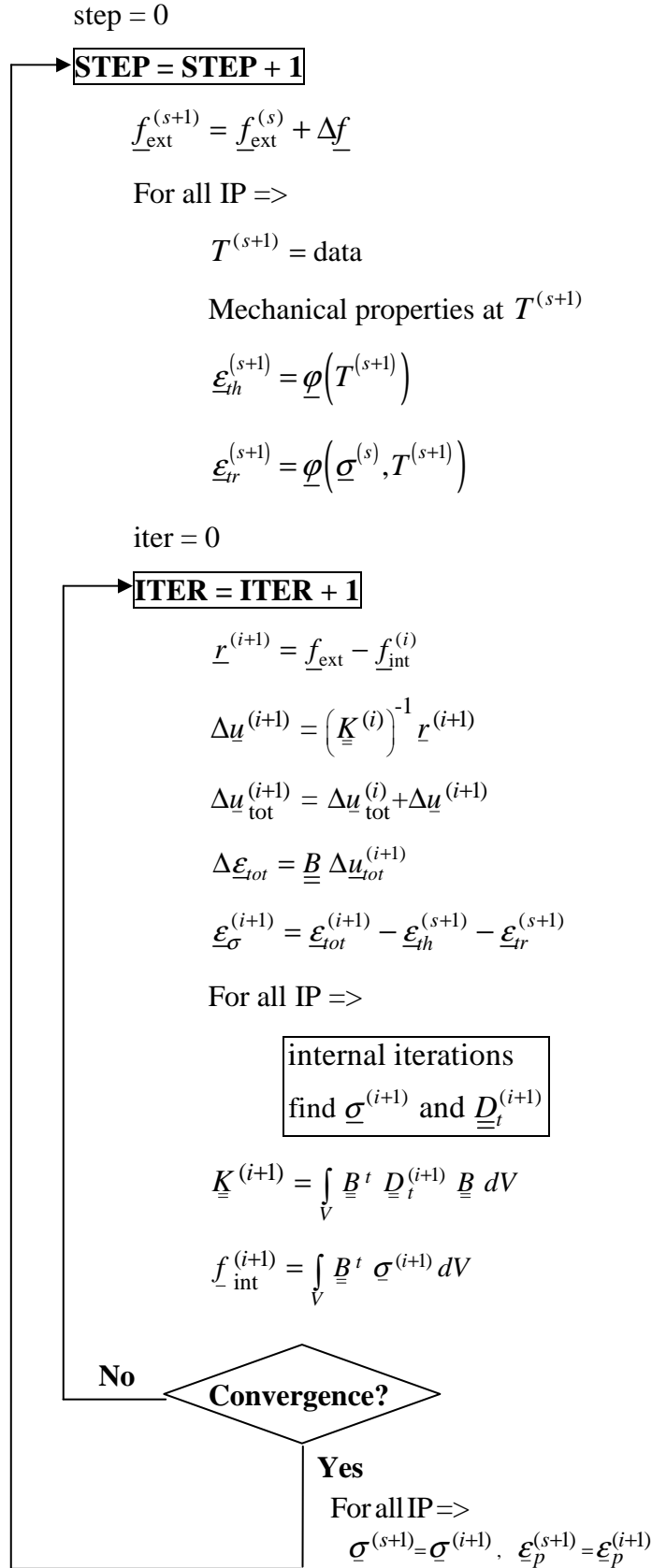
Fig. IV.3-1: General scheme of the numerical algorithm for the structure

In the following, we focus on the resolution of the internal iteration process, i.e. the update of the variables that describe the local state of the material. The problem consists in the integration of the constitutive relationship in terms of the instantaneous stress-related strain, given by Eq. IV.3-6. In this equation, the second-order tensor $\underline{\underline{D}}^{(i+1)}$ represents the damage tensor at iteration $i+1$, rewritten into a six-by-six-components matrix using Voigt notation.

$$\underline{\sigma}^{(i+1)} = \left(\underline{\underline{I}} - \underline{\underline{D}}^{(i+1)} \right) \cdot \underline{\underline{C}}_0 \cdot \left(\underline{\varepsilon}_\sigma^{(i+1)} - \underline{\varepsilon}_p^{(i+1)} \right) \qquad \text{Eq. IV.3-6}$$

The differentiation with respect to time of the constitutive relationship leads to the derivative form of Eq. IV.3-7 (Wu, et al., 2006) for the calculation of the stress rate $\dot{\underline{\sigma}}$.

$$\dot{\underline{\sigma}} = \left(\underline{\underline{I}} - \underline{\underline{w}} \right) \cdot \underline{\underline{C}}_0 \cdot \left(\dot{\underline{\varepsilon}}_\sigma - \dot{\underline{\varepsilon}}_p \right) - \left(\overline{\underline{\sigma}}^+ \dot{d}_t + \overline{\underline{\sigma}}^- \dot{d}_c \right) \qquad \text{Eq. IV.3-7}$$

In Eq. IV.3-7, the second order tensor $\underline{w}$ is obtained by applying the Voigt notation to the symmetric fourth-order tensor $\underline{\underline{W}}$ given by Eq. IV.3-8.

$$\underline{\underline{W}} = d_t \, \underline{\underline{Q}}^+ + d_c \, \underline{\underline{Q}}^- \quad ; \quad \underline{\underline{Q}}^+ = \underline{\underline{P}}^+ + 2 \sum_{i=1, j>i}^{3} \frac{\langle \overline{\sigma}_i \rangle - \langle \overline{\sigma}_j \rangle}{\overline{\sigma}_i - \overline{\sigma}_j} \, \underline{p}_{ij} \otimes \underline{p}_{ij} \quad ; \quad \underline{\underline{Q}}^- = \underline{\underline{I}} - \underline{\underline{Q}}^+ \quad \text{Eq. IV.3-8}$$

The tangent modulus of the constitutive relationship of Eq. IV.3-6 is required to be used by the finite element code in the (global equilibrium) iteration process. The derivative form of Eq. IV.3-7 is used for the calculation of the nominal algorithmic consistent tangent modulus $\underline{\underline{D}}_t^{(i+1)} = \left(d\underline{\sigma} / d\underline{\varepsilon}_\sigma \right)^{(i+1)}$. This calculation is detailed in Section IV.3.4.

The computation of the stress from the instantaneous stress-related strain using Eq. IV.3-6 is decomposed into three parts in the numerical algorithm (Wu, et al., 2006) according to the concept of operator split (Simo and Hugues, 1998). The general scheme of the numerical algorithm is given in Table IV.3-1.

First, an elastic predictor is computed assuming that the step is purely elastic. In this case, there is no variation in the plastic internal variables. As these internal variables govern the evolution laws of the model, there is no variation in the plastic strains neither in the damage variables. This elastic predictor stress state is only acceptable if it does not violate the Kuhn-Tucker conditions; if it does, a plastic corrector has to be computed to return on the yield surface. Computation of the plastic corrector is performed in the second part of the algorithm; an iterative procedure is necessary to find the increments in the plastic multipliers $\Delta \lambda_t$ and $\Delta \lambda_c$ that satisfies the Kuhn-Tucker conditions. Once these plastic multipliers have been found, it is possible to derive the plastic strains and the plastic corrector. Finally, the new damage variables can be computed in the third part. This latter operation is an explicit operation as the damage variables are driven by the plastic internal variables, which have been found previously.

Elastic predictor	Plastic corrector (iterative)	Damage corrector (explicit)
$\begin{cases} \underline{\varepsilon}_\sigma^{(i+1)} = \underline{\varepsilon}_{tot}^{(i+1)} - \underline{\varepsilon}_{th}^{(s+1)} - \underline{\varepsilon}_{tr}^{(s+1)} \\ \Delta\underline{\varepsilon}_\sigma = \underline{\varepsilon}_\sigma^{(i+1)} - \underline{\varepsilon}_\sigma^{(s)} \end{cases}$	$\Delta\underline{\varepsilon}_\sigma = 0$	$\Delta\underline{\varepsilon}_\sigma = 0$
$\begin{cases} \Delta\underline{\varepsilon}_p = 0 \\ \underline{\varepsilon}_p^{(i+1)} = \underline{\varepsilon}_p^{(s)} \end{cases}$	$\begin{cases} \Delta\underline{\varepsilon}_p = \begin{cases} \Delta\lambda_j\ \partial_{\underline{\overline{\sigma}}} G_j \text{ if } F_j = \dot{F}_j = 0 \\ 0 \qquad \text{otherwise} \end{cases} \\ \underline{\varepsilon}_p^{(i+1)} = \underline{\varepsilon}_p^{(s)} + \Delta\underline{\varepsilon}_p \end{cases}$	$\Delta\underline{\varepsilon}_p = 0$
$\begin{cases} \Delta\kappa_t = 0 \ ; \ \Delta\kappa_c = 0 \\ \kappa_t^{(i+1)} = \kappa_t^{(s)} \ ; \ \kappa_c^{(i+1)} = \kappa_c^{(s)} \end{cases}$	$\begin{cases} \Delta\kappa_t = \Delta\lambda_t \ ; \ \Delta\kappa_c = \Delta\lambda_c \\ \kappa_j^{(i+1)} = \kappa_j^{(s)} + \Delta\lambda_j \end{cases}$	$\Delta\kappa_t = 0 \ ; \ \Delta\kappa_c = 0$
$\begin{cases} \Delta\underline{\overline{\sigma}} = \underline{\underline{C}}_0 \cdot \Delta\underline{\varepsilon}_\sigma \\ \underline{\overline{\sigma}}^{(i+1)} = \underline{\underline{C}}_0 \cdot \left(\underline{\varepsilon}_\sigma^{(i+1)} - \underline{\varepsilon}_p^{(s)} \right) \end{cases}$	$\begin{cases} \Delta\underline{\overline{\sigma}} = -\underline{\underline{C}}_0 \cdot \Delta\underline{\varepsilon}_p \\ \underline{\overline{\sigma}}^{(i+1)} = \underline{\underline{C}}_0 \cdot \left(\underline{\varepsilon}_\sigma^{(i+1)} - \underline{\varepsilon}_p^{(i+1)} \right) \end{cases}$	$\Delta\underline{\overline{\sigma}} = 0$
$\begin{cases} \Delta d_t = 0 \ ; \ \Delta d_c = 0 \\ d_t^{(i+1)} = d_t^{(s)} \ ; \ d_c^{(i+1)} = d_c^{(s)} \end{cases}$	$\begin{cases} \Delta d_t = 0 \ ; \ \Delta d_c = 0 \\ d_t^{(i+1)} = d_t^{(s)} \ ; \ d_c^{(i+1)} = d_c^{(s)} \end{cases}$	$\begin{cases} \Delta d_j = \begin{cases} f\left(\kappa_j^{(i+1)}\right) \text{if } F_j = \dot{F}_j = 0 \\ 0 \qquad \text{otherwise} \end{cases} \\ d_j^{(i+1)} = d_j^{(s)} + \Delta d_j \end{cases}$
$\begin{cases} \Delta\underline{\sigma} = \left(\underline{\underline{I}} - \underline{\underline{w}} \right) \cdot \underline{\underline{C}}_0 \cdot \Delta\underline{\varepsilon}_\sigma \\ \underline{\sigma}^{(i+1)} = \left(1 - d_t^{(s)}\right) \underline{\overline{\sigma}}^{+(i+1)} \\ \qquad + \left(1 - d_c^{(s)}\right) \underline{\overline{\sigma}}^{-(i+1)} \end{cases}$	$\begin{cases} \Delta\underline{\sigma} = -\left(\underline{\underline{I}} - \underline{\underline{w}} \right) \cdot \underline{\underline{C}}_0 \cdot \Delta\underline{\varepsilon}_p \\ \underline{\sigma}^{(i+1)} = \left(1 - d_t^{(s)}\right) \underline{\overline{\sigma}}^{+(i+1)} \\ \qquad + \left(1 - d_c^{(s)}\right) \underline{\overline{\sigma}}^{-(i+1)} \end{cases}$	$\begin{cases} \Delta\underline{\sigma} = -\left(\underline{\overline{\sigma}}^+ \Delta d_t + \underline{\overline{\sigma}}^- \Delta d_c \right) \\ \underline{\sigma}^{(i+1)} = \left(1 - d_t^{(i+1)}\right) \underline{\overline{\sigma}}^{+(i+1)} \\ \qquad + \left(1 - d_c^{(i+1)}\right) \underline{\overline{\sigma}}^{-(i+1)} \end{cases}$

Table IV.3-1: Numerical algorithm scheme for the constitutive law

As the damage variables are fixed during the elastic predictor and the plastic corrector steps, solving of these two steps constitutes a standard elastoplastic problem in the effective stress space. The algorithm used to solve this elastoplastic problem is described in Section IV.3.2. Then, update of the damage variables and mapping of the effective stress vector into the nominal stress vector are explicitly performed in the damage-corrector step.

In this work, the resolution of the internal iteration process is presented in total form, which means that at each iteration the updated instantaneous stress related strain $\underline{\varepsilon}_\sigma^{(i+1)}$ and the total form of the constitutive relationship (Eq. IV.3-6) are used. Another possible approach consists in using the incremental form of the constitutive relationship; the derivative form of Eq. IV.3-7 is used to compute the increment in stress $\Delta\underline{\sigma} = \underline{\sigma}^{(i+1)} - \underline{\sigma}^{(s)}$ between time

step s and iteration $i+1$ of time step $s+1$ that corresponds to an increment in instantaneous stress related strain $\Delta\underline{\varepsilon}_\sigma$.

IV.3.2. Elastic predictor and plasticity part

In this section, the algorithm corresponding to the elastic predictor and the plastic corrector steps in Table IV.3-1 is detailed.

It is assumed that we start from a state of equilibrium at time step s. The instantaneous stress-related strains, the plastic strains and the internal variables are known, that is $\left\{\underline{\varepsilon}_\sigma^{(s)} ; \underline{\varepsilon}_p^{(s)} ; \kappa_t^{(s)} ; \kappa_c^{(s)}\right\}$. The elastic strain vector and the effective stress vector are regarded as dependent variables which are always obtained from the basic variables through the elastic stress-strain relationships in the effective space, see Eq. IV.3-9.

$$\underline{\varepsilon}_{el} = \underline{\varepsilon}_\sigma - \underline{\varepsilon}_p \quad , \quad \overline{\underline{\sigma}} = \underline{\underline{C}}_0 \cdot \underline{\varepsilon}_{el} \qquad \text{Eq. IV.3-9}$$

The instantaneous stress-related strain at iteration $i+1$ of time step $s+1$ is given by Eq. IV.3-5; the basic problem is then to update the unknowns in a manner consistent with the elastoplastic constitutive equations of the model. Namely, the effective stress $\overline{\underline{\sigma}}$, the plastic strain $\underline{\varepsilon}_p$ and the plastic hardening variables κ_t, κ_c (equivalent to the plastic multipliers λ_t, λ_c) must satisfy the stress-strain equation of Eq. IV.3-10, the incremental Kuhn-Tucker conditions of Eq. IV.3-11 and the discretized form of the evolution laws (Eq. IV.3-12 and Eq. IV.3-13).

$$\overline{\underline{\sigma}}^{(i+1)} = \underline{\underline{C}}_0 \cdot \left(\underline{\varepsilon}_\sigma^{(i+1)} - \underline{\varepsilon}_p^{(i+1)}\right) \qquad \text{Eq. IV.3-10}$$

$$\Delta\lambda_j \geq 0, \quad F_j\left(\overline{\underline{\sigma}}, \kappa_j\right) \leq 0, \quad \Delta\lambda_j\, F_j\left(\overline{\underline{\sigma}}, \kappa_j\right) = 0 \quad \mid \quad j = t, c \qquad \text{Eq. IV.3-11}$$

$$\underline{\varepsilon}_p^{(i+1)} = \underline{\varepsilon}_p^{(s)} + \Delta\lambda_t\, \frac{\partial G_t}{\partial\overline{\underline{\sigma}}} + \Delta\lambda_c\, \frac{\partial G_c}{\partial\overline{\underline{\sigma}}} \qquad \text{Eq. IV.3-12}$$

$$\kappa_t^{(i+1)} = \kappa_t^{(s)} + \Delta\lambda_t \geq 0, \quad \kappa_c^{(i+1)} = \kappa_c^{(s)} + \Delta\lambda_c \geq 0 \qquad \text{Eq. IV.3-13}$$

Update of the effective stress and the plastic variables at iteration $i+1$ of time step $s+1$ is based on the standard split into an elastic predictor and a plastic corrector using a return-mapping algorithm (Simo and Hugues, 1998). First, the trial elastic effective stress is easily computed from the instantaneous stress-related strain increment using Eq. IV.3-14.

$$\overline{\underline{\sigma}}^{tr(i+1)} = \underline{\underline{C}}_0 \cdot \left(\underline{\varepsilon}_\sigma^{(i+1)} - \underline{\varepsilon}_p^{(s)}\right) = \overline{\underline{\sigma}}^{(s)} + \underline{\underline{C}}_0 \cdot \Delta\underline{\varepsilon}_\sigma \qquad \text{Eq. IV.3-14}$$

In this latter equation, the following notation is adopted: the superscript $(i+1)$ refers to iteration $i+1$ of time step $s+1$, the superscript (s) refers to the converged value at time step

s, $\overline{\underline{\sigma}}^{tr}$ is the trial effective stress and $\Delta\underline{\varepsilon}_\sigma = \underline{\varepsilon}_\sigma^{(i+1)} - \underline{\varepsilon}_\sigma^{(s)}$ is the increment in instantaneous stress-related strain.

The trial elastic effective stress corresponds to the case where the increment of instantaneous stress-related strain $\Delta\underline{\varepsilon}_\sigma$ is purely elastic. In this case, the plastic strains and internal variables are kept constant between time step s and iteration $i+1$ of time step $s+1$ as the step is elastic, i.e. $\Delta\lambda_t = 0, \Delta\lambda_c = 0$. In order to comply with the Kuhn-Tucker conditions of Eq. IV.3-11, it remains to verify that the stress state is not outside the yields surfaces. The yield functions are computed using the trial elastic effective stress vector and the corresponding internal variables, see Eq. IV.3-15.

$$F_t\left(\overline{\underline{\sigma}}^{tr(i+1)}, \kappa_t^{(s)}\right) \leq 0 \,,\, F_c\left(\overline{\underline{\sigma}}^{tr(i+1)}, \kappa_c^{(s)}\right) \leq 0 \qquad \text{Eq. IV.3-15}$$

If Eq. IV.3-15 is satisfied, i.e. if the trial stress is not outside the yield surfaces, the Kuhn-Tucker conditions and the consistency condition are satisfied and the stress state is acceptable. In this case, the step is elastic and the updated variables at iteration $i+1$ of time step $s+1$ are given by Eq. IV.3-16. The tangent matrix is equal to the elastic stiffness matrix, $\underline{\underline{D}}_t = \underline{\underline{C}}_0$

$$\begin{cases} \underline{\varepsilon}_p^{(i+1)} = \underline{\varepsilon}_p^{(s)} \\ \kappa_t^{(i+1)} = \kappa_t^{(s)} \\ \kappa_c^{(i+1)} = \kappa_c^{(s)} \\ \overline{\underline{\sigma}}^{(i+1)} = \overline{\underline{\sigma}}^{tr(i+1)} \end{cases} \qquad \text{Eq. IV.3-16}$$

Yet, if Eq. IV.3-15 is not satisfied, the trial elastic effective stress vector is outside the yield surface and plastic strains develop in the material between time step s and (iteration $i+1$ of) time step $s+1$. The effective stress vector has to be corrected according to Eq. IV.3-17 to satisfy with the Kuhn-Tucker conditions.

$$\overline{\underline{\sigma}}^{(i+1)} = \overline{\underline{\sigma}}^{tr(i+1)} - \underline{\underline{C}}_0 \cdot \Delta\underline{\varepsilon}_p \qquad \text{Eq. IV.3-17}$$

The plastic strain increment $\Delta\underline{\varepsilon}_p$ can be eliminated from the problem by substituting Eq. IV.3-12 in Eq. IV.3-17, which leads to the expression of Eq. IV.3-18.

$$\overline{\underline{\sigma}}^{(i+1)} = \overline{\underline{\sigma}}^{tr(i+1)} - \underline{\underline{C}}_0 \cdot \left(\Delta\lambda_t \frac{\partial G_t\left(\overline{\underline{\sigma}}^{(i+1)}\right)}{\partial \overline{\underline{\sigma}}} + \Delta\lambda_c \frac{\partial G_c\left(\overline{\underline{\sigma}}^{(i+1)}\right)}{\partial \overline{\underline{\sigma}}} \right) \qquad \text{Eq. IV.3-18}$$

The first derivative of the compressive plastic potential G_c can be expressed as an explicit function of the effective stress using matrix notations, see Eq. IV.3-19 to Eq. IV.3-21.

$$G_c = \sqrt{3\bar{J}_2} + \alpha_g \, \bar{I}_1 = \left[\frac{1}{2} \bar{\sigma} \cdot \underline{\underline{P_2}} \cdot \bar{\sigma} \right]^{1/2} + \alpha_g \, \underline{1} \cdot \bar{\sigma} \qquad \text{Eq. IV.3-19}$$

$$\frac{\partial G_c}{\partial \bar{\sigma}} = \frac{\underline{\underline{P_2}} \cdot \bar{\sigma}}{2 \, \psi_2} + \alpha_g \, \underline{1} \qquad \text{Eq. IV.3-20}$$

$$\underline{\underline{P_2}} = \begin{bmatrix} 2 & -1 & -1 & 0 & 0 & 0 \\ -1 & 2 & -1 & 0 & 0 & 0 \\ -1 & -1 & 2 & 0 & 0 & 0 \\ 0 & 0 & 0 & 6 & 0 & 0 \\ 0 & 0 & 0 & 0 & 6 & 0 \\ 0 & 0 & 0 & 0 & 0 & 6 \end{bmatrix} ; \ \underline{1}^T = \{1;1;1;0;0;0\}; \ \psi_2 = \left(\frac{1}{2} \bar{\sigma} \cdot \underline{\underline{P_2}} \cdot \bar{\sigma} \right)^{1/2} \qquad \text{Eq. IV.3-21}$$

However, the first derivative of the tensile plastic potential G_t cannot be expressed explicitly as a function of the effective stress in a generalized multiaxial stress state. Indeed, this derivative depends on $\underline{n}_I$, the normalized eigenvector corresponding to the first principal effective stress; in tensorial notation, this derivative is given by $\partial G_t / \partial \bar{\sigma} = \underline{n}_I \otimes \underline{n}_I$.

As a consequence, the expression of the updated effective stress at (iteration $i+1$ of) time step $s+1$ is an implicit function of the plastic multipliers $\{\Delta\lambda_t, \Delta\lambda_c\}$, see Eq. IV.3-22; it is not possible to derive explicitly the expression of $\bar{\sigma}^{(i+1)} = \underline{f}(\Delta\lambda_t, \Delta\lambda_c)$ in the general case because the normalized eigenvector $\underline{n}_I$ of the first principal effective stress has to be computed. Therefore an iterative procedure has to be implemented for solving Eq. IV.3-22 for a given value of the plastic multipliers $\{\Delta\lambda_t, \Delta\lambda_c\}$. Yet, this operation is needed at each internal iteration in the plastic corrector step, since the effective stress has to be evaluated each time that the plastic multipliers are corrected in order to check the Kuhn-Tucker conditions. This operation introduces thus a third level of iterations in the numerical algorithm. As an alternative, a simplified scheme can be applied to evaluate the effective stress for a given value of the plastic multipliers $\{\Delta\lambda_t, \Delta\lambda_c\}$. For instance, it can be decided to compute the expression of $\partial G_t / \partial \bar{\sigma}$ in the trial effective stress state $\bar{\sigma}^{tr(i+1)}$. In this work, the equation is solved by an iterative procedure using the Newton method. Although this choice leads to a third level of iterations in the algorithm and therefore has a cost in terms of CPU time, it has been preferred to the simplified scheme because it gives a more accurate evaluation of the effective stress for a given value of the plastic multipliers and therefore it can improve the convergence of the return mapping process, with consequences in terms of numerical robustness.

$$\bar{\sigma}^{(i+1)} = \bar{\sigma}^{tr(i+1)} - \underline{\underline{C}}_0 \cdot \left(\Delta\lambda_t \, \frac{\partial G_t \left(\bar{\sigma}^{(i+1)} \right)}{\partial \bar{\sigma}} + \Delta\lambda_c \left(\frac{\underline{\underline{P_2}} \cdot \bar{\sigma}^{(i+1)}}{2 \, \psi_2^{(i+1)}} + \alpha_g \, \underline{1} \right) \right) \qquad \text{Eq. IV.3-22}$$

The set of nonlinear equations can finally be rewritten as a function of the plastic multipliers $\{\Delta\lambda_t, \Delta\lambda_c\}$ using Eq. IV.3-13 for the hardening parameters and Eq. IV.3-22 for the effective stress. By applying an implicit backward Euler difference scheme, the problem is transformed into a constrained-optimization problem governed by discrete Kuhn-Tucker conditions, with the plastic multipliers $\{\Delta\lambda_t, \Delta\lambda_c\}$ as the two unknowns, see Eq. IV.3-23.

$$\begin{cases} \Delta\lambda_t \geq 0, & F_t(\Delta\lambda_t, \Delta\lambda_c) \leq 0, & \Delta\lambda_t\, F_t(\Delta\lambda_t, \Delta\lambda_c) = 0 \\ \Delta\lambda_c \geq 0, & F_c(\Delta\lambda_t, \Delta\lambda_c) \leq 0, & \Delta\lambda_c\, F_c(\Delta\lambda_t, \Delta\lambda_c) = 0 \end{cases}$$

Eq. IV.3-23

An additional complexity in the present model is due to the fact that a multi-surface yield criterion is used. In multi-surface plasticity, the fact that a yield surface is ultimately active (at convergence) cannot be guaranteed in advance based on the trial elastic state. By definition, a yield surface F_j is termed active if $\Delta\lambda_j > 0$. In the trial elastic state, as Eq. IV.3-15 is not satisfied, it is necessary to activate either the tensile yield surface, or the compressive yield surface, or both simultaneously, to return to an admissible stress state. The initial set of active yield surfaces is determined in the trial elastic state by the condition $F_j\left(\underline{\overline{\sigma}}^{tr(i+1)}, \kappa_j^{(s)}\right) > 0$. However, this initial configuration cannot provide a sufficient criterion for determining which surface is active at the end of the time step, as the final location of the yield surfaces and the final location of their intersection are unknown at the beginning of the time step. Therefore, the set of active yield surfaces has to be updated during the iterative resolution of Eq. IV.3-23. In Simo and Hugues (1998), an algorithm is proposed for determining the set of active yield surfaces during the iterative solution procedure for multi-surface plasticity. Yet, it is assumed that the number of active yield surfaces in the final stress state is less than or equal to the number of active yield surfaces in the trial elastic state; therefore a yield surface that was inactive in the trial elastic state cannot be activated during the return-mapping. This assumption is not valid for softening plasticity (Pramono and Willam, 1989) and therefore it cannot be adopted for concrete. In their concrete model, Feenstra and de Borst (1996) allow for the activation of a yield surface during the return-mapping. This latter assumption has been adopted in the present work for determining the set of active yield surfaces in the final stress state.

The constraints c_j are introduced to indicate the current status (activated or not) of the yield function F_j. These constraints are initialized in the trial elastic state according to Eq. IV.3-24.

$$c_t = \begin{cases} 1 & if \quad F_t\left(\underline{\overline{\sigma}}^{tr(i+1)}, \kappa_t^{(s)}\right) > 0 \\ 0 & if \quad F_t\left(\underline{\overline{\sigma}}^{tr(i+1)}, \kappa_t^{(s)}\right) \leq 0 \end{cases} \quad ; \quad c_c = \begin{cases} 1 & if \quad F_c\left(\underline{\overline{\sigma}}^{tr(i+1)}, \kappa_c^{(s)}\right) > 0 \\ 0 & if \quad F_c\left(\underline{\overline{\sigma}}^{tr(i+1)}, \kappa_c^{(s)}\right) \leq 0 \end{cases}$$

Eq. IV.3-24

During the iterative resolution of Eq. IV.3-23, the set of active yield functions is updated using conditions of Eq. IV.3-25.

$$c_t = \begin{cases} 1 & if \quad \Delta\lambda_t > 0 \\ 0 & if \quad \Delta\lambda_t \leq 0 \end{cases} \quad ; \quad c_c = \begin{cases} 1 & if \quad \Delta\lambda_c > 0 \\ 0 & if \quad \Delta\lambda_c \leq 0 \end{cases} \qquad \text{Eq. IV.3-25}$$

Using these constraints, it is possible to rewrite the nonlinear equations in the two unknowns $\{\Delta\lambda_t, \Delta\lambda_c\}$ by Eq. IV.3-26.

$$\begin{cases} c_t \, F_t\left(\Delta\lambda_t, \Delta\lambda_c\right) + \left(1 - c_t\right)\Delta\lambda_t = 0 \\ c_c \, F_c\left(\Delta\lambda_t, \Delta\lambda_c\right) + \left(1 - c_c\right)\Delta\lambda_c = 0 \end{cases} \qquad \text{Eq. IV.3-26}$$

The solution of this system of equations is obtained using a Newton iterative process. We write $\underline{x}$ the vector of the unknowns: $\underline{x} = \left(\Delta\lambda_t, \Delta\lambda_c\right)^T$ and we write n the index of internal iterations performed during iteration $i+1$ of time step $s+1$; as a reminder, these internal iterations are required to solve the system of non linear equations of Eq. IV.3-26 for a given instantaneous stress-related strain $\underline{\varepsilon}_\sigma^{(i+1)}$ at iteration $i+1$ of time step $s+1$. The initial vector of the unknowns corresponds to the trial elastic state, where the plastic multipliers are null: $\underline{x}^{(0)} = \left(0, 0\right)^T$. At each iteration, the increment in the unknowns $\delta\underline{x} = \left(\delta\Delta\lambda_t, \delta\Delta\lambda_c\right)^T$ is computed by Eq. IV.3-27. In this equation, $\underline{\underline{J}}^{(n)}$ is the Jacobian matrix at iteration n and $\underline{F}_{i+1}^{(n)} = \left(F_{t,i+1}^{(n)}, F_{c,i+1}^{(n)}\right)^T$ is the vector of the yield functions evaluated at internal iteration n of (global) iteration $i+1$. The plastic multipliers at iteration $n+1$ are then computed using Eq. IV.3-28.

$$\delta\underline{x}^{(n)} = -\left(\underline{\underline{J}}^{(n)}\right)^{-1} \cdot \underline{F}_{i+1}^{(n)} \qquad \text{Eq. IV.3-27}$$

$$\underline{x}^{(n+1)} = \begin{Bmatrix} \Delta\lambda_t \\ \Delta\lambda_c \end{Bmatrix}^{(n+1)} = \begin{Bmatrix} \Delta\lambda_t \\ \Delta\lambda_c \end{Bmatrix}^{(n)} - \left(\underline{\underline{J}}^{(n)}\right)^{-1} \cdot \begin{Bmatrix} F_t\left(\Delta\lambda_t, \Delta\lambda_c\right) \\ F_c\left(\Delta\lambda_t, \Delta\lambda_c\right) \end{Bmatrix}^{(n)} = \underline{x}^{(n)} + \delta\underline{x}^{(n)} \qquad \text{Eq. IV.3-28}$$

The Jacobian matrix $\underline{\underline{J}}^{(n)}$ is calculated by Eq. IV.3-29 (Hansoulle, 2008). In this expression, the diagonal terms $\underline{\underline{J}}_{k,k}^{(n)}$ are not multiplied by the constraints c_j of the corresponding yield surface. This allows for re-activating a yield surface during the iterative process when $\Delta\lambda_j^{(n+1)}$ becomes positive. At the opposite, the out of diagonal terms $\underline{\underline{J}}_{j,k}^{(n)}$ are multiplied by the product of the constraints $c_t \times c_c$. Therefore, if one of the yield surface is not activated at iteration n, it has no influence on the increment of plastic multiplier of the other yield surface at this iteration as the out of diagonal terms are null.

$$\underline{\underline{J}}^{(n)} = \begin{pmatrix} \dfrac{\partial F_{t,i+1}^{(n)}}{\partial \Delta\lambda_t} & c_t\, c_c\, \dfrac{\partial F_{t,i+1}^{(n)}}{\partial \Delta\lambda_c} \\ c_c\, c_t\, \dfrac{\partial F_{c,i+1}^{(n)}}{\partial \Delta\lambda_t} & \dfrac{\partial F_{c,i+1}^{(n)}}{\partial \Delta\lambda_c} \end{pmatrix} \qquad \text{Eq. IV.3-29}$$

In the situation where the two yield surfaces were active at iteration n but one of the yield surface is deactivated at iteration $n+1$, because $\Delta\lambda_j^{(n+1)}$ has become negative, the influence of this yield surface on the computation of the updated plastic multiplier for the other yield surface has to be cancelled. In this case, the increment in the plastic multiplier $\delta\Delta\lambda_k^{(n)}$ for the yield surface that remains the only active yield surface at iteration $n+1$ is recomputed as $\delta\Delta\lambda_k^{(n)} = -F_{k,i+1}^{(n)}\big/J_{k,k}^{(n)}$.

The iterative process for solving the non linear system of Eq. IV.3-26 is described in Table IV.3-2 and Table IV.3-3; this numerical scheme is based on the work by Hansoulle (2008).

Initialization

$n = 0$

$$\underline{x}^{(0)} = \begin{pmatrix} \Delta\lambda_t^{(0)} \\ \Delta\lambda_c^{(0)} \end{pmatrix} = \begin{pmatrix} 0 \\ 0 \end{pmatrix}$$

$$\begin{pmatrix} \kappa_{t,i+1}^{(0)} \\ \kappa_{c,i+1}^{(0)} \end{pmatrix} = \begin{pmatrix} \kappa_{t,s} \\ \kappa_{c,s} \end{pmatrix} + \begin{pmatrix} \Delta\lambda_t^{(0)} \\ \Delta\lambda_c^{(0)} \end{pmatrix} = \begin{pmatrix} \kappa_{t,s} \\ \kappa_{c,s} \end{pmatrix}$$

$$\overline{\underline{\sigma}}_{i+1}^{(0)} = \overline{\underline{\sigma}}_{i+1}^{tr}$$

$$\underline{F}_{i+1}^{(0)} = \begin{pmatrix} F_{t,i+1}^{(0)} \\ F_{c,i+1}^{(0)} \end{pmatrix} = \begin{pmatrix} \overline{\sigma}_{I,i+1}^{(0)} - \overline{\tau}_t\left(\kappa_{t,i+1}^{(0)}\right) \\ \sqrt{3\overline{J}_{2,i+1}^{(0)}} + \alpha\,\overline{I}_{1,i+1}^{(0)} - (1-\alpha)\,\overline{\tau}_c\left(\kappa_{c,i+1}^{(0)}\right) \end{pmatrix}$$

$$c_j = \begin{cases} 1 & if \quad F_j\left(\overline{\underline{\sigma}}^{tr(i+1)}, \kappa_j^{(s)}\right) > 0 \\ 0 & if \quad F_j\left(\overline{\underline{\sigma}}^{tr(i+1)}, \kappa_j^{(s)}\right) \leq 0 \end{cases}$$

$$\underline{\underline{J}}^{(0)} = \begin{pmatrix} \dfrac{\partial F_{t,i+1}^{(0)}}{\partial\Delta\lambda_t} & c_t\,c_c\,\dfrac{\partial F_{t,i+1}^{(0)}}{\partial\Delta\lambda_c} \\ c_c\,c_t\,\dfrac{\partial F_{c,i+1}^{(0)}}{\partial\Delta\lambda_t} & \dfrac{\partial F_{c,i+1}^{(0)}}{\partial\Delta\lambda_c} \end{pmatrix}$$

Table IV.3-2: Plastic-corrector algorithm: initialization

Iterative solver

Do while $[\,|c_j\; F^{(n)}_{j,i+1}| \ge \text{tol}\quad \text{for } j = t,\, c\,]$

$$\delta \underline{x}^{(n)} = \begin{pmatrix} \delta\Delta\lambda_t^{(n)} \\ \delta\Delta\lambda_c^{(n)} \end{pmatrix} = -\left(\underline{\underline{J}}^{(n)}\right)^{-1} \times \underline{F}^{(n)}_{i+1}$$

    Do $j = t,\, c$

        $\Delta\lambda_{test} = \Delta\lambda_j^{(n)} + \delta\Delta\lambda_j^{(n)}$

        If $[\,\Delta\lambda_{test} \le 0 \text{ and } c_j = 1\,]$

            Do k = t, c

                If $[\,c_k = 1 \text{ and } k \ne j\,]\quad \delta\Delta\lambda_k^{(n)} = -F^{(n)}_{k,i+1}\big/ J^{(n)}_{k,k}$

            End do

        End if

    End do

    Do $j = t,\, c$

        $\begin{vmatrix} \Delta\lambda_j^{(n+1)} = \Delta\lambda_j^{(n)} + \delta\Delta\lambda_j^{(n)} \\[4pt] \Delta\lambda_j^{(n+1)} = \max\left(0;\Delta\lambda_j^{(n+1)}\right) \\[4pt] c_j = 1 \qquad \text{if}\left(\Delta\lambda_j^{(n+1)} > 0\right) \\[4pt] \quad = 0 \qquad\;\; \text{Otherwise} \end{vmatrix}$

    End do

$$\begin{pmatrix} \kappa_{t,i+1}^{(n+1)} \\ \kappa_{c,i+1}^{(n+1)} \end{pmatrix} = \begin{pmatrix} \kappa_{t,s} \\ \kappa_{c,s} \end{pmatrix} + \begin{pmatrix} \Delta\lambda_t^{(n+1)} \\ \Delta\lambda_c^{(n+1)} \end{pmatrix}$$

$$\overline{\underline{\sigma}}_{i+1}^{(n+1)} = f\left(\overline{\underline{\sigma}}_{i+1}^{tr}, \Delta\lambda_t^{(n+1)}, \Delta\lambda_c^{(n+1)}\right)$$

$$\underline{F}_{i+1}^{(n+1)} = \begin{pmatrix} \overline{\sigma}_{I,i+1}^{(n+1)} - \overline{\tau}_t\left(\kappa_{t,i+1}^{(n+1)}\right) \\[6pt] \sqrt{3\overline{J}_{2,i+1}^{(n+1)}} + \alpha\,\overline{I}_{1,i+1}^{(n+1)} - (1-\alpha)\,\overline{\tau}_c\left(\kappa_{c,i+1}^{(n+1)}\right) \end{pmatrix}$$

$$\underline{\underline{J}}^{(n+1)} = \begin{vmatrix} \dfrac{\partial F_{t,i+1}^{(n+1)}}{\partial\Delta\lambda_t} & c_t\,c_c\,\dfrac{\partial F_{t,i+1}^{(n+1)}}{\partial\Delta\lambda_c} \\[12pt] c_c\,c_t\,\dfrac{\partial F_{c,i+1}^{(n+1)}}{\partial\Delta\lambda_t} & \dfrac{\partial F_{c,i+1}^{(n+1)}}{\partial\Delta\lambda_c} \end{vmatrix}$$

    $n = n + 1$

End do

Table IV.3-3: Plastic-corrector algorithm: iterative solver

To compute the Jacobian matrix $\underline{\underline{J}}^{(n+1)}$, the derivatives of the yield functions F_t and F_c are calculated using the chain rule, see Eq. IV.3-30 to Eq. IV.3-33. In these equations, the functions are all evaluated using the values of the variables at internal iteration $n+1$.

$$\frac{\partial F_t\left(\overline{\underline{\sigma}},\overline{\tau}_t\right)}{\partial \Delta\lambda_t} = \frac{\partial F_t}{\partial \overline{\underline{\sigma}}}\cdot\frac{\partial \overline{\underline{\sigma}}}{\partial \Delta\lambda_t} + \frac{\partial F_t}{\partial \overline{\tau}_t}\frac{\partial \overline{\tau}_t}{\partial \Delta\lambda_t} = \frac{\partial F_t}{\partial \overline{\underline{\sigma}}}\cdot\frac{\partial \overline{\underline{\sigma}}}{\partial \Delta\lambda_t} - \frac{\partial \overline{\tau}_t}{\partial \Delta\lambda_t} \qquad \text{Eq. IV.3-30}$$

$$\frac{\partial F_c\left(\overline{\underline{\sigma}},\overline{\tau}_t\right)}{\partial \Delta\lambda_c} = \frac{\partial F_c}{\partial \overline{\underline{\sigma}}}\cdot\frac{\partial \overline{\underline{\sigma}}}{\partial \Delta\lambda_c} + \frac{\partial F_c}{\partial \overline{\tau}_c}\frac{\partial \overline{\tau}_c}{\partial \Delta\lambda_c} = \frac{\partial F_c}{\partial \overline{\underline{\sigma}}}\cdot\frac{\partial \overline{\underline{\sigma}}}{\partial \Delta\lambda_c} - (1-\alpha)\frac{\partial \overline{\tau}_c}{\partial \Delta\lambda_c} \qquad \text{Eq. IV.3-31}$$

$$\frac{\partial F_t\left(\overline{\underline{\sigma}},\overline{\tau}_t\right)}{\partial \Delta\lambda_c} = \frac{\partial F_t}{\partial \overline{\underline{\sigma}}}\cdot\frac{\partial \overline{\underline{\sigma}}}{\partial \Delta\lambda_c} + \frac{\partial F_t}{\partial \overline{\tau}_t}\frac{\partial \overline{\tau}_t}{\partial \Delta\lambda_c} = \frac{\partial F_t}{\partial \overline{\underline{\sigma}}}\cdot\frac{\partial \overline{\underline{\sigma}}}{\partial \Delta\lambda_c} \qquad \text{Eq. IV.3-32}$$

$$\frac{\partial F_c\left(\overline{\underline{\sigma}},\overline{\tau}_c\right)}{\partial \Delta\lambda_t} = \frac{\partial F_c}{\partial \overline{\underline{\sigma}}}\cdot\frac{\partial \overline{\underline{\sigma}}}{\partial \Delta\lambda_t} + \frac{\partial F_c}{\partial \overline{\tau}_c}\frac{\partial \overline{\tau}_c}{\partial \Delta\lambda_t} = \frac{\partial F_c}{\partial \overline{\underline{\sigma}}}\cdot\frac{\partial \overline{\underline{\sigma}}}{\partial \Delta\lambda_t} \qquad \text{Eq. IV.3-33}$$

The derivative of the tensile yield function with respect to the effective stress is given by Eq. IV.3-34 in the tensorial form. In this equation, $\underline{n}_I$ is the normalized eigenvector corresponding to $\overline{\sigma}_I$. The symmetric second-order tensor of Eq. IV.3-34 can be transformed into a vector of six components using the Voigt notation. The derivative of the compressive yield function with respect to the effective stress can be computed using Eq. IV.3-35.

$$\frac{\partial F_t}{\partial \overline{\underline{\underline{\sigma}}}} = \underline{n}_I \otimes \underline{n}_I \qquad \text{Eq. IV.3-34}$$

$$\frac{\partial F_c}{\partial \overline{\underline{\sigma}}} = \frac{\underline{\underline{P}}_2 \cdot \overline{\underline{\sigma}}}{2\,\psi_2} + \alpha\,\underline{1} \qquad \text{Eq. IV.3-35}$$

The derivative of the tensile effective hardening function with respect to the increment in the tensile plastic multiplier is null: $\partial\overline{\tau}_t/\partial\Delta\lambda_t = 0$. The derivative of the compressive effective hardening function with respect to the increment in the compressive plastic multiplier is given by Eq. IV.3-36 if $\kappa_c \leq \kappa_{c1}$ and by Eq. IV.3-37 if $\kappa_c > \kappa_{c1}$.

$$\frac{\partial\overline{\tau}_c}{\partial\Delta\lambda_c} = \exp\left(a_c\,\kappa_c\right)\left(a_c\,f_{c0} + \frac{2\left(f_c - f_{c0}\right)}{\kappa_{c1}\left(1+\left(\kappa_c/\kappa_{c1}\right)^2\right)}\left(a_c\,\kappa_c + \frac{\left(1-\left(\kappa_c/\kappa_{c1}\right)^2\right)}{\left(1+\left(\kappa_c/\kappa_{c1}\right)^2\right)}\right)\right) \qquad \text{Eq. IV.3-36}$$

$$\frac{\partial\overline{\tau}_c}{\partial\Delta\lambda_c} = \exp\left(\left(a_c - b_c\right)\kappa_c + b_c\,\kappa_{c1}\right)\left(f_c \times\left(a_c + b_c\left(a_c - b_c\right)\left(\kappa_c - \kappa_{c1}\right)\right)\right) \qquad \text{Eq. IV.3-37}$$

To compute the Jacobian matrix $\underline{\underline{J}}^{(n+1)}$, it remains to determine the values of the derivative of the stress with respect to the increment in the plastic multipliers. The terms $\partial\overline{\underline{\sigma}}/\partial\Delta\lambda_j$ are developed using Eq. IV.3-38 to Eq. IV.3-40. Finally, the Jacobian matrix $\underline{\underline{J}}^{(n+1)}$

---

is computed using the equations in Table IV.3-4. The functions that appear in these equations are evaluated at internal iteration $n+1$ of iteration $i+1$ of time step $s+1$.

$$\bar{\sigma} = \bar{\sigma}^{tr} - \underline{\underline{C}}_0 \cdot \left(\Delta\lambda_t \frac{\partial G_t}{\partial \bar{\sigma}} + \Delta\lambda_c \frac{\partial G_c}{\partial \bar{\sigma}} \right) \qquad \text{Eq. IV.3-38}$$

$$\frac{\partial \bar{\sigma}}{\partial \Delta\lambda_t} = -\underline{\underline{C}}_0 \cdot \left[\left(\frac{\partial G_t}{\partial \bar{\sigma}} + \Delta\lambda_t \frac{\partial^2 G_t}{\partial \bar{\sigma} \otimes \partial \bar{\sigma}} \cdot \frac{\partial \bar{\sigma}}{\partial \Delta\lambda_t} \right) + \Delta\lambda_c \frac{\partial^2 G_c}{\partial \bar{\sigma} \otimes \partial \bar{\sigma}} \cdot \frac{\partial \bar{\sigma}}{\partial \Delta\lambda_t} \right]$$

$$= -\underline{\underline{C}}_0 \cdot \frac{\partial G_t}{\partial \bar{\sigma}} - \left[\Delta\lambda_t \, \underline{\underline{C}}_0 \cdot \frac{\partial^2 G_t}{\partial \bar{\sigma} \otimes \partial \bar{\sigma}} + \Delta\lambda_c \, \underline{\underline{C}}_0 \cdot \frac{\partial^2 G_c}{\partial \bar{\sigma} \otimes \partial \bar{\sigma}} \right] \cdot \frac{\partial \bar{\sigma}}{\partial \Delta\lambda_t} \qquad \text{Eq. IV.3-39}$$

$$\frac{\partial \bar{\sigma}}{\partial \Delta\lambda_c} = -\underline{\underline{C}}_0 \cdot \left[\Delta\lambda_t \frac{\partial^2 G_t}{\partial \bar{\sigma} \otimes \partial \bar{\sigma}} \cdot \frac{\partial \bar{\sigma}}{\partial \Delta\lambda_c} + \left(\frac{\partial G_c}{\partial \bar{\sigma}} + \Delta\lambda_c \frac{\partial^2 G_c}{\partial \bar{\sigma} \otimes \partial \bar{\sigma}} \cdot \frac{\partial \bar{\sigma}}{\partial \Delta\lambda_c} \right) \right]$$

$$= -\underline{\underline{C}}_0 \cdot \frac{\partial G_c}{\partial \bar{\sigma}} - \left[\Delta\lambda_t \, \underline{\underline{C}}_0 \cdot \frac{\partial^2 G_t}{\partial \bar{\sigma} \otimes \partial \bar{\sigma}} + \Delta\lambda_c \, \underline{\underline{C}}_0 \cdot \frac{\partial^2 G_c}{\partial \bar{\sigma} \otimes \partial \bar{\sigma}} \right] \cdot \frac{\partial \bar{\sigma}}{\partial \Delta\lambda_c} \qquad \text{Eq. IV.3-40}$$

$$\underline{\underline{J}}^{(n+1)} = \begin{pmatrix} \dfrac{\partial F_t}{\partial \bar{\sigma}} \cdot \dfrac{\partial \bar{\sigma}}{\partial \Delta\lambda_t} - \dfrac{\partial \bar{\tau}_t}{\partial \Delta\lambda_t} & c_t \, c_c \dfrac{\partial F_t}{\partial \bar{\sigma}} \cdot \dfrac{\partial \bar{\sigma}}{\partial \Delta\lambda_c} \\[3mm] c_c \, c_t \dfrac{\partial F_c}{\partial \bar{\sigma}} \cdot \dfrac{\partial \bar{\sigma}}{\partial \Delta\lambda_t} & \dfrac{\partial F_c}{\partial \bar{\sigma}} \cdot \dfrac{\partial \bar{\sigma}}{\partial \Delta\lambda_c} - (1-\alpha)\dfrac{\partial \bar{\tau}_c}{\partial \Delta\lambda_c} \end{pmatrix}^{(n+1)} \qquad \text{Eq. IV.3-41}$$

$$\frac{\partial \bar{\sigma}}{\partial \Delta\lambda_t} = -\left[\underline{\underline{I}} + \Delta\lambda_t \, \underline{\underline{C}}_0 \cdot \frac{\partial^2 G_t}{\partial \bar{\sigma} \otimes \partial \bar{\sigma}} + \Delta\lambda_c \, \underline{\underline{C}}_0 \cdot \frac{\partial^2 G_c}{\partial \bar{\sigma} \otimes \partial \bar{\sigma}} \right]^{-1} \cdot \underline{\underline{C}}_0 \cdot \frac{\partial G_t}{\partial \bar{\sigma}} \qquad \text{Eq. IV.3-42}$$

$$\frac{\partial \bar{\sigma}}{\partial \Delta\lambda_c} = -\left[\underline{\underline{I}} + \Delta\lambda_t \, \underline{\underline{C}}_0 \cdot \frac{\partial^2 G_t}{\partial \bar{\sigma} \otimes \partial \bar{\sigma}} + \Delta\lambda_c \, \underline{\underline{C}}_0 \cdot \frac{\partial^2 G_c}{\partial \bar{\sigma} \otimes \partial \bar{\sigma}} \right]^{-1} \cdot \underline{\underline{C}}_0 \cdot \frac{\partial G_c}{\partial \bar{\sigma}} \qquad \text{Eq. IV.3-43}$$

Table IV.3-4: Jacobian matrix used to find the plastic-corrector

The equations given in Table IV.3-4 allow for computing the Jacobian at each (internal) iteration. In these equations, the first and second derivatives of the plastic potential functions G_t and G_c are required. The first derivative of the plastic potential in tension is given by Eq. IV.3-34, whereas the first derivative of the plastic potential in compression is given by Eq. IV.3-35 in which the term α is replaced by α_g. The second derivative of the compressive plastic potential is given by Eq. IV.3-44.

$$\frac{\partial^2 G_c}{\partial \bar{\sigma} \otimes \partial \bar{\sigma}} = \frac{\underline{\underline{P}}_2}{2\,\psi_2} - \frac{\left(\underline{\underline{P}}_2 \cdot \bar{\sigma} \right) \otimes \left(\bar{\sigma} \cdot \underline{\underline{P}}_2 \right)}{4\,\psi_2^{\,3}} \qquad \text{Eq. IV.3-44}$$

The second derivative of the tensile plastic potential, however, cannot be computed analytically in the generalized multiaxial case. Therefore, a numerical differentiation is implemented using a finite difference approach. This numerical differentiation is based on the evaluation of the first derivative of the tensile plastic potential in slightly perturbed stress states; the kth column of the matrix is obtained by perturbing the kth component of the stress, see Eq. IV.3-45. In this equation, $\bar{\sigma}$ is the stress at internal iteration $n+1$ of iteration $i+1$ of time step $s+1$ and ς is a small perturbation applied to the kth component of $\bar{\sigma}$.

$$\left.\frac{\partial^2 G_t}{\partial \bar{\sigma} \otimes \partial \bar{\sigma}}\right|_{l,k} = \left(\frac{\partial G_t(\bar{\sigma} + \varsigma e_k)}{\partial \bar{\sigma}} - \frac{\partial G_t(\bar{\sigma} - \varsigma e_k)}{\partial \bar{\sigma}}\right)\frac{1}{2 \times \varsigma} \qquad \text{Eq. IV.3-45}$$

The process of computing the Jacobian using the exact form of Table IV.3-4, that has to be performed at each internal iteration, is quite heavy because of the computation of the second derivative of the tensile plastic potential. Therefore, it can be chosen to neglect the second order terms in the evaluation of the Jacobian. In this case, the Jacobian given by Eq. IV.3-41 simplifies into the expression of Eq. IV.3-46.

$$\underline{\underline{J}}^{(n+1)} = \begin{pmatrix} -\dfrac{\partial F_t}{\partial \bar{\sigma}} \cdot \underline{\underline{C}}_0 \cdot \dfrac{\partial G_t}{\partial \bar{\sigma}} - \dfrac{\partial \bar{\tau}_t}{\partial \Delta \lambda_t} & -c_t\, c_c \dfrac{\partial F_t}{\partial \bar{\sigma}} \cdot \underline{\underline{C}}_0 \cdot \dfrac{\partial G_c}{\partial \bar{\sigma}} \\[3mm] -c_c\, c_t \dfrac{\partial F_c}{\partial \bar{\sigma}} \cdot \underline{\underline{C}}_0 \cdot \dfrac{\partial G_t}{\partial \bar{\sigma}} & -\dfrac{\partial F_c}{\partial \bar{\sigma}} \cdot \underline{\underline{C}}_0 \cdot \dfrac{\partial G_c}{\partial \bar{\sigma}} - (1-\alpha)\dfrac{\partial \bar{\tau}_c}{\partial \Delta \lambda_c} \end{pmatrix}^{(n+1)} \qquad \text{Eq. IV.3-46}$$

In fact, this latter expression can also be obtained by developing the yield functions in Taylor's series and keeping only the first order terms, as is shown here below. Decomposition of the yield functions $F_{t,i+1}$ and $F_{c,i+1}$ at iteration $i+1$ of time step $s+1$ in Taylor's series at the neighbourhood of the predictor stress $\bar{\sigma}^{tr(i+1)}$ leads to the expressions of Eq. IV.3-47.

$$\begin{aligned} F_{t,i+1} &= F_{t,i+1}^{tr} + \frac{\partial F_t}{\partial \bar{\sigma}} \cdot \left(\bar{\sigma}_{i+1} - \bar{\sigma}_{i+1}^{tr}\right) + \frac{\partial F_t}{\partial \kappa_t}\left(\kappa_{t,i+1} - \kappa_{t,i}\right) + \frac{\partial F_t}{\partial \kappa_c}\left(\kappa_{c,i+1} - \kappa_{c,i}\right) \\[2mm] F_{c,i+1} &= F_{c,i+1}^{tr} + \frac{\partial F_c}{\partial \bar{\sigma}} \cdot \left(\bar{\sigma}_{i+1} - \bar{\sigma}_{i+1}^{tr}\right) + \frac{\partial F_c}{\partial \kappa_t}\left(\kappa_{t,i+1} - \kappa_{t,i}\right) + \frac{\partial F_c}{\partial \kappa_c}\left(\kappa_{c,i+1} - \kappa_{c,i}\right) \end{aligned} \qquad \text{Eq. IV.3-47}$$

After inserting Eq. IV.3-18 into Eq. IV.3-47, one eventually obtains the expressions of Eq. IV.3-48.

$$\begin{aligned} F_{t,i+1} - F_{t,i+1}^{tr} &= \left(-\frac{\partial F_t}{\partial \bar{\sigma}} \cdot \underline{\underline{C}}_0 \cdot \frac{\partial G_t}{\partial \bar{\sigma}} + \frac{\partial F_t}{\partial \kappa_t}\right)\Delta \lambda_t + \left(-\frac{\partial F_t}{\partial \bar{\sigma}} \cdot \underline{\underline{C}}_0 \cdot \frac{\partial G_c}{\partial \bar{\sigma}} + \frac{\partial F_t}{\partial \kappa_c}\right)\Delta \lambda_c \\[2mm] F_{c,i+1} - F_{c,i+1}^{tr} &= \left(-\frac{\partial F_c}{\partial \bar{\sigma}} \cdot \underline{\underline{C}}_0 \cdot \frac{\partial G_t}{\partial \bar{\sigma}} + \frac{\partial F_c}{\partial \kappa_t}\right)\Delta \lambda_t + \left(-\frac{\partial F_c}{\partial \bar{\sigma}} \cdot \underline{\underline{C}}_0 \cdot \frac{\partial G_c}{\partial \bar{\sigma}} + \frac{\partial F_c}{\partial \kappa_c}\right)\Delta \lambda_c \end{aligned} \qquad \text{Eq. IV.3-48}$$

By identification, it can be verified that the Jacobian in the neighbourhood of the predictor stress is given by Eq. IV.3-46, after noting that $\partial \bar{\tau}_j / \partial \Delta \lambda_j = \partial \bar{\tau}_j / \partial \kappa_j$. Consequently, this verification confirms that the simplified form of the Jacobian given by Eq. IV.3-46 corresponds to a first order approximation of the exact Jacobian. The decision of

using the simplified form rather than the exact form for computing the Jacobian at each internal iteration results from a compromise between the number of iterations required for convergence and the number of operations required for computation of the Jacobian, with the aim to minimize the total CPU time during the internal iteration process. In the present work, it was chosen to use the exact form given by Table IV.3-4. That decision is based on the will to limit the number of internal iterations because a third level of iterations is required at each of the internal iteration for computation of the stress.

Finally, application of the algorithm of Table IV.3-3 leads to the updated values of the plastic multipliers $\Delta\lambda_t$ and $\Delta\lambda_c$ at iteration $i+1$ of time step $s+1$. As a result, the effective stress, the plastic strain and the plastic internal variables can be updated following the plastic-corrector step described in Table IV.3-1. The next operation deals with the update of the damage variables.

IV.3.3. Damage part

The computation of the tensile and the compressive damage variables at iteration $i+1$ of time step $s+1$ is an explicit operation as these variables depend on the plastic internal variables $\kappa_t^{(i+1)}$ and $\kappa_c^{(i+1)}$, which have been determined in the plastic part of the algorithm. The tensile damage variable is computed using Eq. IV.3-49. The model parameter a_t that appears in this equation is given by Eq. IV.1-47. As this parameter does not depend on temperature, it remains constant at each time step and therefore the superscript *(s+1)* has not been applied to this parameter.

$$d_t^{(i+1)} = 1 - \left[\frac{1}{2}\exp\left(-a_t\ \kappa_t^{(i+1)}\right) + \frac{1}{2}\exp\left(-6\ a_t\ \kappa_t^{(i+1)}\right) \right] \qquad \text{Eq. IV.3-49}$$

The compressive damage variable is computed using Eq. IV.3-50. The model parameter $a_c^{(s+1)}$ that appears in this equation is calculated using Eq. IV.1-44; as this parameter depends on temperature, it is calculated at each time step when the mechanical properties at temperature $T^{(s+1)}$ are evaluated, see Fig. IV.3-1.

$$d_c^{(i+1)} = 1 - \exp\left(\ln\left(1 - d_c^{(s)}\right) - a_c^{(s+1)}\left(\kappa_c^{(i+1)} - \kappa_c^{(s)}\right) \right) \qquad \text{Eq. IV.3-50}$$

The updated damage tensor can then be computed using Eq. IV.1-6 where the projection tensors apply to the effective stress $\overline{\sigma}^{(i+1)}$ at iteration $i+1$ of time step $s+1$. Finally, the nominal stress is calculated using Eq. IV.3-51.

$$\underline{\sigma}^{(i+1)} = \left(\underline{\underline{I}} - \underline{\underline{D}}^{(i+1)}\right) \cdot \underline{\underline{C}}_0 \cdot \left(\underline{\varepsilon}_\sigma^{(i+1)} - \underline{\varepsilon}_p^{(i+1)}\right) \qquad \text{Eq. IV.3-51}$$

IV.3.4. Consistent tangent matrix

The Newton-Raphson method is used in the global iteration process for solving the equilibrium of the structure. This method is based on the estimation of a tangent stiffness matrix, which is built for the structure from the operators linking the increment of stress to the linearized increment in strain at each integration point. These operators are computed once the processes of plastic-corrector and damage-corrector have been performed, i.e. at the end of the process of internal iterations in Fig. IV.3-1. At a given integration point, the operator $\underline{\underline{D}}_{t,i+1}$ linking the increment of stress to the linearized increment in strain computed at iteration $i+1$ of time step $s+1$ is defined by Eq. IV.3-52. This operator, which is written in the nominal stress space and is derived consistently with the algorithm for updating the nominal stress, is called the nominal algorithmic consistent tangent modulus.

$$d\underline{\sigma}_{i+1} = \underline{\underline{D}}_{t,i+1} \cdot d\underline{\varepsilon}_{\sigma,i+1} \qquad \text{Eq. IV.3-52}$$

The developments leading to the expression of the nominal algorithmic consistent tangent modulus are detailed herein. In the following, the subscript $(i+1)$ has been omitted to simplify the notation; however it is noted that all the variables are evaluated at iteration $i+1$ of time step $s+1$.

Based on the rate form of the constitutive equation (Eq. IV.3-7), the total differential of the constitutive law can be written according to Eq. IV.3-53.

$$d\underline{\sigma} = \left(\underline{\underline{I}} - \underline{\underline{w}}\right) \cdot \underline{\underline{C}}_0 \cdot \left(d\underline{\varepsilon}_{\sigma} - d\underline{\varepsilon}_p\right) - \left(\overline{\underline{\sigma}}^+ d\left(d_t\right) + \overline{\underline{\sigma}}^- d\left(d_c\right)\right) \qquad \text{Eq. IV.3-53}$$

The term $\underline{\underline{C}}_0 \cdot \left(d\underline{\varepsilon}_{\sigma} - d\underline{\varepsilon}_p\right)$ that appears in Eq. IV.3-53 represents the differential form of the effective stress $d\overline{\underline{\sigma}}$.

Evaluation of the tangent modulus in the nominal stress space requires first the evaluation of the tangent modulus in the effective stress space; this effective elastoplastic consistent tangent modulus $\overline{\underline{\underline{D}}}_t$ is defined as: $d\overline{\underline{\sigma}} = \underline{\underline{C}}_0 \cdot \left(d\underline{\varepsilon}_{\sigma} - d\underline{\varepsilon}_p\right) = \overline{\underline{\underline{D}}}_t \cdot d\underline{\varepsilon}_{\sigma}$. To determine this tangent modulus, the discretized form of the flow rule is differentiated according to Eq. IV.3-54.

$$d\underline{\varepsilon}_p = \left(\Delta\lambda_t \frac{\partial^2 G_t}{\partial\overline{\underline{\sigma}} \otimes \partial\overline{\underline{\sigma}}} + \Delta\lambda_c \frac{\partial^2 G_c}{\partial\overline{\underline{\sigma}} \otimes \partial\overline{\underline{\sigma}}}\right) \cdot d\overline{\underline{\sigma}} + d\Delta\lambda_t \frac{\partial G_t}{\partial\overline{\underline{\sigma}}} + d\Delta\lambda_c \frac{\partial G_c}{\partial\overline{\underline{\sigma}}} \qquad \text{Eq. IV.3-54}$$

In this equation, $d\Delta\lambda_t$ and $d\Delta\lambda_c$ represent the differentials of the increments in the plastic multipliers at iteration $i+1$. The first and second derivatives of the plastic potentials are evaluated at $\overline{\underline{\sigma}} = \overline{\underline{\sigma}}_{i+1}$.

Using Eq. IV.3-54 to replace the expression of $d\underline{\varepsilon}_p$, the effective algorithmic relationship is defined by Eq. IV.3-55, in which $\underline{\underline{\bar{D}}}_a$ is the effective algorithmic modulus given by Eq. IV.3-56.

$$\mathrm{d}\underline{\bar{\sigma}} = \underline{\underline{\bar{D}}}_a \cdot \left(\mathrm{d}\underline{\varepsilon}_\sigma - \mathrm{d}\Delta\lambda_t \frac{\partial G_t}{\partial \underline{\bar{\sigma}}} - \mathrm{d}\Delta\lambda_c \frac{\partial G_c}{\partial \underline{\bar{\sigma}}} \right)$$

Eq. IV.3-55

$$\underline{\underline{\bar{D}}}_a = \left[\underline{\underline{C}}_0^{-1} + \Delta\lambda_t \frac{\partial^2 G_t}{\partial\underline{\bar{\sigma}} \otimes \partial\underline{\bar{\sigma}}} + \Delta\lambda_c \frac{\partial^2 G_c}{\partial\underline{\bar{\sigma}} \otimes \partial\underline{\bar{\sigma}}} \right]^{-1}$$

Eq. IV.3-56

It remains to express the terms $\mathrm{d}\Delta\lambda_t$ and $\mathrm{d}\Delta\lambda_c$ as a function of $\mathrm{d}\underline{\varepsilon}_\sigma$ to obtain the expression of the effective elastoplastic consistent tangent modulus. The consistency condition of Eq. IV.3-26 is differentiated, which leads to Eq. IV.3-57.

$$\begin{cases} c_t \left[\dfrac{\partial F_t}{\partial \underline{\bar{\sigma}}} \cdot \mathrm{d}\underline{\bar{\sigma}}_{i+1} + \dfrac{\partial F_t}{\partial \kappa_t} \mathrm{d}\Delta\lambda_t \right] + (1 - c_t)\mathrm{d}\Delta\lambda_t = 0 \\[4mm] c_c \left[\dfrac{\partial F_c}{\partial \underline{\bar{\sigma}}} \cdot \mathrm{d}\underline{\bar{\sigma}}_{i+1} + \dfrac{\partial F_c}{\partial \kappa_c} \mathrm{d}\Delta\lambda_c \right] + (1 - c_c)\mathrm{d}\Delta\lambda_c = 0 \end{cases}$$

Eq. IV.3-57

From Eq. IV.3-57, it is possible to express $\mathrm{d}\Delta\lambda_t$ and $\mathrm{d}\Delta\lambda_c$ as functions of $\mathrm{d}\underline{\varepsilon}_\sigma$. After a few operations, the relationships of Eq. IV.3-58 and Eq. IV.3-59 are obtained. The notations ∂F_t, ∂F_c, ∂G_t, ∂G_c, e_1 and e_2 that appear in these relationships are given in Eq. IV.3-60.

$$\mathrm{d}\Delta\lambda_t = \frac{-\left(\partial F_t \cdot \underline{\underline{\bar{D}}}_a \cdot \partial G_c\right)\left(\partial F_c \cdot \underline{\underline{\bar{D}}}_a\right) + \left(\partial F_c \cdot \underline{\underline{\bar{D}}}_a \cdot \partial G_c - e_2\right)\left(\partial F_t \cdot \underline{\underline{\bar{D}}}_a\right)}{\left(\partial F_t \cdot \underline{\underline{\bar{D}}}_a \cdot \partial G_t - e_1\right)\left(\partial F_c \cdot \underline{\underline{\bar{D}}}_a \cdot \partial G_c - e_2\right) - \left(\partial F_c \cdot \underline{\underline{\bar{D}}}_a \cdot \partial G_t\right)\left(\partial F_t \cdot \underline{\underline{\bar{D}}}_a \cdot \partial G_c\right)} \cdot \mathrm{d}\underline{\varepsilon}_\sigma$$

Eq. IV.3-58

$$\mathrm{d}\Delta\lambda_c = \frac{\left(\partial F_t \cdot \underline{\underline{\bar{D}}}_a \cdot \partial G_t - e_1\right)\left(\partial F_c \cdot \underline{\underline{\bar{D}}}_a\right) - \left(\partial F_c \cdot \underline{\underline{\bar{D}}}_a \cdot \partial G_t\right)\left(\partial F_t \cdot \underline{\underline{\bar{D}}}_a\right)}{\left(\partial F_t \cdot \underline{\underline{\bar{D}}}_a \cdot \partial G_t - e_1\right)\left(\partial F_c \cdot \underline{\underline{\bar{D}}}_a \cdot \partial G_c - e_2\right) - \left(\partial F_c \cdot \underline{\underline{\bar{D}}}_a \cdot \partial G_t\right)\left(\partial F_t \cdot \underline{\underline{\bar{D}}}_a \cdot \partial G_c\right)} \cdot \mathrm{d}\underline{\varepsilon}_\sigma$$

Eq. IV.3-59

$$\partial F_t = c_t \frac{\partial F_t\left(\underline{\bar{\sigma}}_{i+1}\right)}{\partial \underline{\bar{\sigma}}}, \partial F_c = c_c \frac{\partial F_c\left(\underline{\bar{\sigma}}_{i+1}\right)}{\partial \underline{\bar{\sigma}}}, \partial G_t = \frac{\partial G_t\left(\underline{\bar{\sigma}}_{i+1}\right)}{\partial \underline{\bar{\sigma}}}, \partial G_c = \frac{\partial G_c\left(\underline{\bar{\sigma}}_{i+1}\right)}{\partial \underline{\bar{\sigma}}}$$
$$e_1 = 1 - c_t\left(1 + \frac{\partial \bar{\tau}_t}{\partial \kappa_t}\right), e_2 = 1 - c_c\left(1 + \frac{\partial \bar{\tau}_c}{\partial \kappa_c}\right)$$

Eq. IV.3-60

The expressions of the plastic multipliers as a function of $\mathrm{d}\underline{\varepsilon}_\sigma$ are inserted in Eq. IV.3-55 and Eq. IV.3-56. The incremental relationship between the effective stress and the instantaneous stress-related strain can finally be expressed by Eq. IV.3-61, where the effective elastoplastic consistent tangent modulus $\underline{\underline{\bar{D}}}_t$ is given by Eq. IV.3-62.

$$\mathrm{d}\underline{\bar{\sigma}} = \underline{\underline{\bar{D}}}_a \cdot \mathrm{d}\underline{\varepsilon}_\sigma - \left(\underline{\underline{\bar{D}}}_a \cdot \partial G_t\right)\mathrm{d}\Delta\lambda_t - \left(\underline{\underline{\bar{D}}}_a \cdot \partial G_c\right)\mathrm{d}\Delta\lambda_c = \underline{\underline{\bar{D}}}_t \cdot \mathrm{d}\underline{\varepsilon}_\sigma$$

Eq. IV.3-61

$$\underline{\underline{\bar{D}}}_t = \underline{\underline{\bar{D}}}_a - \frac{-\left(\partial F_t \cdot \underline{\underline{\bar{D}}}_a \cdot \partial G_c\right)\left(\underline{\underline{\bar{D}}}_a \cdot \partial G_t\right) \otimes \left(\partial F_c \cdot \underline{\underline{\bar{D}}}_a\right) + \left(\partial F_c \cdot \underline{\underline{\bar{D}}}_a \cdot \partial G_c - e_2\right)\left(\underline{\underline{\bar{D}}}_a \cdot \partial G_t\right) \otimes \left(\partial F_t \cdot \underline{\underline{\bar{D}}}_a\right)}{\left(\partial F_t \cdot \underline{\underline{\bar{D}}}_a \cdot \partial G_t - e_1\right)\left(\partial F_c \cdot \underline{\underline{\bar{D}}}_a \cdot \partial G_c - e_2\right) - \left(\partial F_c \cdot \underline{\underline{\bar{D}}}_a \cdot \partial G_t\right)\left(\partial F_t \cdot \underline{\underline{\bar{D}}}_a \cdot \partial G_c\right)}$$

$$-\frac{\left(\partial F_t \cdot \underline{\underline{\bar{D}}}_a \cdot \partial G_t - e_1\right)\left(\underline{\underline{\bar{D}}}_a \cdot \partial G_c\right) \otimes \left(\partial F_c \cdot \underline{\underline{\bar{D}}}_a\right) - \left(\partial F_c \cdot \underline{\underline{\bar{D}}}_a \cdot \partial G_t\right)\left(\underline{\underline{\bar{D}}}_a \cdot \partial G_c\right) \otimes \left(\partial F_t \cdot \underline{\underline{\bar{D}}}_a\right)}{\left(\partial F_t \cdot \underline{\underline{\bar{D}}}_a \cdot \partial G_t - e_1\right)\left(\partial F_c \cdot \underline{\underline{\bar{D}}}_a \cdot \partial G_c - e_2\right) - \left(\partial F_c \cdot \underline{\underline{\bar{D}}}_a \cdot \partial G_t\right)\left(\partial F_t \cdot \underline{\underline{\bar{D}}}_a \cdot \partial G_c\right)}$$

Eq. IV.3-62

Once the effective elastoplastic consistent tangent modulus $\underline{\underline{\bar{D}}}_t$ has been derived, the nominal algorithmic consistent tangent modulus $\underline{\underline{D}}_t$ can be calculated. The total differential of the constitutive law in the nominal stress space is rewritten in Eq. IV.3-63.

$$d\underline{\sigma} = \left(\underline{\underline{I}} - \underline{\underline{w}}\right) \cdot \underline{\underline{\bar{D}}}_t \cdot d\underline{\varepsilon}_\sigma - \left(\underline{\bar{\sigma}}^+ d\left(d_t\right) + \underline{\bar{\sigma}}^- d\left(d_c\right)\right)$$

Eq. IV.3-63

The differentials of the tensile and the compressive damage variables are calculated by Eq. IV.3-64 and Eq. IV.3-65 respectively.

$$d\left(d_t\right) = \left(\frac{a_t}{2}\exp\left(-a_t \, \kappa_t\right) + \frac{6a_t}{2}\exp\left(-6 \, a_t \, \kappa_t\right)\right) d\Delta\lambda_t$$

Eq. IV.3-64

$$d\left(d_c\right) = a_c \exp\left(-a_c \, \kappa_c\right) d\Delta\lambda_c$$

Eq. IV.3-65

The differentials of the increment in plastic multipliers that appear in these expressions have to be eliminated using Eq. IV.3-58 and Eq. IV.3-59. For convenience, the expressions of the increment in plastic multipliers are rewritten as: $d\Delta\lambda_t = \underline{v}_t \cdot d\underline{\varepsilon}_\sigma$ and $d\Delta\lambda_c = \underline{v}_c \cdot d\underline{\varepsilon}_\sigma$, where the vectors $\underline{v}_t$ and $\underline{v}_c$ are used to replace the large expressions of Eq. IV.3-58 and Eq. IV.3-59. Finally, the nominal algorithmic consistent tangent modulus $\underline{\underline{D}}_t$ is obtained, see Eq. IV.3-66.

$$\underline{\underline{D}}_t = \left.\frac{d\underline{\sigma}}{d\underline{\varepsilon}_\sigma}\right|_{i+1} = \left(\underline{\underline{I}} - \underline{\underline{w}}\right) \cdot \underline{\underline{\bar{D}}}_t - \left(\frac{a_t}{2}\exp\left(-a_t \, \kappa_t\right) + \frac{6a_t}{2}\exp\left(-6 \, a_t \, \kappa_t\right)\right)\left(\underline{\bar{\sigma}}^+ \otimes \underline{v}_t\right)$$
$$- a_c \exp\left(-a_c \, \kappa_c\right)\left(\underline{\bar{\sigma}}^- \otimes \underline{v}_c\right)$$

Eq. IV.3-66

IV.3.5. Plane stress model

The constitutive model presented in this chapter has been developed as a fully three-dimensional multiaxial model, so that it can be applied in the most general case for any multiaxial stress state. However in many applications of structural engineering, it can be considered in the models that the structural elements develop stresses only in particular directions and therefore it is not necessary to consider three-dimensional stress states. For instance, it is usually assumed that the stress field in linear members such as beams and columns is unidirectional following the axis of the element, whereas a plane stress state is often considered in plane elements such as slabs or walls. Accordingly, the constitutive

models can be simplified when they are associated to finite elements that model these structural elements.

For linear members, a uniaxial concrete model has been developed in Chapter III. Its applicability to be used with beam finite elements has been highlighted in several numerical simulations.

The model developed in the present chapter is intended to be used with elements that develop three-dimensional stress states. Therefore the model can be applied to solid three-dimensional elements. So, it remains to treat the case of plane structural elements for which a plane stress state can be assumed.

Two strategies can be adopted to obtain a plane stress constitutive model from a fully three-dimensional model. First, the model can be rewritten considering a plane stress state. The advantage of this method is that several simplifications can be made in the equations of the model and its numerical implementation due to the consideration of a plane stress state. For instance, the first principal stress and its derivatives can be written analytically, which allows for simplifying considerably some parts of the numerical implementation. Namely, the effective stress can be expressed as an explicit function of the increment in plastic multipliers in plane stress state, which was not the case in the general three-dimensional case. However, the disadvantage of this method is that the entire model has to be rewritten and implemented separately in the numerical code. This represents a considerable amount of work and it leads to the necessity for the developer to handle two distinct models in parallel. The second strategy consists in implementing an additional piece of numerical code in the algorithm of the fully three-dimensional model to deal with the particular case of plane stress (Charras, 2010 implemented in CAST3M, 2003). The advantage of this method is its consistency as a single material model is used for the three-dimensional stress states and plane stress states; the plane stress state is indeed considered as a particular case of the most general three-dimensional stress state. The disadvantage of this method is the fact that no benefit is taken in terms of CPU time from the fact that the stress state is simplified to a plane stress state. In the present work, it was chosen to use this second strategy in order to avoid rewriting a different model for plane stress states.

The numerical solution to particularize the fully three-dimensional model to plane stress state is schematized in Table IV.3-5. In case of plane structural elements, the elastic predictor effective stress is computed using the plane stress linear-elastic stiffness matrix $\underline{\underline{C}}_0^{ps}$, see Eq. IV.3-67 and Eq. IV.3-68.

$$\overline{\underline{\sigma}}^{tr(i+1)} = \underline{\underline{C}}_0^{ps} \cdot \left(\underline{\varepsilon}_\sigma^{(i+1)} - \underline{\varepsilon}_p^{(s)} \right) \qquad\qquad \text{Eq. IV.3-67}$$

$$
\underline{\underline{C}}_0^{ps} = \frac{E}{1-\nu^2}
\begin{bmatrix}
1 & \nu & 0 & 0 & 0 & 0 \\
 & 1 & 0 & 0 & 0 & 0 \\
 & & 0 & 0 & 0 & 0 \\
 & & & 1-\nu & 0 & 0 \\
 & & & & 0 & 0 \\
 & & & & & 0
\end{bmatrix}
\qquad \text{Eq. IV.3-68}
$$

Then, an additional condition is implemented in the plastic corrector step to ensure that the process of return mapping leads to a plane stress state. In the plastic corrector step, internal iterations are performed to find the increment of the plastic multipliers that allow for returning on the yield surface (Table IV.3-2 and Table IV.3-3). In plane stress, an additional loop is implemented in the internal iteration process to ensure that, for each correction in the increment of plastic multipliers $\delta\Delta\lambda_j^{(n)}$ that is computed during the plastic corrector step, the out-of-plane component of the effective stress vector remains null: $\bar{\sigma}_{3,i+1}^{(n+1)} = 0$. This additional loop is detailed in Table IV.3-5.

Initialization

Iteration $n = 0$

Trial effective stress in plane stress $\bar{\underline{\sigma}}_{i+1}^{(0)} = \bar{\underline{\sigma}}_{i+1}^{tr}$

Initialize $test_{cp}$ to enter in the loop: $test_{cp} = 10 \times \text{tol}$

Iterative solver

Do while $[\left| c_j \, F_{j,i+1}^{(n)} \right| \geq \text{tol} \quad \text{for } j = t, \, c]$

    Save the effective stress at internal iteration n: $\bar{\underline{\sigma}}^{cp,in} = \bar{\underline{\sigma}}_{i+1}^{(n)}$

    Additional plane stress loop

    Do while $[\, test_{cp} \geq \text{tol} \,]$

        Calculate the Jacobian $\underline{\underline{J}}\left(\bar{\underline{\sigma}}_{i+1}^{(n)}\right)$

        Calculate the correction in the increment of plastic multipliers $\delta\Delta\lambda_j^{(n)}$

        Calculate the increment in effective stress $\Delta\bar{\underline{\sigma}}_{i+1}^{(n+1)} = -\delta\Delta\lambda_j^{(n)} \, \underline{\underline{C}}_0 \cdot \partial_{\bar{\underline{\sigma}}} G_j$

        $test_{cp} = \left| \Delta\bar{\sigma}_{3,i+1}^{(n+1)} + \bar{\sigma}_{3,i+1}^{(n)} \right|$

        $\begin{cases} \bar{\sigma}_3^{cp,f} = -\Delta\bar{\underline{\sigma}}_{3,i+1}^{(n+1)} \\ \bar{\sigma}_1^{cp,f} = \bar{\underline{\sigma}}_1^{cp,in} - \Delta\bar{\underline{\sigma}}_{3,i+1}^{(n+1)} \times \left(\nu/(1-\nu)\right) \\ \bar{\sigma}_2^{cp,f} = \bar{\underline{\sigma}}_2^{cp,in} - \Delta\bar{\underline{\sigma}}_{3,i+1}^{(n+1)} \times \left(\nu/(1-\nu)\right) \end{cases}$

        $\bar{\underline{\sigma}}_{i+1}^{(n)} = \bar{\underline{\sigma}}^{cp,f}$

    End do

    $\bar{\underline{\sigma}}_{i+1}^{(n+1)} = \bar{\underline{\sigma}}_{i+1}^{(n)} + \Delta\bar{\underline{\sigma}}_{i+1}^{(n+1)} \qquad \left(\bar{\sigma}_{3,i+1}^{(n+1)} = 0\right)$

    Update the internal variables $\kappa_{j,i+1}^{(n+1)}$

    Calculate the yield functions $F_j\left(\bar{\underline{\sigma}}_{i+1}^{(n+1)}\right)$

    $n = n + 1$

End do

Table IV.3-5: Algorithm for return mapping in plane stress

IV.4.   Conclusion

In this chapter, a constitutive model has been developed for the mechanical behavior of concrete under multiaxial stress states. This model can be applied at ambient temperature and in the fire situation. A numerical algorithm has been proposed for implementation of the model in a finite element software.

As the concrete model developed in the present work relies on a coupled elastoplastic-damage theory, it is well adapted to capture the different phenomena exhibited by concrete at the macroscopic level. The development of permanent strains in the material is treated in the plastic part of the model whereas the degradation of the elastic properties is handled in the damage part of the model. We used the concept of effective stress to derive the plastic response following the standard approach for elastoplasticity in the effective stress space. Then, we used a fourth-order damage tensor to map the effective stress into the nominal stress. This latter development allows for capturing properly the isotropic state of damage in concrete, including the stiffness recovery when the stress changes from tension to compression due to the closure of tensile cracks.

The number of parameters has been limited to ten in the model and all these parameters can be obtained using three simple tests. This aspect was an important requirement for the practical applicability of the model. However, the price to limit the number of parameters was notably the adoption of one assumption that can be controversial in certain cases, i.e. the decision to link damage to the plastic internal variables in the model. Recent research has shown that concrete can develop plasticity without degradation of its elastic properties at very high confinement. It was decided to exclude the extreme stress states considered in the research mentioned above from the domain of applicability of the present model, considering that these stress states are very unusual in structural (fire) engineering.

An important contribution of the present model is the consideration of the temperature effects. The original model presented in Chapter III for transient creep strain in uniaxial stress state has been generalized to multiaxial stress state based on the assumption of isotropy generally adopted in the literature. As the transient creep strain is computed explicitly in the new model, the dependency in the stress-temperature path and the irreversibility of this strain component are taken into account. Following the approach that has been adopted in uniaxial situation, the evolution laws that have been postulated in the multiaxial model allow for reproducing the response of the Eurocode 2 concrete model in a situation of uniaxial stress state and transient test. Besides, proper temperature-dependent relationships have been adopted for the material parameters. When available, these relationships were adopted from the literature, for instance the relationships given in the Eurocode for the evolution of the uniaxial compressive and tensile strength. However, models are scarce for the temperature-dependency of some concrete parameters and therefore it was necessary to develop relationships for the evolution with temperature of Poisson's ratio and for the ratio between the equibiaxial and uniaxial compressive strengths. These relationships were developed to capture the experimental results given in the literature and presented in Chapter I but it is

noted that more experimental data are needed for establishing the temperature-dependency of some of the concrete parameters.

A significant part of this chapter has focused on the numerical implementation of the model. The numerical integration of the constitutive relationship has been decomposed into the computation of an elastic predictor, a plastic corrector and finally a damage corrector, according to the concept of operator split. Among these three parts, the computation of the plastic corrector is the most complex as it is an implicit process. The use of multi-surface plasticity has lead to the necessity to update the set of active yield surfaces during the return-mapping in order to determine which surface is active at the end of the time step. A solution has been implemented taking into account the fact that a yield surface that was inactive in the trial elastic state can be activated during the return-mapping in softening plasticity. Another difficulty is related to the fact that the model is written in the most general multiaxial case. Accordingly, some analytical developments were limited, for instance for the first principal effective stress, whereas these developments can be made in plane stress and lead to simplifications in the numerical computation process. In the present work, the application of the multiaxial model to plane stress elements has been made possible by an adaptation of the plastic corrector algorithm, which allows for using a single model for the three-dimensional stress state and the plane stress state.

Due to the softening behavior of concrete, the smeared-crack approach that has been adopted in this work may result in a mesh sensitivity of the solution due to the localization of the deformations in the numerical integration process. The regularization of continuum models to avoid such mesh-dependency of the global structural response is a challenging issue that has been studied by researchers for many years; promising solutions include the development of nonlocal models or gradient models. It was considered that the development of such elaborated solutions was beyond the scope of the present work as it could be the subject of an entire research. Therefore in this work, the issue of mesh sensitivity was only partly treated through the consideration of crack energy and the introduction of a characteristic length. This characteristic length is computed as a function of the size of the finite element and allows for specifying the size of the failure process zone. However, this solution is probably adapted when a single crack develops in the structure but its validity may be questioned when numerous cracks develop, as is generally the case with reinforced concrete structures. Therefore, future works should focus on this mesh-dependency issue in order to enhance the understanding of the phenomenon and probably implement a more elaborated solution. To the author's opinion, it would be very interesting to give an insight into the implications of the different strategies of localization limiters on the results of numerical simulations for structural members in reinforced concrete. Besides, the effects related to high temperatures should be further analyzed; notably, the temperature-dependency of the crack energy in tension and in compression is still poorly documented in the literature.

CHAPTER V - NUMERICAL SIMULATIONS AND EXPERIMENTAL VALIDATION OF THE MODEL

This chapter presents the results of numerical simulations conducted with a finite element software using the concrete model developed in this thesis. The numerical simulations deal with the mechanical behavior of concrete samples and (reinforced) concrete structures at ambient and at high temperatures. The objective is to validate the concrete model and to show that it can be used for practical applications in structural fire engineering.

The chapter is divided into three parts. First, experimental tests performed in the literature on concrete samples are simulated in order to validate the ability of the concrete model to capture properly the mechanical behavior of concrete. Different tests have been selected to cover a significant range of situations in terms of loads and temperature states in the material. This first part allows us to calibrate the parameters of the model. In the second part, experimental tests performed on structural elements are simulated using the values of the material parameters previously established. These analyses validate the ability of the model to predict the behavior of structural elements at ambient and at high temperature. Finally, numerical simulations of large structures are presented in the third part of the chapter. These latter simulations apply to the structures presented in the first chapter in which membrane action develop, therefore underlining that the concrete model can be applied to real applications of structural fire engineering.

V.1. Simulation of experimental tests on concrete samples

In this section, the behavior of concrete samples is modeled in various situations of applied stress and/or temperature. The reponse obtained using the multiaxial concrete model developed in Chapter IV is compared to the experimental stress-strain response published in the literature for these sample tests. To focus on the concrete constitutive model, the numerical simulations are conducted using a single finite element; this finite element is a cube-shaped three-dimensional element made of eight nodes. During the simulations, it is verified that all the integration points in this finite element have the same stress-strain response. The numerical simulations are performed with the software SAFIR (Franssen, 2005b), which allows to verify the correct implementation of the concrete model in this software.

The simulations of the tests presented in this section allow calibrating the parameters of the model. For each test, the material parameters are calibrated to fit the experimental results. Then, at the end of this section, the different adopted values are summarized and discussed. The objective is to establish the typical values of the parameters based on simple tests on concrete samples. Then, numerical simulations of structural elements will be presented in the following section with the values of the material parameters defined on basis of the simple tests. For the numerical simulation of structural elements, no calibration of the parameters will thus be made.

V.1.1. At ambient temperature

V.1.1.1. _Uniaxial compression_

The concrete model is first tested in uniaxial compression. In the test, one side of the concrete sample is subjected to increasing negative displacement in one direction whereas the two perpendicular directions are free.

The following material parameters can be calibrated in the model based on uniaxial compression test: the uniaxial compressive strength f_c, the uniaxial peak-stress strain ε_{c1}, the compressive limit of elasticity f_{c0}, the compressive damage at peak-stress $\tilde{d}_c$, the compressive dissipated energy parameter x_c, Poisson's ratio υ and the dilatancy parameter α_g. The uniaxial compressive strength and the uniaxial peak-stress strain are determined based on the concrete behavior at peak stress. The compressive limit of elasticity is determined as the stress beyond which the response stops being linear. The compressive damage at peak-stress is calibrated based on a uniaxial loading-unloading sequence in a compression test to capture the proper degradation of the elastic properties in compression.

The compressive dissipated energy at peak-stress is calibrated to fit the softening branch in compression as this parameter affects the ductility of the response. Finally, Poisson's ratio and the dilatancy parameter are calibrated to give the proper volumetric strain response.

Four uniaxial compression tests have been simulated. Two of the tests include experimental data of the volumetric strains (van Mier, 1984; Kupfer, et al., 1969), whereas two others include several loading-unloading sequences in uniaxial compression (Karsan and Jirsa, 1969; Poinard, et al., 2010).

After proper calibration of the material parameters, the model is able to capture the experimental response in uniaxial compression, see Fig. V.1-1. The numerical results obtained with the multiaxial model agree with the experimental results. The volumetric behavior of the concrete samples, characterized by volumetric contraction followed by volumetric expansion (dilatancy), is reproduced by the model as highlighted in the two first simulations of Fig. V.1-1. The degradation of the elastic properties in compression is clearly visible when unloading-reloading sequences are performed. The numerical simulations highlight the fact that the multiaxial concrete model accounts for this degradation owing to the damage component. The set of material parameters that has been used for the different tests is given in Table V.1-1.

TEST	$f_c\,[\mathrm{MPa}]$	$f_{c0}/f_c\,[-]$	$\varepsilon_{c1}\,[\%]$	$\tilde{d}_c\,[-]$	$x_c\,[-]$	$v\,[-]$	$\alpha_g\,[-]$
Comp.(VM)	50	0.30	0.25	0.20	0.17	0.22	0.31
Comp. (Ku)	33	0.30	0.21	0.25	0.16	0.18	0.25
Comp. (Ka)	28	0.30	0.20	0.30	0.19	0.20	0.25
Comp. (P)	40	0.30	0.21	0.29	0.19	0.20	0.25

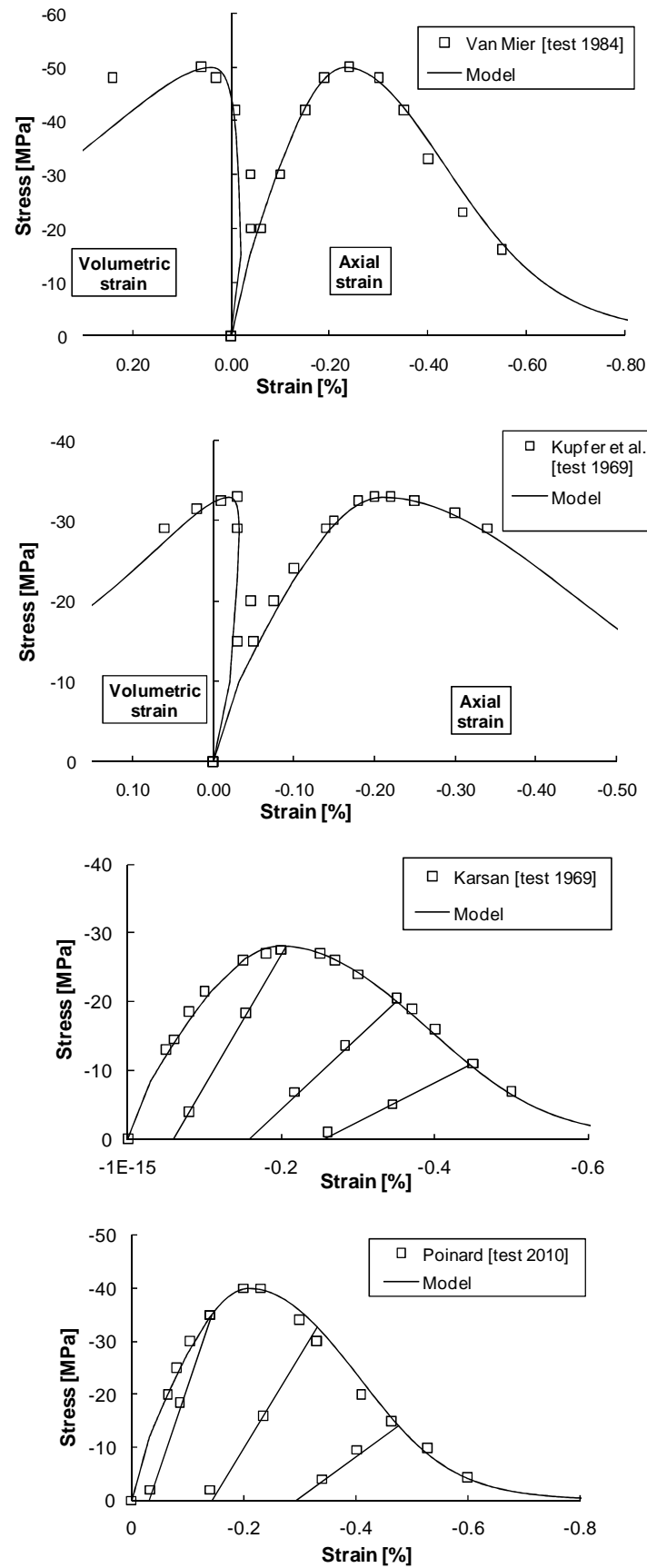Table V.1-1: Material parameters used for the numerical simulation of the compression tests

Fig. V.1-1: Measured and computed results for concrete in uniaxial compression

V.1.1.2. *Uniaxial tension*

This test deals with the behavior of concrete in uniaxial tension. The numerical results obtained with the new concrete model are compared with experimental results by Gopalaratnam and Shah (1985) in Fig. V.1-2.

The model includes two parameters that have to be calibrated on the behavior in uniaxial tension: the uniaxial tensile strength f_t and the tensile crack energy density g_t. The uniaxial tensile strength corresponds to the peak stress in uniaxial tension, whereas the tensile crack energy density affects the softening response in tension. The computed results plotted in Fig. V.1-2 have been obtained using $f_t = 3.5\,\text{MPa}$ and $g_t = 450\,\text{N/m}^2$. As shown in Section IV.1.3.2, the value of the tensile crack energy density g_t is not an intrinsic property of the material as it depends on the meshing; this mesh dependency is dealt with through the dependency in the characteristic length. However, it is not easy to evaluate this characteristic length. It can be noted that the application of the CEB formula (CEB-FIB, 1990) for the evaluation of the crack energy in tension $\bar{G}_t$ typically leads to values between 50-150 N.m/m²; accordingly, the value of g_t found here corresponds to a characteristic length l_c comprised between 0.11 m and 0.33 m, which is typically the order of magnitude of a concrete sample.
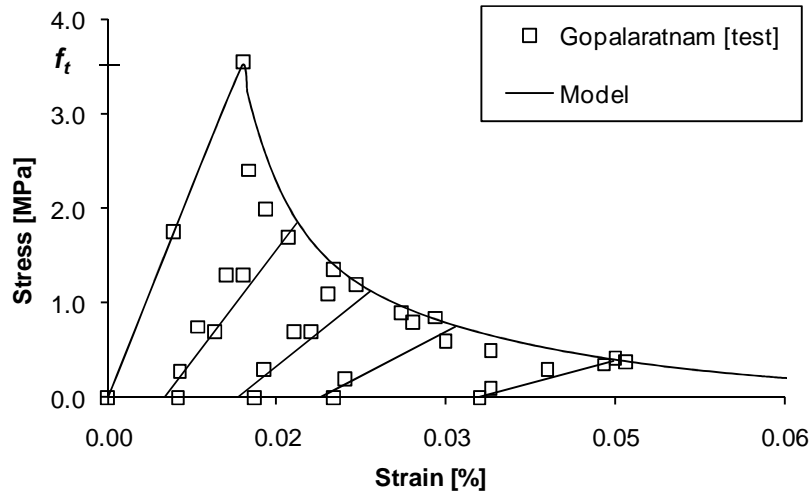

Fig. V.1-2: Measured and computed results for concrete in uniaxial tension

V.1.1.3. *Unilateral effect*

It has been shown in the previous chapter that the model is able to capture the stiffness recovery associated with the closure of tensile cracks when the stress changes from tension to compression. As shown in Fig. V.1-3, the new concrete model succeeds in capturing the degradation of the elastic properties due to tensile damage and then the stiffness recovery due to the unilateral effect, whereas the elastoplastic concrete model previously implemented in SAFIR was unable to capture these phenomena.
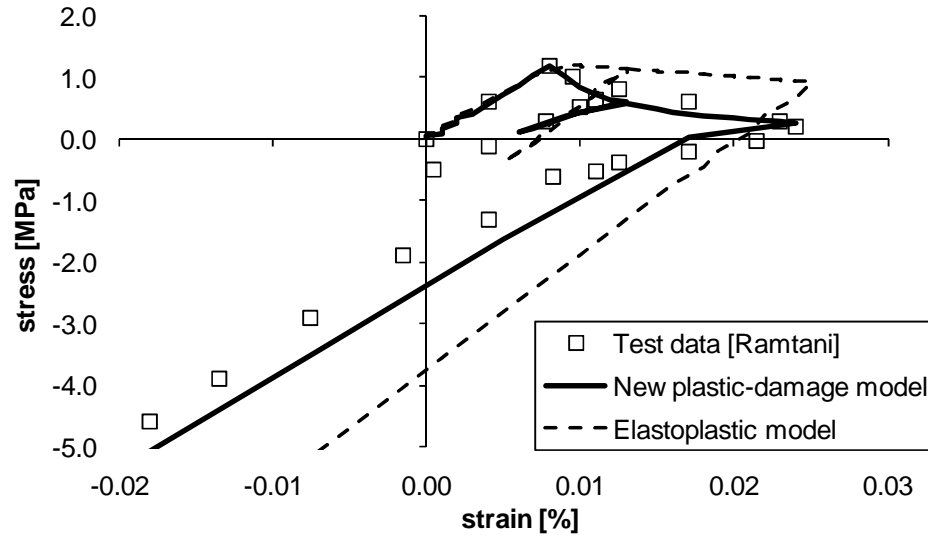
Fig. V.1-3: Measured (Ramtani, 1990) and computed results for concrete in tension-compression test

Proper modelling of the unilateral effect is an important asset of the new model as stresses variations from tension to compression are much likely to arise in concrete elements subjected to high temperatures, due to the thermal gradients that develop in the section. Indeed at the beginning of the fire, severe thermal gradients typically appear in the concrete section and these gradients cause tensile thermal stresses in the central part of the section. The concrete in the central part of the section can be subjected to tension due to these thermal stresses, see Chapter I Section I.3.2. Then, the combined effects of the progressive decrease of the thermal gradients and the stiffness decrease of the peripheral concrete, due to its temperature, lead to a decrease in the tensile thermal stresses in the central part of the section. The stress state in the central concrete thus return to compression and it is important to properly model the closure of the tensile cracks at this stage.

Besides, it is noteworthy than the new concrete model does not require any material parameter to capture the unilateral effect; this effect is automatically treated owing to the use of the fourth order damage tensor.

The set of material parameters used for the unilateral test is given in Table V.1-2.

TEST	f_c [MPa]	$\dfrac{f_{c0}}{f_c}$ [−]	f_t [MPa]	ε_{c1} [%]	$\tilde{d}_c$ [−]	x_c [−]	υ [−]	α_g [−]	g_t [Pa]
Unilateral	19	0.30	1.2	0.25	0.30	0.19	0.20	0.25	130

Table V.1-2: Material parameters used for the numerical simulation of the unilateral test

The values of the parameters obtained from calibration on the uniaxial compressive tests have been adopted for the relative compressive limit of elasticity f_{c0}/f_c, the compressive damage at peak-stress $\tilde{d}_c$, the compressive dissipated energy parameter x_c, Poisson's ratio υ and the dilatancy parameter α_g. For the tensile crack energy density g_t, a value of 130 N/m² allows for a better calibration on the softening response in tension in the

---

unilateral test, compared with the value of 450 N/m² obtained in the uniaxial tension test. This value of 130 N/m² corresponds to a characteristic length l_c comprised between 0.38 m and 1.15 m, considering that the crack energy in tension $\overline{G}_t$ is comprised between 50-150 N.m/m².

V.1.1.4. *Biaxial compression*

The multiaxial concrete model has been tested in biaxial compression; in such test, the concrete sample is subjected to compression in two directions (referred as x and y in Fig. V.1-4) whereas the third direction (z) is free. Two different situations have been considered: in the first one, the applied compressive load is the same in the two directions, whereas in the second situation the compressive load in the x-direction increases twice faster than the compressive load in the y-direction. The results of the numerical simulations have been plotted in Fig. V.1-4 and can be compared with the experimental results given by Kupfer, et al. (1969).

The biaxial compression tests are used to calibrate the biaxial compressive strength parameter $\beta_{20} = f_b / f_c$. It is found that a value of 1.16 for this latter parameter allows for a proper estimation of the increase in strength due to the confinement effect in biaxial compression; this value is typically found in the literature as was said in Chapter IV.

Table V.1-3 gives the value of the parameters used in the numerical simulations of Fig. V.1-4. The value adopted for the compressive dissipated energy parameter x_c is lower for the biaxial compression tests (0.12) compared with the uniaxial compression tests (0.17-0.19). Indeed, an increase in ductility is observed in biaxial compression compared with uniaxial compression. For the experiments simulated here, this effect is partially captured by the model when the same values are adopted for the parameters as in uniaxial compression, but the effect is still underestimated compared with the experimental response. A better calibration is obtained after decreasing the value of the parameter x_c.
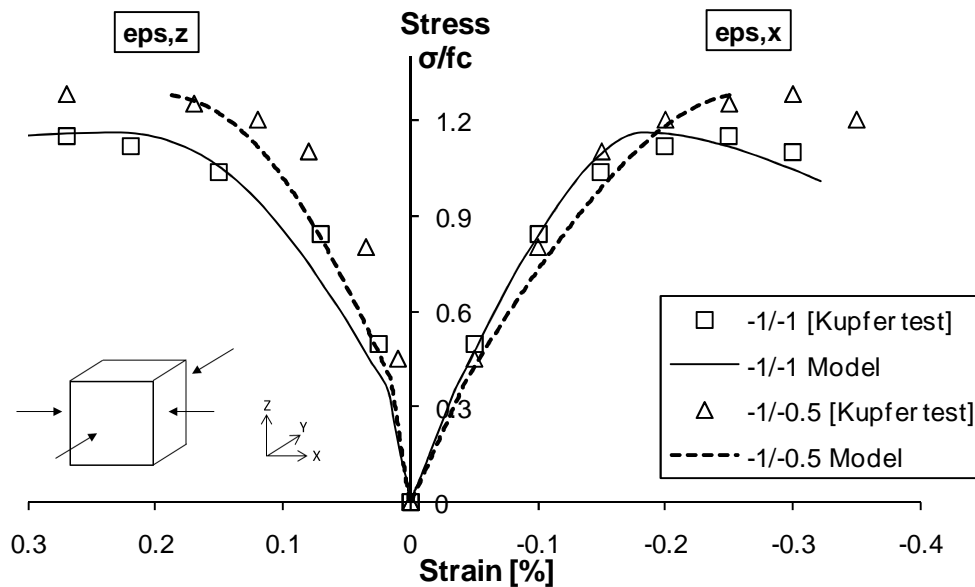

Fig. V.1-4: Measured and computed results for concrete in biaxial compression test

TEST	f_c [MPa]	f_{c0}/f_c [−]	f_b/f_c [-]	ε_{c1} [%]	$\tilde{d}_c$ [−]	x_c [−]	v [−]	α_g [−]
Bi-comp.	30	0.30	1.16	0.25	0.30	0.12	0.20	0.25

Table V.1-3: Material parameters used for the simulation of the biaxial compression tests

V.1.1.5. *Triaxial compression*

Experimental tests of triaxial compression on concrete samples have been simulated using the new concrete model. The considered tests have been presented in Chapter I. In the first series of tests, concrete samples are subjected to three levels of confinement and then to increasing deviatoric stress in one direction until failure (Imran, 1994). The second test is interested in the behavior of concrete at very high confinement level (Poinard, et al., 2010). The values of the material parameters used for the simulation of these tests are given in Table V.1-4.

TEST	f_c [MPa]	f_{c0}/f_c [−]	f_b/f_c [-]	ε_{c1} [%]	$\tilde{d}_c$ [−]	x_c [−]	v [−]	α_g [−]
Tri-comp. (I)	28.6	0.30	1.16	0.25	0.30	0.10	0.20	0.25
Tri-comp. (P)	40	0.30	1.16	0.25	0.30	0.19	0.20	0.25

Table V.1-4: Material parameters used for the simulation of the triaxial compression tests

Fig. V.1-5 presents the comparison between the computed results obtained with the new concrete model and the experimental data from Imran. The concrete, which has a uniaxial compressive strength of 28.6 MPa, was subjected to hydrostatic stress of 2.1 MPa, 8.4 MPa and 21 MPa. It is observed that the concrete strength and ductility increase with confinement; for significant confinement the behavior becomes highly ductile. The model qualitatively captures the increase of strength with increasing level of confinement but this increase of strength is underestimated by the model. Similarly, the model predicts an increase in ductility with increasing level of confinement but this effect is not as pronounced as experimentally observed.

In fact, a closer look at the results of Fig. V.1-5 shows that the model is relatively good at capturing the experimental response until it reaches the model peak stress. The increase in stiffness at the different levels of confinement is quite accurately modeled, as well as the pre-peak evolution of the transversal strains ε_1 and ε_2. The relationship between the stress and the strain in the direction of the applied deviatoric stress is also relatively well assessed until approximately $\varepsilon_3 = \varepsilon_{c1}$. Then, the model reaches a peak stress and the computed results beyond this level of strain significantly differ from the experimental results. The experimental results show that the post-peak behavior of concrete changes from softening to hardening behavior with increasing level of confinement, whereas this effect is not represented in the model and the post-peak behavior remains a softening behavior in the simulations of the three tests. At 2.1 MPa confinement ($= 0.07 \times f_c$), the experimental response exhibits softening and the computed response reasonably agree with the experimental response. However at 8.4 MPa confinement ($= 0.29 \times f_c$), the experimental response exhibits hardening and, as the model

fails at reproducing this effect, the computed response stops being accurate beyond a strain of approximately $\varepsilon_3 = 2 \times \varepsilon_{c1}$. Modeling of the concrete post-peak behavior in triaxial compression thus constitutes a limitation of the model in case of significant confinement. The following example will help to give a further insight into this limitation.
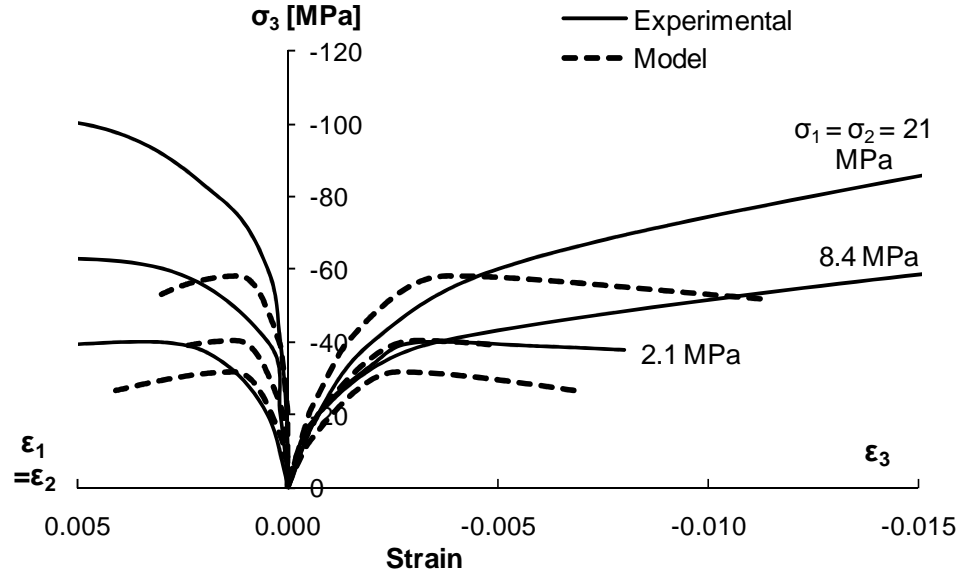

Fig. V.1-5: Measured (Imran, 1994) and computed results for concrete in triaxial compression under three levels of confinement

Fig. V.1-6 presents the comparison between the computed results obtained with the new concrete model and the experimental data from Poinard, et al. The test was conducted on a concrete cylinder of 40 MPa uniaxial compressive strength subjected to 200 MPa confinement. The sample was then subjected to increasing axial deviatoric stress. The computed response agree with the experimental results in the first part of the test, until reaching a deviatoric stress of approximately 115 MPa and an axial strain equal to $2 \times \varepsilon_{c1}$. However, the computed response beyond this level of stress completely differs from the experimental response, because the computed response then presents a softening behavior whereas the experimental results clearly indicate a hardening behavior. Very interesting information can be obtained from Poinard's test owing to the fact that several unloading-reloading sequences have been applied to the sample. Indeed, the analysis of the slope of the unloading branches indicates that no damage develops in concrete under such very high confinement level, as these unloading branches remain parallel to the initial stiffness of the material. This conclusion was underlined by the authors of the experiments (Poinard, et al., 2010) and has been discussed in the previous chapters of this thesis. On the contrary, the model assumes that damage starts to develop in the concrete as soon as plasticity develops, as these two phenomena have been linked in the model. Consequently, significant damage develops during the numerical simulation of the triaxial test; this is confirmed by the degradation of the elastic properties that can be observed on the computed curves in Fig. V.1-6. The fact that damage develops in the model for concrete under high confinement contributes to explain why the model is not able to properly capture the post-peak behavior of concrete in these situations. In order to enhance the modeling in case of important triaxial

compressive stress states, it would be necessary to govern the evolutions of plasticity and damage with distinct internal variables.
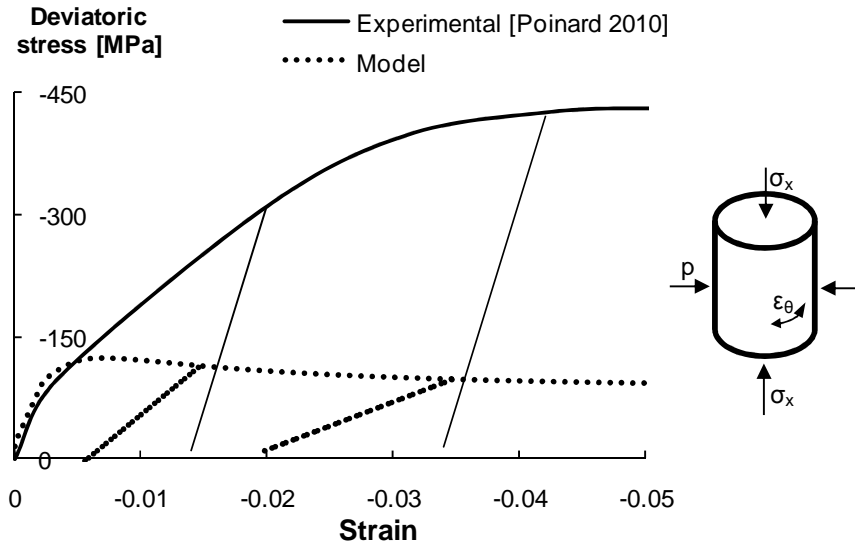

Fig. V.1-6: Measured (Poinard, et al., 2010) and computed results for concrete in triaxial compression at 200 MPa confinement

V.1.2.   At high temperature

V.1.2.1. Transient tests

The transient tests conducted by Anderberg and Thelandersson (1976) and presented in Chapter I have been simulated using the new concrete model. The numerical simulation was performed with the software SAFIR and the same single finite element model as used at ambient temperature. In the transient tests, calcareous concrete samples have been subjected to constant applied stress and increasing temperature. Three levels of applied stress α were considered, with α defined as the ratio between the applied stress and the compressive strength at ambient temperature. The values of the material parameters used for the simulation of these tests are given in Table V.1-5.

TEST	f_c [MPa]	f_{c0}/f_c [−]	f_b/f_c [-]	ε_{c1} [%]	$\tilde{d}_c$ [−]	x_c [−]	υ [−]	α_g [−]
Transient	30	0.30	1.16	0.25	0.30	0.19	0.20	0.25

Table V.1-5: Material parameters used for the simulation of the transient tests

Fig. V.1-7 gives the evolution of the axial strain as a function of the temperature for the three samples. The measured and computed results reasonably agree. The temperature at which the failure arises is well predicted by the model, as well as the decrease in total strain with increasing applied stress level during heating. The development of transient creep strain is thus accurately taken into account by the model.

The computed results show rather abrupt changes in the slope of the curves at every 100°C. This is due to the fact that the temperature-dependent laws of some parameters of the

concrete model are defined as linear interpolations between discrete values defined every 100°C. This is the case, for instance, for the compressive strength the temperature-dependent law of which has been adopted from Eurocode. It is also the case for the peak-stress strain. These laws are continuous functions of the temperature but their derivative is not continuous. The most visible abrupt change is observed at 600°C for the curve with applied stress level of 0.225. This change in the slope is directly related to the temperature-dependent law for the peak-stress strain, as in the Eurocode model this peak-stress strain varies from 0.0150 to 0.0250 between 500°C and 600°C and then remains constant beyond 600°C. As the new concrete model has been calibrated to yield the same mechanical strain as the Eurocode model in the situation of transient test, this abrupt variation in the derivative of the temperature-dependent law of the peak-stress strain is reflected on the results of Fig. V.1-7. This effect is usually not perceived in numerical simulations of concrete elements because the model usually comprises an important number of integration points which reach the transition temperatures at different times.
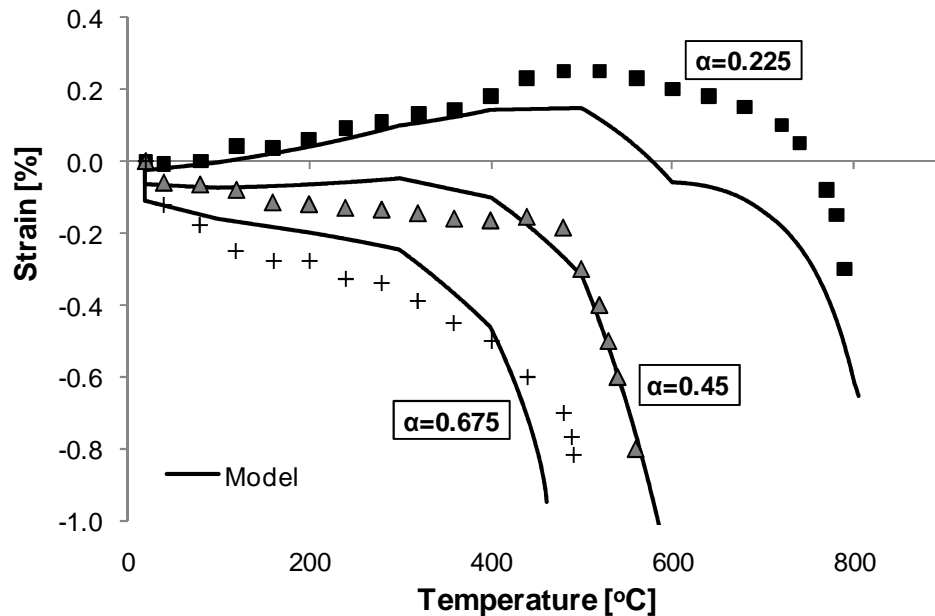

Fig. V.1-7: Measured (Anderberg and Thelandersson, 1976) and computed results for concrete in transient tests for different applied stress levels

V.1.2.2. _Biaxial compression test_

The behavior of concrete in biaxial compression at high temperature is investigated here. The experiments on siliceous concrete samples (Ehm and Schneider, 1985) presented in Chapter I have been simulated and the comparison between measured and computed results is plotted in Fig. V.1-8. In these steady-state tests, the samples are first heated and then subjected to stress increase in directions 1 and 2 simultaneously and of the same magnitude, whereas direction 3 is free. The material parameters used in the numerical simulations are given in Table V.1-6.

The concrete model qualitatively captures the decrease in stiffness and equibiaxial compressive strength with temperature. Besides, the model takes into account the experimentally observed increase in the confinement effect with increasing temperature;

namely, the decrease in equibiaxial compressive strength is less pronounced than the decrease in uniaxial compressive strength at a given temperature.

The maximum relative stress $\sigma/f_{c,20}$ yield by the numerical simulations does not fit perfectly with the experimental results at high temperatures. This is due to the fact that the concrete tested by Ehm and Schneider does not follow the Eurocode model for the decrease in the uniaxial compressive strength. For instance the uniaxial compressive strength of the tested concrete was equal to $0.610 \times f_{c,20}$ at 450°C, as indicated by the results presented in Chapter I, whereas the relationship of Eurocode yields a uniaxial compressive strength of $0.675 \times f_{c,20}$ for siliceous concrete at 450°C. In the model, the equibiaxial compressive strength at high temperature depends on the uniaxial compressive strength at high temperature. As this latter parameter is taken from Eurocode in the model, the maximum relative stress reached in equibiaxial compression at 450°C is slightly overestimated by the model due to the overestimation of the uniaxial compressive strength at this temperature.
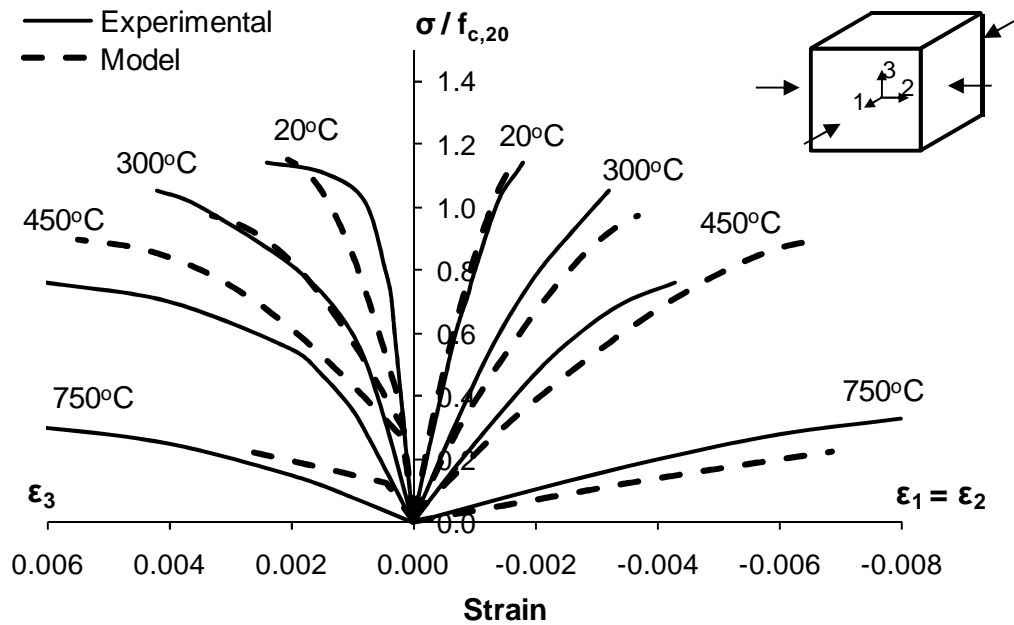

Fig. V.1-8: Measured (Ehm and Schneider, 1985) and computed results for concrete in equibiaxial compressive loading at elevated temperatures

TEST	f_c [MPa]	f_{c0}/f_c [−]	f_b/f_c [-]	ε_{c1} [%]	$\tilde{d}_c$ [−]	x_c [−]	υ [−]	α_g [−]
Bicomp.	41	0.30	1.16	0.25	0.30	0.19	0.20	0.25

Table V.1-6: Material parameters used for the simulation of the biaxial compression tests

V.1.2.3. *Uniaxial tension*

The uniaxial tension tests performed at high temperature (Felicetti and Gambarova, 1999) have been simulated using the new concrete model. The results of the numerical simulations are plotted in Fig. V.1-9, next to the experimental results.

The siliceous high strength concrete used in the test has a 5.5 MPa tensile strength at ambient temperature. For the tensile crack energy density g_t, calibration on the experimental results leads to a value of 3000 N/m². It can be seen that the softening branch of the computed and experimental results at 20°C agree very well using this value of g_t. This value of 3000 N/m² is significantly higher than the values of 130 N/m² and 450 N/m² found in the simulations of the previous tests. Yet, it is interesting to note that the CEB formula for evaluation of the crack energy in tension takes into account the mean compressive strength and therefore leads to higher values of $\overline{G}_t$ for high strength concrete than for normal concrete. As the concrete tested by Felicetti and Gambarova is a high strength concrete, this could partly explain the high value of g_t that is obtained here.

The response to uniaxial tension at high temperature is qualitatively captured by the model. As shown by the experiment, high temperatures lead to a decrease in tensile strength and a relative increase in ductility after peak stress in the model. Yet, a quantitative discrepancy is observed in Fig. V.1-9 between the computed and experimental values of the tensile strength at high temperature. It must be noted that the temperature-dependent relationship for the evolution of tensile strength in the model has been adopted from Eurocode and thus it has not been calibrated on the particular tests of Fig. V.1-9.
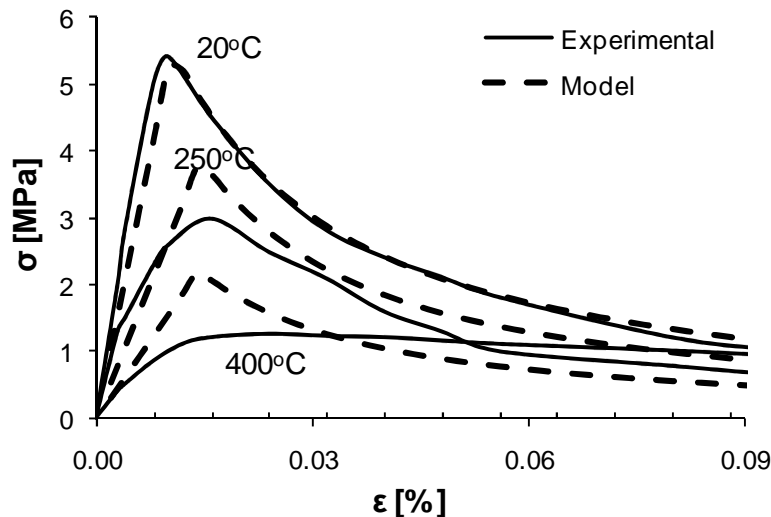

Fig. V.1-9: Measured (Felicetti and Gambarova, 1999) and computed results for concrete in uniaxial tension at high temperatures

V.1.3.   Calibration of the material parameters

In the numerical simulations of the experimental tests presented above, the material parameters have been calibrated in order to fit the experimental response. It has been shown that the model was able to reproduce the results of experimental tests in a large range of situations of applied stress and temperature. However, it is also important for the model to be available for predictive calculations in which no calibration of the parameters can be performed. Therefore, typical values of the material parameters must be indicated to the user of the model in order to provide him with a standard set of parameters that can be used when the objective is to perform a predictive calculation.

Based on the simulations performed in this section, standard values are established for seven of the parameters in the model, see Table V.1-7. These values have been found by calibration on the experimental response in uniaxial and biaxial compression tests and they have been successfully used in the numerical simulations of other tests on concrete samples. Some of these parameters varied a bit between different numerical simulations presented in this section. The peak-stress strain had been found equal to 0.20%, 0.21% and 0.25% in the uniaxial compression tests but the value of 0.25% has been adopted because it is the value given in the Eurocode. The dilatancy parameter had been calibrated to 0.25 and 0.31 in the uniaxial compression tests where the volumetric strain was recorded; the value of 0.25 has been arbitrarily chosen as recommended standard value when no additional information is available. For the compressive dissipated energy parameter x_c, values of 0.10 and 0.12 had been adopted in some of the multiaxial compression tests for better modeling of the post-peak behavior in highly confined stress states. However, the inability of the model to capture this behavior is an inherent limitation that has been discussed in Section V.1.1.5. The modification in the value of x_c only allows for improving slightly the model post-peak response in highly confined stress states but the transition from damage-brittle behavior to ductile behavior cannot be reproduced by the model. Accordingly, it was decided to consider the calibration on the uniaxial compression tests for defining the standard value of x_c and the value of 0.19 was chosen; meanwhile, it should be remembered that the model is limited in case of very high confinement level.

	f_{c0}/f_c [$-$]	f_b/f_c [-]	ε_{c1} [%]	$\tilde{d}_c$ [$-$]	x_c [$-$]	υ [$-$]	α_g [$-$]
Predictive	0.30	1.16	0.25	0.30	0.19	0.20	0.25

Table V.1-7: Standard values for the parameters of the concrete model

The model contains three additional parameters, which are the uniaxial compressive strength, the uniaxial tensile strength and the tensile crack energy density. The uniaxial compressive and tensile strengths must necessarily be specified by the user of the model as a function of the strength class of the concrete used in the project, so that no standard value can be given for these parameters. Finally, the last parameter is the tensile crack energy density. For this parameter, the calibration on the experimental tests presented in this section has lead to values that ranges from 130 N/m² to 3000 N/m². The different values were obtained by calibration of the softening response in uniaxial tension tests conducted at 20°C by different

researchers. Due to the significant scatter in the obtained results, it is not possible to provide a standard value for the parameter g_t. Meanwhile, it is noted that this parameter is not an intrinsic property of the material but depends on the parameters $\bar{G}_t$ and l_c, which are directly related to the localization issue. The localization issue is only partly treated in the present thesis; future works should give a further insight into the problem of localization and, as part of this study, they should probably conduct further analyses of the parameters $\bar{G}_t$, l_c and g_t at ambient and at high temperature if these parameters are kept in the model for regularization. In this thesis, the recommendation for calculations at ambient temperature using plane stress elements is to evaluate the value of g_t using the formula $g_t = \bar{G}_t / l_c$, in which the value of the crack energy in tension $\bar{G}_t$ is adopted in the range of typical values given by the CEB formula (50-150 N.m/m²) and the value of the characteristic length is evaluated by the formula $l_c = \sqrt{A_e}$ for quadratic finite elements. At high temperatures, it is difficult to give a recommendation as the uncertainty on these parameters is even more pronounced; see for instance the scatter in the experimental data reported in Chapter I about the temperature-dependency of the tensile crack energy. Besides, the integration of the material law may be difficult during the numerical analysis of large structures in fire and it has been observed that the numerical convergence can sometimes be improved by modifying the parameter g_t, due to the fact that this parameter affects the brittle behavior of concrete in tension. Therefore, it may be helpful for the user to have a certain freedom in the definition of the parameter g_t for numerical reasons, but of course it should then be ensured that the concrete tensile properties defined in the model do not influence the response of the studied structure. An alternative to avoid defining this parameter consists in using a tensile strength equal to 0 in the simulation.

V.2. Simulation of experimental tests on structural elements

V.2.1.   Mixed-mode fracture of plain concrete

The test simulated in this section has been experimentally studied by Nooru-Mohamed (1992); since then, it has been widely used in the literature to test the efficiency of concrete constitutive models in biaxial stress states (di Prisco, et al., 2000; Nechnech, 2000; Abu Al-Rub and Kim, 2010). The test consists in a double-edge-notched (DEN) specimen of plain concrete subjected to a loading path combining shear and tension at ambient temperature. The specimen is a square plate of 200 mm long and 50 mm thick with two symmetrical notches of 25 mm by 5 mm size. During the experiment, the specimen was fixed at the bottom and along the right hand side below the notch and the loading was applied through a loading frame that was glued to the specimen, see Fig. V.2-1. The dimensions indicated in this figure are in mm. The loading frame that was used in the experimental set-up consists of two loading plates at top and left upper parts, but a right upper part was added in the numerical simulation to prevent the numerical failure of the upper right corner of the specimen due to stress concentration; this approach was also adopted by Abu Al-Rub and Kim (2010) for the same reason.
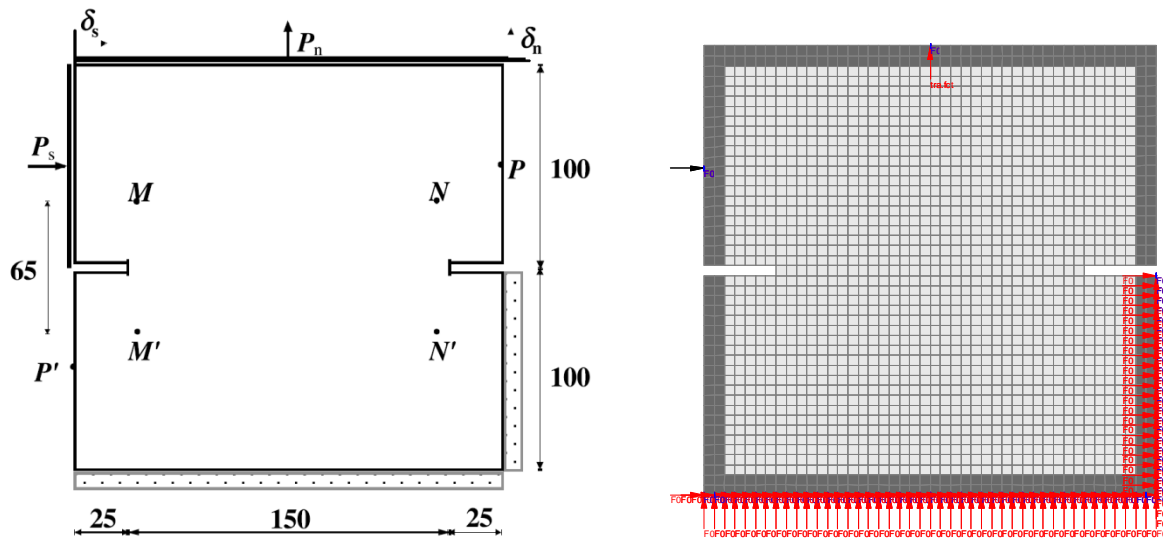

Fig. V.2-1: Geometry of the specimen (from di Prisco, et al., 2000) and FE model in SAFIR

The loading path consists in the application of a shear force followed by tension under deformation control. A shear force P_s of 5 kN is first applied through the frame along the left-hand side of the specimen above the notch. Then, a tension loading is applied by imposing a vertical displacement at the top of the specimen, while the shear force P_s remains constant equal to 5 kN. The test is continued until failure of the specimen. The vertical deformation of the specimen in the fracture zone was assessed by taking the average of the measured

displacements between the points M and M' on the left as well as between N and N' on the right.

Due to the small thickness of the specimen, the analysis is performed in plane stress condition; therefore, shell finite elements are used in SAFIR. The size of the mesh elements has been taken as 5.0 mm x 5.0 mm, see Fig. V.2-1. To reproduce the experimental support conditions, all the nodes located at the bottom edge and the lower part of the right edge are fixed (vertical and lateral displacement = 0). As the loading frame is glued to the specimen and is very stiff compared with the specimen, in the model the lines of nodes located at the top edge and the upper part of the left edge are forced to remain horizontal and vertical respectively. This condition is realized by imposing identical displacements to the nodes in the corresponding directions.

The specimen was made of normal weight concrete. Measured compressive and tensile splitting strengths of respectively 38.4 MPa and 3.0 MPa have been reported (di Prisco, et al., 2000). For the used quadratic elements of size 5.0 mm x 5.0 mm, the evaluation of the characteristic length l_c leads to: $l_c = \sqrt{A_e} = 5$ mm . Considering a typical value of 75 N.m/m² for the crack energy in tension $\bar{G}_t$, this leads to a value of 15 kN/m² for the tensile crack energy density $g_t = \bar{G}_t / l_c$. The values of the other material parameters used in the analysis are given in Table V.1-7; these values correspond to the values obtained by calibration on the simple tests presented in the first part of this chapter. No calibration of the parameters is thus required on the specimen studied here.

The final shape of the crack pattern obtained in the experiment has been reported by di Prisco, et al. (2000) and can be seen in Fig. V.2-2. This experimental crack pattern can be compared with the numerical results; the computed displacement isolines and membrane forces in the specimen have been represented in Fig. V.2-2. In the representation of the membrane forces, the color blue is used for compressive forces whereas the color red represents tensile forces. The numerical results capture the cracks propagation from the two notches and the concentration of the displacements and forces in a fracture zone in the center of the specimen. The trajectories of the crack are qualitatively captured by the numerical simulation.

The relationship between the tensile load and the average normal displacement in the direction of U is plotted in Fig. V.2-3. The computed results are compared with the experimental results. The computed initial stiffness fits almost perfectly the test results but the computed peak load is slightly overestimated. It is noteworthy that this overestimation of the computed peak load has been observed by other researchers when modelling the same experimental test (di Prisco, et al., 2000). After the peak load, the specimen exhibits a softening response. The softening regime is well reproduced, which tends to validate the value used for the crack energy in tension.
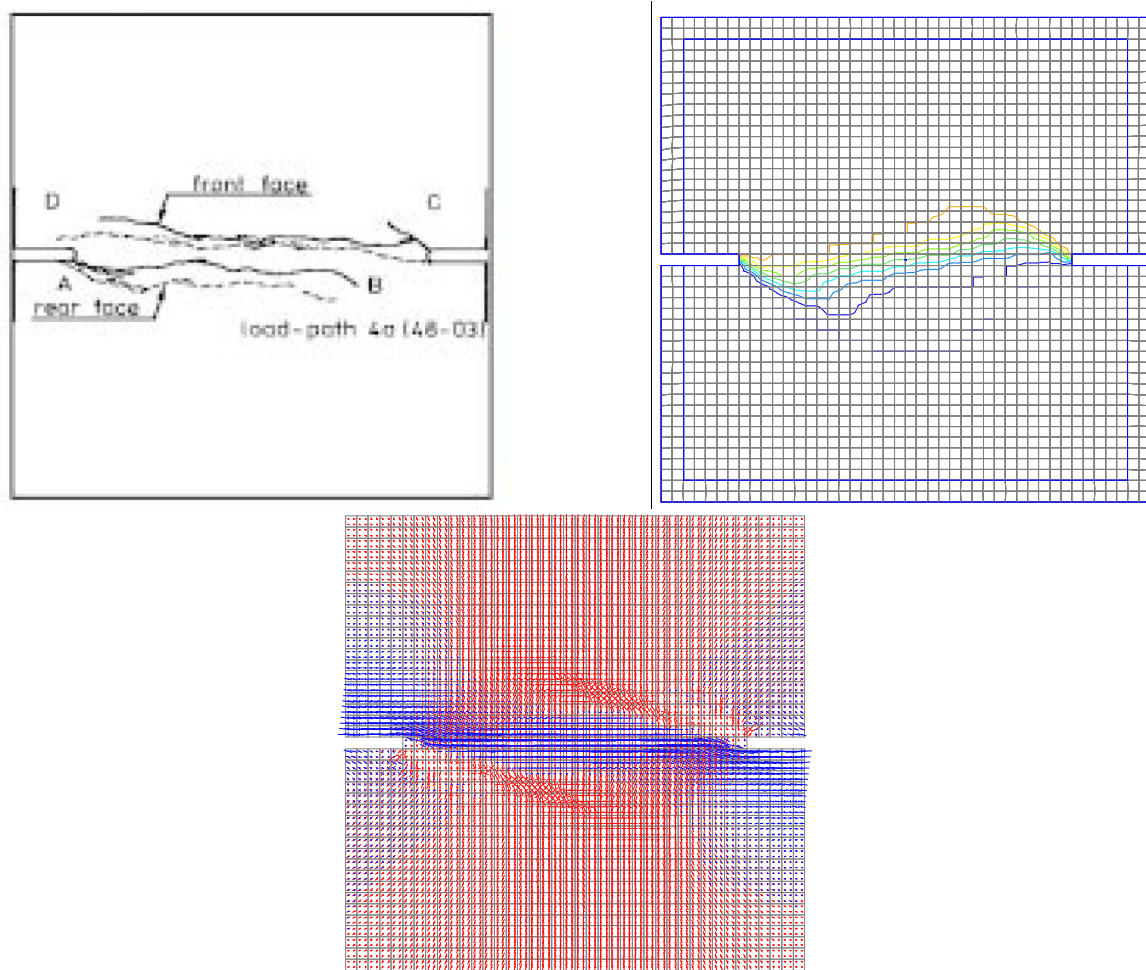
Fig. V.2-2: Crack pattern experimentally obtained by Nooru-Mohamed (upper left), displacement pattern computed with SAFIR (upper right) and membrane forces computed with SAFIR (lower)
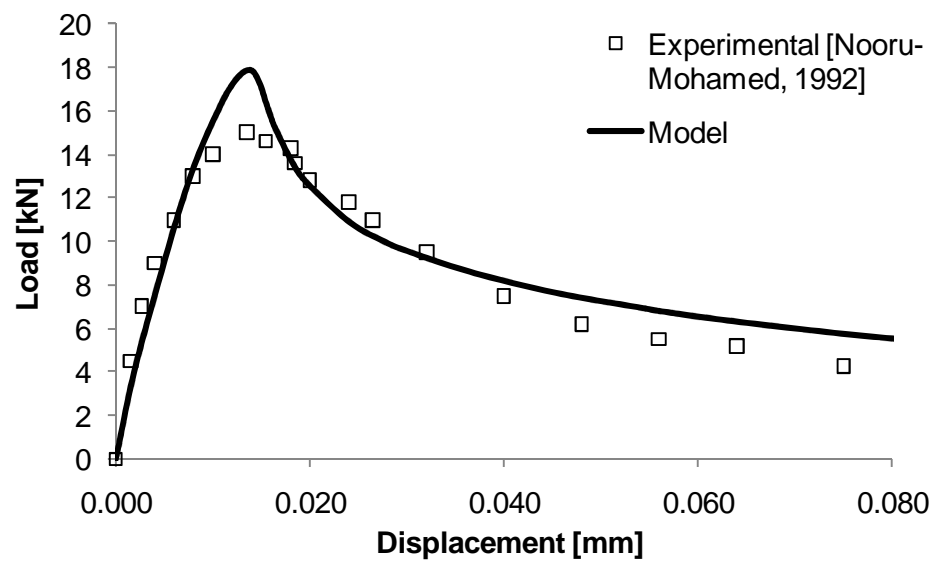

Fig. V.2-3: Measured (Nooru-Mohamed, 1992) and computed results for the mixed-mode fracture test on plain concrete

V.2.2. Reinforced concrete slabs at ambient temperature

V.2.2.1. *General data*

The following simulations deal with the behavior of reinforced concrete slabs subjected to combined inplane and transversal loads at ambient temperature. The experimental tests that are modeled have been performed at University of Alberta (Ghoneim and MacGregor, 1992). A series of tests have been conducted to analyze different configurations in terms of specimen dimensions and loading paths. Very detailed information about the tests can be found in the technical report from Ghoneim and MacGregor; the main information has been reproduced here for the eleven tests that have been considered. Table V.2-1 gives the length (L), width (l) and average thickness (t) of the specimens as well as the concrete compressive strength (f_c) and tensile strength (f_t). The length and width are considered as distances between supports, see Fig. V.2-4. Table V.2-2 and Table V.2-3 provide the information about the area and location of the steel reinforcement in the concrete slabs; the locations indicated in Table V.2-3 must be read as indicated in Fig. V.2-5. The ultimate strength of the steel reinforcement was 620 MPa. No yield point was clearly defined; the 0.2% offset yield was 450 MPa.

specimen	L [mm]	l [mm]	t [mm]	f_c [MPa]	f_t [MPa]
B1	2745	1829	68.2	18.70	1.60
B2	2745	1829	66.8	19.27	1.65
B3	2745	1829	66.7	19.53	1.67
B4	2745	1829	65.3	20.82	1.78
C1	1829	1829	67.8	25.21	2.08
C2	1829	1829	67.6	25.27	2.10
C3	1829	1829	68.5	25.30	2.10
C4	1829	1829	70.0	25.35	2.10
C5	1829	1829	70.1	25.81	2.30
C6	1829	1829	67.4	25.44	2.11
C7	1829	1829	66.5	25.56	2.12

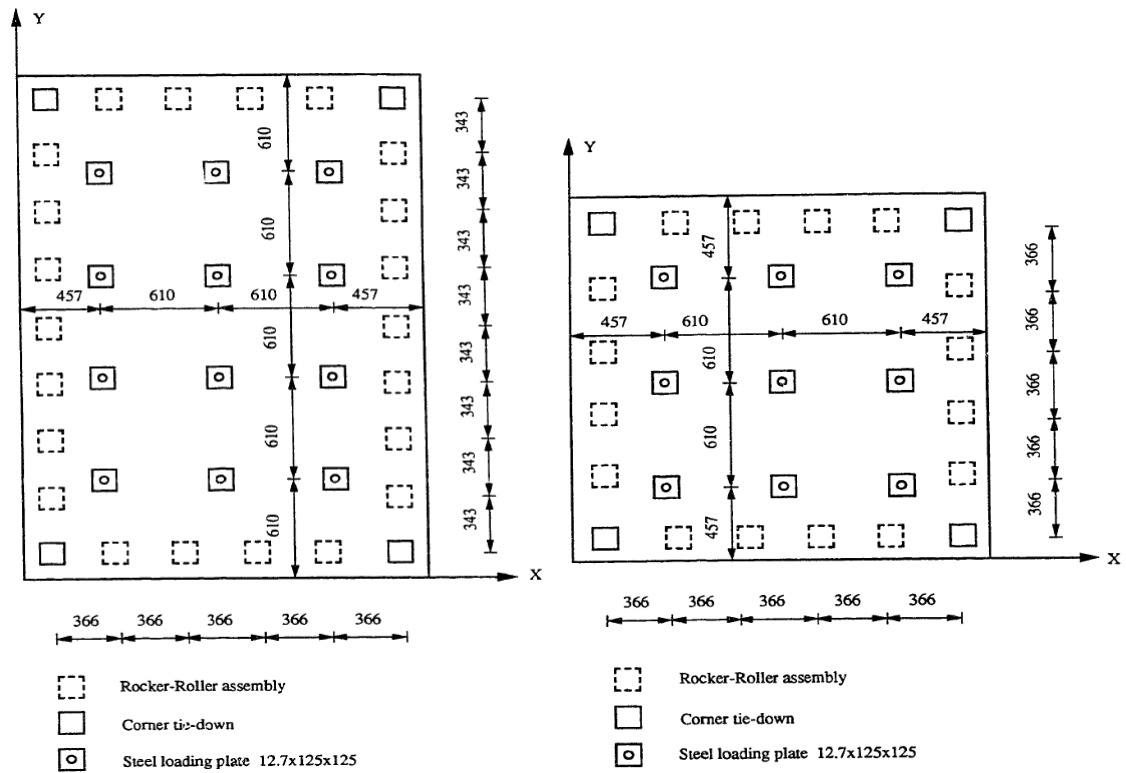Table V.2-1 : Side dimensions, average measured thickness and concrete properties

Fig. V.2-4: Locations of the lateral load and support points for series B (left) and series C (right) (from Ghoneim and MacGregor, 1992)

specimen	X-direction		Y-direction	
	Area of top rebar [mm²/m]	Area of bottom rebar [mm²/m]	Area of top rebar [mm²/m]	Area of bottom rebar [mm²/m]
B1	260	260	260	260
B2	260	260	260	260
B3	260	260	260	260
B4	260	260	260	260
C1	260	260	260	260
C2	260	260	260	260
C3	260	260	260	260
C4	260	260	520	520
C5	520	520	260	260
C6	260	260	260	260
C7	260	260	260	260

Table V.2-2 : Area of Reinforcement in X- and Y-Directions

specimen	X-direction		Y-direction	
	dx [mm]	d'x [mm]	dy [mm]	d'y [mm]
B1	55.0	22.3	48.7	16.0
B2	53.5	20.5	47.2	14.2
B3	53.3	20.2	47.0	13.9
B4	50.3	19.7	44.0	13.4
C1	56.8	21.9	50.5	15.6
C2	57.6	19.7	51.3	13.4
C3	57.6	19.9	51.3	13.6
C4	58.5	20.9	52.2	14.6
C5	52.5	14.4	58.8	20.7
C6	56.1	18.1	49.8	11.8
C7	55.3	17.9	49.0	11.6

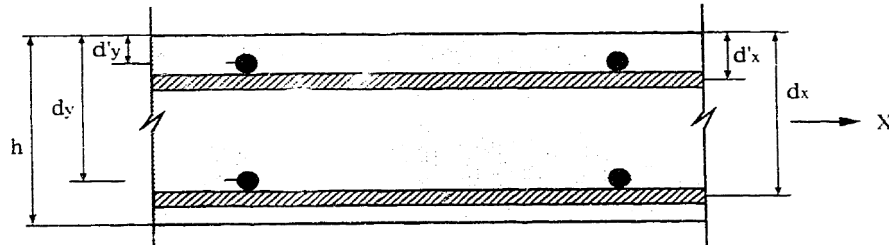Table V.2-3 : Average locations of top and bottom reinforcement from compressive face

Fig. V.2-5: Location of the reinforcement from compressive face (Ghoneim and MacGregor, 1992)

V.2.2.2. _Loading_

The maximum applied loads are given in Table V.2-4 for the eleven tests. In this table, the loads N_x and N_y are compressive inplane loads in kN/m respectively in the x and y directions (see Fig. V.2-4 for the orientation of the axes), whereas the load q_u is the transversal load in kN/m².

The specimens were subjected to different loading paths. Specimens B1 and C1 were subjected to transversal loads only; the transversal load was increased until failure of these specimens. The other specimens were tested under a combination of transversal loads and compressive inplane loads. For these latter specimens except C3, the full inplane load was applied first, then the transversal load was increased until failure whereas the inplane load remained constant; see for instance the loading path for specimen C2 in Fig. V.2-6. In specimen C3, the inplane and transversal loads were applied proportionally until failure at the rate: "inplane loads : transversal loads = 14.8 kN/m : 1.0 kN/m²". The three different types of loading paths are illustrated in Fig. V.2-6.

specimen	a/b	N_x [kN/m]	N_y [kN/m]	q_u [kN/m²]
B1	1.50	0.0	0.0	45.91
B2	1.50	0.0	514.0	23.27
B3	1.50	0.0	353.8	25.52
B4	1.50	516.0	0.0	19.51
C1	1.00	0.0	0.0	73.88
C2	1.00	0.0	653.9	52.59
C3	1.00	0.0	647.0	51.56
C4	1.00	0.0	656.5	59.47
C5	1.00	0.0	652.5	67.83
C6	1.00	657.8	657.8	69.16
C7	1.00	362.5	362.5	60.03

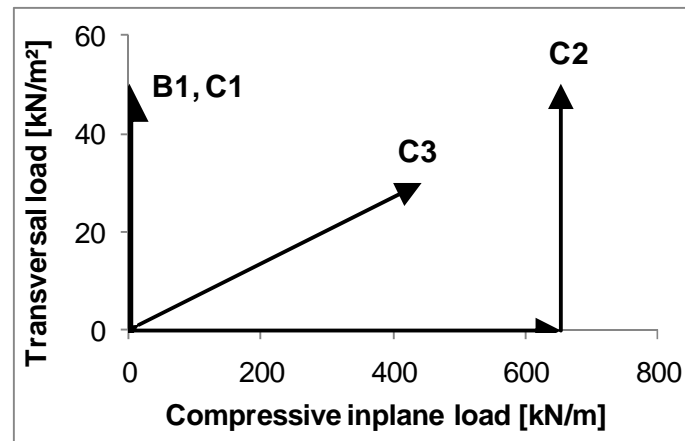Table V.2-4 : Maximum loads for the eleven slabs

Fig. V.2-6: Different loading paths followed in the slab tests

V.2.2.3. _Numerical model_

Numerical simulations of the tests have been performed using the finite elements software SAFIR. The reinforced concrete slabs are modeled by means of shell finite elements. Due to the symmetry of the configurations, only a quarter of the slab is represented in the models, see Fig. V.2-7. Vertical supports are considered at the location of the support points in the experimental configuration illustrated in Fig. V.2-4. The application of transversal and inplane loads in the numerical model follows the different loading paths discussed here above.

Application of the load is simulated by increasing the load over time (force control) in the model; therefore failure of the structure is reached at the maximum load level and it is not possible to increase further the displacement in the simulations. The simulation cannot be conducted by increasing the displacement (deformation control) because the load must be applied simultaneously in different points. However in the experiments, the specimen can be unloaded after reaching the maximum load as it is stated by the authors in their report (Ghoneim and MacGregor, 1992): "In all tests, the loading system was initially controlled by

load increments but near the maximum load, the further loading was controlled by imposing deflection increments". Consequently the experimental results of the applied transversal load versus vertical deflection include part of the softening regime after the maximum load level, whereas this post-peak behavior is not handled by the numerical simulations in this case.
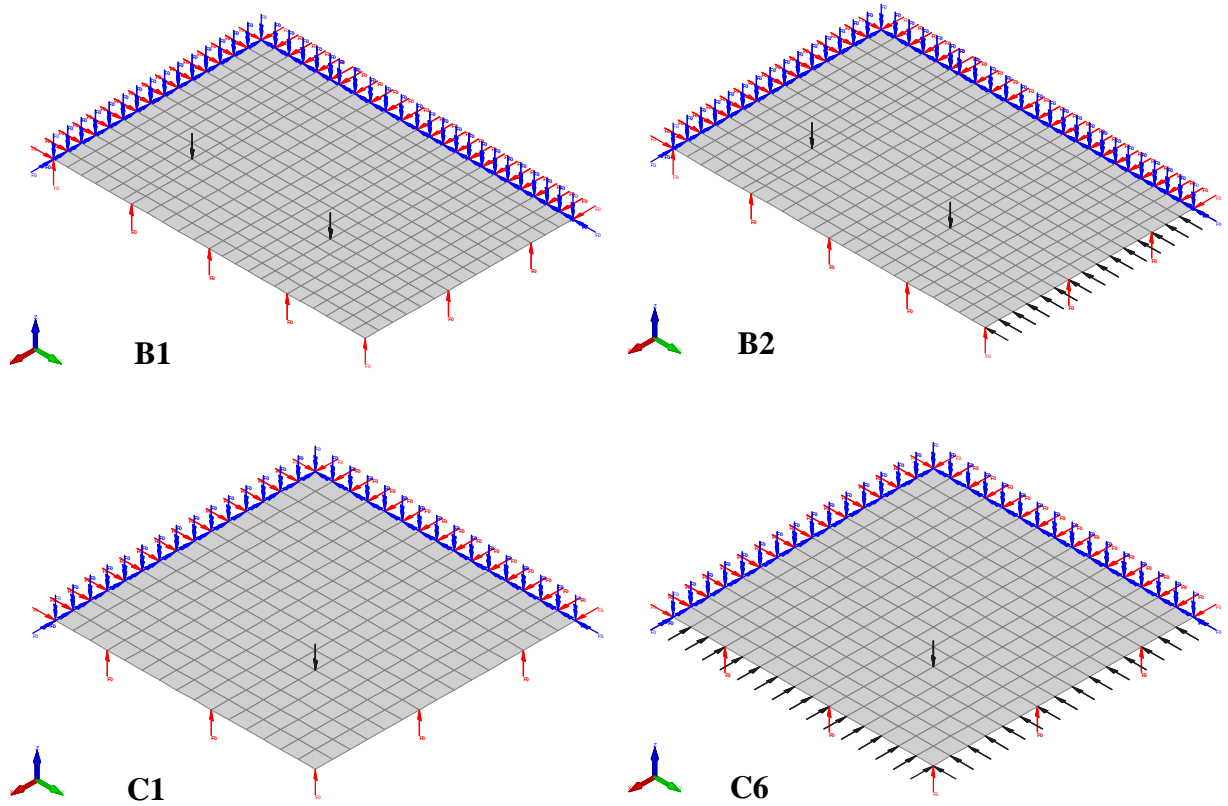

Fig. V.2-7: Numerical model of the slabs

The concrete model developed in the present thesis is used for the concrete shell elements. The mesh used in the numerical model is approximately 0.06 m side. Considering a crack energy in tension $\overline{G}_t$ of 75 N.m/m² in the simulations, the tensile crack energy density g_t is equal to $g_t = \overline{G}_t/l_c = 1250$ N/m². The compressive and tensile strengths are taken equal to the measured values given in Table V.2-1. The other material parameters of the concrete model have been calibrated on the elementary tests presented in the first part of this chapter and no additional calibration is done here for modeling of the considered experiments; the values listed in Table V.1-7 have thus been used in all the simulations.

The steel rebars are considered in the shell elements. The uniaxial mechanical properties of steel follow the model of Eurocode 2; the stress-mechanical strain relationship is non-linear until 2%, with a horizontal plateau from 2 to 15% and a descending branch thereafter; unloading is plastic. The effective yield strength is taken equal to 620 MPa.

V.2.2.4. *Numerical results*

The experimental results and the results of the numerical simulations performed with SAFIR are plotted in Fig. V.2-8. For each test, the relationship between the applied transversal load in kN/m² and the central vertical deflection in mm is given. The numerical simulations succeed at capturing the initial stiffness of the structure in the different situations of combined inplane and transversal loading. The maximum load is reasonably well predicted by the simulations except for tests B2 and B3, where the computed maximum load exceeds the value that is experimentally observed.

The distribution of the membrane forces in the slab C1 at failure is plotted in Fig. V.2-9; the color blue represents compressive forces whereas red represents tensile forces. It can be seen that the slab develops tensile membrane action to sustain the applied load. Important tensile forces develop in the steel mesh located in the central part of the slab whereas a compressive ring develops in the concrete. In this slab, failure eventually occurs by excessive yielding of the steel rebars; the strain in part of the steel rebars exceeds 15% at failure.

The deformed shape of specimen B1 at failure is plotted in Fig. V.2-10. The central vertical deflection exceeds 100 mm, which corresponds approximately to L/27 and l/18 for this slab. This important deflection is due to the fact that the slab behaves as a membrane; important vertical deflections are therefore required to equilibrate the vertical applied forces by means of tensile forces in the (originally horizontal) steel mesh.
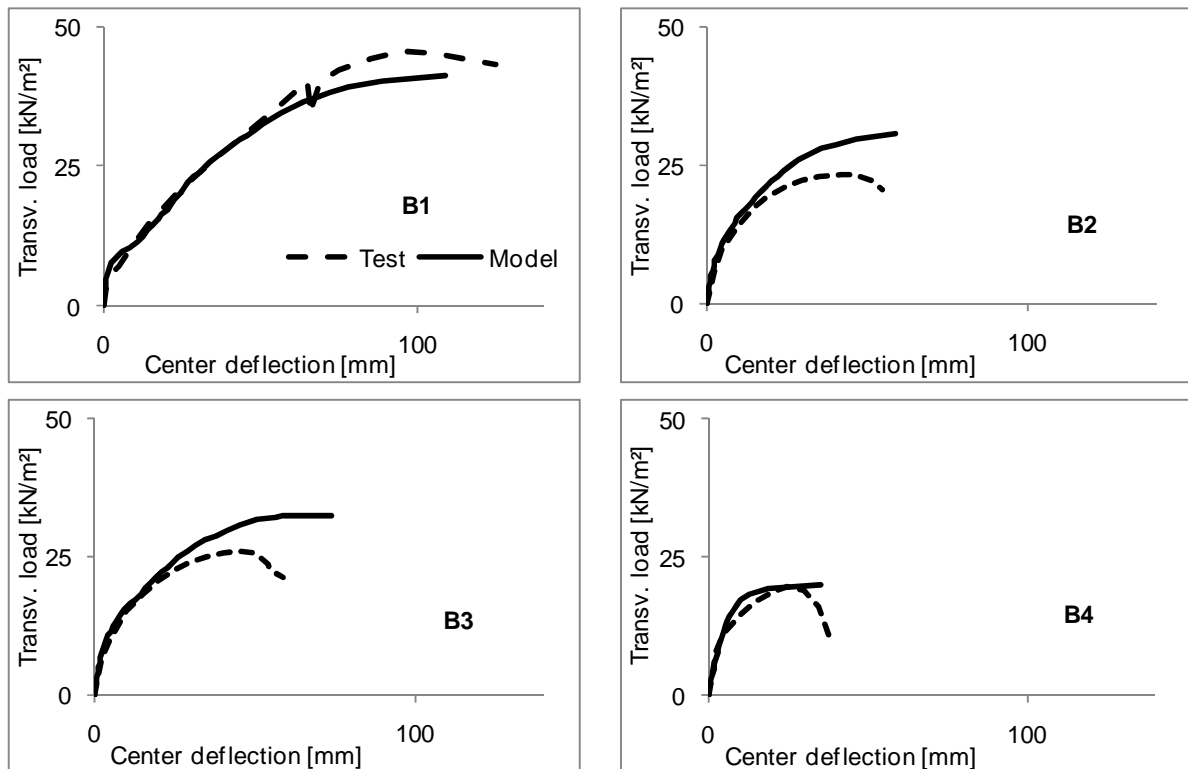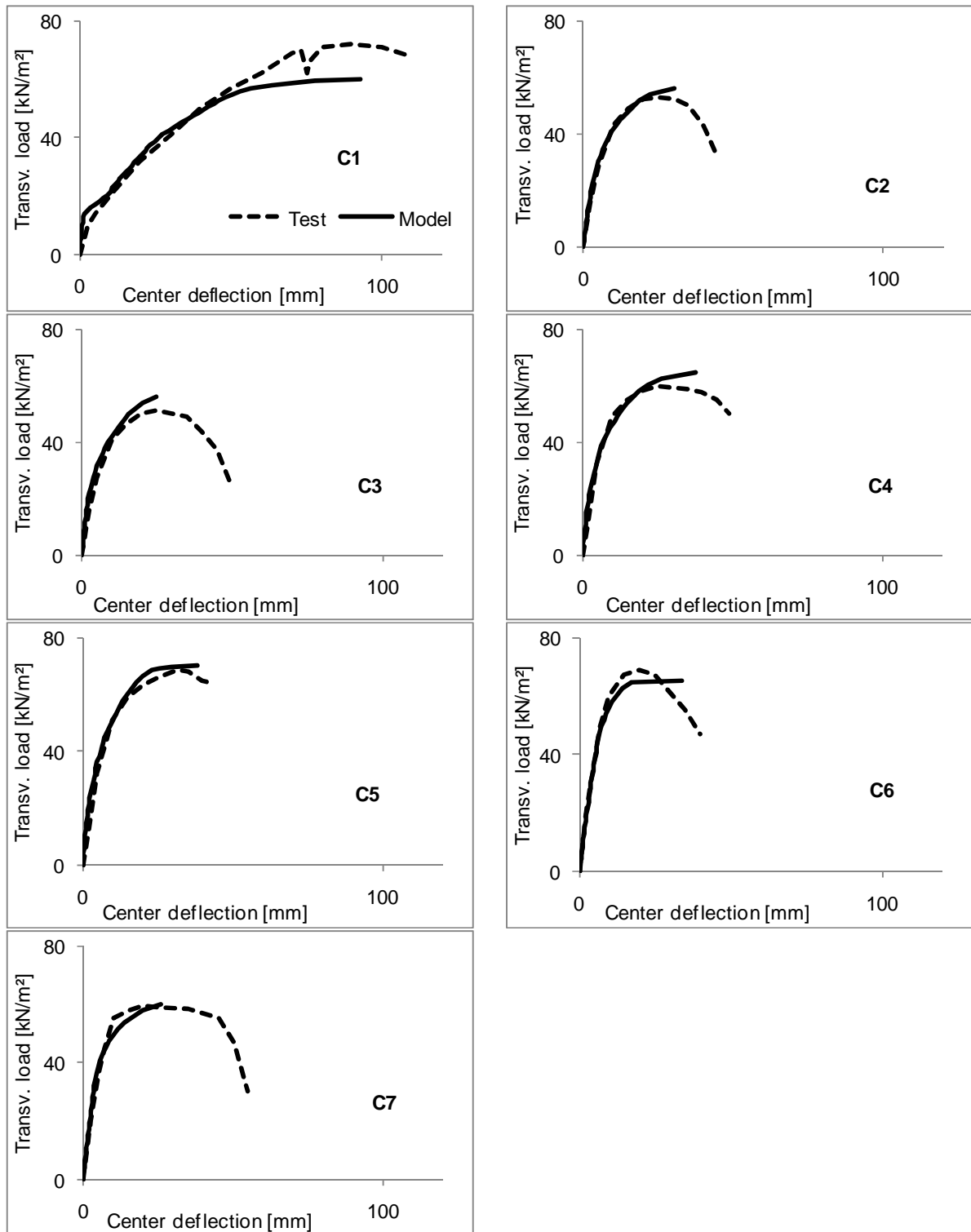

Fig. V.2-8: The results of the numerical simulations with the new concrete model agree with the experimental results by Ghoneim and MacGregor (1992) for the different RC slabs tested
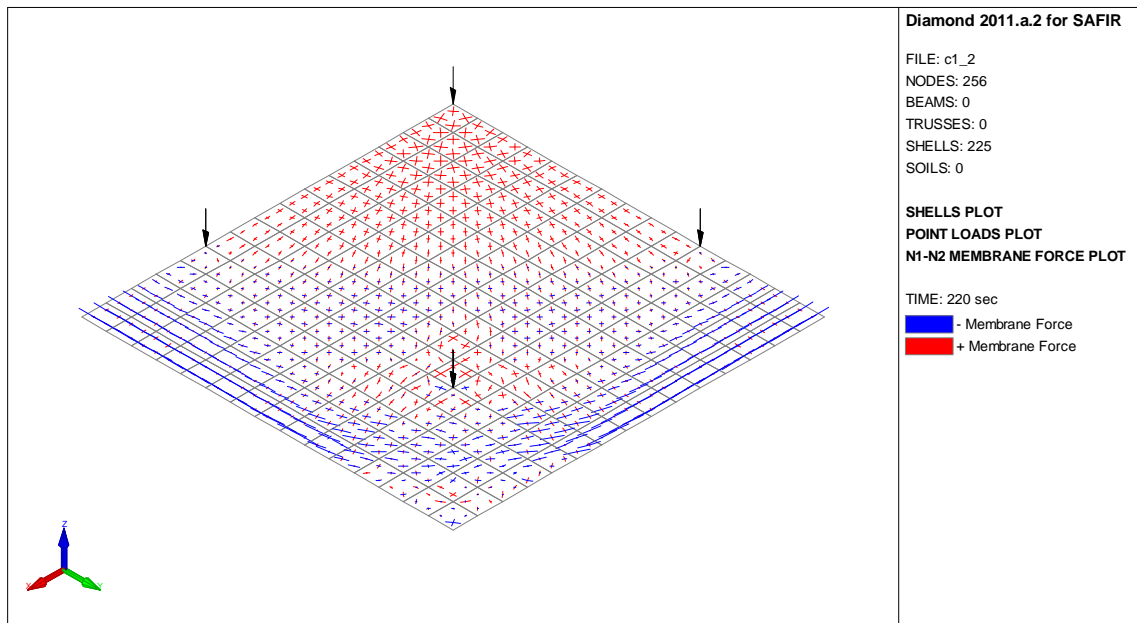
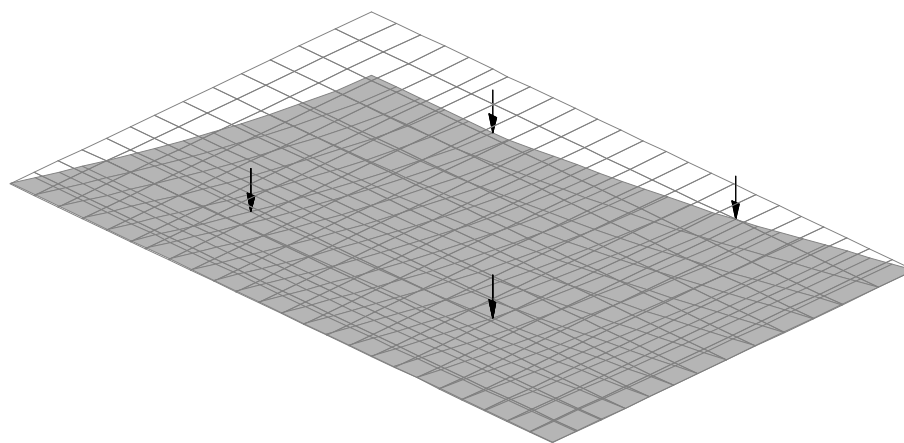Fig. V.2-9: Distribution of membrane forces in slab C1 at failure

Fig. V.2-10: Deformed shape in slab B1 at failure

V.2.3.   Reinforced concrete slab in fire

An experimental fire test carried out at Building Research Association of New Zealand (Lim and Wade, 2002; Lim, et al., 2004) on a reinforced concrete flat slab in fire is modeled in this section. The numerical analysis of the fire test is performed with the software SAFIR using the new concrete model, in order to validate the ability of the model to predict the behavior of a structural element in fire situation.

The tested slab is 3.30 m wide by 4.30 m long with a clear span between the supports in the long and the short directions of 4.15 m and 3.15 m, respectively. The slab is simply supported at all four edges with the edges horizontally unrestrained. The flat slab is 100 mm thick and is reinforced by 200 mm²/m steel reinforcement in each direction with a concrete cover of 25 mm. The yield strength of the steel used in the slab is 565 MPa. The concrete that was used in the test is a normal weight concrete with siliceous aggregates. The concrete

compressive strength determined by cylinder crushing test is 37 MPa (Lim and Wade, 2002). The slab was subjected to ISO fire exposure for 3 hours while carrying a constant uniformly distributed load equal to 3.0 kN/m². The slab, which deformed into double curvature, survived the 3 h ISO fire exposure without collapse.

The numerical simulation of this experiment is performed in two steps in the software SAFIR. First, the thermal analysis is conducted to determine the temperature distribution in the concrete slab during fire. Then, the structural analysis is carried out to determine the structural behavior of the reinforced concrete slab in fire.

The transient temperature distribution on the thickness of the shell finite elements is determined by means of a 2D thermal analysis, assuming that the temperature gradient is perpendicular to the slab. Quadrangular conductive elements are used with temperature dependent thermal properties. The evaporation of moisture is implicitly considered by a modification of the specific heat of the material. At the boundaries, convection and radiation heat transfer are taken into account. The thermal properties for concrete are taken from Eurocode 2. Siliceous concrete was chosen, with a density of 2400 kg/m³ and a water content of 72 kg/m³. The emissivity was taken as 0.7 and the coefficient of convection was 25 W/m²K. Temperatures in the slab were recorded during the test at the heated surface, at the unheated surface and at 55 mm depth within the slab. Fig. V.2-11 gives the comparison between the temperatures predicted by SAFIR and the measured temperatures at these locations; predicted and measured temperatures agree well.
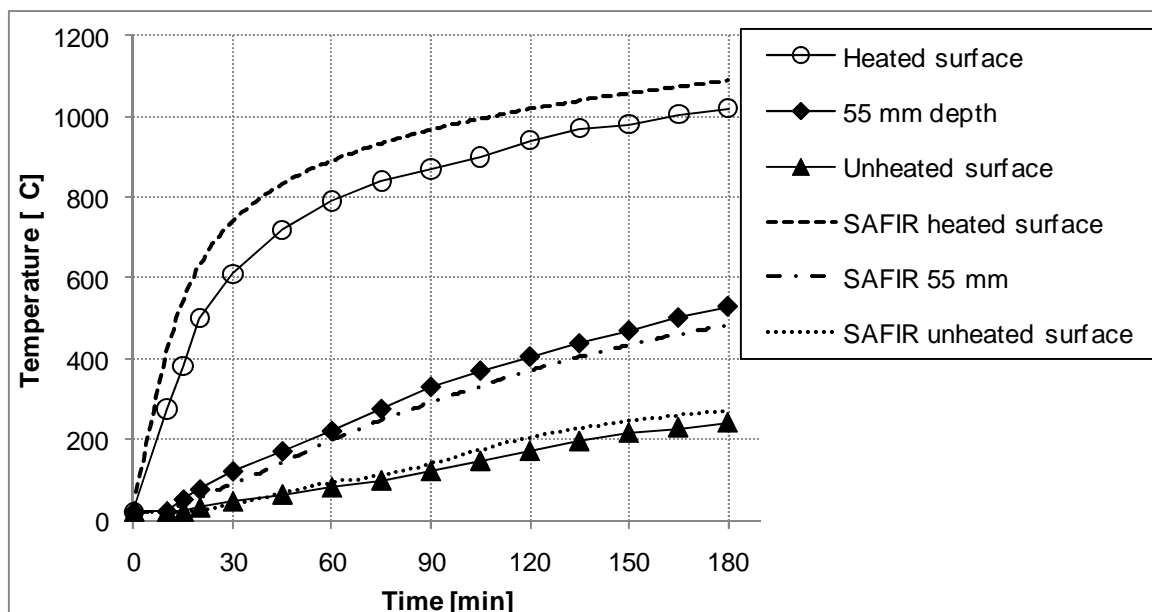

Fig. V.2-11: The measured (Lim, et al., 2004) and computed
temperatures in the flat slab agree

For the structural analysis, shell finite elements are used for modelling the slab. Only a quarter of the full slab is modeled to take advantage of the symmetrical load and support conditions, see Fig. V.2-12. The model includes the unheated edge of the slab which is located over the line of vertical support. The slab is subjected to a uniformly distributed load of 5.4 kN/m² which represents the sum of the self-weight, 2.4 kN/m², and the applied load,

3.0 kN/m². This load of 5.4 kN/m² corresponds to a load ratio of approximately 0.40 for this slab. The temperature evolution in the slab is taken from the SAFIR thermal analysis. The concrete model presented in this thesis is used for the thermo-mechanical behavior of concrete whereas the material model for the steel reinforcement is taken from Eurocode 2. The concrete compressive and tensile strength are 37.0 MPa and 1.0 MPa. A tensile crack energy density g_t of 5000 N/m² is adopted for the simulation. Based on the adopted mesh, the characteristic length is equal to $l_c = \sqrt{A_e} = 0.09$ m and therefore the crack energy in tension $\overline{G}_t$ is taken equal to 450 N.m/m. The reason for using this higher value of $\overline{G}_t$ compared with the value used in the two previous simulations is that numerical issues arose during the simulation when a value of 75 N.m/m² was used due to the severe softening behavior in tension. The value of 450 N.m/m² allows for avoiding these numerical issues. The values of the other material parameters are taken from Table V.1-7 and no calibration on the slab is required for these parameters.
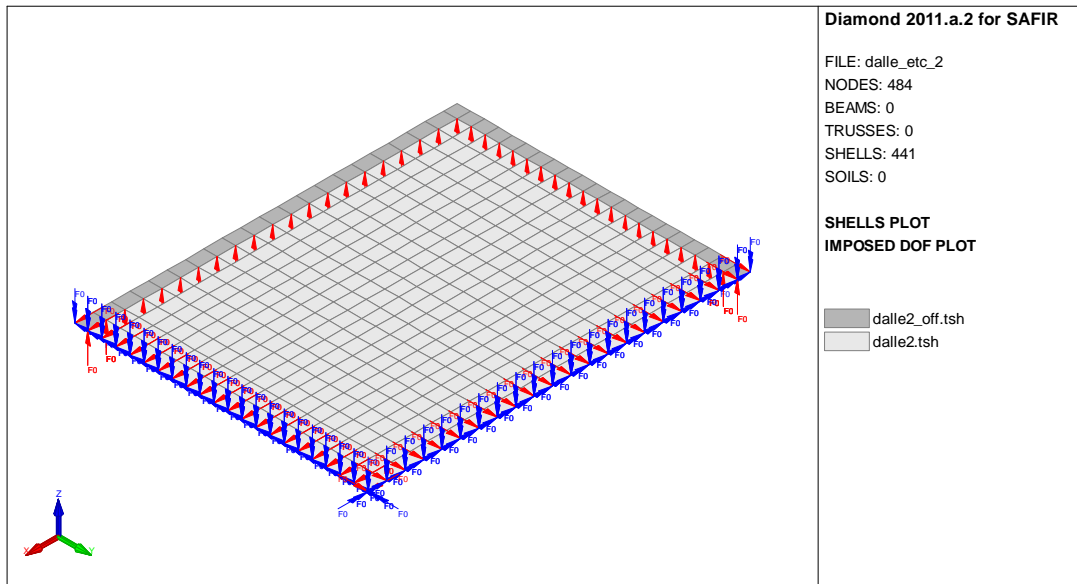

Fig. V.2-12: Finite elements model of the flat slab

The predicted and measured vertical deflections at mid-span of the slab in fire are shown in Fig. V.2-13. Three phases can be distinguished in the evolution of the deflection. First, a high deflection rate is observed at the beginning of the fire during approximately the first 30 min due to significant thermal bowing. Then, the deflection rate decreases and remains approximately constant during almost 120 min. Finally, the deflection rate increases again in the final 30 min due to the heating of the steel rebars and the subsequent decrease in stiffness of these rebars. The results of the numerical simulation using the new concrete model agree with the experimental results; particularly, the three phases are reproduced in the numerical simulation. The simulation is able to capture with accuracy the behavior of the slab during the 3 hours of the fire. The present example illustrates the ability of the new concrete model to be used in numerical simulations of structural elements in fire situation.
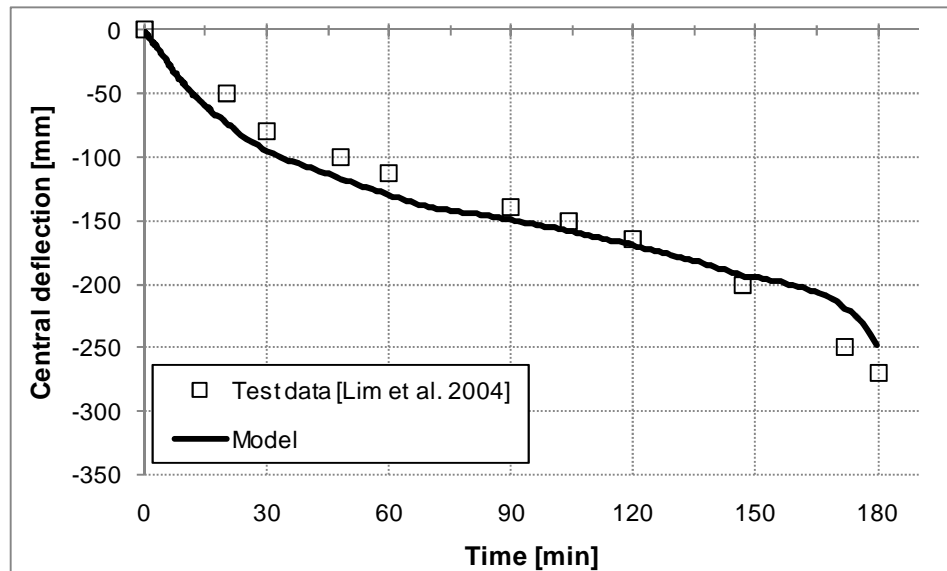
Fig. V.2-13: The concrete model is successfully used in the numerical simulation of a reinforced concrete slab subjected to ISO fire

The distribution of membrane forces in the slab and the deformed shape are plotted after 90 minutes of fire exposure in Fig. V.2-14. The compressive membrane forces are drawn in blue whereas the tensile membrane forces are represented in red. The compression ring typical of tensile membrane action is developed in the slab. Significant deflections are observed even though no failure occurs after 3 hours fire exposure; the final deflection reaches 0.25 m, which corresponds to L/16.6 and l/12.6.
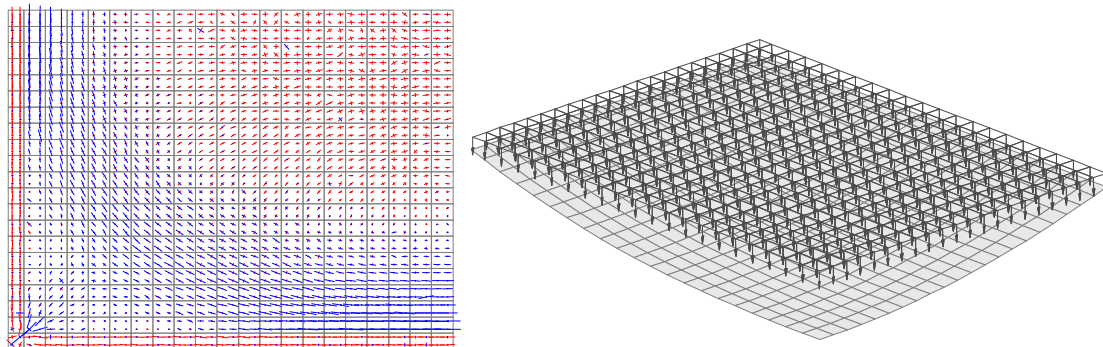

Fig. V.2-14: Distribution of membrane forces and deformed shape after 90 minutes

V.3. Application to structures in fire

V.3.1.   Ulster large-scale fire test

This section presents the numerical simulation of the Ulster full scale fire test. The test, conducted on a steel-concrete composite floor subjected to natural fire, has been presented in Chapter I; see Section I.3.3.2 for its description. This test investigates the development of tensile membrane action in a large composite structure made of cellular steel beams connected to composite slabs. The experimental behavior has been recorded until complete burnout of the fire, including the cooling down phase. Therefore, this large-scale fire test is representative of the challenging applications with which structural fire engineers have to deal nowadays and it represents a very interesting application for testing the capabilities of the concrete model.

Numerical simulation of the test is performed using the software SAFIR. This section gives the main information about the numerical modeling of the test and the obtained results; yet for more information, a comprehensive description of the numerical simulations has been given in a technical report (Gernay and Franssen, 2010).

As the objective is to evaluate the ability of the concrete model to be used for predictive calculations in the field of structural fire engineering, a blind approach (Beard, 2000) has been adopted for the simulations. This blind approach is characterized by the three conditions defined by Beard:

1.   "The test results from an experiment of the variable being used for a comparison between prediction and experiment have not been used by the modeler."
2.   "Some data from the experiment being used for comparison have been used."
3.   "No adjustment of input parameter values has taken place."

According to this approach, the temperature evolution in the compartment has been assessed by numerical simulation using the software OZone (Cadorin and Franssen, 2003; Cadorin, et al., 2003). The numerical code OZone includes a single compartment fire model that combines a two-zone model and a one-zone model for assessing the temperature evolution in a compartment. The computed temperatures have then been used as input data for the SAFIR thermal analysis. The choice of using the computed temperatures rather than the temperatures measured during the experiment for the numerical analysis is based on the first condition of blind comparison. The parameters and assumptions used for the OZone analysis are as follows (Vassart, et al., 2011):

- The fire load density: 700 MJ/m²
- Combustion model: extended fire duration
- Fuel height: 0.5 m
- RHR_f: 1250 kW/m²

- Combustion heat of fuel: 17.5 MJ/kg
- Fire growth: medium
- Combustion efficiency: 0.8

The comparison between the measured temperatures in the compartment and the OZone predictions is given in Fig. V.3-1. The experimental fire was slightly more intense than the predicted fire. The maximum computed temperature is 921°C and it arises after 76 min, whereas the maximum recorded temperature in the compartment is 1074°C after 64 min.
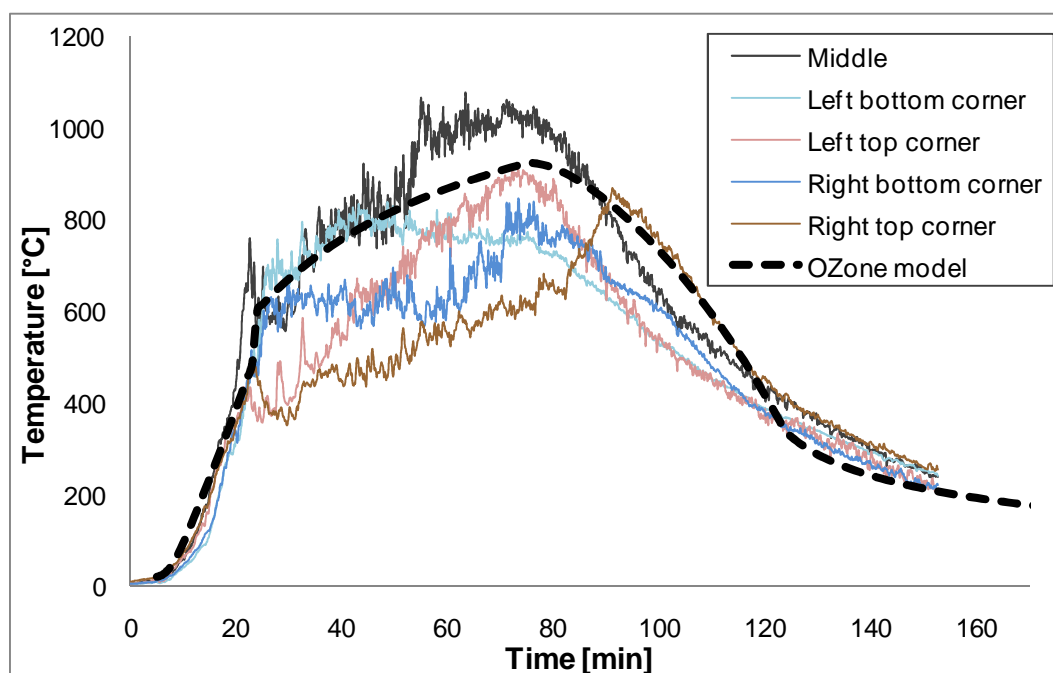

Fig. V.3-1: Comparison between measured temperatures in the compartment and OZone predictions

The temperature evolutions in the beams and in the slab sections have be determined by 2D non linear transient thermal analyses using SAFIR software.

For the steel beams, the material properties are taken from Eurocode 3 (European Committee for Standardization, 2005). As a natural fire is considered, the convection coefficient on hot surfaces is 35.0 W/m²K. For the unprotected central steel beams, the shadow factor is equal to 0.716. The cellular beam profiles are modeled as beam finite elements in SAFIR. The section that is considered for these beam finite elements is the section passing through the center of a circular opening, see Fig. V.3-2 left, because the longitudinal stresses of a beam model cannot "enter" in the web posts that separate two openings.

The concrete slab is modeled in the thermal analysis of the steel profiles in order to take into account its capacity of absorbing heat. Siliceous concrete following the material law of Eurocode 2 has been adopted with a moisture content of 72 kg/m³ and a convection coefficient on hot surfaces of 35 W/m²K. For the protected sections, the insulation material is also taken into account in the thermal analysis. The protected steel sections are affected by the fire on one side and on the bottom flange, while the other side of the profile, in front of a wall, is supposed to be an adiabatic boundary, see Fig. V.3-2 right.
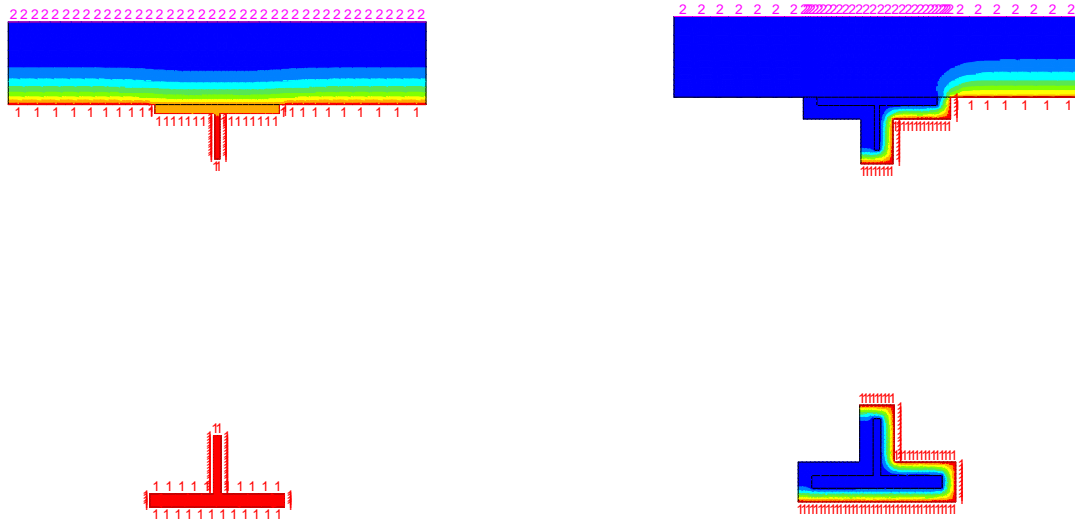
Fig. V.3-2: Double tee section considered for the cellular beam profiles; central unprotected (left) and peripheral protected (right) sections.

The slab used in the Ulster fire test is a composite steel-concrete slab made of a steel deck and a concrete cover. For the thermal analysis, an equivalent height of concrete has been defined for this slab using the effective thickness model of Eurocode 4 (European Committee for Standardization, 2004c). This equivalent height of concrete is used for assessing the thermal response of the composite slab, whereas only the concrete cover is considered for the mechanical response. In the present case, the height of the concrete cover is 69 mm and the additional height of thermal concrete to consider for the thermal analysis is 41 mm.

The finite element model built in SAFIR for the analysis of the mechanical behavior of the structure is presented in Fig. V.3-3. The model uses beam elements for the steel profiles and shell elements for the composite slab, assuming full connection between the slab and the beams. The edge beams are simply supported at the location of the columns as indicated in the figure. The slab and beams are axially unrestrained.
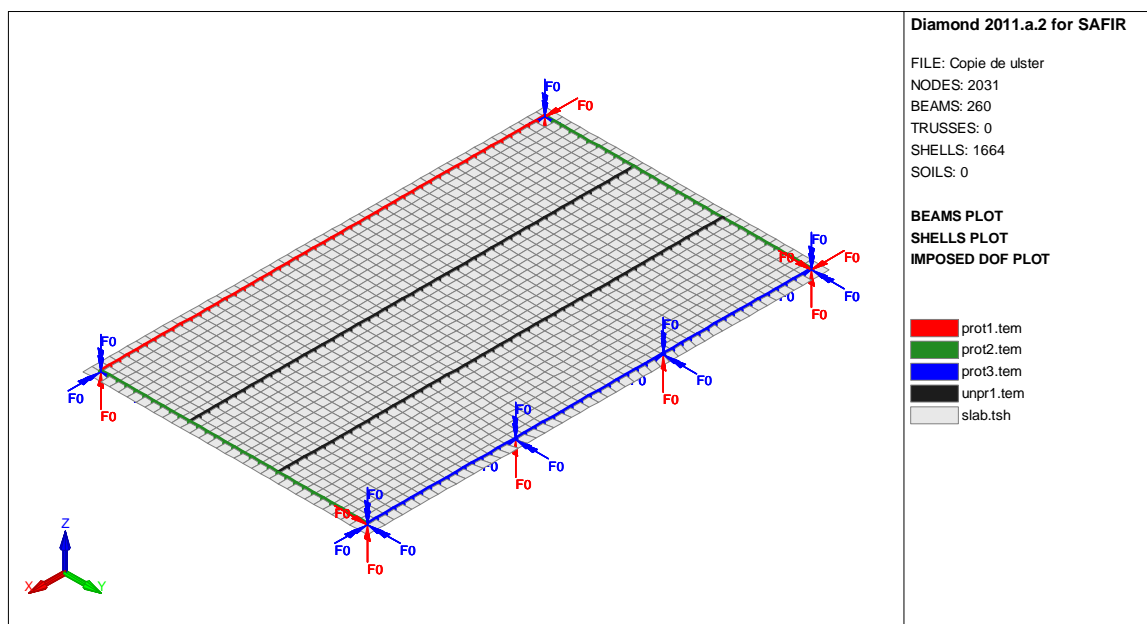

Fig. V.3-3: Finite element model of the Ulster fire test

The beam finite elements used for modeling the cellular beams cannot take into account the web post buckling instabilities. Yet, web post buckling has been observed experimentally in the two central steel beams, due to the high temperatures reached in these unprotected beams. Therefore, considering the double tee section plotted in Fig. V.3-2 for the model of the central steel beams would lead to unsafe results as in reality the web post buckling prevents the bottom tee of these beams from playing any structural function. To take into account in a simplified way this instability phenomenon, a special material has been implemented for the bottom flange of the unprotected beams. This material has the same mechanical properties as the steel from Eurocode 3 for temperatures below 500°C but it loses entirely and irreversibly its material properties between 500°C and 600°C. This range of temperature has been chosen because it is representative of the critical temperature at which a cellular steel beam develops web post buckling. It is important to note that the strategy adopted here to take into account the web post buckling phenomenon did not require any calibration on the experimental results; web post buckling of the unprotected beams was foreseen in the Ulster fire test and the measured critical temperatures of these beams were not incorporated in the special material model. Therefore, the use of this special material model for the bottom tee of the central steel beams is not contradictory to the blind approach followed in this simulation.

As the temperatures in the protected steel beams did not reach 500°C, no web post buckling instabilities developed in these beams. The material model from Eurocode 3 could then be used for the steel of the protected beams.

The steel profiles are made of 355 MPa yield strength steel. The siliceous concrete used for the slab had a measured average cube strength of 54.8 N/mm2 at 28 days; therefore the cylinder compressive strength is estimated equal to 45 N/mm² based on the recommendation of Eurocode. The compressive strength in the concrete model is taken equal to this latter value of 45 N/mm² according to the second condition defined by Beard. The new concrete model is used for the reinforced concrete shells using the parameters of Table V.1-7. Regarding the value of the parameters in tension, i.e. the tensile strength and the tensile crack energy density, it is found that these parameters have an influence on the numerical robustness of the analysis. When using a non-null tensile strength in the model, for instance a value of 1.0 N/mm², it is necessary to use a large value for the crack energy density to avoid numerical issues and to be able to run the simulation until the end. In this case, the crack energy density is taken equal to 10 kN/m². As the size of the adopted mesh is 0.30 m x 0.30 m, this leads to a characteristic length of 0.30 m and a crack energy in tension $\overline{G}_t$ of 3000 N.m/m². This value of the crack energy is larger than the values recommended at ambient temperature. In order to check whether this value of the tensile crack energy affects the structural response, the simulation is run again assuming that the concrete has no tensile strength. In this case, the value adopted for the crack energy has no influence as the concrete cannot develop any tensile stress. The numerical simulation considering $f_t = 0$ is able to run during the 180 minutes of the fire, although the CPU time for this simulation is significantly larger (11h14) than the CPU time for the simulation with a tensile strength of 1 N/mm² (7h52).

The computed results obtained with the two values of the tensile parameters are compared with the measured results in Fig. V.3-4. The comparison is about the evolution of the vertical deflection in the central steel beam. A good correlation is obtained between the

FEM models and the real behavior of the test; the numerical simulations qualitatively capture the evolution of the vertical deflection of the structure during the different phases of the natural fire. Besides, it can be seen that the values adopted for the tensile parameters do not have a significant influence on the computed structural behavior for the considered analysis, which gives some confidence that the increased value adopted for numerical reasons for the tensile crack energy density did not lead to erroneous results in the simulation with a tensile strength equal to 1.0 N/mm².
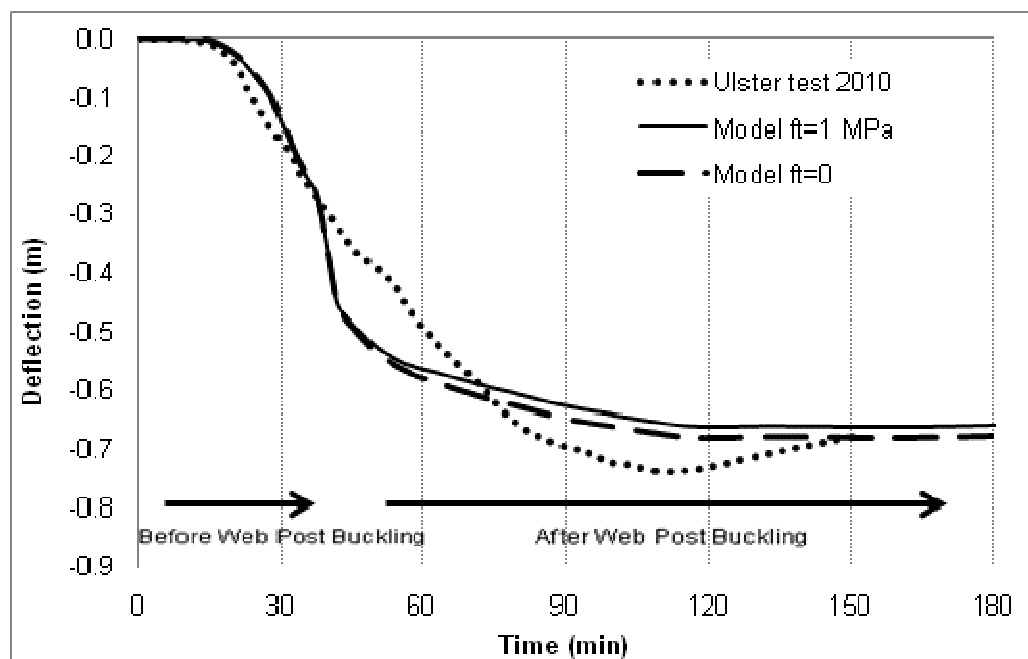

Fig. V.3-4: Evolution of the deflection of the central beam

Fig. V.3-5 shows the deformed shape at ambient temperature and after 60 min fire exposure; in this figure, a different amplification factor has been used for plotting the deformed shape at ambient temperature (x20) and at high temperature (x2). Fig. V.3-6 shows the distribution of membrane forces within the slab at elevated temperature and after 60 min fire exposure. It can be seen that the mechanism in the composite slab changes from flexural mode to tensile membrane action. After 60 min fire exposure, the unprotected steel beams have experienced web post buckling; as a result they have lost their stiffness and cannot provide support to the slab. As a consequence, the span of the slab has changed from 3.0 m to 9.0 m. Due to this excessive span, the slab cannot sustain the applied loads by flexural mode strength. Nevertheless, by developing a membrane behavior the slab finds equilibrium. Tensile membrane forces develop in the central part of the slab; the steel mesh is in tension and the concrete is cracked. On the other hand, a compressive ring develops within the concrete around the perimeter of the slab, see Fig. V.3-6, to equilibrate the horizontal components of the in-plane forces developed within the slab. The development of tensile membrane action in the slab is confirmed experimentally by observation of the deformed shape of the structure, see the picture in Fig. V.3-7. Besides, the picture also highlights the instabilities that appear in the central steel beams.
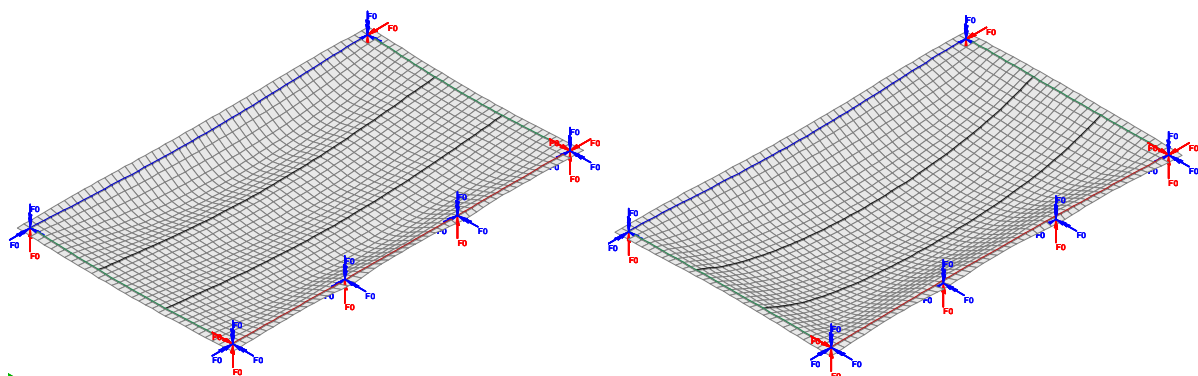
Fig. V.3-5: Deformed shape at ambient temperature (left) and at high temperature (right)
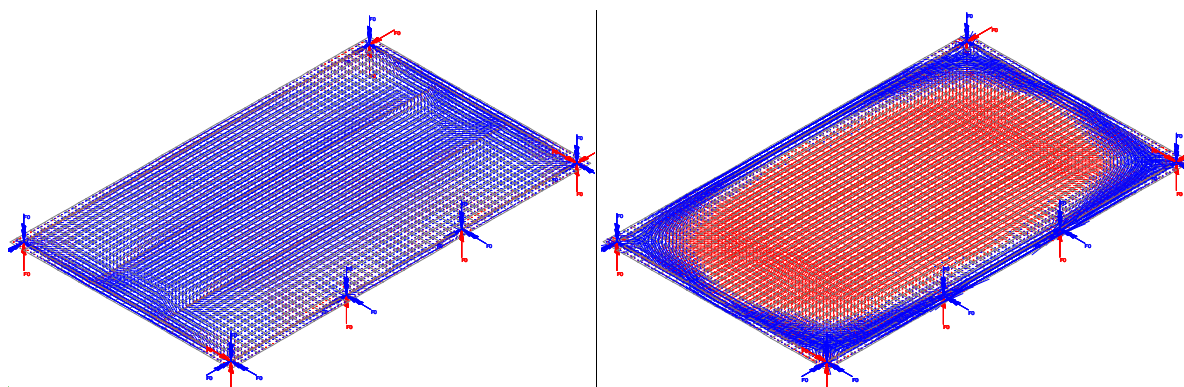
Fig. V.3-6: Membrane forces at ambient temperature (left) and at elevated temperature (right)

Fig. V.3-7: Picture of the Ulster building structure at the end of the fire showing the deflected membrane shape of the slab and the web post buckling instabilities in the central steel beams.

It is interesting to note that the numerical simulation was able to qualitatively capture the experimental behavior of a complete structure subjected to natural fire although a blind comparison was performed. Indeed, a better correspondence between the measured and computed results of the vertical deflection in Fig. V.3-4 could probably be obtained by adapting the variables of the finite element model to fit with the measured values. For instance, the real temperatures measured in the sections could be used instead of the temperatures computed by

a SAFIR thermal analysis. However, it was deliberately decided to fulfill the blind comparison conditions in order to put ourselves closer to the real conditions met by structural engineers. A second factor that can explain the quantitative difference in the results is related to the simplifications adopted in the model. Examples of simplifications are the modelling of the instability phenomenon of the unprotected beams and the modelling of the columns as perfect vertical supports. The reason for which these simplifications are adopted is the will to limit the complexity of the numerical model. For instance, the steel cellular beams could be modeled with shell elements in order to take into account the instability, but such model would be too large for practical applications. Hence the obtained results give some confidence that this quite simplified model is capable of predicting the fire behavior of a large scale structure in fire with a satisfying level of accuracy in the conditions of a blind comparison.

V.3.2. Fire resistance of an arch shell roof structure

The last example presented in this thesis deals with the arch shell roof structure discussed in Chapter I. The fire resistance of the roof structure depicted in Fig. V.3-8 has been numerically analyzed in the framework of the building refurbishment project. This study was funded by *Ingénieurs Conseils en Bâtiments* (ICB), Luxemburg. A comprehensive description of the numerical analyses is available in a technical report (Gernay and Franssen, 2011). The building studied in this project is an industrial hall located in Luxemburg; however, this type of arch shell roof structure is used in many other structures, see for instance the *Amphithêatres de l'Europe* at University of Liege by architect D. Dethier (Fig. V.3-9, picture taken from ULg-Globalview).
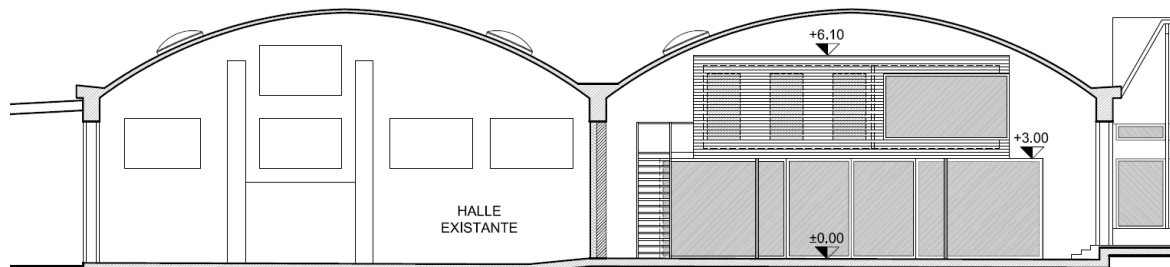

Fig. V.3-8: Elevation view of the building structure

Fig. V.3-9: The *Amphithêatres de l'Europe* in Liege are another example of structure designed with concrete bent roofs (© ULg-Globalview)

The dimensions of the structure have been detailed in Chapter I, Section I.3.3.3. The objective is to assess the fire resistance of the structure in the situation of ISO fire in one or the two compartments and eventually propose measures to improve this fire resistance. The fire analysis of the structure is performed under self-weight loads. The numerical simulations presented in this section are conducted with the software SAFIR.

First, the temperature distribution in the shells and the tie beams is determined by 2D transient thermal analyses. For these analyses, the thermal properties of steel and concrete are taken from Eurocode 2. Different thermal analyses are conducted for the tie beams using different thermal protections, with the aim to determine the minimum amount of thermal protection that will eventually lead to a global fire resistance of 30 minutes for the roof structure. The temperature evolution in the tie beams subjected to ISO fire depends on their thermal protection, see Fig. V.3-10.
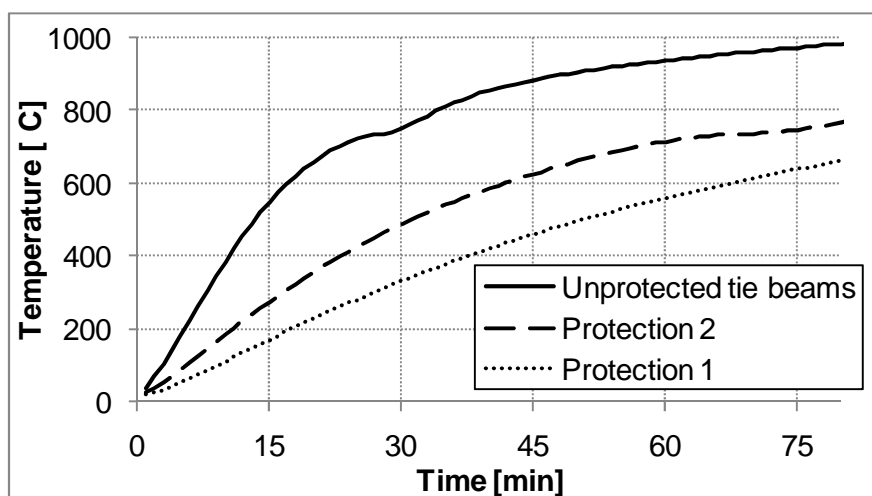

Fig. V.3-10: Temperature evolution in the tie beams as a function of the thermal protection
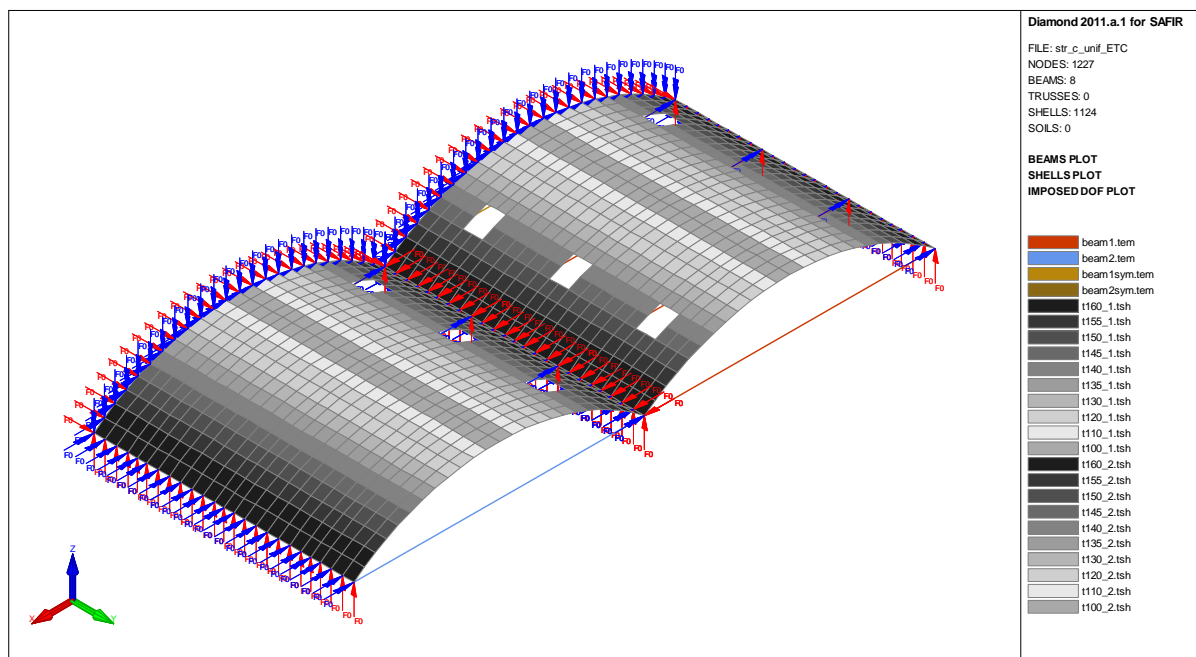

Fig. V.3-11: Finite element model of the shell roof structure

Then, the finite element model for the mechanical analysis is built in SAFIR. This model uses shell elements to model the shell roof and beam elements for the tie beams. Only half of the roof has been modeled, thus a length of 13.50 m comprising three entire tie beams plus half of a tie beam at one extremity, with proper symmetry conditions imposed at the edge of the model (Fig. V.3-11). The cupolas have been modeled as openings in the roof. The supports are indicated on the figure; the structure is free to expand in both horizontal directions. As the shell structure has variable thickness, 10 different sections have been used in the model with a thickness varying from 160 mm to 100 mm. The concrete shell roof is reinforced in both directions by means of steel reinforcement mesh.

For the material behavior of the steel of the tie beams, the model of Eurocode 3 has been adopted. For the concrete shells, the new concrete model has been employed with the standard values of the material parameters given in Table V.1-7. The concrete compressive strength is 20 MPa, the concrete tensile strength is 1.0 MPa, the reinforcement steel yield strength if 400 MPa and the tie beams yield strength is 235 MPa. The characteristic length is evaluated equal to 0.65 m and a crack energy in tension $\bar{G}_t$ of 3000 N.m/m² has been used in the simulation.

The mechanical analysis is first performed at ambient temperature to analyze the structural behavior and the failure mode. Increasing uniformly distributed loads are applied on the structure until failure. Failure arises for a fire load multiplication factor of 1.87, where the fire load corresponds to the self-weight of the structure. The deformed shape at failure is shown in Fig. V.3-12. The evolutions of the mid-span deflection of the shell and the tie beam axial force are plotted in Fig. V.3-13. Failure arises due to yielding of the tie beams; for a yield force of 211 kN the tie beams lose their stiffness and therefore their ability to sustain the horizontal arch force, and the structure collapses.
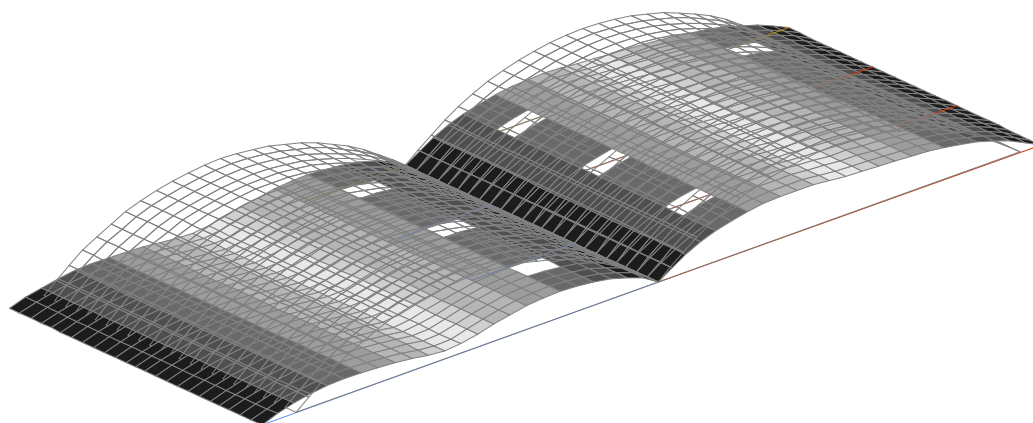
Fig. V.3-12: Deformed shape at failure (x3) at ambient temperature

The membrane forces in the roof under self-weight loads are shown in Fig. V.3-14 and Fig. V.3-15. The distribution of the membrane forces at ambient temperature indicates that the structural behavior is compressive membrane action. The applied loads are transmitted by the concrete shell through compressive forces toward the supports and the steel tie beams. The convergence of the compressive in-plane forces within the shell toward the tie beams anchors is clearly visible in Fig. V.3-15. As a conclusion, at ambient temperature, the structure carries

the applied load by compressive membrane action in the reinforced concrete shells equilibrated by tension in the steel tie beams and failure arises when the applied load is such that excessive tensile forces develop in the steel tie beams.

Fig. V.3-13: Loading of the structure at ambient temperature

Fig. V.3-14: Membrane forces in the structure under self-weight at ambient temperature

Fig. V.3-15: Membrane forces in the vicinity of an opening (left) and at the anchor of a tie beam (right)

At elevated temperature, the temperature increase in the steel tie beams leads to thermal expansion and decrease in stiffness and strength of these beams. Based on the observed behavior at ambient temperature, the expected failure mode at elevated temperature is the collapse o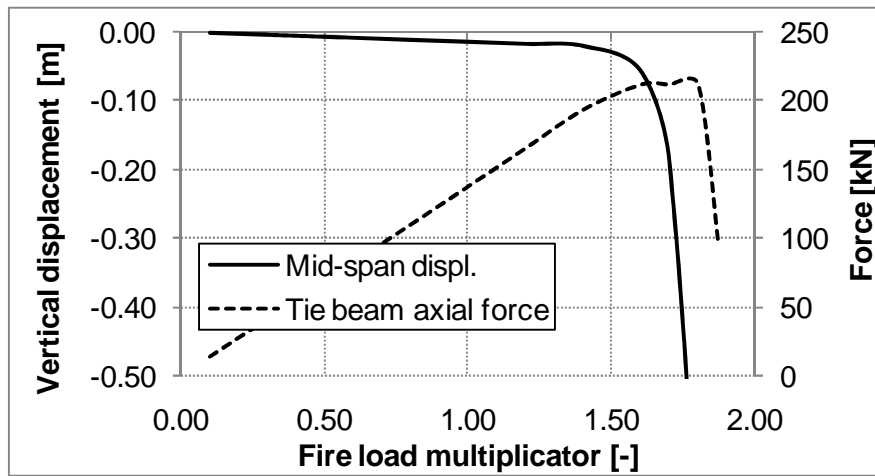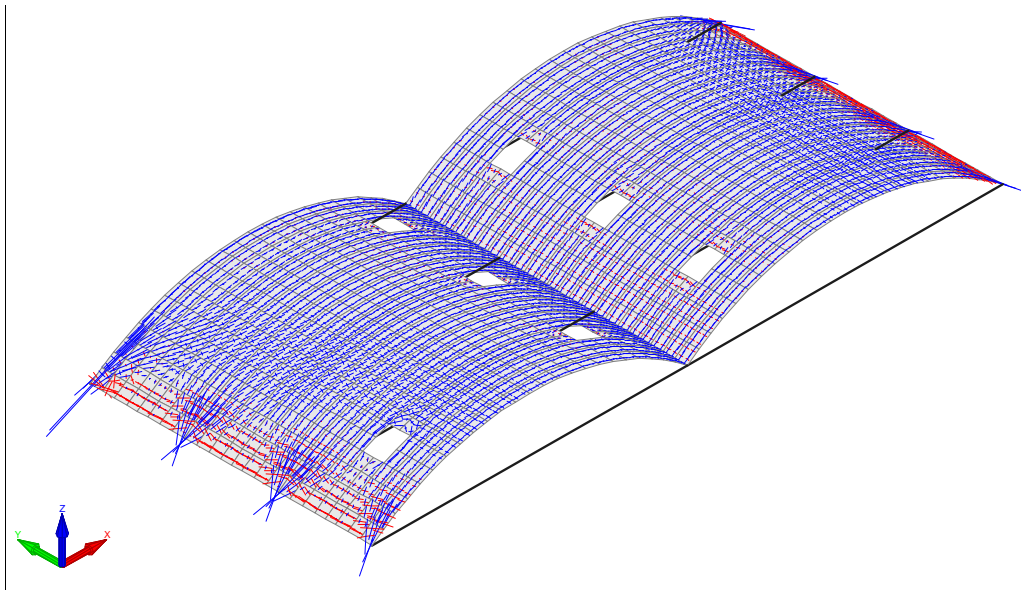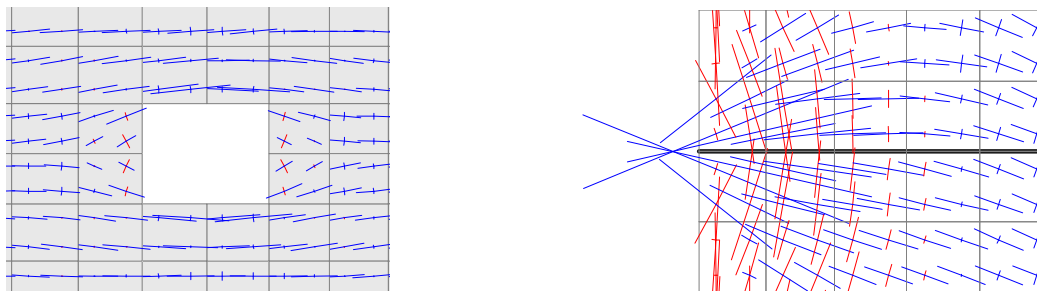f the shells due to lack of horizontal restraint by the heated tie beams. A second failure mode could theoretically be observed at elevated temperature if the temperature in the tie beams was maintained sufficiently low during the fire, as the restrained thermal bowing of the shells could lead to failure by excessive compressive forces in the concrete.

Numerical simulations are performed for the different thermal protection of the tie beams. The evolutions of the vertical deflection at mid-span of the shell are plotted as a function of time in Fig. V.3-16. It can be seen that the fire resistance of the structure highly depends on the temperature evolution in the tie beams. Results indicate that failure arises by collapse of the concrete shells (Fig. V.3-17), when the temperature increase in the tie beams is such that the tie beams cannot provide sufficient horizontal restraint to the concrete shells and consequently the compressive membrane action cannot be mobilized in the structure. The critical temperature of the tie beams at which collapse arises is approximately 550°C. Thus, an efficient way to improve the fire resistance of the structure is to delay the temperature increase in the steel tie beams by providing thermal protection.

It is interesting to note that, if the temperature in the tie beam is maintained at 20°C, no collapse occurs in the structure during the 3 hours fire exposure, which was the duration of the simulation. Temperature elevation in the concrete shells leads to important thermal bowing, and the maximum upward shell roof deflection reaches about 10 cm after 3 hours fire exposure. Yet, no collapse occurs by excess of restrained forces in the shell as could be expected. As a conclusion, the more thermal protection of the tie beams, the better is the fire performance for this structure.
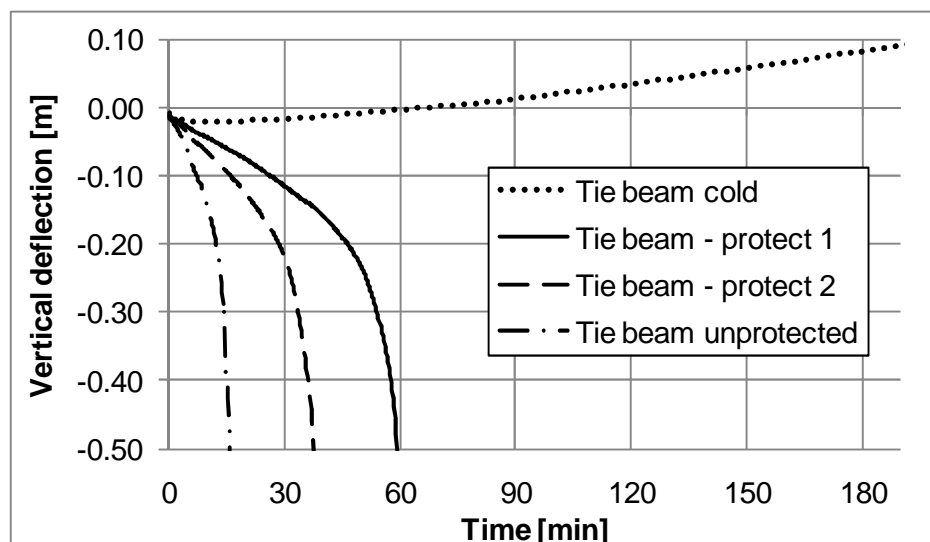
Fig. V.3-16: Mid-span deflection of the fire-exposed shell roof as a function of the thermal protection of the tie beams
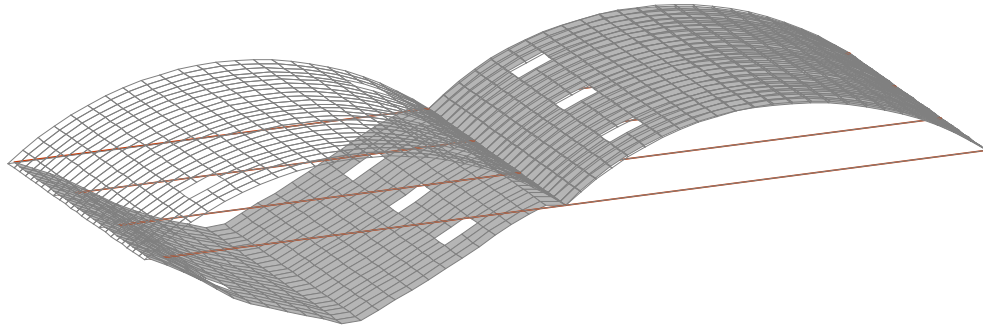
Fig. V.3-17: Deformed shape at collapse under ISO fire

This practical example, taken from a real project, illustrates the ability of the concrete model to be used for structural fire engineering applications. The robustness of the multiaxial concrete model is highlighted by this example as it was possible to simulate the structural behavior of a large structure in fire until collapse. The consistency of the concrete model for capturing the behavior of a complex structure is highlighted by the analysis of the membrane forces distribution in Fig. V.3-14 and Fig. V.3-15.

V.4. Conclusion

This last chapter has presented a significant number of numerical simulations performed with a finite elements software using the concrete model developed in this thesis. The objective was to validate the concrete model and to show that this model can be used for practical applications in structural fire engineering. The analysis of the numerical results has also allowed clarifying the validity domain of the model.

The numerical simulations of experimental tests on concrete samples have shown that the concrete model is able to capture properly the concrete behavior in numerous situations of stress and temperature states. Yet, a limitation of the model has appeared in highly confined stress states; the concrete model is not adapted for modeling the post-peak behavior of concrete subjected to multiaxial compression beyond a certain level of confinement. This limitation is related to the assumptions in the model stating that concrete continues to develop damage phenomena and softening behavior in highly confined stress states, which is refuted by the experiments. However, this limitation of the model has a marginal effect on the objectives of this work as it appears for very high levels of triaxial confinement, which are unusual stress states in structural concrete used in building applications.

The simulations of concrete samples tests have lead to the definition of a standard set of values for the parameters of the model. In many situations, it is not possible to get the values of the parameters for the particular concrete mix that will be used in the project at the time of the calculation. The standard values can then be used when a predictive calculation has to be performed using the concrete model. This method was applied successfully except for the tensile crack energy density parameter for which it was not possible to give a clear recommendation. This latter parameter is related to the localization issue and should be further studied in future works.

The simulations of experimental tests on structural elements have highlighted the reliability and accuracy of the concrete model. The model succeeded in capturing the crack pattern in a plain concrete specimen and the influence of the loading path on reinforced concrete slabs, as well as the effect of fire. For these numerical simulations, the previously defined standard set of values was used for the model parameters in order to reproduce the conditions of a predictive calculation; no calibration process was required on the structural elements.

Finally, the behavior of two large structures in fire was analyzed with a finite elements software using the concrete model. The fire analyses of these structures made part of real projects and therefore the numerical simulations presented in this chapter were challenging practical applications for the concrete model. These particular structures were chosen because they develop tensile or compressive membrane action. The numerical results highlight the ability of the concrete model to be used for such large-scale applications of structural fire engineering, which notably implies interesting properties in terms of numerical robustness.

GENERAL CONCLUSION

Summary

The aim of this thesis is to develop a model for characterization of the mechanical behavior of concrete under multiaxial stress states and high temperatures, with the purpose of using the model in practical applications of structural fire engineering. To clarify the objectives of the work, the research gives an insight into the requirements of a concrete model, based on the analysis of the experimental behavior of the material and on the study of the specific needs related to the type of applications for which the model is developed.

Combination of the elastoplastic and the damage theories is found to be an efficient strategy for the development of a concrete model that meets the defined requirements. Indeed, the elastoplasticity theory is well adapted for capturing the phenomena of dilatancy and permanent strains whereas the damage theory is suitable for modeling of stiffness degradation and unilateral effect. In addition, these theories are included in the general framework of continuum constitutive models based on a smeared crack approach, which remains very appealing for applications with large scale concrete structures and multi-cracked concrete elements.

The generalization of the multiaxial concrete model to take into account the effect of high temperatures is done by incorporating into the model the free thermal strain, the transient creep strain and proper relationships for the temperature-dependency of the material parameters. For the transient creep strain, an original model is developed to capture accurately this phenomenon while making the link with the uniaxial concrete model of Eurocode.

The multiaxial concrete model is implemented in the finite elements software SAFIR dedicated to the analysis of structures in fire. The numerical integration of the constitutive model relies on the concept of operator split with the computation of an elastic predictor and then a plastic and a damage corrector. The model is a fully three-dimensional model; therefore it can be used for any stress state. The particularization to plane stress states is treated in order to provide a proper model for shell finite elements. Besides, a model in uniaxial stress states is also derived in this work for beam finite elements.

A significant number of numerical simulations highlight the capabilities of the model. The concrete model was used successfully to simulate the behavior of concrete samples and structural elements at ambient and at high temperatures. The thesis also gives an insight into the practical implications of the transient creep strain model on the structural behavior based on experimental tests simulations on reinforced concrete columns subjected to natural fire. Finally, the simulations of two real structures subjected to fire are presented to demonstrate the applicability of the model to real applications of structural fire engineering.

Contributions to the field

This thesis proposes a new multiaxial constitutive model for concrete in fire situations. Although the model relies on the well-accepted theoretical backgrounds of elastoplasticity and damage theories and incorporates several developments presented by researchers in the literature, the thesis introduces a number of original developments. The main contributions of the study to the research field are summarized here below.

Plastic-damage model at high temperature

- Although the theoretical framework of plastic-damage formulation has been found appealing by many researchers for modeling concrete at ambient temperature, the development of a concrete plastic-damage model at high temperature has been hardly treated in the literature. The pioneer work by Nechnech, et al. (2002) was promising but presented a series of limitations. For instance, the modeling of damage by two scalars did not allow for capturing the unilateral effect, the model was only developed in plane stress state and its applicability for practical applications of structural fire engineering has not been demonstrated. In this context, the present thesis gives a further insight into the development of plastic-damage models for concrete at high temperature and it confirms the assets of the plastic-damage theoretical framework when the concrete model is intended to be used in structural applications.
- The thesis adopted the fourth-order tensor representation of isotropic damage proposed by Wu, et al. (2006) at ambient temperature, and extended its application to high temperatures. This representation by a fourth-order damage tensor that contains two damage scalar variables is required for proper modeling of the isotropic state of damage in concrete because of the different damage mechanisms that develop in tension and compression and because of the unilateral effect.

Transient creep strain

- The transient creep phenomenon is investigated in details in this thesis due to its importance in heated concrete. Transient creep models have been proposed by different authors but none of these models has imposed itself for practical applications. The models present different degrees of complexity and there exists some confusion about the phenomena that are treated and their nomenclature. The study clarifies this situation with a structural-oriented mind. It shows that the concrete models that account for the phenomenon of transient creep can be divided into two types depending on the presence or not of an explicit term for this phenomenon in the strain decomposition. Yet, it is demonstrated that only explicit models can capture the irreversibility of the phenomenon and its dependency in the stress-temperature path. It is also found that the lowest common denominator between all explicit transient creep models in the literature is the dependency on the temperature, the applied stress and the type of aggregate.

- Despite the existence of several transient creep models in the literature, it was decided to develop a new model in this study. The reason is that it is found interesting to propose a uniaxial model for concrete that includes an explicit term for transient creep strain and that is built as a generalization of the current Eurocode concrete model. Whereas the Eurocode implicit model had been developed for prescriptive design, the new model is able to compute accurately the transient creep strain that develops in performance-based situations, which may include cooling phases or load redistributions. Meanwhile, the new model can be seen as a generalization of the Eurocode model since it remains generic and it yields the same results as the Eurocode model in the simple prescriptive situations. The obvious advantage is that the Eurocode model has been widely used in the last decades and is well accepted by authorities and regulators for building design.
- The improvements of the new model compared with the Eurocode model are illustrated by several simulations. The results show that the new model gives a more accurate description of the structural response and that the Eurocode model could lead to unsafe results in performance-based design situations.
- The new model for transient creep strain has then been generalized to multiaxial stress state for incorporation in the multiaxial plastic-damage model.

Numerical implementation

- The thesis presents the numerical implementation of the model in a finite elements software dedicated to the analysis of structures in fire; therefore the model can be used by researchers in the field.
- The numerical implementation of the model raises several difficulties that have been treated in the work. Perhaps the main difficulty was related to the process of return mapping because of the use of multi-surface plasticity and softening behavior. The solution that is implemented allows for the reactivation of the yield surfaces during the return mapping according to a technique developed by Hansoulle (2008).
- The model is developed as a fully three-dimensional model. As many of the models presented in the literature are developed in plane stress state, it was of particular interest to make available a model for applications with solid three-dimensional finite elements. In addition, this allows us discussing applications in triaxial stress states such as the recent tests by Poinard, et al. (2010), which have raised interesting conclusions about the validity domain of the model.
- The application of the multiaxial model to plane stress elements is treated in the work by implementing an additional loop in the plastic corrector algorithm using a technique developed by Charras (2010), which allows for keeping the same model for three-dimensional and plane stress states. Besides, a uniaxial model is also developed in the work for use with linear members such as beams and columns and the response of the multiaxial model in uniaxial stress state is consistent with the response of the uniaxial model.

Applicability for structural fire engineers

- The thesis contributes to clarify the requirements of a constitutive model intended to be used in structural fire engineering, taking into account the new challenges in the field and the increased use of performance-based design instead of prescriptive design. Among others, the work underlines the importance of the clear identification of the parameters, the numerical robustness and the cooling phases.

- It is shown that the concrete behavior can be modeled with sufficient accuracy using a limited number of parameters, as the model contains only ten parameters that can be calibrated from three simple tests. The parameters can be calibrated when the objective is to reproduce the results of a test or when the concrete properties are well defined in the case of a very large project. However, in many cases, no calibration of the material parameters can be performed in the case of predictive calculations; therefore a standard set of values of the parameters is clearly defined in this work and it is shown that predictive calculations can successfully be performed using these parameters.

- The thesis presents numerical simulations of large structures in fire, in which complex behaviors develop such as the transition from flexural mode to membrane action. Such examples of applications are particularly demanding for the constitutive models but they are rarely considered in the literature for testing concrete models.

- Performance-based design in structural fire engineering raises the need for considering natural fire scenarios including cooling phases; however, the issues related to the behavior of concrete members during the cooling phase are still poorly documented in the literature. The thesis gives some insight into the possible risk of collapse for concrete structures during or after the cooling phase of a fire. As the practical significance of studying the cooling phase is established for concrete structures, the concrete constitutive models have to be valid also during cooling. Following this requirement, the model developed in the thesis takes into account the irreversibility of transient creep strain and the additional loss of concrete strength when cooling.

- The work incorporates some features of the Eurocode in the model; for instance the response in uniaxial compression under constant stress and increasing temperature is calibrated on the Eurocode model, and the temperature dependency of the compressive strength is taken from the Eurocode. This reference to a widely used international standard is an asset of the model with a view to its adoption by practitioners in the field.

Perspectives

The scope of the research was defined in order to meet the predefine objectives and this definition implied a series of simplifying assumptions. To conclude this thesis, it is useful to draw a non exhaustive list of the topics that could be elaborated in future research.

Spalling

The phenomenon of spalling, which may be observed in fire-exposed concrete structures, has not been studied in this research despite its possible influence on the structural response. The reason of this simplification is that, as this phenomenon depends on the combined effect of stresses and pore pressure, its modeling requires the consideration of the mass transfers and phase changes phenomena in the material model. In the future, further developments of the model to render it able to predict spalling could be an interesting step forward, although it is noteworthy that current research is making significant progress in finding design solutions for eliminating this phenomenon, for instance by adding polypropylene fibers in the concrete mixes.

Structural applications with three-dimensional solid finite elements

One important asset of the model is the fact that it is written in fully three-dimensional stress state; therefore the model can be applied to the analysis of structural elements with a real three-dimensional behavior. Practical applications in the field of building structures include, for instance, the analyses of joints, shear punching in flat slabs, or concrete filled steel tubular columns. However, no structural application using the three-dimensional version of the model is presented in this thesis because of the difficulty to find experimental data. Consequently, the study of this class of problems using the concrete model appears as a very interesting perspective for future works and this study should probably include the carrying out of experimental tests to validate the three-dimensional model at the structural level.

Internal variables driving the damage phenomenon

An important assumption of the model consists in linking the phenomena of damage and plasticity in the equations, by using plastic internal variables to drive the evolution of damage. This assumption allows for simplifying the model and reducing the number of parameters, but it also results in a limitation of the validity domain as it prevents an accurate modeling of the post-peak behavior in highly confined stress states. Recent investigations by Poinard, et al. (2010) improve the understanding of the concrete behavior in triaxial

compression notably by showing that concrete develops plasticity without degradation of its elastic properties at high level of confinement. Therefore, further developments could incorporate this knowledge into the model by using disctinct internal variables to drive the evolution of plasticity and damage in the material. Yet, it is noted that the high level of triaxial confinement considered in this discussion is very unusual in buildings; it only concerns very specific applications such as the study of impact loading in the design of nuclear vessels.

Localization

The adoption of a smeared-crack model for modeling the concrete behavior may result in a mesh-sensitivity of the numerical solution due to localization issues. In this research work, this well-known challenge in the field of concrete modeling has only been partly tackled by the introduction in the model of the material crack energies and the mesh-dependent characteristic length. Although this simplified model allows to regularize the numerical solution when a single crack develops in a concrete element, a more elaborated solution should probably be implemented to avoid the mesh-dependency in structural applications with reinforced concrete, in which numerous cracks develop. When tackling this issue, it it the author's opinion that the study has to consider the specificity of the concrete structures applications simultaneously with the concrete material behavior; for instance, the implemented solution should consider the effects of the steel reinforcement, it should not increase the computational time too much and it should be numerically robust.

REFERENCES

Abrams, M.S., 1971. Compressive strength of concrete at temperatures to 1600°F. *Temperature and Concrete*. Detroit (MI): American Concrete Institute, pp. 33-59.

Abu Al-Rub, R.K. and Voyiadjis, G.Z., 2009. Gradient-enhanced Coupled Plasticity-anisotropic Damage Model for Concrete Fracture: Computational Aspects and Applications. *International Journal of Damage Mechanics*, 18(2), pp. 115-154.

Abu Al-Rub, R.K. and Kim, S.M., 2010. Computational applications of a coupled plasticity-damage constitutive model for simulating plain concrete fracture. *Engineering Fracture Mechanics*, 77, pp. 1577–1603.

American Society for Testing and Materials, 2007. *ASTME119-00 - Standard Methods of Fire Test of Building Construction and Materials*. West Conshohocken, PA, USA.

Anderberg, Y., 1976. *Fire-exposed hyperstatic concrete structures - An experimental and theoretical study*. University of Lund, Sweden.

Anderberg, Y. and Thelandersson, S., 1976. *Stress and deformation characteristics of concrete at high temperatures: 2 experimental investigation and material behavior model*. Bulletin 54, Lund Institute of Technology, Sweden.

Annerel, E., 2010. *Assessment of the residual strength of concrete structures after fire exposure*. Ph. D. Universiteit Gent.

Bailey, C.G., Lennon, T. and Moore, D.B., 1999. The behaviour of full-scale steel framed buildings subjected to compartment fires. *The Structural Engineer*, 77(8), pp. 15-21.

Bailey, C.G., 2001. Membrane action of unrestrained lightly reinforced concrete slabs at large displacements. *Engineering Structures*, 23, pp. 470–483.

Bailey, C.G., 2004. Membrane action of slab/beam composite floor systems in fire. *Engineering Structures*, 26, pp. 1691–1703.

Baker, G., 1996. The effect of exposure to elevated temperatures on the fracture energy of plain concrete. *Materials and Structures*, 29, pp. 383-388.

Baker, G. and de Borst, R., 2005. An anisotropic thermomechanical damage model for concrete at transient elevated temperatures. *Phil. Trans. R. Soc. A.*, 363, pp. 2603-2628.

Bazant, Z.P., Caner, F.C., Carol, I., Adley, M.D. and Akers, S.A., 2000. Microplane model M4 for concrete: I Formulation with work-conjugate deviatoric stress. *Journal of Engineering Mechanics*, 126(9), pp. 944-953.

Beard, A.N., 2000. On a priori, blind and open comparisons between theory and experiment. *Fire Safety J.*, 35(1), pp. 63-66.

Belytschko, T. and Black, T., 1999. Elastic crack growth in finite elements with minimal remeshing. *Int. J. Numer. Meth. Engrg*, 45, pp. 601–620.

Belytschko, T., Moës, N., Usui, S. and Parimi, C., 2001. Arbitrary discontinuities in finite elements. *International Journal for Numerical Methods in Engineering*, 50(4), pp. 993–1013.

Bratina, S., Saje, M. and Planinc, I., 2007. The effects of different strain contributions on the response of RC beams in fire. *Eng structures*, 29, pp. 418-430.

Cadorin, J.F. and Franssen, J.M., 2003. A tool to design steel elements submitted to compartment fires – OZone V2. Part 1: pre- and post-flashover compartment fire model. *Fire Safety J*, 38, pp. 395-427.

Cadorin, J.F., Pintea, D., Dotreppe, J.C. and Franssen, J.M., 2003. A tool to design steel elements submitted to compartment fires – OZone V2. Part 2: Methodology and application. *Fire Safety J.*, 38, pp. 429-451.

Carol, I., Rizzi, E. and Willam, K., 2001a. On the formulation of anisotropic elastic degradation. I. Theory based on a pseudo-logarithmic damage tensor rate. *International Journal of Solids and Structures*, 38, pp. 491-518.

Carol, I., Rizzi, E. and Willam, K., 2001b. On the formulation of anisotropic elastic degradation. II. Generalized pseudo-Rankine model for tensile damage. *International Journal of Solids and Structures*, 38, pp. 519-546.

CAST3M, 2003. *Commissariat à l'Energie Atomique*. Available at http://www-cast3m.cea.fr/.

Comité Euro-International du Béton-Fédération internationale du béton, 1990. *CEB-FIB Model code 1990 Bulletin d'information*. Lausanne, Switzerland.

Cervenka, J. and Papanikolaou, V.K., 2008. Three dimensional combined fracture-plastic material model for concrete. *International Journal of Plasticity*, 24, pp. 2192-2220.

Charras, T., 2010. Communication privée, CEA, France.

Coleman, B.D. and Gurtin, M.E., 1967. Thermodynamics with internal state variables. *Journal of Chemistry and Physics*, 47, pp. 597–613.

Comi, C. and Perego, U., 2001. Fracture energy based bi-dissipative damage model for concrete. *Int. J. Solids Structures*, 38, pp. 6427-6454.

de Borst, R. and Peeters, P., 1989. Analysis of concrete structures under thermal loading. *Computer methods in applied mechanics and engineering*, 77, pp. 293-310.

de Borst, R., Remmers, J.C., Needleman, A. and Abellan, M.A., 2004. Discrete vs smeared crack models for concrete fracture: bridging the gap. *Int. J. Numer. Anal. Meth. Geomech.*, 28, pp. 583–607.

de Sa, C. and Benboudjema, F., 2011. Modeling of concrete nonlinear mechanical behavior at high temperatures with different damage-based approaches. *Materials and Structures*, 44, pp. 1411–1429.

Desmorat, R., Gatuingt, F. and Ragueneau, F., 2007. Nonlocal anisotropic damage model and related computational aspects for quasi-brittle materials. *Engineering Fracture Mechanics*, 74, pp. 1539–1560.

di Prisco, M., Ferrara, L., Meftah, H., Pamin, J., de Borst, R., Mazars, J. and Reynouard, J.M., 2000. Mixed mode fracture in plain and reinforced concrete: some results on benchmark tests. *Int. J. of Fracture*, 103(2), pp. 127-148.

Dimia, M.S., Guenfoud, M., Gernay, T. and Franssen, J.M., 2011. Collapse of concrete columns during and after the cooling phase of a fire. *Journal of Fire Protection Engineering*, 21(4), pp. 245–263.

Dvorkin, E.N., Cuitino, A.M. and Gioia, G., 1990. Finite elements with displacement embedded localization lines insensitive to mesh size and distortions. *Int. J. Numer. Methods Engrg.*, 30, pp. 541–564.

Ehm, C. and Schneider, U., 1985. The high temperature behavior of concrete under biaxial conditions. *Cement Concrete Res*, 15, pp. 27-34.

European Committee for Standardization, 1995. *CEN Eurocode 2 - Design of concrete structures - Part 1-2: General rules - Structural fire design. European Prestandard*. Brussels.

European Committee for Standardization, 2004a. *CEN Eurocode 2 - Design of concrete structures - Part 1-1: General rules and rules for buildings.* Brussels.

European Committee for Standardization, 2004b. *CEN Eurocode 2 - Design of concrete structures - Part 1-2: General rules – Structural fire design.* Brussels.

European Committee for Standardization, 2004c. *CEN Eurocode 4 - Design of composite steel and concrete structures - Part 1-2: General rules – Structural fire design.* Brussels.

European Committee for Standardization, 2005. *CEN Eurocode 3 - Design of steel structures - Part 1-2: General rules – Structural fire design.* Brussels.

Faria, R., Oliver, J. and Cervera, M., 1998. A strain-based plastic viscous-damage model for massive concrete structures. *Int. J. Solids Structures*, 35(14), pp. 1533-1558.

Feenstra, P.H. and de Borst, R., 1995. A plasticity model and algorithm for mode-I cracking in concrete. *Int J for Numerical Methods in Engineering*, 38, pp. 2509-2529.

Feenstra, P.H. and de Borst, R., 1996. A composite plasticity model for concrete. *International Journal of Solids and Structures*, 33, pp. 707-730.

Felicetti, R. and Gambarova, P.G., 1999. *On the residual properties of high performance siliceous concrete exposed to high temperature. Mechanics of quasi-brittle materials and structures*. Pijaudier-Cabot, G., Bittnar, Z. and Gérard B. Hermes: Paris.

Fike, R.S. and Kodur, V.K.R., 2009. An approach for evaluating the fire resistance of CFHSS columns under design fire scenarios. *Journal of Fire Protection Engineering*, 19(4) pp. 229-259.

Fletcher, I.A., Welch, S., Torero, J.L., Carvel, R.O. and Usmani, A., 2007. Behaviour of concrete structures in fire. *Thermal Science*, 11(2), pp. 37-52.

Franssen, J.-M., 1987. *Etude du comportement au feu des structures mixtes acier-beton.* Ph. D. thesis University of Liege, Belgium.

Franssen, J.-M., 1993. *Thermal elongation of concrete during heating up to 700°C and cooling; Stress-strain relationship of Tempcore steel after heating up to 650°C and cooling.* Liege, Belgium : Univ. of Liege.

Franssen, J.-M., 1997. *Contributions à la modélisation des incendies dans les bâtiments et de leurs effets sur les structures.* Post doctoral thesis University of Liege, Belgium..

Franssen, J.-M., 2005a. Plastic analysis of concrete structures subjected to fire. In: Gambarova, P.G., Felicetti, R., Meda, A. and Riva, P. *Proceedings of the Workshop Fire Design of Concrete Structures: What now? What next?*, Brescia: Starrylink Editrice Brescia, pp. 133-145.

Franssen, J.-M., 2005b. SAFIR: A thermal/structural program for modeling structures under fire. *Engineering Journal - A.I.S.C*, 42(3), pp. 143-158.

Franssen, J.-M., Gernay, T., Hanus, F. and Peigneux, C., 2010. Evaluation of structural fire performance. Today and tomorrow. *Buildsoft 20th anniversary*: Brussels.

Gawin, D., Pesavento, F. and Schrefler, B.A., 2004. Modelling of deformations of high strength concrete at elevated temperatures. *Materials and Structures: Concrete Science and Engineering*, 37, pp. 218-236.

Gernay, T. and Franssen, J.M., 2010. *FICEB W.P.6 final report: Numerical simulations of the large scale fire test*. Liege: ULg, 2010.

Gernay, T. and Dimia, M.S., 2011. Structural behavior of concrete columns under natural fires including cooling down phase. In: Barros, H., Faria, R., Pina, C. and Ferreira, C. *Proceedings of The International Conference on Recent Advances in Nonlinear Models - Structural Concrete Applications*, Coimbra, Portugal 24-25 Nov. 2011. RAGRAF, pp. 637-656.

Gernay, T. and Franssen, J.M., 2011. *Analysis of the fire resistance of a concrete shell roof structure*. Liege: ULg, 2011.

Gernay, T. and Franssen, J.-M., 2012. A formulation of the Eurocode 2 concrete model at elevated temperature that includes an explicit term for transient creep. *Fire safety journal*, 51, pp. 1-9.

Gernay, T., 2012. Effect of Transient Creep Strain Model on the Behavior of Concrete Columns Subjected to Heating and Cooling. *Fire Technology.* 48(2), pp. 313-329.

Ghoneim, M.G. and MacGregor, J.G., 1992. *Strength and Stability of Reinforced Concrete Plates Under Combined Inplane and Lateral Loads*. Structural Engineering Report No. 176. Alberta, Canada: Department of Civil Engineering, University of Alberta.

Gopalaratnam, V.S. and Shah, S. P., 1985. Softening Response of Plain Concrete in Direct Tension. *ACI Journal Proceedings*, 82(3), pp. 310-323.

Grassl, P., Lundgren, K. and Gylltoft, K., 2002. Concrete in compression: a plasticity theory with a novel hardening law. *International Journal of Solids and Structures*, 39, pp. 5205-5223.

Grassl, P. and Jirasek, M., 2006. Damage-plastic model for concrete failure. *International Journal of Solids and Structures*, 43, pp. 7166-7196.

Hansoulle, T., 2008. *Modélisation numérique des lois de matériaux en état plan de contrainte - théorie de la plasticité*. Projet FIRST 5380. Liege.

Heinfling, G., 1998. *Contribution à la modélisation numérique du comportement du béton et des structures en béton armé sous sollicitations thermo-mécaniques à hautes températures*. Ph. D. thesis INSA Lyon.

Hillerborg, A., Modeer, M. and Petersson, P.E., 1976. Analysis of crack formation and crack growth in concrete by means of fracture mechanics and finite elements. *Cement and concrete research*, 6(6), pp. 773-782.

Hilsdorf, H.K. and Brameshuber, W., 1991. Code-type formulation of fracture mechanics concepts for concrete. *International Journal of Fracture*, 51, pp. 61-72.

Hody, P., 2004. *Seven Swiss Firefighters Die in Collapsed Parking Garage*. [online] Available at <http://www.firehouse.com/news/lodd/seven-swiss-firefighters-die-collapsed-parking-garage>. [Accessed 09 Sep 2011].

Hugues, B.P. and Chapman, G.P., 1966. The deformation of concrete and micro-concrete and tension with particular reference to aggregate size. *Magazine of Concrete Research*, 18(54), pp. 19-24.

Imran, I., 1994. *Applications of nonassociated plasticity in modeling the mechanical response of concrete*. Ph. D. thesis University of Toronto.

International Standards Office, 1975. *ISO834 – Fire resistance tests - elements of building construction*. Geneva: ISO.

Japanese Industrial Standards, 1969. *JIS A-1304 - Method of testing the fire resistance of construction parts*, Enforcement No.2999. Ministry of Construction of Japan.

Jason, L., Huerta, A., Pijaudier-Cabot, G. and Ghavamian, S., 2006. An elastic-plastic damage formulation for concrete: Application to elementary tests and comparison with an isotropic damage model. *Computed Methods in Applied Mechanics and Engineering*, 195(52), pp. 7077-7092.

Jirasek, M. and Bazant, Z.P., 2002. *Inelastic analysis of structures*. Chichester: Wiley.

Ju, J., 1989. On energy-based coupled elasto-plastic damage theories: constitutive modeling and computational aspects. *Int. J. Solids Struct.*, 25, pp. 803-833.

Ju, J., 1990. Isotropic and anisotropic damage variables in continuum damage mechanics. *J. Eng. Mech. ASCE*, 116(12), pp. 2764–2770.

Karsan, I.D. and Jirsa, J.O., 1969. Behavior of concrete under compressive loadings. *J. Struct. Div. ASCE.*, 95(12), pp. 2535-2563.

Khennane, A. and Baker, G., 1992. Thermoplasticity Model for Concrete under Transient Temperature and Biaxial Stress. *Proc. R. Soc. Lond.*, 439, pp. 59-80.

Khoury, GA., Grainger, BN. and Sullivan, PJE., 1985a. Transient thermal strain of concrete: literature review, conditions within specimen and behavior of individual constituents. *Mag. Concrete Research*, 37(132), pp. 131-144.

Khoury, GA., Grainger, BN. and Sullivan, PJE., 1985b. Strain of concrete during first heating to 600°C under load. *Magazine of Concrete Research*, 37(133), pp. 195-215.

Kirby, B.R., Lapwood, D.G. and Thomson, G., 1986. *The reinstatement of fire damaged steel and Iron Framed Structures*. Swinden Laboratories: British Steel Corporation.

Kodur, V.K.R., 1999. Performance-based Fire Resistance Design of Concrete-filled Steel Columns. *J. Constr. Steel Res. Institute*, 51, pp. 21-36.

Koiter, W.T., 1953. Stress-strain relations, uniqueness and variational theorems for elastic-plastic materials with a singular yield surface. *Q. Appl. Math.*, 11, pp. 350-354.

Krätzig, W. and Pölling, R., 2004. An elasto-plastic damage model for reinforced concrete with minimum number of material parameters. *Computers and Structures*, 82(15-16), pp. 1201-1215.

Kupfer, H.B., Hilsdorf, H.K. and Rüsch, H., 1969. Behavior of concrete under biaxial stresses. *Journal of the American Concrete Institute*, 66, pp. 656-666.

Kupfer, H.B. and Gerstle, K.H., 1973. Behavior of concrete under biaxial stresses. *Journal of the Engineering Mechanics Division ASCE.*, 99, pp. 853-866.

Launay, P. and Gachon, H., 1971. Strain and ultimate strength of concrete under triaxial stress. In: Commission of European Communities. *Proc. 1st Int. Conf. on Struct. Mech. in Reactor Technol. (SMiRT1)*. Vol. 3, pp. 1-12. Brussels: T. Jaeger.

Law, A. and Gillie, M., 2008. Load induced thermal strain: implications for structural behavior. In: Tan, K.H., Kodur, V., Tan, T.H. *Proc. of the Fifth International Conference Structures in Fire SIF 2008*. Nanyang Techn. University, Singapore, pp. 488-496.

Lee, J. and Fenves, G.L., 1998. Plastic-damage model for cyclic loading of concrete structures. *Journal of Engineering Mechanics ASCE*, 124(8), pp. 892-900.

Lemaitre, J., Chaboche, J.L., Benallal, A., Desmorat, R., 2009. *Mécanique des matériaux solides*. Paris: Dunod, 3rd edition.

Li, L. and Purkiss, J., 2005. Stress-strain constitutive equations of concrete material at elevated temperatures. *Fire Safety Journal*, 40, 669-686.

Li, T. and Crouch, R., 2010. A C2 plasticity model for structural concrete. *Computers and Structures*, 88(23-24), pp. 1322–1332.

Li, Y.H. and Franssen, J.M., 2011. Test results and model for the residual compressive strength of concrete after a fire. *J. of Struct. Fire Eng.*, 2(1), pp. 29-44.

Lie, T.T., 1992. *Structural fire protection*. New York: American Society of Civil Engineers.

Lim, L. and Wade, C., 2002. *Experimental Fire Tests of two-way concrete slabs*. Fire Engineering Research Report 02/12. Porirua City, New Zealand: BRANZ Limited, p. 106.

Lim, L., Buchanan, A., Moss, P. and Franssen, J.M., 2004. Numerical modelling of two-way reinforced concrete slabs in fire. *Engineering Structures*, 26, pp. 1081-1091.

Lin, W.M., Lin, T.D. and Powers-Couche, L.J., 1996. Microstructure of fire damaged concrete. *ACI Mat J.*, 93(3), pp. 199–205.

Lubliner, J., Oliver, J., Oller, S. and Onate, E., 1989. A plastic-damage model for concrete. *Int. J. Solids Struct.*, 25(3), pp. 299-326.

Luccioni, B.M., Figueroa, M.I. and Danesi, R.F., 2003. Thermo-mechanic model for concrete exposed to elevated temperatures. *Engineering Structures*, 25(6), 729-742.

Majorana, C.E., Salomoni, V.A., Mazzucco, G. and Khoury, G.A., 2010. *An approach for modelling concrete spalling in finite strains. Mathematics and Computers in Simulation*, 80, pp. 1694-1712.

Maréchal, J.C., 1970. *Variations in the modulus of elasticity and poisson's ratio with temperature.* In: ACI. *Int. Seminar on CNR*. Berlin.

Matallah, M. and La Borderie, C., 2009. *Inelasticity-damage-based model for numerical modeling of concrete cracking. Engineering Fracture Mechanics*, 76, pp. 1087-1108.

Mazars, J., 1984. *Application de la mécanique de l'endommagement au comportement non linéaire et à la rupture du béton de structure.* Ph. D. thesis Université Paris VI.

Meacham, B.J. and Custer, R.P.L., 1992. Performance-based Fire Safety Engineering: An Introduction of Basic Concepts. *J. Constr. Steel Res. Institute*, 7, pp. 35–54.

Menetrey, Ph. and Willam, K.J., 1995. Triaxial failure criterion for concrete and its generalization. *ACI Structural Journal*, 92, pp. 311-318.

Menou A., Mounajed, G., Boussa, H., Pineaud, A. and Carre, H., 2006. Residual fracture energy of cement paste, mortar and concrete subject to high temperature. *Theoretical and Applied Fracture Mechanics*, 45(1), pp. 64-71.

Meschke, G., Lackner, R. and Mang, H., 1998. An anisotropic elastoplastic-damage model for plain concrete. *Int J for Numerical Methods in Engineering*, 42(4), pp. 703-727.

Nechnech, W., 2000. *Contribution à l'étude numérique du comportement du béton et des structures en béton armé soumises à des sollicitations thermiques et mécaniques couplées: Une approche thermo-élasto-plastique endommageable.* Ph. D. thesis INSA Lyon.

Nechnech, W., Meftah, F. and Reynouard, J.M., 2002. An elasto-plastic damage model for plain concrete subjected to high temperatures. *Engineering Structures*, 24, pp. 597-611.

Nielsen, C.V., Pearce, C.J. and Bicanic, N., 2002. Theoretical model of high temperature effects on uniaxial concrete member under elastic restraint. *Magazine of Concrete Research*, 54(4), pp. 239-249.

Nielsen, C.V. and Bicanic, N., 2003. Residual fracture energy of high-performance and normal concrete subject to high temperature. *Materials and Structures*, 36, pp. 515-521.

Nooru-Mohamed, M.B., 1992. *Mixed-mode fracture of concrete: an experimental approach.* Ph. D. thesis, Delft University of Technology.

Oliver, J., Linero, D.L., Huespe, H.E. and Manzoli, O.L., 2008. Two-dimensional modeling of material failure in reinforced concrete by means of a continuum strong discontinuity approach. *Computer Methods in Applied Mechanics and Engineering*. 197(5), pp. 332-348.

Onate, E., Oller, S., Oliver, J. and Lubliner, J., 1993. A constitutive model for cracking of concrete based on the incremental theory of plasticity. *Engineering Computations: Int J for Computer-Aided Engineering*, 5(4), pp. 309-319.

Ortiz, M., 1985. A constitutive theory for the inelastic behavior of concrete. *Mechanics of Materials*, 4, pp. 67-93.

Ottosen, N.S., 1977. A failure criterion for concrete. *J. Eng. Mech. Div. ASCE*, 103, pp. 527-535.

Pandolfi, A. and Ortiz, M., 2002. An efficient adaptive procedure for three-dimensional fragmentation Simulations. *Engrg. Comput.*, 18, pp. 148–159.

Papanikolaou, V.K. and Kappos, A.J., 2007. Confinement-sensitive plasticity constitutive model for concrete in triaxial compression. *Int. J. Solids and Struct.*, 44, pp. 7021-7048.

Park, H. and Kim, J.-Y., 2005. Plasticity model using multiple failure criteria for concrete in compression. *Int J of Solids and Structures*, 42, pp. 2303–2322.

Pearce, C.J., Nielsen, C.V. and Bićanić, N., 2004. Gradient enhanced thermo-mechanical damage model for concrete at high temperatures including transient thermal creep. *Int J Numerical and Analytical Methods in Geomechanics*, 28(7-8), pp. 715-735.

Persson, B., 2003. *Self-compacting concrete at fire temperature*. Report TVBM-3110. Sweden (Lund): Division of building materials, Lund Institute of Technology.

Petkovski, M., 2010. Effects of stress during heating on strength and stiffness of concrete at elevated temperature. *Cement and concrete research*, 40, pp. 1744-1755.

Pivonka, P., Ožbolt, J., Lackner, R. and Mang, H.A., 2004. Comparative studies of 3D-constitutive models for concrete: application to mixed-mode fracture. *Int. J. Numer. Meth. Engng.*, 60, pp. 549–570.

Poinard, C., Malecot, Y. and Daudeville, L., 2010. Damage of concrete in a very high stress state: experimental investigation. *Materials and Structures*, 43, pp. 15-29.

Pramono, E. and Willam, K.J., 1989. Implicit integration of composite yield surfaces with corners. *Engng Comput.*, 7, pp. 186-197.

Purkiss, J.A., 1996. *Fire safety engineering, design of structures*. Oxford: Butterworth Heinemann.

Ramtani, S., 1990. *Contribution à la modélisation du comportement multiaxial du béton endommagé avec description du caractère unilatéral*. Ph. D. thesis Université de Paris VI E.N.S. de Cachan.

Reinhardt, H.W., 1984. Fracture mechanics of an elastic softening material like concrete. Heron, 29(2), pp. 1-42.

Richard, B., Ragueneau, F., Cremona, C. and Adelaide, L., 2010. Isotropic continuum damage mechanics for concrete under cyclic loading: Stiffness recovery, inelastic strains and frictional sliding. *Engineering Fracture Mechanics*, 77, pp. 1203–1223.

Rots, J.G., 1988. Computational modelling of concrete fracture. Ph. D. thesis, Delft University of Technology.

Schneider, U., 1982. *Behavior of concrete at high temperatures*. Berlin: Deutscher Ausschuss fur Stahlbeton, 337.

Schneider, U., 1985. *Properties of materials at high temperatures: concrete*. Kassel, Germany: RILEM.

Schneider, U., 1988. Concrete at high temperatures - a general review. *Fire Safety Journal*, 13, pp. 55-68.

Schneider, U., Morita, T. and Franssen, J.-M., 1994. A concrete model considering the load history applied to centrally loaded columns under fire attack. In: *Proc. Of the Fourth Int Symposium on Fire Safety Science*. Ottawa, pp. 1101-1112.

Schneider, U., Schneider, M. and Franssen, J.-M., 2008. Consideration of nonlinear creep strain of siliceous concrete on calculation of mechanical strain under transient temperatures as a function of load history. In: Tan, K.H., Kodur, V., Tan, T.H. *Proc. of the Fifth International Conference Structures in Fire SIF 2008*. Nanyang Techn. University, Singapore. pp. 463-476.

Schneider, U. and Schneider, M., 2009. An Advanced Transient Concrete Model for the Determination of Restraint in Concrete Structures Subjected to Fire. *Journal of Advanced Concrete Technology*, 7(3), pp. 403-413.

Schrefler, B.A., Majorana, C.E., Khoury, G.A. and Gawin, D., 2002. Thermo-hydro-mechanical modelling of high performance concrete at high temperatures. *Engineering Computations*, 19(7), pp. 787-819.

Shah, S.P., Swartz, S.E. and Ouyang, C., 1995. *Fracture mechanics of concrete: applications of fracture mechanics to concrete, rock and other quasi-brittle materials*. New York: John Wiley & Sons.

Simo, J.C. and Hugues, T.J.R., 1998. *Computational inelasticity*. New York: Springer.

Sluys, L.J. and Berends, A.H., 1998. Discontinuous failure analysis for mode-I and mode-II localization problems. *Int. J. Solids Structures*, 35(31-32), pp. 4257-4274.

Tao, X. and Phillips, D., 2005. A simplified isotropic damage model for concrete under biaxial stress states. *Cement and Concrete Composites*, 27, pp. 716-726.

Tenchev, R. and Purnell, P., 2005. An application of a damage constitutive model to concrete at high temperature and prediction of spalling. *Int J Solids Struct.*, 42, pp. 6550-6565.

Terro, M., 1998. Numerical modeling of the behavior of concrete structures in fire. *ACI Structural Journal*, 95(2), pp. 183-193.

Thelandersson, S., 1987. Modelling of combined thermal and mechanical action in concrete. *ASCE J. Engrg. Mech.*, 113, pp. 893-906.

ULg-Globalview. *ULg Photographies*. [photograph online] (c) ULg-Globalview. Available at <http://www.ulg.ac.be/cms/c_18014/europe> [accessed 15 May 2012].

van Mier, J.G.M., 1984. *Strain-softening of concrete under multiaxial loading conditions*. Ph. D. thesis Technical University of Eindhoven.

Vassart, O., Bailey, C.G., Hawes, M., Nadjai, A., Simms, W.I., Zhao, B., Gernay, T. and Franssen, J.M., 2011. Large-Scale Fire Test of Unprotected Cellular Beam Acting in Membrane Action. *Journal of Structural Fire Engineering*, 2(4), pp. 259-268.

von Mises, R., 1913. Mechanik der festen Körper im plastisch deformablen Zustand. *Nachrichten von der Königlichen Gesellschaft der wissenschaften zu Göettinger, Mathematisch-physikalische Klasse*, pp. 582-592.

Voyiadjis, G., Taqieddin, Z. and Kattan, P., 2008. Anisotropic damage-plasticity model for concrete. Internation Journal of Plasticity, 24(10), pp. 1946–1965.

Wald, F. and Kallerova, P., 2009. *Draft Summary of Results from Fire Test in Mokrsko 2008*. Prague : Ceska technika, ISBN 978-8004267-0.

Wang, Y.C., 1996. Tensile membrane action in slabs and its application to the Cardington tests. In: *Fire, static and dynamic tests of building structures, Proceedings of the Second Cardington Conference*, England, 12–14 March, pp. 55–67.

William, K.J. and Warnke, E.P., 1974. Constitutive model for the triaxial behavior of concrete. *Seminar on Concrete Structures Subjected to Triaxial Stresses. Int. Assoc. of Bridge and Struct. Engng. Conf.*, Bergamo, Italy.

Williams-Leir, G., 1983. Creep of structural steel in fire: analytical expressions. *Fire and Materials*, 7(2), pp. 73-78.

Wu, B., Li, Y.H. and Chen, S.L., 2010. Effect of heating and cooling on axially restrained RC columns with special-shaped cross section. *Fire Technology*, 46, pp. 231-249.

Wu, J.Y., Li, J. and Faria, R., 2006. An energy release rate-based plastic-damage model for concrete. International Journal of Solids and Structures, 43, pp. 583–612.

Xiaoa, J. and Konig, G., 2004. Study on concrete at high temperature in China - an overview. *Fire Safety Journal*, 39, pp. 89-103.

Xu, Y., Wong, Y.L., Poon, C.S. and Anson, M., 2003. Influence of PFA on cracking of concrete and cement paste after exposure to high temperatures. *Cement and Concrete Research*, 33, pp. 2009-2016.

Youssef, M.A. and Moftah, M., 2007. General stress-strain relationship for concrete at elevated temperatures. *Engineering structures*, 29, pp. 2618-2634.

Zhao, B., Roosefid, M. and Vassart, O., 2008. Full scale test of a steel and concrete composite floor exposed to ISO fire. In: Tan, K.H., Kodur, V., Tan, T.H. *Proc. of the Fifth International Conference Structures in Fire SIF 2008*. Nanyang Techn. University, Singapore.